DISSERTATION

Submitted to the
Combined Faculties of Natural Sciences and Mathematics
of the Ruperto-Carola University
Heidelberg, Germany
for the degree of
Doctor of Natural Sciences

Put forward by
M.Sc. Maria Carolina Amorim Catunda
Born in São Paulo, Brazil
Oral examination: 23.07.2021

Subsurface heat transport in the North Atlantic during the Middle and Late Pleistocene

Referees:

PD Dr. André Bahr

Prof. Dr. Zhang Xu

Abstract

Due to the large thermal inertia of water, the oceans are Earth's largest heat reservoir and the primary regulator of global climate on long timescales. The ocean absorbs, stores and distributes heat through the planet, and shifting ocean circulation patterns can disrupt established climate regimes. Comparably, the cryosphere modulates the Earth's climate because ice sheets reflect radiation from the Sun and serve as a reservoir of freshwater, thereby modulating sea level, which affects the large human populations that inhabit coastal zones. Thus, ocean and cryosphere are two significant agents of Earth's climate system and tightly connected by feedbacks on millennial and orbital timescales. Understanding the internal mechanisms that control such feedbacks is crucial for refining numerical and conceptual models and aid public policy decisions to deal with the repercussions of anthropogenic climate change. However, scientific knowledge about long-timescale ocean-cryosphere interactions is hampered by the geographically sparse and relative short length of observational records. The reconstruction of climate patterns on longer timescales requires the production and interpretation of proxy records and are the scope of this thesis.

The close proximity between ice sheets and areas of deep-water formation makes the North Atlantic one of the most climate sensitive areas on the planet. There, the transition zone between the subtropical and subpolar gyres is susceptible to latitudinal shifts of oceanic fronts and was reached by icebergs laden with debris during periods of ice-sheet destabilization since the beginning of the Pleistocene. Additionally, subsurface density layers that connect both gyres at depth are the pathway through which low-latitude heat may reach high latitudes and either feed moisture or accelerate the demise of ice sheets. To assess the relationship between the ocean heat transport and the cryosphere over millennial and orbital timescales, two sets of proxy records were produced from deep-sea marine sediment cores retrieved from the transition zone between both gyres in the North Atlantic.

The first set of records allowed for the reconstruction of subsurface temperatures and salinity during the Last Glacial Maximum and last glacial termination, a period of ice-sheet demise. During this time interval, the climate of the northern hemisphere went through several abrupt shifts accompanied by equally abrupt changes in oceanic circulation, that resulted in a sea-level rise of ca. 120 m above the glacial baseline. A compilation of new and published proxy records showed that subsurface warming preceded the deposition of debris transported by icebergs, implicating that northward heat transport triggered or accelerated the demise of glacial ice sheets.

A second set of proxy records produced from materials of the same location was used to reconstruct subsurface temperatures at mid-latitudes and oceanic circulation patterns between mid and high latitudes during the Mid-Pleistocene Transition. This interval was characterized by the transition from 40-kyr to 100-kyr glacial-interglacial cyclicity of the Late Pleistocene and was period of significant ice-sheet enlargement. The produced data suggested a prominent role for low-latitude forcing in driving the

northward transport of heat when cold surface temperatures and low atmospheric CO_2 would have starved ice sheets of moisture and hampered their growth. Additionally, modern-like gradients between mid- and high-latitude oxygen isotope records from the surface, intermediate and deep ocean, indicate the establishment of the Late Pleistocene ocean circulation during this second interval.

In ensemble, the data produced within the framework of this thesis were used to suggest a new mechanism of northward heat transport that is closely coupled to the fate of northern hemisphere ice sheets during the Middle and Late Pleistocene. Furthermore, the new data suggest that the causal relationship between northward heat transport and deep-water formation may need to be revaluated to better constrain climate and oceanic circulation in future high-CO_2 model scenarios.

Kurzfassung

Die erhebliche thermische Trägheit von Wasser macht die Ozeane zum größten Wärmereservoir der Erde und damit zum primären Regler für globale klimatische Veränderungen über lange Zeitintervalle. Ozeane absorbieren, speichern und verteilen Wärme über den Planeten. Eine sich verändernde ozeanische Zirkulation kann daher etablierte klimatische Bedingungen unterbrechen und verändern. Vergleichbar ist dies mit der Kryosphäre, die das Klima der Erde moduliert, indem Sonnenstrahlung durch vorhandenes Eis reflektiert wird. Vereisungen stellen zudem ein großes Süßwasser-Reservoir dar, dessen Masse den Meeresspiegel steuert und damit menschliche Ansiedlungen, insbesondere in Küstenregionen, stark beeinflusst. Die Ozeane und die Kryosphäre sind die bedeutendsten Komponenten des Klimasystems der Erde und über Rückkopplungs-Mechanismen, die sich zyklisch über orbitale Zeitskalen verändern, eng miteinander verknüpft. Das Verständnis der internen Mechanismen, die solche Rückkopplungen steuern, ist entscheidend für die Verfeinerung numerischer und konzeptioneller Modelle und unterstützt daher auch öffentliche politische Entscheidungen im Umgang mit den Auswirkungen des anthropogenen Klimawandels. Dennoch sind wissenschaftliche Erkenntnisse über die langzeitlichen Wechselwirkungen zwischen Ozeanen und Kryosphäre vor allem durch mangelnde globale Abdeckung von klimatischen Archiven und zeitlich nicht ausreichende Beobachtungsintervalle eingeschränkt. Die Rekonstruktion klimatischer Muster über längere Zeitskalen erfordert das Erarbeiten und die Interpretation neuer Proxy-Daten, was Gegenstand der vorliegenden Arbeit ist.

Die enge räumliche Nähe von großen Eismassen und Bereichen, in denen Tiefenwasser gebildet wird, macht den Nordatlantik zu einem der klimatisch sensibelsten Gebiete der Erde. Eine dortige Übergangszone zwischen dem subtropischen und dem subpolaren Wirbel ist empfänglich für die Breitenverschiebung ozeanischer Fronten. Seit dem Beginn des Pleistozäns erreichten während Phasen instabiler Vereisungen immer wieder Eisberge zusammen mit glazialen Sedimenten dieses Areal. Dichtere Wassermassen direkt unterhalb der atmosphärisch beeinflussten Wasseroberfläche, die die beiden Wirbel in der Tiefe miteinander verbinden, sind darüber hinaus ein Weg, über den Wärme aus niedrigen Breitengraden wiederum in die hohen Breiten gelangen kann, und entweder Feuchtigkeit zuführen oder den Zerfall der Eisschilde beschleunigen kann. Um die Beziehung zwischen ozeanischem Wärmetransport und der Kryosphäre über orbitale Zeitskalen zu beurteilen, wurden zwei zusammenhängende Proxy-Datensätze aus Tiefsee-Sedimentkernen gewonnen, die aus der Übergangszone zwischen beiden Wirbeln im Nordatlantik stammen.

Ein erster Datensatz ermöglichte die Rekonstruktion von Temperaturen und Salinitäten unterhalb der Wasseroberfläche während des letzten glazialen Maximums und dessen Abklingen, und der damit einhergehenden Reduktion von Vereisungen. Während dieser Zeitspanne änderten sich die klimatischen Bedingungen in der nördlichen Hemisphäre mehrfach abrupt. Diese Umschwünge gingen einher mit

ähnlich abrupten Änderungen der ozeanischen Zirkulation, die zu einem zur Vereisung relativen Meeresspiegelanstieg von ca. 120 m führten. Mithilfe der Evaluation von bereits publizierten und neu erarbeiteten Proxy-Daten kann gezeigt werden, dass ein Anstieg der Wassertemperaturen unterhalb der Oberfläche bereits vor der Ablagerung von glazialen Sedimenten stattfand, die durch Eisberge in den Nordatlantik antransportiert wurden. Die Daten führen daher zur Annahme, dass der Wärmetransport unterhalb der Wasseroberfläche in höhere Breiten das Abschmelzen von Gletschern beschleunigt oder sogar ausgelöst hat.

Ein weiterer Proxy-Datensatz aus Sedimenten derselben Lokalität wurde verwendet, um Temperaturen unter der Wasseroberfläche in mittleren Breiten, und die ozeanischen Zirkulationsmuster zwischen mittleren und hohen Breiten des Nordatlantiks während der mittelpleistozänen Klimarevolution zu rekonstruieren. Charakteristisch für dieses Zeitintervall, den Übergang von einer 40-ka-Glazial-Interglazial-Zyklizität hin zur 100-ka-Zyklizität des Oberpleistozäns, ist eine signifikante Zunahme der Eismasse. Die vorliegenden Daten legen eine herausragende Rolle der Präzession nahe, die einen ozeanischen Wärmetransport in den Norden antreibt, während geringe Oberflächentemperaturen und eine geringe Konzentration von atmosphärischem CO_2 den Gletschern Feuchtigkeit entziehenund so ihr Wachstum behindern würden. Darüber hinaus deuten Gradienten in der Sauerstoff-Isotopie zwischen mittleren und hohen Breiten, die mit rezenten Daten aus verschiedenen Wassertiefen vergleichbar sind, auf die Bildung der oberpleistozänen Ozeanzirkulation während dieses zweiten Zeitintervalls hin.

Zusammenfassend führen die Daten, die im Rahmen der vorliegenden Arbeit gewonnen wurden, zur Erarbeitung und Präsentation eines neuen Mechanismus für den ozeanischen Wärmetransport in nördliche Breiten. Dieser Mechanismus ist eng verknüpft mit glazialen Veränderungen in der nördlichen Hemisphäre während des mittleren und späten Pleistozäns. Zudem zeigen die neuen Daten, dass ein ursächlicher Zusammenhang zwischen dem Wärmetransport in den Norden und der dortigen Bildung von Tiefenwasser neu bewertet werden muss. Dadurch kann eine detailliertere Berücksichtigung von klimatischen Bedingungen und ozeanischer Zirkulation bei zukünftigen Klimamodellen mit höheren CO_2-Konzentrationen erreicht werden.

Da minhoca com olhos de jabuticaba para quem a trouxe na cauda de um cometa.
Caiu do céu, andou pelo mato, saltou no mar e quer ir pro fim do mundo.

-Jabuticabal da Guarucaia

Contents

List of abbreviations

AAIW – Antarctic Intermediate Water

AIS – Antarctic Ice Sheets

amcd – adjusted meters composite depth

AMOC – Atlantic Meridional Overturning Circulation

BWT – bottom-water temperature

$\delta^{13}C$ – isotopic ratio between ^{13}C and ^{12}C

$\delta^{18}O$ – isotopic ratio between ^{18}O and ^{16}O

$\Delta\delta^{13}C$ – vertical carbon gradient between deep-thermocline and bottom waters

DIC – dissolved inorganic carbon

DSDP – Deep Sea Drilling Project

eSPG – eastern subpolar gyre

EIS – European Ice Sheets

GNAIW – Glacial North Atlantic Intermediate Water

ISOW – Iceland-Scotland Overflow Waters

IODP – Integrated Ocean Drilling Project

IRD – Ice-rafted debris

ITCZ – Intertropical Convergence Zone

ka – kiloannum, kiloyear before present

kyr – kiloyear

LGM – Last Glacial Maximum

LIS - Laurentide Ice Sheets

LIW – Levantine Intermediate Water

LSW - Labrador Sea Water

Ma – Megaannum, million years before present

mcd – meters composite depth

MHF – meridional heat flux

MIS – Marine Isotope Stage

MOW – Mediterranean Outflow Water

MPT – Mid-Pleistocene Transition

NAC – North Atlantic Current

NADW – North Atlantic Deep Water

NEADW – Northeastern Atlantic Deep Water

NENA – Northeastern North Atlantic

NH – Northern Hemisphere

NSW – northern-sourced waters

NSOW - Nordic Seas Overflow Water

NWNA – Northwestern North Atlantic

OSNAP – Overturning in the Subpolar Gyre Program

ppm – parts per million

psu – practical salinity units

σ_0 – density of sea water subjected to the pressure of 1 atmosphere in kg/m^3

SEM – Scanning Electron Microscopy

SMOW – Standard Mean Ocean Water

SPG - subpolar gyre

SPMW - Subpolar Mode Waters

SST – sea-surface temperatures

SSW – southern-sourced waters

STG - subtropical gyre

STMW – Subtropical Mode Water

Θ – potential temperature of sea water

T_{crass} – deep-thermocline temperatures based on Mg/Ca ratios of *G. crassaformis*

T_{trunc} – deep-thermocline temperatures based on Mg/Ca ratios of *G. truncatulinoides* (d)

VPDB – Vienna Pee Dee Belemnite

WMDW – Western Mediterranean Deep Water

List of Figures

1 Scientific motivation and rationale

Anthropogenically-induced climate change has the potential to impact the Earth's energy balance and therefore poses a large-scale societal hazard. By preventing the escape of infrared radiation to space, greenhouse gases increase the surface energy budget leading to increased unpredictability of weather and climate patterns centuries (IPCC, 2014). The projected higher frequency of abrupt climate-related events and decreased agricultural output threatens human lives and infrastructure around the globe. Therefore, the accuracy of climate-model projections is of the utmost importance to predict climate shifts and base adaptation programmes; however, these models are limited by the scientific understanding about long-term climate system interactions and feedback loops. As instrumental records are geographically sparse and limited to the last ~150 years, proxy studies are necessary to affirm knowledge and shed light into background processes that drive climate change on timescales longer than a few centuries (IPCC, 2014).

The ocean is the Earth's largest sink and reservoir of heat and carbon, and is thus a significant modulator of climate on timescales longer than a decade (Speich, 2019). On longer timescales, the dynamics of climate are strongly controlled by the behavior of the oceans since the ocean circulation moves large amounts of heat around the planet (Rahmstorf & Willebrand, 1995). The oceans influence climate in several ways: (1) by absorbing solar radiation and releasing heat needed for driving atmospheric circulation, (2) by releasing aerosols that influence cloud cover, (3) by emitting most of the water that falls on land as rain, (4) by absorbing carbon dioxide from the atmosphere and storing it for years to millions of years (IPCC, 2014). Ocean's circulation, driven by the wind and by density contrasts is much slower than the atmosphere's because of water's large thermal inertia. Consequently, the oceans damp high-frequency temperature changes and function as a source of (low-frequency) natural climate variability on longer timescales. Additionally, ocean circulation modulates the trajectory of global warming by controlling the rate at which heat and carbon are sequestered in the deep ocean and exchanged with the atmosphere. Changes in ocean circulation have been projected and inferred as a result of human-induced climate change, mainly due to the disruption of deep-water formation by freshwater from melting of ice sheets (Rahmstorf, 2002; Rahmstorf et al., 2015). However, the extend through which ocean circulation can be impacted by freshwater fluxes is not well defined.

The relationship between oceanic heat transport and the cryosphere are of particular importance to constrain the effects of human-induced climate change on the Earth's environment. Continental ice sheets are another key component of the climate system, and sea-level rise due to their decay is an additional dire future prospect. With as many as 270 million people presently living in near-coastal lowlands, future sea-

level rise as predicted by climate models for the next centuries (IPCC, 2014) will have a direct influence on people's lives (Mimura, 2013). The demise of ice sheets also provides a positive feedback on global warming because their high albedo impacts the Earth's radiation balance, determining the amount of solar energy that is absorbed by the Earth and reemitted to the atmosphere via infrared radiation. Nevertheless, the mechanistic understanding of waxing and waning of the polar ice sheets remains as a big question and the long-term feedbacks that determine their growth and decay are poorly understood.

The ocean and cryosphere are interconnected in a multitude of ways and given the role of the ocean as the Earth's largest reservoir of heat, freshwater, and carbon, it is also the most likely medium through which modulating feedbacks are transmitted to the cryosphere. Evaporation from the ocean provides snowfall that builds and sustains the ice sheets and glaciers. Ocean temperature and sea level affect ice-sheet, glacier, and ice-shelf stability in places where the base of ice bodies are in direct contact with sea water. Since the response of ice volume to ocean temperature changes is nonlinear, even slight increases in ocean temperature have the potential to rapidly melt and destabilize large sections of an ice sheet or ice shelf (IPCC, 2014). Freshwater fluxes from melting ice sheets disrupt ocean circulation, leading to changes in the distribution of heat in the ocean and thus, anomalous climate patterns also at lower latitudes (Stocker & Johnsen, 2003). Although extremely significant, ocean-cryosphere feedbacks across all timescales are also not well stablished (Lozier et al., 2010).

Classically, oceanic heat transport has been understood as a function of the efficiency of the thermohaline circulation in driving mass transport in the Atlantic Ocean, a concept that is widely referred to as "The Great Ocean Conveyor" (Broeker, 1991). Uniquely in the Atlantic Ocean, warm and salty waters are transported northwards throughout all latitudes. As these reach the subpolar North Atlantic, the salty upper layer loses heat to the atmosphere, sinks, and is exported at depth back southwards. As around Antarctica the remaining heat of subducted waters upwells by passive advection, the strength of overturning (deep-water formation) in the North Atlantic is both considered crucial for surface heat transport and distribution throughout the oceans and particularly sensitive to salt and freshwater fluxes to the surface of the subpolar North Atlantic.

As the ocean's upper layer is itself controlled by atmospheric processes, salt and freshwater fluxes to areas of deep-water formation have mostly been considered a passive process driven by the position and strength of wind belts (that control precipitation and evaporation) and summer insolation (that control sea-surface temperatures and ice-sheet stability). However, recent observational oceanography studies have questioned the direct surface connection between net evaporative (warm and salty) areas and the *loci* of deep-water formation in the North Atlantic (Burkholder & Lozier, 2014; Foukal & Lozier, 2016)). This is now understood to take place at intermediate levels, below the layer directly forced by the atmosphere, and via density layers that connect the subsurface at the subtropics to subpolar areas of deep-water

formation. Thus, processes that modulate sea-water density (temperature and salinity) at the subsurface of the North Atlantic may be crucial for oceanic circulation and its interaction with the cryosphere, but if and how conditions at the subsurface affected or responded to waxing and waning of ice sheets throughout the Earth's climatic past is unknown.

The scope of this thesis is therefore to constrain how cryosphere-ocean dynamics may have worked in the past. To tackle this main question, subsurface paleotemperature and paleosalinity records from the mid-latitudes of the North Atlantic have been generated. These encompass critical periods of ice-sheet evolution and climate change of the Pleistocene, namely the Termination I (the most recent period of glacial ice-sheet demise) and the Mid-Pleistocene Transition (MPT), a period of ice-sheet enlargement. The following four chapters of this thesis provide a general introduction to the discussed topics divided as follows. Chapter 2 provides a review of the general oceanography of the Atlantic Ocean with special focus on the North Atlantic. Chapter 3 offers an overview about the state-of-the-art knowledge about the Mid-Pleistocene Transition. Chapter 4 details the materials and methods used in this thesis. Chapter 5 provides a summary about the main water mass occupying the deep thermocline of the North Atlantic and discusses how this may be affecting northward heat transport. These are followed by three discussion chapters (6 - 8) on the results of this research. Chapter 9 contains a summary of the main conclusions of this dissertation and provides future perspectives.

Within the discussion chapters 6, 7, and 8, the following scientific questions will be addressed:

Question 1 (*Chapter 6*): How did the meridional heat transport affect/was affected by the demise of the circum-Atlantic ice sheets during the most recent glacial termination?

Between 25 and 11 thousand years (ka) before present (taken as 1950 A.D.) the Earth's climate system emerged from a fully glaciated state (Last Glacial Maximum, LGM) to the modern interglacial period. During this time interval, referred to as Termination I, the Earth's continental cryosphere decreased by ~ 65% (equivalent to a ~ 125 m sea level rise), ocean circulation underwent profound changes and atmospheric CO_2 concentrations rose by 80 ppm. Because of the chronological proximity to the modern period and record availability, this interval is the most studied transition between a glacial to interglacial state in the scientific literature and serves as a paradigm for older deglaciations. Deep-thermocline temperature and salinity records were produced from a deep-dwelling planktic foraminifera in parallel with stable isotopes from a benthic foraminifera species (indicative of global ice volume and deep-ocean ventilation). The absence of chronostratigraphic uncertainties between records allowed for the assessment of potential associations between northward heat transport, ice-sheet demise and deep-ocean ventilation changes.

Questions 2 and 3 (*Chapters 7 and 8*): Did upper ocean circulation change across the MPT? Is there a connection between meridional heat transport variability and the glacial-interglacial cyclicity shift that occurred during the MPT?

The MPT, encompassing the interval between ~1200 and 600 ka ago, comprises arguably the most profound change of the global climate system throughout the entire Pleistocene. It marks the emergence of quasi-periodic ~100 kyr glacial cycles, in contrast to the previously dominant ~41 kyr periodicity. Intrinsically coupled to this change in the global climatic beat is the rapid expansion of Northern Hemisphere continental ice sheets. Although there have been numerous studies on the MPT, the exact mechanism explaining the ice-sheet growth and the ensuing periodicity shift has remained elusive so far. To discuss this topic, deep-thermocline temperature and salinity records were produced once again in parallel with stable isotopic records from benthic foraminifera. These allowed for the novel assessment of deep thermocline circulation variability across the MPT and indicate that this also changed significantly during the studied interval, which so far had not been established (Chapter 7). Chapter 8 elaborates on these upper ocean circulation changes and provides evidence about the potential connection between upper circulation and the accelerated ice-sheet enlargement during the MPT.

2 Modern circulation in the Atlantic Ocean and the meridional heat transport

The circulation in the Atlantic Ocean is considered to play a fundamental role in the climate of the Atlantic realm, mainly due to its poleward transport of large amounts of heat (Clark et al., 2002). The northward-flowing Atlantic surface waters are warm, whereas the southward-flowing deep waters are cold, defining the meridional heat flux (MHF), which peaks at about 1.2 ± 0.3 PW (1 PW equals 10^{15} Watts) at 24ºN (Ganachaud & Wunsch, 2000) and is usually described in terms of strength of the Atlantic Meridional Overturning Circulation (AMOC; Kuhlbrodt et al., 2007). The net northward transport of heat and salt across the North Atlantic via the surface ocean is a key process for the modulation of European climate. It is also essential for the densification or overturning of the surface waters, hence the formation of deep waters as part of the thermohaline circulation. By modulating latitudinal sea-surface temperature gradients, the MHF also affects the position of the Intertropical Convergence Zone (ITCZ) and, therefore, rainfall variability in the lower latitudes of both northern and southern hemispheres (Deplazes et al., 2013; McGee et al., 2014). Although changes in the AMOC are implicated in almost every scenario of climate change in the past (Hernández-Almeida et al., 2015; Lehman & Keigwin, 1992; Menviel et al., 2020; Pena & Goldstein, 2014), its controlling mechanisms are still not completely understood.

A dominant paradigm in oceanography is that long-term MHF variability derives from changes in the rate of deep-water mass formation, which stemmed from the anomalous interhemispheric northward heat transport in the Atlantic Ocean observed since the mid-20th century (Wüst, 1957; Bennet 1976). This anomaly led to the model of the "Great Ocean Conveyor" (Broeker, 1991), that defined northward heat transport to be a direct consequence of deep-water formation in the northern North Atlantic, at the time considered to take place in the Labrador and Greenland Seas. As a result, the term "AMOC" refers to northward heat transport, overturning and deep-water circulation without distinction and, as the strength of the overturning circulation is highly susceptible to freshwater fluxes over *loci* of deep-water formation, so too would be the MHF.

The gathering of continuous data from monitoring mooring arrays installed across the subtropical and subpolar gyres have been contributing to the rapid pace of scientific developments regarding the nature of the AMOC (Lozier et al., 2010, 2019) and have put into question the direct causal link between water-mass formation, export and the MHF (Lozier, 2012; Lozier et al., 2010, 2019). While earlier studies pictured the western North Atlantic to be the main area of deep-water formation and convection in the Atlantic because of the extremely deep mixed layer (1500 – 2000 m) of that region. However, continuous monitoring data from the OSNAP arrays (Overturning in

the Subpolar North Atlantic Program; Lozier et al., 2016) showed that deep-water formation (i.e., overturning, oceanic heat loss) and deep-water convection (i.e., sinking of water masses) are decoupled in the Subpolar Gyre (SPG; Lozier et al., 2019). The western North Atlantic is indeed a region of deep-water convection, but cooling and freshening in the Labrador Sea counteract one another in terms of density, resulting in very small overturning rates (i.e., deep-water formation). Most of the *de facto* conversion of warm, salty and shallow Atlantic waters into colder, fresher and deep waters (i.e., overturning or "densification") was found to occur rather in the northeastern North Atlantic; in the Iceland and Irminger basins and the Nordic Seas (Lozier et al., 2019). The western North Atlantic Maximum overturning rates along OSNAP were found at σ_0 = 27.53 (~950 m), at the Rockall Trough and significant correlated with northward heat transport (i.e., the more heat was transported northwards the higher the rates of deep-water formation and vice versa).

At subtropical latitudes, data from the RAPID-MOCHA array (Rapid Climate Change Programme and associated Meridional Overturning and Heatflux Array; at 26.5°N; (Cunningham et al., 2007; Johns et al., 2011)) show that AMOC strength is highly variable in all measured timescales and not coherent between the subtropical and subpolar gyres. According to the "ocean conveyor" view, the AMOC and MHF should be latitudinally coherent (i.e., more overturning leading to a stronger MHF). However, period-matched observations found the subsurface of the STG to be warmer when AMOC was weak and vice-versa (Lozier et al., 2010). Thus, the classic view about ocean circulation as a "Great Ocean Conveyor" does not explain observed AMOC variability. Rather, observational oceanographers find the AMOC to be modulated by zonal (instead of meridional) density gradients across the North Atlantic (Buckley & Marshall, 2016).

The concept of a purely thermohaline-driven AMOC is also challenged by theoretical model-based studies of oceanic circulation (Gnanadesikan, 1999; Kuhlbrodt et al., 2007). According to this view, the thermohaline circulation is decisive in setting the deep-water properties but is it not the main energetic driver of deep-ocean circulation. Embedded in this disagreement is the question about which mode of meridional heat and freshwater transport is prevalent in the ocean interior, across or along layers of equal density (isopycnals). Diapycnal transport refers to the turbulent energy-intensive mixing of water across density surfaces that partly drives the AMOC via thermohaline circulation. In contrast, isopycnal transport refers to warm and cold water mixing along the same density surfaces, a process that is essentially adiabatic and requires little energy expenditure. The contrast between these two modes of transport is reflected in isopycnal diffusivities (~$10^2 m^2/s$) being several orders of magnitude higher than diapycnal diffusivities (~$10^{-4} m^2/s$; Ledwell et al., 1993), which imply that the role of overturning (diapycnal flow) may be secondary to that of isopycnal geometry in the distribution of properties and tracer on the ocean. Hence, also in palaeoceanographic studies, density indicators (e.g., $\delta^{18}O_{calcite}$) should be

assessed, when possible, in order to establish patterns of heat and freshwater fluxes below the mixed layer.

The degree to which deep-water mass formation in the ocean interior is the most important modulator of heat transport and deep-water ventilation, or whether the circulation in the Atlantic Ocean is essentially adiabatic is a subject of intense discussion and it's been suggested to depend on the analyzed timescale (Johnson et al., 2019). This question will be addressed in the context of multicentennial to multimillennial timescales in Chapter 6, by analyzing subsurface temperatures during periods of catastrophic meltwater discharges over the SPG and weakening of the overturning circulation (McManus et al., 2004) known as Heinrich Events (Bond et al., 1992). As temperature anomalies are more efficiently transmitted along rather than across density surfaces, processes that mold the geometry and/or heat content within oceanic density layers are prime candidates to drive the MHF.

2.1 Detailed North Atlantic hydrography

2.1.1 The upper AMOC branch: surface circulation and mode waters

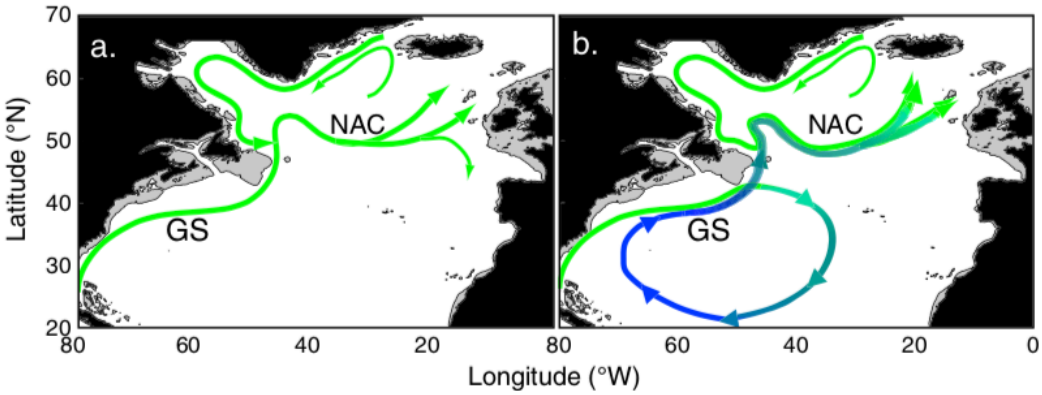

Figure 2.1. (a) Traditional versus (b) present view of North Atlantic circulation and meridional heat flux. Green (blue) arrows indicate surface (subsurface) water pathways. Figure extracted from Burkholder & Lozier (2014).

The surface hydrography of the North Atlantic Ocean is characterized by a double-gyre circulation pattern (STG and SPG), fuelled by combined wind-driven and buoyancy forcings from the western and eastern ocean boundaries, respectively (Hogg & Gayen, 2020). Connectivity between the gyres, via the upper limb of the AMOC, has strong implications for poleward heat transport and its variability in the basin. Eulerian studies have moulded the traditional view, which assumed that the heat transmission between gyres occurred via surface advection of heat anomalies along the Gulf Stream - North Atlantic Current (NAC) pathway into the eastern SPG (Sutton & Allen, 1997). Recent Lagrangian modeling of water pathways and drifter studies on the North Atlantic heat connectivity between the STG and the SPG, however, have determined that communication between the gyres at the surface is limited due to southward Ekman velocities and a strong surface vorticity gradient (Burkholder & Lozier, 2011; Foukal & Lozier, 2016). As these constraints on the inter-gyre connectivity decrease with depth, a more direct pathway exists for heat stored within

the subsurface STG to flow northwards, along the density surfaces (isopycnals) that outcrop in the high-latitude northern North Atlantic (Figure 2.1). The discovery of this subsurface pathway implies that thermal anomalies are transmitted to higher latitudes from a much larger depth than previously expected (Burkholder & Lozier, 2011), with maximum flow to eastern SPG detected along isopycnal σ_0=27.1 located at 700 m water depth below the Gulf Stream and the surface of northeastern North Atlantic (NENA; Burkholder & Lozier, 2011).

Barred northwards by the strong vorticity gradient, Gulf Stream waters from the Ekman layer (~100 m water depth) diverge east around 40ºN, offshore of the Grand Banks, feeding into the Azores Current. Gulf Stream waters under the Ekman layer continue north along isopycnals feeding into the NAC. While the main heat source to the surface northwards of the vorticity gradient is supplied along isopycnals, ocean-atmosphere interaction in the winter causes the convection of thick surface-water parcels, which sink across density layers (diapycnally) becoming mode waters and occupy the thermocline. Waters within the Gulf Stream and STG form Subtropical Mode Water (STMW, σ_0=26), also known as "Eighteen Degree Water" (Talley, 2011). Along the NAC, from the transition zone between the STG towards the northeastern North Atlantic, mode waters progress from Eastern North Atlantic Central Waters to Subpolar Mode Waters (SPMW, 8-15 ºC, 35.5-36.2 psu and σ_0=26.9-27.75) (García-Ibáñez et al., 2018; Hanawa & Talley, 2001). Mode water variability in this region is usually interpreted as a result of air-sea interaction and winter convection, however the paradigm shift from a surface to a subsurface advective pathway requires mode water formation in the SPG to be reassessed, which has so far not been done (further discussed in Chapter 5).

2.1.2 Lower AMOC branch – intermediate water masses

Wind-driven northward-flowing waters from the upper AMOC branch are vertically isolated from the southward-flowing intermediate and deep waters in the lower AMOC branch by the pycnocline, defined as the vertical level with the highest density gradient. The pycnocline is typically found between 500 and 1000 m water depth, below the Subtropical Gyre (STG) and outcrops at intermediate- and deep-water sinking zones. The high vertical density gradient acts as a barrier to the downward propagation of oceanic particulates, tracers (e.g., gases, salt and nutrients), and heat, thereby allowing overturned waters below to maintain their distinct physiochemical properties, set at their *locus* of formation.

The intermediate levels of the North Atlantic Ocean are occupied by three distinct water masses identified by vertical salinity and oxygen extrema; the low-salinity/high-oxygen Labrador Sea Water (LSW) in the north, the high-salinity/low-oxygen Mediterranean Outflow Water (MOW, detailed in Section 5.1) in the central North Atlantic, and the low-salinity/high-oxygen AAIW (Figure 2.2) in the southern part of the North Atlantic.

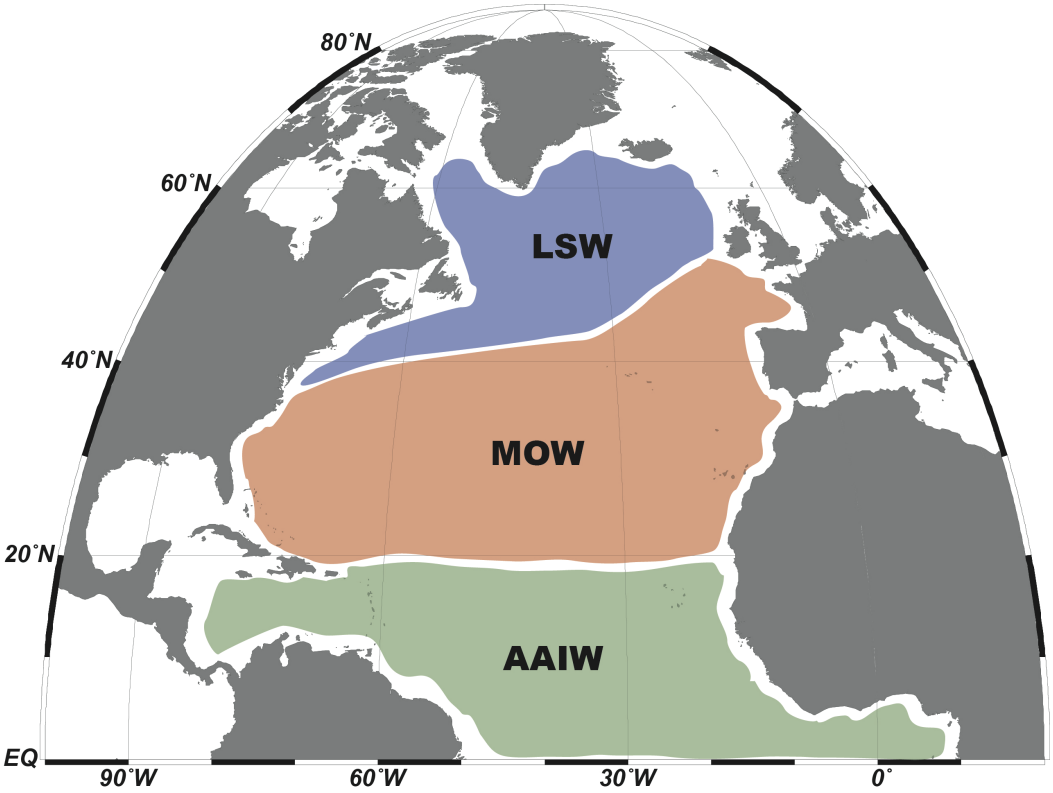

Figure 2.2: Dominant intermediate water masses in the North Atlantic (Talley, 2008). Antarctic Intermediate Water (AAIW), Mediterranean Outflow Water (MOW), Labrador Sea Water (LSW).

Southwards of 20ºN, intermediate levels in the North Atlantic are occupied by the fresh and oxygenated AAIW, formed in the Antarctic Subpolar Front. Despite the erosion of its original properties along its way northwards, AAIW can be very clearly identified by a salinity minimum. As it reaches below the STG, AAIW loses its main characteristics as it mixes with the upper part of the saline and oxygen-depleted MOW (Reid, 1994). Although volume transport from the Gulf of Cadiz is very small (<1 Sv), MOW's salinity and temperature are extremely high in comparison with any water at equivalent depth and density ranges. As a result, AAIW's salinity minimum disappears, but the water mass can still be traced northwards to 32ºN (van Aken, 2000; Tsuchiya et al., 1992) by its relatively high silicate content (it is negligible compared to Antarctic Bottom Water, but high compared to other intermediate waters in the North Atlantic). Waters within AAIW's density level continue northward, with its volume providing a medium for heat and salt (from MOW) to reach the northeastern North Atlantic (Reid, 1994). Typical thermohaline values given to this water mass in the North Atlantic are in the ranges $6 < \theta < 7.98$ºC, and $34.9 < S < 35.0$ psu.

The LSW (3.6°C, 34.91 psu, 27.75 σ_θ; Talley & McCartney, 1982) is the dominant intermediate water mass of the northern North Atlantic and occupies from the surface in northwestern North Atlantic down to 2000 m water depth (McCartney, 1982). After sinking in Labrador Sea, LSW spreads eastwards towards the Nordic Seas and southwards. Along its pathway LSW is entrained by Iceland-Scotland Overflow Waters (ISOW) in northeastern North Atlantic and mixes quasi-isopycnally with

MOW below the STG, losing its typical low salinity and contributing to the formation of North Atlantic Deep Water (NADW).

2.1.3 The components of North Atlantic Deep Water

Between about 1500 and 3500 m water depth, the North Atlantic is occupied by the NADW, which dominates in terms of net volume transport. Its characteristics, high salinity and oxygen and low nutrient content are a consequence of its superficial origins and relatively young age in relation to other deep-water masses of the Atlantic Ocean. Its sources are the Nordic, Labrador and Mediterranean seas, by the way of their Nordic Seas Overflow Water (NSOW), LSW, and MOW, respectively. In the subpolar and subtropical North Atlantic, these specific components of NADW are still distinguishable and enable the division of this water mass into the upper and lower components. Upper NADW is formed from the mixing between LSW and MOW at mid latitudes and below the STG (Talley, 2011). Lower NADW is mostly formed by entrainment of ISOW (the most volumetrically significant waters from the Nordic Seas; García-Ibáñez et al., 2018) into intermediate and abyssal waters accumulated below 2000 m east of the Mid-Ocean Ridge (García-Ibáñez et al., 2018, Talley et al., 2011). The resulting waters (referred as Northeastern Atlantic Deep Water by Garcia-Ibanez et al., 2018, and Talley et al., 2011) occupy the whole eastern North Atlantic and flow cyclonically towards the western North Atlantic through the Charlie-Gibbs Fracture Zone. In the western North Atlantic, these join the Deep Western Boundary Current and are exported southwards as NADW.

3 Climate system interactions during the Mid-Pleistocene Transition

The Pleistocene epoch, between 2.58 Ma and 11.7 ka (Gibbard et al., 2010), is characterized by repeated cycles of glaciation and partial deglaciation, primarily paced by orbital parameters (Lisiecki & Raymo, 2005). Between 1.2 and 0.6 Ma, during the MPT, glacial-interglacial cycles intensified and became longer, with a marked increase in the amplitude of ice-volume variations (Boer et al., 2014; Elderfield et al., 2012; Rohling et al., 2014) and the appearance, although muted, of precession in periodograms of the glacial-interglacial rhythm (Figure 3.1; Imbrie et al., 1993). There have been numerous studies on the MPT, however the exact mechanism explaining the ice-sheet growth and ensuing periodicity shift remains elusive so far.

The quasi-100 kyr cyclicity that dominated the Late Pleistocene after 0.6 Ma was initially interpreted as reflective of the orbital modulation by eccentricity, which in its turn modulates precession (Imbrie et al., 1993; Ruddiman et al., 1989). However, eccentricity has by far the weakest influence on insolation amount received by Earth and the lack of mechanistic understanding of how and why eccentricity would have begun dictating the pace of climate cycles during the MPT characterized the intensely discussed "100-kyr problem" (Maslin & Brierley, 2015). Mathematical model studies (Feng & Bailer-Jones, 2015) show that the observed cyclicity can be explained by a combination of obliquity and precession with obliquity being the dominant pacer for glacial cycles over the whole Pleistocene and precession only becoming important after the MPT. As a result, scientists have long searched for internal climate feedbacks that would increase the sensitivity of ice sheets to precession forcing.

Early studies on the MPT suggested that the increase in precession forcing in global ice volume may be explained by the simple southward migration of the continental edges of NH ice sheets, because at mid-latitudes these would be subjected to stronger precessional forcing (Ruddiman & McIntyre, 1981). However, reconstructions of the Laurentide Ice Sheets (LIS) meltwater discharges suggested that the LIS frequently expanded into mid-latitudes already in the Early Pleistocene, and even though these expansions were heavily paced by NH summer insolation (itself paced by precession) they apparently had little impact in the overall obliquity-paced glacial/interglacial cyclicity of that period (Shakun et al., 2016). Sedimentary deposits on the North American continent further suggested that the repeated erosion of substrate below ice sheets throughout the Early Pleistocene increased friction between ice and bedrock and therefore allowed for taller, more resilient ice sheets to develop, which is usually referred to as the "regolith hypothesis" (Clark & Pollard, 1998). (Kutzbach, 1981) proposed that high-latitude ice sheets may have become more sensitive to precessional insolation heating of low- and mid-latitude land masses at

latitudes south of the ice sheets, but why and how this change would have happened during the MPT remains unclear.

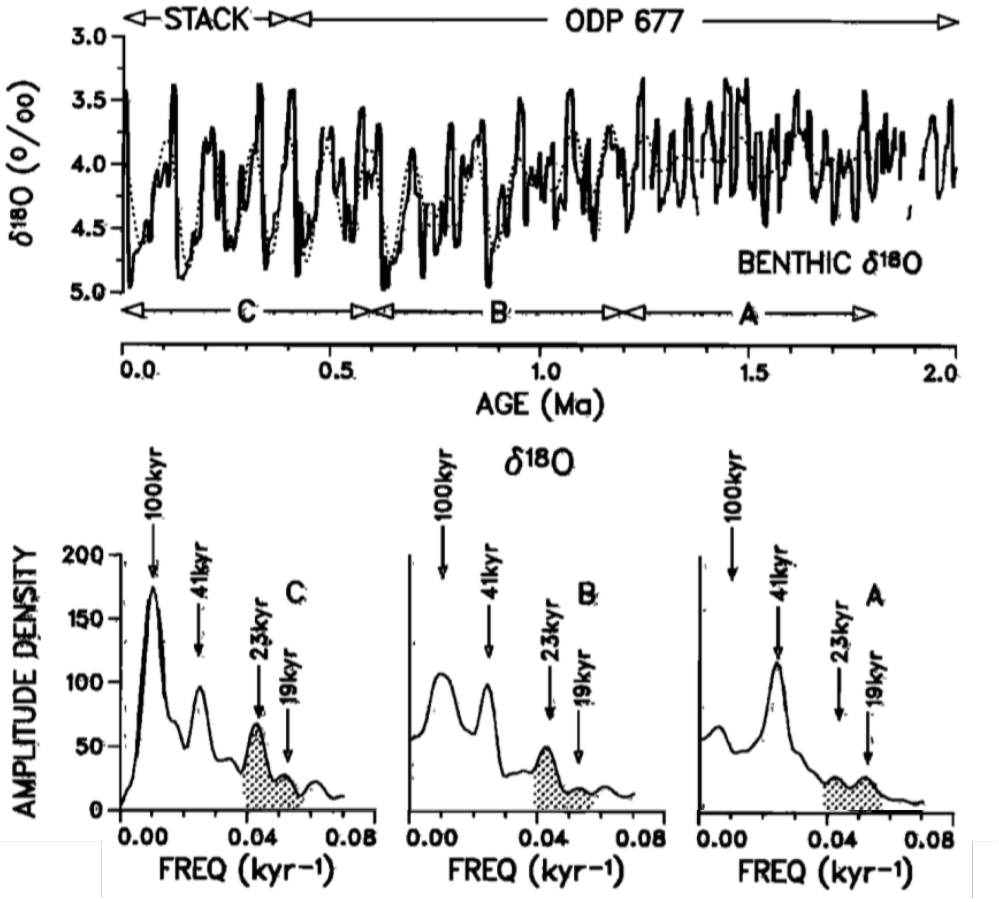

Figure 3.1. (top) Combined stacked benthic $\delta^{18}O$ record from Imbrie et al. (Imbrie et al., 1992) and record from Ocean Drilling Program site 677 (Shackleton et al., 1990). (bottom) The $\delta^{18}O$ spectra of Early Pleistocene (A), Mid-Pleistocene (B), and Late Pleistocene (C). Extracted from (Imbrie et al., 1993).

Recently, discussions regarding the MPT moved southwards, instead focusing on the transition of Antarctic ice sheets (AIS) from terrestrial to marine-based ice-shelves around 1 Myr (Raymo et al., 2006). According to this concept, referred to as the "Antiphase hypothesis", the pre-MPT 41-kyr cyclicity was a product of the anti-phased precession-driven variability in ice volume between hemispheres being cancelled out in global $\delta^{18}O$, leaving the in-phase obliquity signal to dominate during Early to Mid-Pleistocene. The post-MPT 100-kyr cyclicity would be then a result of the expansion and stabilization of AIS margins into the glaciomarine realm. Drill cores on the edge of the Ross Sea, confirmed AIS had more dynamic margins in the Early to Mid-Pleistocene and underwent significant expansion around 0.8 Ma, in support of the "Antiphase hypothesis" (McKay et al., 2012). As a result, a substantial proportion of the sea-level drop detected during the MPT's mid-point (MIS 22) has been attributed to Antarctica (Elderfield et al., 2012). Implicit in the "Antiphase hypothesis" is the increased sensitivity of the global climatic system to ice-volume variability in the NH during and after the MPT. Sea-level variations driven by the waxing and waning of the NH ice sheets would have preconditioned seaward expansion and retreat

of AIS after the MPT because glaciomarine ice sheets are very sensitive to calving due to sea-level rise (Raymo et al., 2006). Although current hypotheses are not in agreement about which hemisphere would have led in terms of ice-sheet enlargement during the MPT, substantial ice-sheet enlargement in the NH is considered to be instrumental for the MPT cyclicity shift (Berger and Jansen, 1994; Clark et al. 2006, Raymo et al., 1997) and is confirmed by proxy records documenting the southward shift of wind systems in the Pacific and Atlantic Oceans, the prolonged extension of sea ice over the Bering Strait, the intensified erosion of the continental regolith in North America and ice-sheet growth in the Alps and Greenland (Clark et al., 2006; Ford & Raymo, 2019; Kender et al., 2018; Seo et al., 2015; Thiede et al., 2010). Therefore, climatic feedbacks supporting ice-accumulation or triggering ice-sheet instability in the NH are crucially important to resolve glacial-interglacial cyclicity change that occurred during the MPT (Berger & Jansen, 1994; Clark et al., 2006; Raymo, 1997).

Changes to the Earth's climate system during the MPT were not only restricted to the cryosphere, but also included an ocean circulation "crisis" during the crucial Marine Isotope Stages 24 and 22 (the so-called "900-kyr event", 0.94 – 0.87 Ma; Pena & Goldstein, 2014; Raymo et al., 1990; Schmieder et al., 2000) and an abrupt drop in atmospheric CO_2 concentrations (Chalk et al., 2017; Hönisch et al., 2009). Because more than 90% of the combined oceanic, atmospheric and terrestrial carbon resides in the deep ocean, ocean circulation variability is believed to play a primary role in regulating atmospheric CO_2 (Broecker, 1982; Sigman & Boyle, 2000). A permanent change in the mechanisms of ocean-air CO_2 transfer may have allowed the general cooling of the climate system and acted as a positive feedback to increased ice-sheet build-up at the onset of 100-kyr cycles (Chalk et al., 2017; Farmer et al., 2019; Hasenfratz et al., 2019).

The close geographical proximity between the ice sheets and the main areas of deep-water formation in the NH make the North Atlantic one of the most climatically sensitive regions in the world's oceans (Hodell & Channell, 2016). There, ocean circulation and ice-sheet variability are tightly coupled by feedbacks involving heat and freshwater fluxes on millennial and orbital timescales (Alvarez-Solas et al., 2019; Timmermann et al., 2010; Zhang et al., 2014). While AMOC-driven northward heat transport impacts ice-sheets mass balance by modulating sea-surface temperatures and atmospheric moisture content, freshwater flux from ice sheets may hamper deep-water formation and ocean circulation, which then affects the oceanic carbon reservoir. Hence, internal oceanic mechanisms that modulate northward heat transport to the high-latitudes of the North Atlantic are prime candidates to regulate the stability of NH ice sheets and glacial-interglacial cyclicity. Chapter 7 presents a novel oceanic mechanism for northward heat transport that was active during the MPT and may have supplied the moisture that supported ice-sheet growth despite low atmospheric temperatures and decreased atmospheric CO_2.

4 Study material, site and methods

4.1 Foraminifera as paleoceanographic proxies

Foraminifera are among the most abundant shelled organisms in marine planktic and benthic environments. They are single-celled protists recognizable in the fossil record by their shells (tests). These are often composed of calcite and calcified in partial or complete chemical equilibrium with sea water. Their chemical composition is, thus, ideally suited for reconstructing chemical variations of the ocean in paleoclimate and paleoceanography studies (Gooday, 2003).

Planktic foraminifera are widely used for upper water column reconstructions. To reconstruct deep-thermocline variability across the LGM and MPT, two abundant deep-dwelling species have been chosen and analysed. *Globorotalia truncatulinoides* and *Globorotalia crassaformis* belong to the non-spinose macroperforate Globorotaloidea superfamily (Schiebel & Hemleben, 2017). As all constituents of this group, these two species are nonsymbiotic and therefore believed to precipitate their shell calcite at or close to equilibrium with seawater (Fairbanks et al., 1980), allowing the dismissal of species-specific vital effects. Their chemical composition is interpreted to reflect the properties of the specific depths or geochemical niches in which they dwell (Rohling & Cooke, 1999).

4.1.1 Globorotalia truncatulinoides (d)

Figure 4.1. Scanning electron microscopy images of Globorotalia truncatulinoides. Figures extracted from Schiebel and Hemleben (2016). Scale given by white bars at the bottom with 100 μm.

Appearing at the Pliocene-Pleistocene transition, the test of *G. truncatulinoides* is trochospiral, medium to high conical in the umbilical side and flat on the spiral side (Figure 4.1). It has 4.5-5.5 chambers in the last whorl and presents a keel at its periphery. Cosmopolitan, *G. truncatulinoides* is a deep-dwelling planktic foraminifera featuring coiling dimorphism with a complex life cycle superfamily (Schiebel &

Hemleben, 2017). It has been shown to migrate vertically within the water column according to its different life stages and for reproduction (Kemle-von-Mücke & Oberhänsli, 1999). Juvenile specimens calcify their test in the upper few hundred meters of the water column. As *G. truncatulinoides* ages, it continues to grow and calcify new chambers as it slowly sinks in the permanent thermocline. Adult specimens migrate upwards to reproduce, but otherwise live specimens have been found down to 1000 m water depth in the subtropical North Atlantic (Hemleben et al., 1985). This species' distribution is usually found to be the highest in relatively warm sea waters and deep permanent thermoclines (Lohmann, 1992). Their reconstructed calcification depth is usually determined to fall between 300 and 600 m in the Atlantic Ocean (Cléroux et al., 2013; Feldmeijer et al., 2015). As a result, their test calcite records the integrated deep-thermocline characteristics.

4.1.2 Globorotalia crassaformis

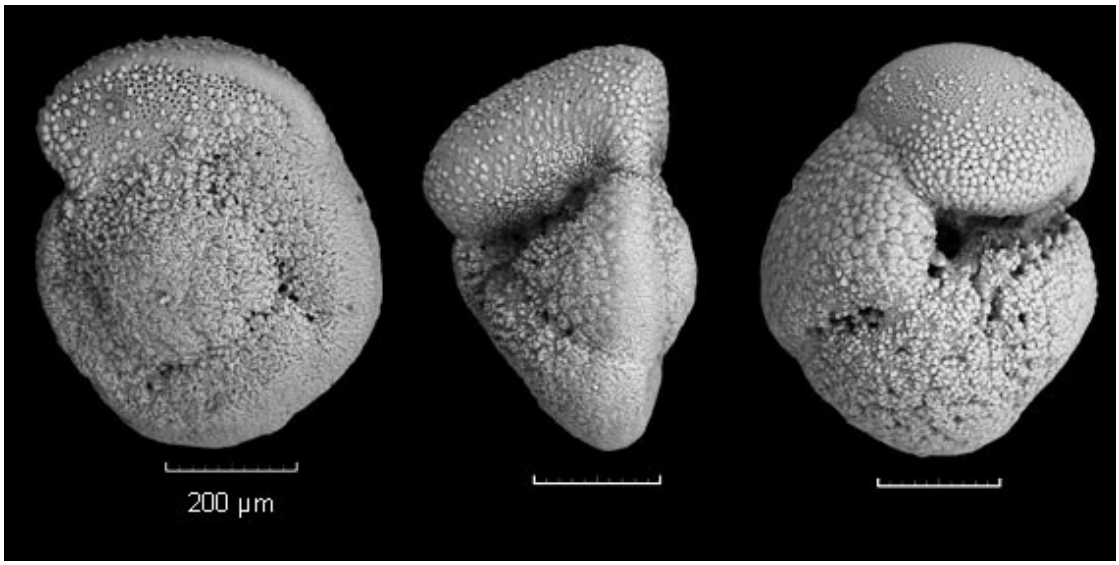

Figure 4.2. Scanning electron microscopy images of Globorotalia crassaformis. Figures extracted from (Bylinskaya, 2005).

Appearing in the geological record during the Late Miocene, *G. crassaformis* bears a trochospiral and planoconvex test with 4 to 4.5 chambers in the last whorl (Figure 4.2). Its test's surface is smooth and peppered with pustules, which merge and form a thick calcite crust. This species is cosmopolitan and found to dwell at the permanent thermocline of tropical and subtropical oceans (Schiebel & Hemleben, 2016). In the Atlantic Ocean, *G. crassaformis* has been found to dwell between 450 and 950 m water depth (Cléroux et al., 2013; Schiebel & Hemleben, 2016). Its biological niche has been repeatedly associated with enhanced biological productivity at the surface and oxygen depletion at habitat depth (Kemle-von-Mücke & Oberhänsli, 1999). In their detailed thermocline reconstruction study, Cléroux et al. (2013) found that the calcification depth of *G. crassaformis* is symmetric relative to the Equator, with shallower depth in the equatorial region (~600 m), greater depths in the

subtropical regions (~1000 m) and shoaling toward higher latitudes. This distribution matched the depth of the 3.2 ml/l oxygen level along their studied transect, consistent with abundant *G. crassaformis* found at the minimum oxygen level in the water column in the eastern equatorial Atlantic (Kemle-von-Mücke & Oberhänsli, 1999). Given its observed deep habitat depth, these authors speculated that this species occupies the oxygen minima of the upper water column where predation pressure is much lower. This biological niche is rich in organic matter aggregates that originate from bacterial activity in the oxygen minimum zones underlying the high productivity areas (Gowing & Wishner, 1998). In the subtropical North Atlantic, this minimum oxygen level coincides with the pycnocline, which is the high-density gradient interface that divides surface and intermediate water levels by definition. The occupation of this specific biological niche gives new significance to the interpretations of records composed by *G. crassaformis*, as it potentially allows researchers to gather chemical signals from the bottom of the thermocline and intermediate levels.

4.2 Marine sediment cores from Site U1313

Marine sediment cores from Integrated Ocean Drilling Project (IODP) Site U1313 (41°00'04"N, 32°57'25"W, 3424 mbsl) were raised from the central North Atlantic during IODP Expedition 306 (IODP Expedition Scientists, 2005). Site U1313 was a re-drill of the benchmark Deep Sea Drilling Project (DSDP) Site 607, situated at the base of the western flank of the Mid-Atlantic Ridge. Sediments retrieved from holes U1313A, U1313B, U1313C and U1313D consist mainly of nannofossil ooze with varying amounts of foraminifera and fine-grained terrigenous material. Regular occurrences of drop stones and coarser terrigenous fractions were interpreted as a product of Northern Hemisphere ice-sheet instability across the Pleistocene. Bio- and magnetostratigraphy indicated stable sedimentation rates of ~4.5 cm/k.y. during the Pleistocene epoch. The core sections from the four drilled holes are stored in the IODP Core Repository in Bremen, Germany.

4.2.1 Shipboard splice and preliminary age models of Site U1313

Sediments obtained at Site U1313 allowed the production of two complete spliced stratigraphic sections for the Pleistocene 306 (IODP Expedition Scientists, 2005). Holes U1313B and U1313C constitute the primary splice and holes U1313A and U1313D constitute the secondary splice. The shipboard age model was constructed by matching distinct lightness parameter (L*) variations with glacial and interglacial terminations. Such comparison was based on the assumption that the lightness parameter (L*), which reflects changes in the carbonate content due to variations in terrestrial input, and mimics variations in the global benthic oxygen isotope stack (LR04; Lisiecki & Raymo, 2005) without temporal offsets. Naafs et al. (2012) adjusted the original meter composite depth (mcd)-scales from holes U1313A, C, and D by tying them to the mcd-scale for Hole U1313B and creating the common adjusted mcd

(amcd) depth scale. The authors also refined the shipboard age model for the last 1 Ma by combining the lightness parameter with some benthic foraminiferal $\delta^{18}O$ data and tuning these once more to the LR04 benthic stack (Lisiecki & Raymo, 2005)

For the Late Pleistocene records of U1313 (LGM and deglaciation, Chapter 6), the age model was further refined by Naafs et al. (2013) by tuning XRD and XRF records of Sites U1313 and U1308, respectively. The age model for Site U1308 had been determined by radiocarbon dating up to 35ka (Hodell et al., 2008). For the Mid-Pleistocene records of U1313 (MPT, Chapters 7 and 8), the age model of Site U1313 has been further refined using new benthic $\delta^{18}O$ data tuned to the LR04 benthic stack (see Chapter 4.3.3).

4.2.2 Local hydrography of IODP Site U1313

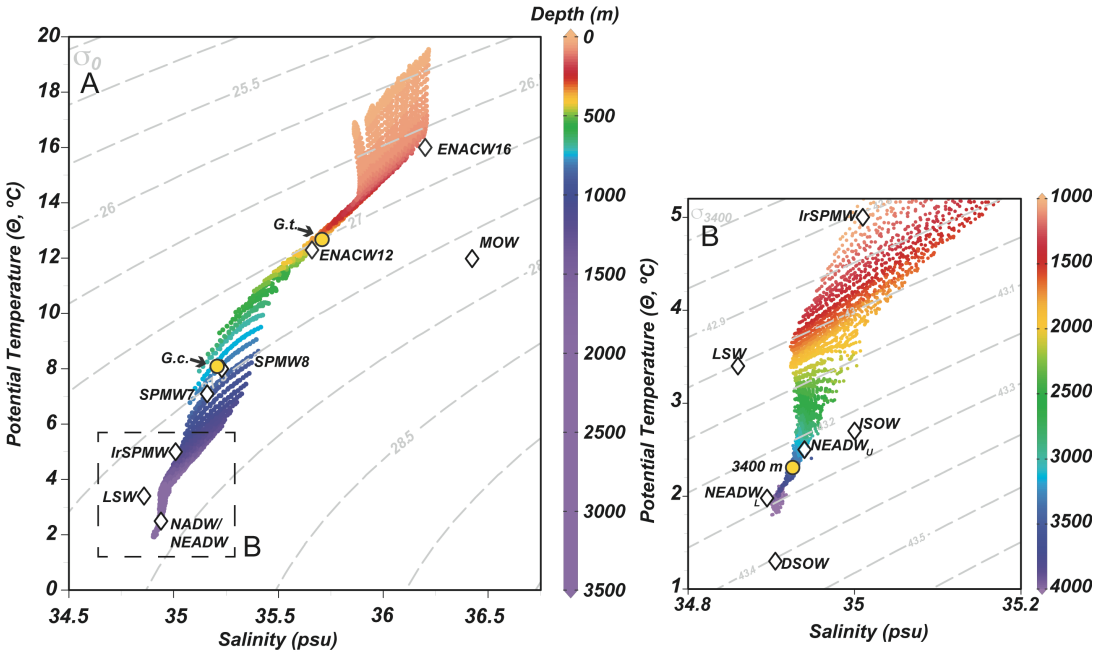

Figure 4.3. Θ-S diagrams used to distinguish the water masses at the study site. (A) Θ-S distribution from the surface to 3500 m water depth. Yellow circles mark the estimated habitat depths of the foraminifera discussed in the text (G.t.: G. truncatulinoides (d), 450 m, and G.c.: G. crassaformis, 800 m). Dashed gray box outlines the detailed in Figure B. (B) Θ-S distribution of water column below 1000 m water depth. Yellow circle marks the depth of Site U1313. Figure produced using the software Ocean Data View (Schlitzer, 2018) with data of the World Ocean Atlas 2018 from a 10°x10° square centered around the location of Site U1313 (Locarnini et al., 2019, Zweng et al., 2019). Colors represent depth. Diamonds represent the end-members of the water masses as characterized by García-Ibáñez et al. (2018). $ENACW_{16}$ and $ENACW_{12}$ are the Eastern North Atlantic Central Waters of 16°C and 12°C, respectively. $SPMW_8$, $SPMW_7$, IrSPMW are the Subpolar Mode Waters of 8°C, 7°C and Irminger Seas, respectively. LSW corresponds to Labrador Sea Water, ISOW, Iceland-Scotland Overflow Water, and DSOW, Denmark Strait Overflow. MOW is the Mediterranean Outflow close to Cape St. Vincent (Baringer and Price, (Baringer & Price, 1999).

Site U1313 is ideally suited to track heat-transport variability to the higher latitudes as it is located in the intergyre region, between the STG and the SPG. At the surface, Site U1313 is located along the pathway of the NAC, which is characterized by saline and warm waters (18°C annual average surface temperature; Locarnini et al., 2019). At present, the uppermost 150 m of the water column at Site U1313 comprise

the mixed layer and the seasonal thermocline (Figure 4.3A). The permanent thermocline, between 150 m and 1100 m, is extremely deep due to entrainment of MOW into central waters in the eastern North Atlantic (Spall, 1999) and contains the whole progression of mode waters formed within the inter-gyre region and eastern SPG (Brambilla & Talley, 2008; García-Ibáñez et al., 2018). Eastern North Atlantic Central Waters of 16ºC and 12ºC originate in the intergyre regions and occupy between 150 m and 650 m water depth above Site U1313. Between 650 m and 1100 m water depth, the bottom of the pycnocline in the central North Atlantic, the water column above U1313 is occupied by Subpolar Mode Waters (SPMW) formed east and west of the Iceland and Irminger basins ($SPMW_8$, $SPMW_7$, and IrSPMW, respectively). Between 1100 m and 2000 m water depth, fresh and oxygenated LSW mixes isopycnally with the saline and warm MOW (36.4 psu and 12°C off the Cape San Vincent; Baringer & Price, 1999). Below ca. 2000 m, waters above Site U1313 have average characteristics between LSW and ISOW (Figure 4.3B) and bottom waters at 3426 m water depth above Site U1313 are classified as Northeastern Atlantic Deep Waters (García-Ibáñez et al., 2018) These formed in the deep northeastern North Atlantic with significant contribution from ISOW (Garcia-Ibanez et al, 2018).

4.3 Methods

4.3.1 Core sampling and sample processing

Sections from the primary splice (holes U1313B and U1313C) were sampled every 4 cm between 0.24 mcd and 1.5 mcd and every 5 cm between 26.82 mcd and 56.77 mcd at the IODP Core Repository in Bremen, Germany. The approximately 10 cm^3 big samples were then freeze dried, weighted, wet sieved over 125 μm and 63 μm combined meshes, rinsed with Milli-Q water and dried at 40˚C at the Institute of Earth Sciences at Heidelberg University. When present, around 20 tests (~1000 μg) of the deep-dwelling planktic foraminiferal species *G. truncatulinoides* dextral (for the Late Pleistocene) or *G. crassaformis* (for the Middle Pleistocene) have been picked under a binocular microscope from the 315–400 μm size fraction in order to avoid size-related ontogenetic effects (Friedrich et al., 2012). The tests were then cracked between glass plates and a third of the crushed shell fragments was separated for stable isotope measurements while the remaining portion was reserved for trace-element analyses. For age model refinement, around 4 tests (~200 μg) of the benthic foraminiferal species *Cibicidoides wuellerstorfi* or *Uvigerina peregrina* were picked under a binocular microscope from the >250 μm size fraction. These tests were cracked between glass plates and between 40 and 80 μg of shell fragments was used per stable isotope measurement.

4.3.2 Stable isotope analyses of foraminifera

Oxygen and carbon stable isotopes are traditional paleoceanographic proxies used for reconstructing the physical and chemical characteristics of water masses and

ocean circulation. The isotopic composition of foraminiferal shells is usually assumed to be precipitated in equilibrium with ambient sea water and therefore to reflect paleoceanographic characteristics of ancient sea water. The $\delta^{18}O$ of marine carbonates has been widely applied for assessing past variability in ocean circulation (Lynch-Stieglitz et al., 2006), continental ice volume (Waelbroeck et al., 2002), sea-water salinity (Adkins et al., 2002) and temperature (Emiliani, 1955). The $\delta^{13}C$ of foraminiferal calcite can provide a wealth of information on the carbon cycling of the oceans and has been used to infer the distribution of deep-water masses and their geographic and bathymetric distributions (Curry & Oppo, 2005), biological productivity and variations in the global carbon cycle (Duplessy et al., 1988).

The isotopic composition of a sample is expressed using the δ notation (*i.e.*, $\delta^{18}O$ and $\delta^{13}C$), which represents the difference between the ratio of the least over the most abundant isotope of a sample and an internationally recognized standard, expressed in parts per thousand (*i.e.*, ‰). Equation 1 exemplifies the calculation of $\delta^{18}O$. For carbonate isotopic ratios the most used standard is Vienna Pee Dee Belemnite (VPDB), normalized in relationship to the chemical composition of *Belemnitella americana* fossil shells from the Cretaceous Pee Dee Formation in the United States and provided by the International Atomic Energy Agency in Vienna, Austria.

Equation 1:

$$\delta^{18}O_{sample} = \left[\frac{\left({}^{18}O/{}^{16}O\right)_{sample} - \left({}^{18}O/{}^{16}O\right)_{standard}}{\left({}^{18}O/{}^{16}O\right)_{standard}}\right] x10^3$$

, which can be written as:

$$\delta^{18}O_{sample} = \left[\frac{\left({}^{18}O/{}^{16}O\right)_{sample}}{\left({}^{18}O/{}^{16}O\right)_{standard}} - 1\right] x10^3$$

4.3.2.1 Stable oxygen isotope ratio

The oxygen isotopic composition of marine carbonates varies with temperature, the isotopic composition of seawater, and physiologically induced factors or vital effects (Rohling & Cooke, 1999). The fractionation of oxygen isotopes in precipitated carbonate is heavily temperature-dependent, with higher fractionation coefficients at lower temperatures and vice versa. This relationship allowed the determination of a number of paleotemperature equations relating temperature and $\delta^{18}O$ (Bemis et al., 1998; Kim & O'Neil, 1997; Marchitto et al., 2014; Shackleton, 1974), from which the following approximate values were derived: 0.25‰ per ºC at ~10ºC and 0.20‰ per ºC at ~40ºC (Kim & O'Neil, 1997). However, these equations require the estimation of the offset between calcite and sea-water $\delta^{18}O$ ($\delta^{18}O_{sw}$), which in turn, varies according to the global ice volume and the hydrological cycle (precipitation and evaporation) at the formation sites of intermediate- and deep-water masses. During glacial periods, the

increased accumulation of light oxygen isotopes in the ice caps led to a global depletion of ^{16}O in the world's oceans. Paleoceanographic studies of the Pleistocene usually correct $\delta^{18}O_{calcite}$ for ice volume by subtracting between 0.008-0.01 ‰ per meter of sea level increase (Spratt & Lisiecki, 2016). As sea-water density is similarly affected by compensating temperature and salinity effects, $\delta^{18}O$ can be interpreted as a qualitative density proxy, indicative of the strength of horizontal (isopycnal) circulation (LeGrande et al., 2004; Lynch-Stieglitz et al., 1999). After $\delta^{18}O$ is set at the surface, it becomes a conservative sea-water property, that can only change due to mixing between water masses (assuming negligible geothermal and pressure heating effects; Oppo et al., 2015).

$\delta^{18}O$ equilibrium deviations in organically precipitated carbonates can be caused by a variety of biological effects (*i.e.*, ontogenetic, symbiont photosynthesis, respiration, gametogenic) and changes in carbonate ion concentration in sea water [CO_3^{2-}]. The few studies available on the effect of carbonate ion concentration show decreasing $\delta^{18}O$ with increasing [CO_3^{2-}], with the magnitude of this effect being species specific (Spero et al., 1997). Nevertheless, the resultant carbonate ion effect is one to two orders of magnitude smaller (0.002-0.005 ‰ per $\mu mol.kg^{-1}$ [CO_3^{2-}]) than the expected effect attributable to salinity or temperature changes, so its effect on foraminiferal $\delta^{18}O$ is not considered in this study.

4.3.2.2 Stable carbon isotope ratio

Foraminifera use marine total dissolved inorganic carbon (DIC) to precipitate their calcite tests, thereby recording the $\delta^{13}C$ of seawater. Tests of planktic foraminifera are generally assumed to be precipitated in equilibrium with the isotopic carbonate composition of ambient seawater (Rohling & Cooke, 1999) and therefore foraminiferal $\delta^{13}C$ has been widely used to reconstruct primary productivity, carbon dioxide concentration, and the carbonate ion concentration of ancient oceans (Lear et al., 2016). Possible disequilibria in calcite $\delta^{13}C$ and $\delta^{13}C$ of DIC can be caused by biological (*i.e.,* vital effects and presence of symbionts) and carbonate ion concentration effects. Similarly to its effect on $\delta^{18}O$, higher carbonate ion concentrations decrease calcite $\delta^{13}C$. The signal magnitude is species specific (Spero et al., 1997) and probably due to kinetic fractionation (Rohling & Cooke, 1999). To avoid having to account for most biological effects in $\delta^{13}C$, paleoceanographic studies focus on single species samples collected from narrow granulometric ranges (Friedrich et al., 2012). Since this thesis focusses on the deep thermocline characterization, non-spinose and non-symbiont-bearing globorotaliids were selected because these species are believed to accurately record $\delta^{13}C_{DIC}$ (Ravelo & Fairbanks, 1995).

Dissolved inorganic carbon comprises the sum of the concentrations of CO_2 (aqueous carbon dioxide), HCO^{3-} (bicarbonate, the most abundant), and CO_3^{2-}, with seawater pH controlling the relative proportion of the different components (Kroopnick, 1985). Biological primary production in the euphotic zone (~200 meters water depth) strongly fractionates stable carbon isotopes, concentrating the light

isotope ^{12}C in organic matter, and enriching surficial water in ^{13}C (Freeman & Hayes, 1992). As organic matter falls though the water column, ^{12}C-rich organic matter is oxidized and remineralized, adding nutrients, and effectively transferring carbon with low $\delta^{13}C$ to deep waters (Duplessy et al., 1984). Maximum remineralization rates are found between 100 m and 1200 m water depth, below the photic zone and above the pycnocline, where high-density gradients promote the accumulation of organic matter (Feely et al., 2004). Therefore, increased productivity will enhance $\delta^{13}C$ gradients between surface and deep waters. Less ventilated water masses ("older") will also tend to have a lower $\delta^{13}C$ signal relative to waters that have been recently exposed to the surface ("younger"). As a result of these processes, nutrient levels and the $\delta^{13}C_{DIC}$ are generally negatively correlated (Kroopnick, 1985). High nutrient concentrations and low $\delta^{13}C$ in Antarctic Bottom Water, for example, reflect the longer time these waters have spent away from the surface, collecting nutrients and ^{13}C-poor carbon from the decay of organic matter transported to abyssal depths in particulate and dissolved forms. Conversely, NADW's low nutrient content and high $\delta^{13}C$ reflect relatively recent convection of nutrient poor and ^{13}C-rich surface waters from the upper to the lower AMOC limb. Following the same logic, extensive sea-ice cover at the *locus* of formation of a deep-water mass tend to decrease its $\delta^{13}C$ values, due to incomplete nutrient usage and increased accumulation of remineralized organic matter. The relative "age" of a water mass (i.e., amount and time of exposure to organic-matter decay) can also be qualitatively assessed by vertical $\delta^{13}C$ gradients in basins with active convection or upwelling (Hodell et al., 2003; Ziegler et al., 2013). Efficient vertical transport of carbon (generalized as ventilation) results in low $\delta^{13}C$ gradients between the upper water column and sea bottom, while the opposite is true in non-overturning basins with "old", poorly ventilated, deep waters (Rohling & Cooke, 1999). The $\delta^{13}C$ in surface waters is also influenced by air-sea gas exchange, which is favored in cold, windy regions (Broecker & Reimer, 1992), such as the Subantarctic Frontal Zone. ^{13}C enrichment of dissolved CO_2 in surface seawater results from the temperature-dependent fractionation of $^{13}C/^{12}C$ during the exchange of CO_2 at the water-atmosphere interface (Mook et al., 1974). Colder waters display a larger fractionation and higher $\delta^{13}C_{DIC}$ (0.105‰ / $°C^{-1}$).

4.3.2.3 Methodology used for stable isotope analyses

Stable carbon and oxygen isotope ratios were measured on a Thermo Fischer MAT 253 Plus IRMS gas isotope ratio mass spectrometer with a coupled Kiel IV automated carbonate preparation device at the Institute of Earth Sciences, Heidelberg University. The instrument was calibrated using an in-house standard (Solnhofen limestone), which is itself calibrated against the IAEA-603. The standard deviations (reproducibility) for repeated measurements of the in-house standard were 0.04‰ for $\delta^{13}C$ and 0.08‰ for $\delta^{18}O$. The results were normalized according to Paul et al. (2007). The standard deviations (reproducibility; n=10) for repeated sample measurements were 0.12‰ for $\delta^{13}C$ and 0.08‰ for $\delta^{18}O$. All reported uncertainties are 1σ.

4.3.3 Age model refinement of the Middle Pleistocene section of Site U1313

The existing age model for the Middle Pleistocene portion of U1313 {Naafs:2012ep} has been updated in the framework of this thesis since this period was previously only covered by low-resolution benthic isotope records between 696–607 ka and 885–854 ka. For this purpose, 297 new benthic stable oxygen isotope data points for the interval 1203–543 ka have been generated using *C. wuellerstorfi* and *U. peregrina* from the primary splice (Figure 4.4; Naafs et al., 2011). The new measurements were then combined with the previously published benthic data from the primary splice (Naafs et al., 2011; 2012), and high-resolution benthic oxygen isotope data from the secondary splice of U1313, that covered the interval between 840 and 800 ka (Ferretti et al., 2015). To allow for a continuous record comprising data of both species, $\delta^{18}O$ values of *C. wuellerstorfi* were corrected to *U. peregrina* $\delta^{18}O$ values by adding 0.64‰ (Shackleton & Opdyke, 1973). For depth-age conversion, the combined and species-adjusted benthic $\delta^{18}O$ record of Site U1313 was tuned to the LR04 benthic stack (Lisiecki & Raymo, 2005) using the software AnalySeries 2.0.8 (Figure 4.4; Paillard et al., 2011). All tie points used are listed in Table A1 (Data appendix). The sedimentation rate averaged 4.6 cm/kyr, close to the expected rate for the Pleistocene (IODP Expedition Scientists, 2005).

4.3.4 Magnesium/Calcium ratios of planktic foraminifera as temperature proxy

Variations in the ratio of magnesium to calcium (Mg/Ca) in carbonate tests of foraminifera are widely used as a paleotemperature proxy (Anand et al., 2003; Barker et al., 2005; Cléroux et al., 2008, 2013; Nürnberg et al., 1996). Mg is incorporated directly in foraminiferal calcite from sea water during test precipitation, with an average sensitivity around 10% per 1ºC (Anand et al., 2003). Apart from sea-water temperature, Mg/Ca ratios may also be affected by (1) the ontogenetic development of planktic foraminifera species, test size and the presence of symbionts (Elderfield et al., 2002), and (2) sea-water salinity (Arbuszewski et al., 2010). Ontogenetic and size related effects are avoided by selecting single species samples from narrow granulometric fractions. Salinity may increase Mg/Ca incorporation, but the so far available data from laboratory studies suggests that its effect is small relative to temperature (4 ± 3% per psu; Dueñas-Bohórquez et al., 2009; Gray & Evans, 2019). Given the regional salinity variations expected in most of the ocean over glacial-interglacial cycles (less than ±1 PSU, 2σ), a salinity sensitivity of ~4% per PSU should not pose a major problem for Mg/Ca paleothermometry in the framework of this study (Gray et al., 2018).

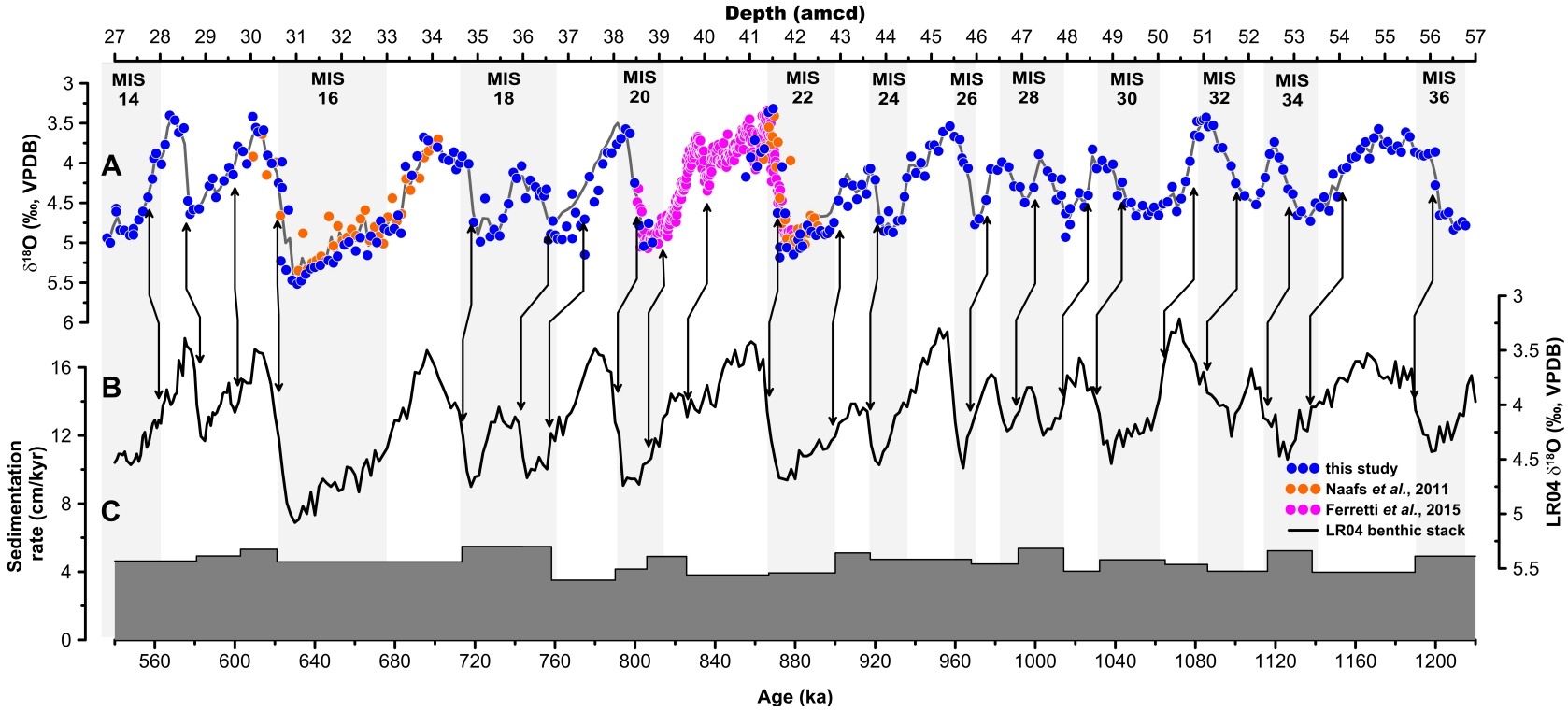

Figure 4.4. Chronostratigraphy of Site U1313 between MIS 36 and 14. (A) Benthic $\delta^{18}O$ data for Site U1313 on the amcd depth scale (Naafs et al., 2012). Orange circles represent data from Naafs et al. (2011), pink circles from Ferretti et al. (2015), and blue circles represent data produced for this study. The black line represents the resampling every 0.09 m (amcd). (B) LR04 benthic $\delta^{18}O$ stack used as tuning target. Tie points (Table 1) are illustrated by arrows. (C) Sedimentation rate for Site U1313 in cm/kyr. Grey bars represent MIS stages according to Lisiecki and Raymo (2005).

4.3.4.1 Methodology used for Mg/Ca analyses

The cracked foraminiferal tests were cleaned following the procedures described by Martin & Lea (2002) without the DTPA step. This method includes a reductive step for the removal of metal-oxides with an ammonium citrate/hydrazine solution and an oxidative step with H_2O_2 for the removal of organic matter. A total of 836 trace-elemental analyses were performed on a Thermo Scientific Agilent 720 ICP-OES at the Institute of Earth Sciences, Heidelberg University. Blanks were measured alongside the samples to detect potential contamination during the cleaning process. Standard deviation from replicates (n=20) was ± 0.18 mmol/mol for Mg/Ca.

Fe/Ca, Mn/Ca and Sr/Ca ratios were additionally analyzed to monitor contamination by siliciclastic material and diagenetic overgrowths. Mg/Ca, Fe/Ca and Mn/Ca results were normalized to the external standard ECRM752-1 (3.762 mmol/mol for Mg/Ca, 0.17 mmol/mol for Fe/Ca, and 0.132 mmol/mol for Mn/Ca; Greaves et al., 2008). Linear correlation between normalized Fe/Ca and Mg/Ca was inferred as siliciclastic contamination and led to the exclusion of 12 data points with Fe/Ca higher than 0.2 mmol/mol. Linear correlation between normalized Mn/Ca and Mg/Ca was interpreted as a sign of diagenetic overgrowth and led to the further exclusion of 5 data points with Mn/Ca higher than 0.26 mmol/mol.

4.3.5 Choice of paleotemperature equations

4.3.5.1 Globorotalia crassaformis

Core-top and sediment-trap studies from the North Atlantic realm unanimously show that *G. crassaformis* calcifies in the deep thermocline (Anand et al., 2003; Cléroux et al., 2013; Regenberg et al., 2009). Accordingly, calculated calcification depths vary depending upon the investigated oceanographic region, between 330–600 m in the Caribbean and Equatorial Atlantic (Regenberg et al., 2009), 500–800 m in the Sargasso Sea (Anand et al., 2003) and 600–900 m in the equatorial and mid-latitude North Atlantic (Cléroux et al., 2013). The species-specific *G. crassaformis* paleotemperature equation established by Cléroux et al. (2013; Equation 2) was applied to convert Mg/Ca ratios into subsurface temperatures (T_{crass}). This equation was chosen because (i) the samples used in this study are the most representative of the hydrographic conditions at Site U1313, and (ii) the Mg/Ca data produced for this project were generated using the same cleaning protocol, which also includes a reductive step.

(Equation 2) $$Mg/Ca = 0.658 \pm 0.006\ e^{0.122 \pm 0.016T}$$

4.3.5.2 *Globorotalia truncatulinoides (d)*

As different cryptospecies of *G. truncatulinoides* have different Mg assimilation proportion in relation to temperature, the choice of paleotemperature equation for this species should consider the geographical distribution of different cryptospecies. The species-specific temperature equation for this species published by Cléroux et al. (2013) was excluded because it was generated using specimens from a large latitudinal range within the Atlantic Ocean. The authors take note that their samples contained three different *G. truncatulinoides* (d) populations/cryptospecies, which may help explain why their calculations led to unrealistically cold temperatures (<0ºC) during the LGM (Figure 4.5). The "cold water" equation from (Regenberg et al., 2009) was also excluded because it is a more general equation that bundled data from several deep dwellers. This equation also yielded colder-than-expected values for the youngest Holocene samples compared to modern temperature at the calculated calcification depth of *G. truncatulinoides* (d) at Site U1313 (~450 m water depth; Cléroux et al., 2013). Thus, for this thesis the species-specific equation determined by Cléroux et al. (2008; Equation 3) has been chosen because the calculated temperature values for the youngest Holocene samples match the modern temperature for the estimated calcification depth temperature at our study site (Figure 4.5) and because it was determined using only dextral specimens from the North Atlantic. To account for the lack of a reductive step in the cleaning methodology used by Regenberg et al. (2009) and Cléroux et al. (2008), ECRM normalized Mg/Ca values were adjusted using Equation 4 (Regenberg et al., 2014) before being applied to those paleotemperature equations. The reported uncertainty of Equation 3 is ±1.4ºC.

(Equation 3) $$Mg/Ca = 0.62 \pm 0.16\ e^{0.074 \pm 0.017 * T}$$

(Equation 4) $$Mg/Ca_{red} = -0.019 + 0.978 * Mg/Ca_{non\text{-}red}$$

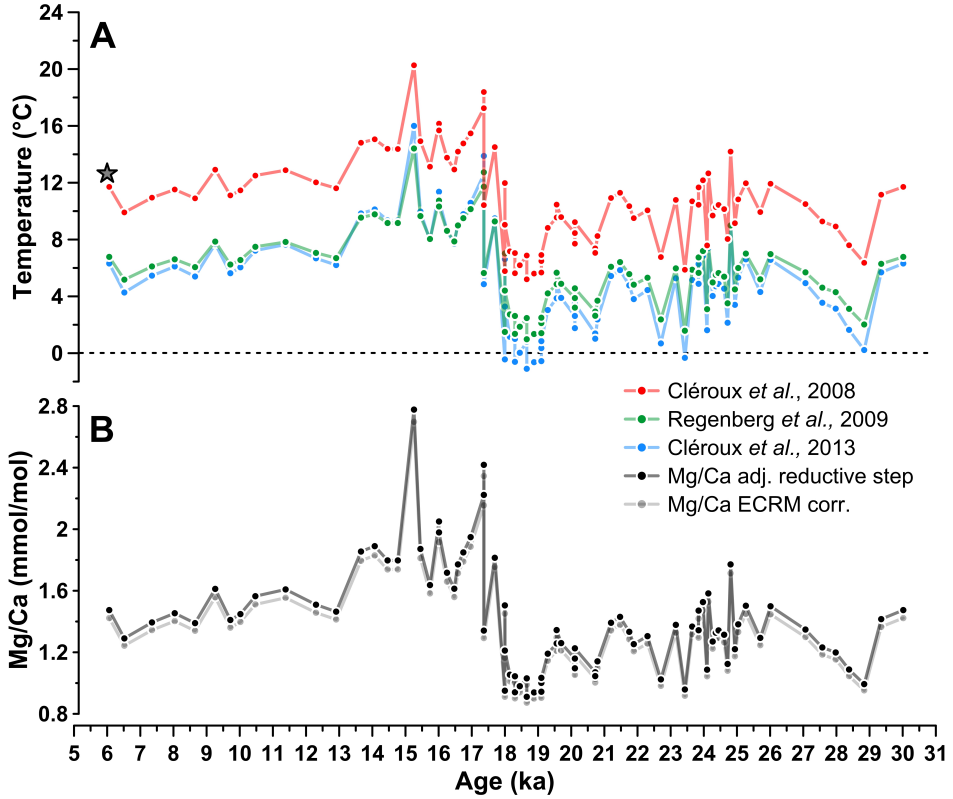

Figure 4.5. ***(A)*** *ECRM-corrected Mg/Ca results from ICP-OES analyses performed on G. truncatulinoides (d) samples with and without adjustment for the reductive cleaning step (Regenberg et al., 2014).* ***(B)*** *Calculated paleotemperatures according to Cléroux et al., 2008, Regenberg et al., 2009, and Cléroux et al., 2013. Dashed line in graph* ***(A)*** *marks 0°C and grey star represents modern subsurface temperature at the calculated calcification depth (450 m) of G. truncatulinoides (d) at the latitude of Site U1313 (Locarnini et al., 2019)..*

4.3.6 Ice-volume correction and calculation of $\delta^{18}O$ of seawater

Ice-volume corrected $\delta^{18}O$ of seawater ($\delta^{18}O_{sw\text{-}ivc}$) was used as an approximation for sea-water salinity. It was computed using the "low-light" equation by Bemis et al. (1998) followed by a correction for global ice volume. For salinity estimates during the Late Pleistocene interval, the ice-volume component of $\delta^{18}O_{sw}$ was estimated by scaling the sea-level record of Lambeck et al. (2014) to a factor of 0.009‰.m^{-1} (Rohling et al., 2014) and then subtracting it from $\delta^{18}O_{sw}$.

4.3.7 Modern oceanographic analysis and dataset

All oceanographic figures were prepared using the software Ocean Data View (Schlitzer, 2002) and data from the World Ocean Atlas 2018 (Locarnini et al., 2019; Zweng et al., 2019). This dataset is composed of time integrated data from over 15 million stations measured between 1955 and 2018, which is particularly relevant for the very long timescales of this study as it averages the effects of decadal variability.

5 The relationship between Atlantic Meridional Overturning Circulation and the Mediterranean Outflow

5.1 The Mediterranean Outflow Water

The Mediterranean Outflow Water (MOW) is a modulator of temperature and salinity at intermediate depths within the subtropical North Atlantic (Potter & Lozier, 2004), thus playing a crucial role in determining upper ocean stratification in the basin (Feucher et al., 2016) .The flux of this warm and saline water mass into the North Atlantic Ocean contributes with 30% to the total salinity that reaches high latitudes of the North Atlantic with the remaining 70% being attributed to subtropical evaporation in the open-ocean (Talley, 2011). As a result, though its flow is small in magnitude (<1 Sv at the Strait of Gibraltar) compared to other circulation features of the upper North Atlantic, the MOW is considered crucial for the thermohaline structure of this basin (Hecht et al., 1997), and may have a disproportional impact on the overall water-mass distribution of the northern Atlantic basin (Reid, 1979).

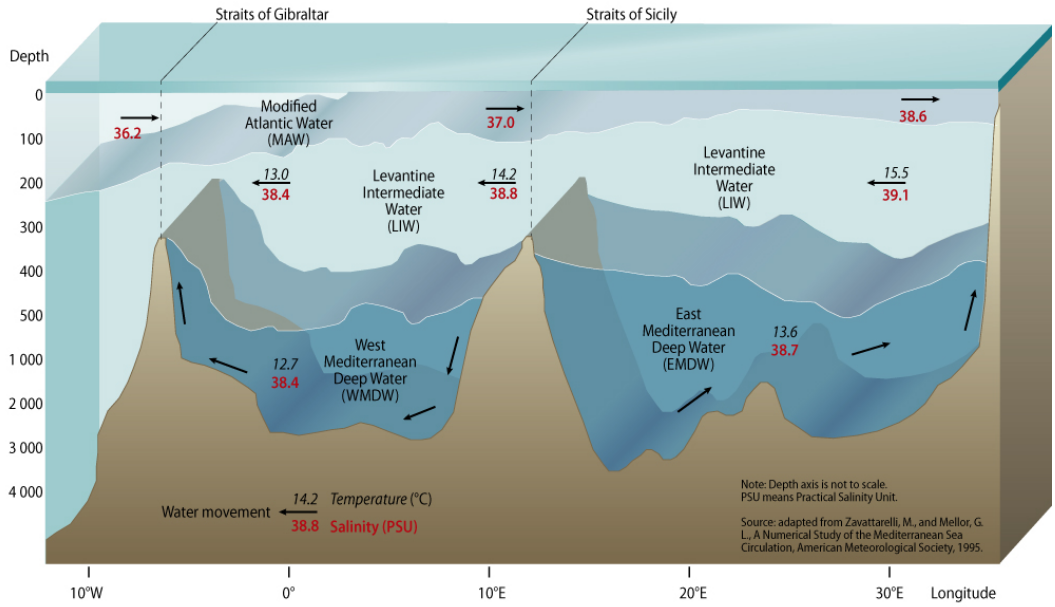

Figure 5.1. Vertical distribution of water masses in the Mediterranean Sea (GRID-Arendal, 2014)

Surface Atlantic waters inflow the Mediterranean through the Strait of Gibraltar (~0.8 Sv, ~15.5ºC and 36.5 psu; Millot, 2009; Soto-Navarro et al., 2015) and flow eastward, cooling and becoming more saline on their way due to positive net evaporation. Mainly during boreal winter, when the Mediterranean is subjected to stronger westerlies, dry and cold winds from the European continent induce convection

and precondition the formation of endogenous intermediate- and deep-water masses. The Levantine Intermediate Water (LIW, ~15.5ºC and ~39 psu, Hayes et al., 2019) is the most voluminous water mass produced in the Mediterranean (Skliris, 2013) and is formed primarily in the Levantine Basin. The LIW dominates the Mediterranean water column between 350 and 600 m water depth and accounts for more than 60% of the final modern MOW (Millot et al., 2009). In the Gulf of Lion, winter convection is responsible for the formation of the Western Mediterranean Deep Water (Figure 5.1, WMDW, 12,7ºC and ~38.4 psu; Zavatarielli & Mellor, 1995), which accounts for around 20% of the final outflow although this proportion is believed to increase during colder winters and glacial stages (Kinder & Parrilla, 1987; Lafuente et al., 2002). Both water masses then flow westward, pouring over the Strait of Gibraltar to form MOW. Once it reaches the eastern Atlantic, the outflow plunges downward (0.7-1 Sv, ~15.5ºC and 36.5 psu, Soto-Navarro et al., 2015), entraining into surrounding central waters and increasing three- to fourfold in volume from the Strait of Gibraltar to up to ~3 Sv within the first 100 km eastwards (Baringer & Price, 1999). Entrainment of overlying central waters decreases the density of the Mediterranean plume, which then becomes neutrally buoyant in the deep thermocline / upper pycnocline of the North Atlantic near Cape St. Vincent (Baringer & Price, 1999; Price et al., 1993). Notwithstanding entrainment, MOW sustains excess salinity and temperature, providing a source of heat and salt for both the North Atlantic's subtropical and subpolar gyres (Iorga & Lozier, 1999). Because of the topography of the Gulf of Cadiz, MOW splits into two stability levels (Baringer & Price, 1999). The upper core is centered around 700 m and constitutes the northward branch of the MOW, which flows geostrophically as an eastern boundary current along the European continental margin to the Irish Seas and Rockwall Trough (Rogerson et al., 2012). The westward or descending branch develops from the denser lower core, centered around 1000 m and with density range similar to LSW (Talley, 2011). The denser lower core forms the MOW's westward branch, which descends further into the main thermocline and achieves neutral buoyancy centered around 1100 m (between 800 to 1300 m; Price et al., 1993) with density similar to LSW (Talley, 2011).

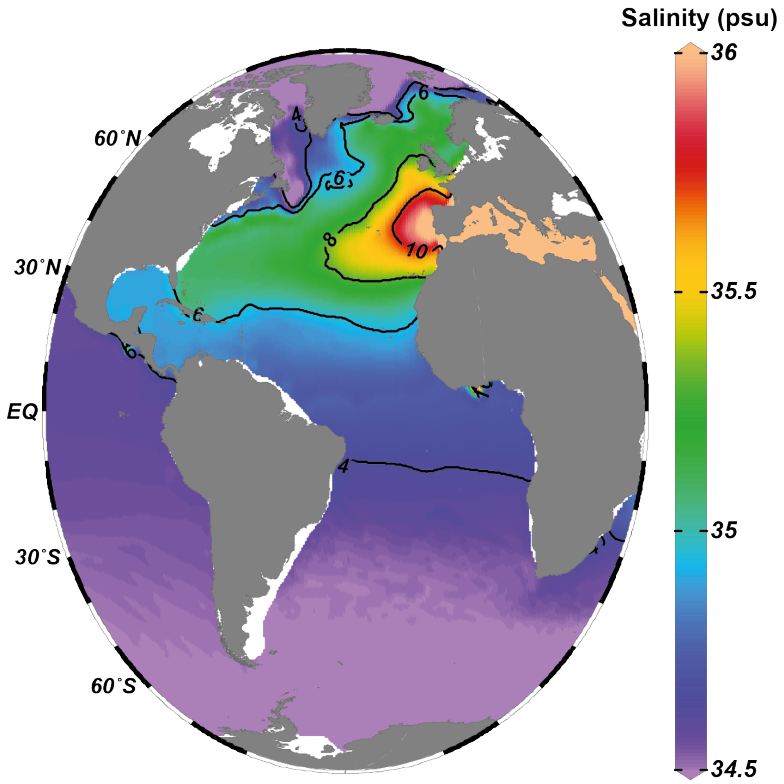

Figure 5.2 – Salinity (colors) and temperature (contours) at σ_0 = 27.53, the density layer with maximum overturning in the northeastern North Atlantic (Lozier et al., 2019). This density layer is found between 900 m and 1000 m in the subtropical North Atlantic. Figure produced using the software Ocean Data View (Schlitzer, 2013) and data from the World Ocean Atlas 2018 (Locarnini et al., 2019; Zweng et al., 2019). Note the salinity and temperature anomaly originating from the outflow of the MOW via the Gulf of Cadiz.

The MOW's westward branch recirculates only to 35°W, with no clear advective flow past this meridian (Iorga & Lozier, 1999; Mazé et al., 1997). Beyond that, the transport of saline water into the North Atlantic interior is through the propagation of anticyclonic submesoscale eddies (meddies; Armi & Zenk, 1984; Richardson et al., 1991). The release of meddies is a MOW-specific mechanism for large-scale mixing of outflow water into the subtropical North Atlantic (Richardson et al., 1989). After their formation near Cape St. Vincent (Bower et al., 1997), they propagate past the Mid-Atlantic Ridge, transporting approximately 25% of the total MOW's salinity anomaly. Along their way eastwards, meddie decay releases extra heat and salinity into the large-scale flow of deep thermocline and upper-intermediate levels (Spall, 1999). Meddies have also been detected as far as the Bahamas, below the core of the subtropical gyre (McDowell & Rossby, 1978). As a result of all these processes, MOW's westward transport forms and maintains a permanent subsurface salinity maximum between 700 m and 1500 m water depth that extends to the eastern edge of the North Atlantic (Figure 5.2; Baringer & Price, 1999; Price et al., 1993). The upper part of the salinity anomaly interacts with central waters, influencing the physical properties of the flow that later joins NAC. The lower layer of the salt tongue represents the interaction between the deep MOW and LSW (Spall, 1999), which characterizes the upper NADW (1300 m and 2500 m water depth) and flows southward

as part of the lower branch of the AMOC. Finally, MOW also interacts directly with waters from the Nordic Seas via its northward branch, that reaches the northern end of the Rockall Trough, near 60°N. There, isopycnals containing these warm and saline waters rise above the Wyville-Thomson Ridge as part of the Atlantic Inflow (Lozier & Stewart, 2008; Reid, 1979). This way, the MOW affects both upper and deep branches of the meridional circulation and is an essential part of North Atlantic circulation.

Although the MOW's most typical characteristic is its high salinity content, numerical modeling shows that it dramatically increases the potential temperature within the central North Atlantic above 900 m (Jia et al., 2007). Long-term studies of hydrographic changes in the subtropical North Atlantic found that the MOW was a significant source of long-term warming and salinification of mid-depths Atlantic (Potter & Lozier, 2004) and has contributed to 0.159°C temperature increase per decade at mid-depths in the eastern North Atlantic since the 1950s. Numerical models also found that, in the absence of Mediterranean outflow, the eastern North Atlantic thermocline would be cooler (Jia et al., 2007) with deepened isopycnals from below the STG outcropping to the east of the gyre (Spall, 1999). The presence of the MOW places these isopycnals below the outflow, effectively deepening the thermocline in the eastern North Atlantic (Spall, 1999) and connecting outflow and subtropical gyre at depth through density layers.

Despite suggestions that salinity and heat from the MOW are intrinsically connected to AMOC variability (Reid, 1979), modern physical oceanography studies question its role beyond the salinification that would be affected by a freshwater loss of about 0.05 Sv over a comparable area of the Atlantic (Johnson et al., 2019). The questioning is understandable, given MOW's absolute flux is very small in comparison with other circulation features of the upper North Atlantic (e.g., ~ 30 Sv of the Gulf Stream). It is possible, nonetheless, that MOW's influence on the AMOC is a matter of timescale. A study reproducing pathways of Argo floats to study the distribution of intermediate-water masses over a wide range of timescales found that tracers starting from the Gulf of Cadiz accumulated in the STG, potentially altering thermohaline characteristics of this gyre over timescales longer than a century (Sévellec et al., 2017). As the MHF transports warm water from under the STG to the eastern SPG, this suggests that the thermal effect of MOW on northward heat transport via the upper AMOC branch may be significant on centennial timescales.

5.2 On the subsurface heat transport in the North Atlantic

Scientific understanding about northward heat transport has changed considerably over the last decade. The simplistic direct surface heat transport from the STG to the eastern SPG (eSPG) via the Gulf Stream and the NAC is now understood to be tridimensional, taking place along layers of equal density (Foukal et al., 2016). This has profound implications on the scientific understanding about heat transport and variability on longer timescales, because it implies that the meridional heat

transport to eastern subpolar gyre should depend on inter-gyre density connectivity. Consequently, mechanisms that determine isopycnal geometry and density-compensated heat gradients along isopycnals may be crucial to understand the sequence of events during periods of abrupt climate change.

The shape of isopycnals connecting eastern SPG to STG and Gulf of Cadiz (Figure 5.4), the main sources of heat and salt to high-latitudes North Atlantic, can be interpreted as indicative of connectivity between gyres. Studies about northward heat transport and overturning highlighted density surfaces σ_0=27.10 and σ_0=27.53. The former being the layer of maximum flow from the STG to the surface of the SPG (Burkholder & Lozier, 2011) and the latter being the surface of maximum overturning across the OSNAP line (Chapter 2; Lozier et al., 2019). As any subsurface heat is ultimately derived from surface anomalies, spice (i.e., density-compensated heat) distribution within a density layer can indicate the geographical origin of heat at the subsurface (Figure 5.3).

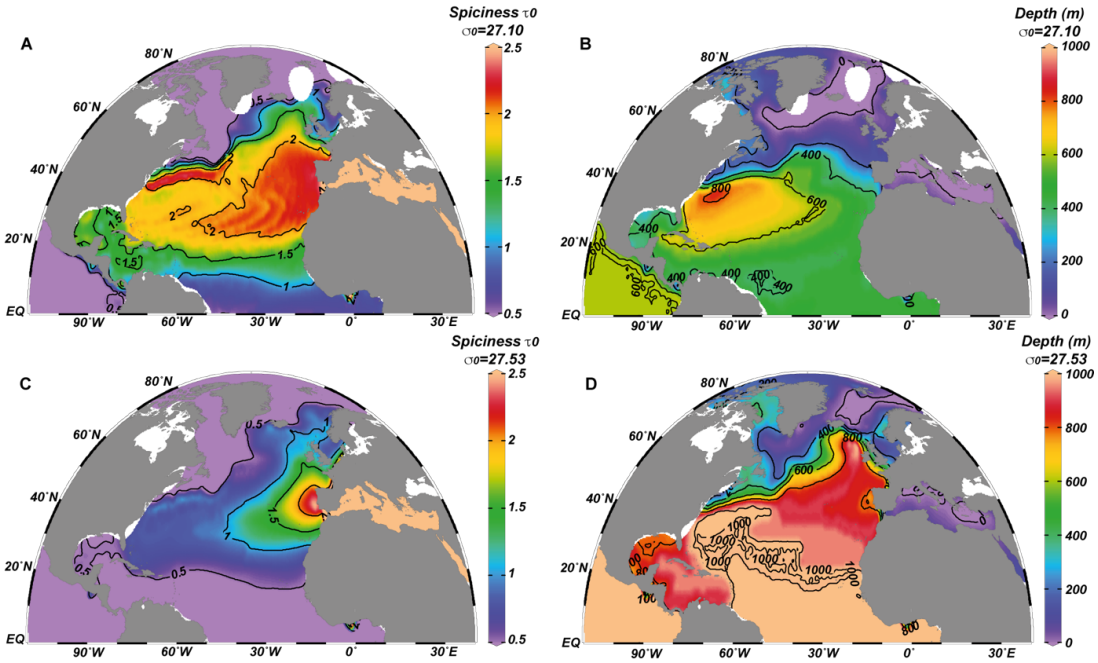

Figure 5.3. Spice distribution (A, C) at and depth (B, D) of the density layers σ_0=27.10 and σ_0=27.53. Spice distribution in layers σ_0=27.10 and σ_0=27.53suggests the MOW strongly influences heat variability in the NAC and in the upper AMOC branch.

Distribution of salt-compensated heat at σ_0=27.10 (maximum flow to eSPG) shows the two sources of spice to this density layer: the "Northwest Corner" under the Gulf Stream (east of Grand Banks) and the Mediterranean outflow off the Gulf of Cadiz (Figure 5.3A). Depth distribution of this layer shows the typical bulging of isopycnals below the STG, where σ_0=27.10 is the deepest (between 700 m and 800 m, Figure 5.3B). This layer rises to the surface at the high latitudes of the North Atlantic bringing central waters to the surface of eSPG (Burkholder and Lozier, 2014) transporting a mixture of STMW and entrained MOW along isopycnals. MOW's

contribution to the physiochemical characteristics of surface and mode waters in eSPG have been suggested by Harvey (1982) and Reid (1994), but usually ignored because of the classic surface-to-subsurface directionality bias in oceanographical studies. According to the canonic interpretation, surface waters in eSPG undergo winter convection to form the different types of SPMW (Brambilla and Talley, 2008; Garcia-Ibanez et al., 2018). The new understanding about pathways of northward heat transport (Burkholder and Lozier, 2014; Foukal and Lozier, 2016) is in better agreement with the cyclonic circulation of the SPG and can account for a decreasing spice gradient between the Gulf of Cadiz and eSPG (Figure 5.3A).

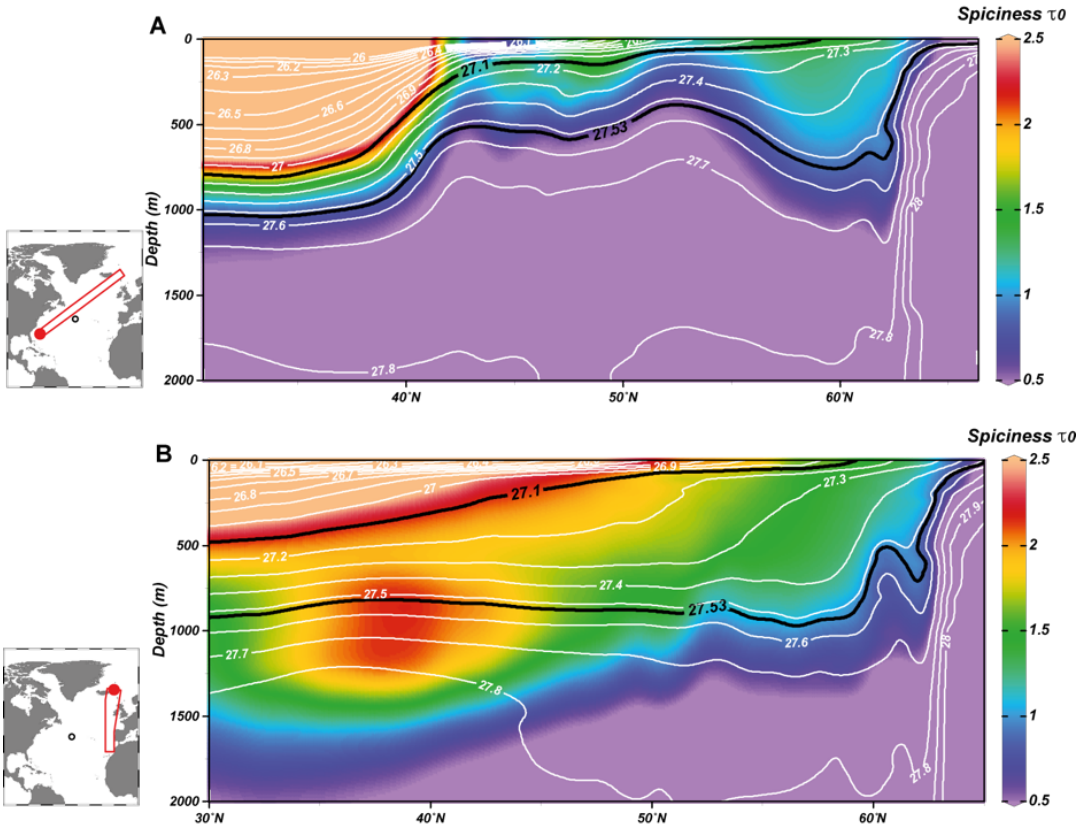

Figure 5.4 Spice distribution and isopycnal geometry (A) between the Gulf Stream and eastern Subpolar Gyre, (B) along the North Atlantic's eastern boundary. Black lines in A and B highlight σ_0=27.10 and σ_0=27.53. The color scales for spice are equal.

The significance of Mediterranean spice for northward heat transport, thus overturning, in the North Atlantic is even more evident at σ_0=27.53 (Figure 5.3C), the layer with maximum northward flow in the upper AMOC branch (Lozier et al., 2019). As any subsurface heat is ultimately derived from surface anomalies, spice maximum at a density layer should correspond to the location of where this spice originates. In the case of density layer 27.53, this does not correspond to eastern subpolar gyre as previously expected, but to the Gulf of Cadiz (Figure 5.3C). This layer outcrops only in the Nordic and eastern Mediterranean Seas, pointing to the intrinsic connection between heat loss in that basin with density-compensated heat from the eastern Mediterranean (Figure 5.3D).

Isopycnal geometry and spice gradients between the Gulf Stream, Gulf of Cadiz and eSPG further corroborate the connection between MHF and the MOW (Figure 5.4). Along the western boundary pathway (Figure 5.4A), density layers containing the warm and salty waters of the STG outcrop at the boundary between gyres due to strong vorticity gradients and southward Ekman velocities (Foukal and Lozier, 2016). As a result, these waters accumulate in the STG, as inferred by Burkholder and Lozier (2011; 2014). Spice along these isopycnals, including σ_0=27.10, decreases and then increases again, suggesting lateral spice advection and not a continuous transport between the STG and eSPG. In contrast, along the eastern boundary pathway (Figure 5.4B) spice decreases northwards continuously, which would be expected due to continuous heat loss to the atmosphere. Thick density layers below the STG (thus below the mixed layer) show the isopycnal connection is well established. A pattern that is due to the existence of MOW at this location. The vertical distribution of spice along the eastern boundary pathway (Figure 5.4B) can be confidently attributed to the Mediterranean outflow between σ_0=27.3 and σ_0=27.8, which confirms that MOW's contribution to σ_0=27.10 (Figure 5.3A) is likely completely attributed to entrainment in subtropical central waters. According to OSNAP's data review (Lozier et al., 2019), the upper (northward flowing) and lower (southward flowing) AMOC branches were divided along the σ_0 = 27.66 density in the SPG. Thus, the northward transport of MOW warms the subsurface of the eSPG and below σ_0 = 27.66 MOW's spice is transported southwards as part of the upper NADW in the lower AMOC branch.

The contribution of subsurface spice to northward heat transport has likely gone unnoticed because of the two paradigms: (1) of the ocean being forced by the atmosphere, and (2) the surface as the only origin for spice. Regarding the first, this is true at the surface and on short timescales, but on climatic timescales such as the ones discussed in this thesis (i.e., Chapters 6, 7 and 8), the atmosphere can be considered in thermal equilibrium with the ocean due to its low thermal capacity and fast adjustment times (Rahmstorf & Willebrand, 1994). Therefore, on climatic timescales it is more likely that the atmosphere (and thus surface circulation in the ocean as well) is forced by internal oceanic variability and interactions between the ocean and cryosphere. Regarding the second paradigm, although the origin of the spice at the subsurface of eastern is indeed at the surface, it is the surface of the Mediterranean Sea, not of the North Atlantic. Therefore, in the latter basin, spice is supplied both downwards from the surface of the STG and laterally via the outflow off the Gulf of Cadiz. As most models do not have resolution enough to resolve outflows from narrow marginal basins (Johnson et al., 2019), potential effects of MOW on northward heat flux in the North Atlantic have not yet been estimated. However, the Mediterranean Sea in practice imports heat from surface waters and exports it at depth, deepening the thermocline and "thickening" isopycnals in the upper AMOC branch, thus acting as a gateway for heat in the deep STG to be transmitted to the SPG over the long timescale focus of this dissertation. There, the anomalously warm surface (relative to its latitude) cedes (mostly latent) heat to the atmosphere, warming western Europe and providing moisture to very high latitudes. This is in agreement with model and observational

studies showing that the strength of the AMOC at 40ºN is not significantly correlated to overturning in the SPG but rather modulated by zonal density gradients across the North Atlantic (Levang and Schmitt, 2020; Lozier 2010).

As the density compensated heat by the MOW was displayed so clearly in the analyzed density layers, it is to be expected that strength and settling depth of the MOW in relationship to the STG, should be intrinsically connected to northward heat transport in the North Atlantic, a concept which is so far unexplored. The strength, settling depth and northward extension of MOW were very different during the last glacial stage and before and after the MPT (Kano et al., 2007; Rogerson et al. 2005, 2010; Schönfeld and Zahn, 2000; Wienberg et al., 2020) and would have affected the northward heat transport during these intervals. The variability of the STG-MOW system in modulating the oceanic heat transport in the North Atlantic and its interaction with the cryosphere are the focus of the Chapters 6 to 8.

6 On the relationship between subsurface warming and the Atlantic Meridional Overturning Circulation across the Last Glacial Maximum and deglaciation

6.1 Introduction

The AMOC is inferred to play a significant role in modulating the global and regional climate via the redistribution of oceanic heat, salt, and carbon (Chapters 1 and 2), but its evolution throughout the last deglaciation is still not well constrained. The delivery of positive buoyancy fluxes to the upper subpolar North Atlantic has long been evoked as the main mechanism for weakening the AMOC (Manabe & Stouffer, 1988; Stommel, 1961) and have been inferred to cause the near collapse of deep convection in the northwestern North Atlantic during massive ice-rafted debris deposition events (McManus et al., 2004; Böhm et al., 2015, Ng et al., 2018). Episodic calving from the circum-Atlantic ice sheets during Heinrich Events (HE) has also been associated with abrupt subsurface warming (Alvarez-Solas & Ramstein, 2011; Marcott et al., 2011), which would trigger the melting of buttressing ice sheets and thus lead to (more) freshwater discharge over the North Atlantic (Alvarez-Solas & Ramstein, 2011). However, the initial trigger for subsurface warming has not yet been established. Warm and saline waters within the intermediate North Atlantic have been invoked as a crucial factor for restarting the AMOC at the onset of the Bølling-Allerød/Greenland Interstadial 1 (B-A; Rasmussen, S. et al., 2006; Thiagarajan et al., 2014), while others argue that the accumulation of heat in the deep North Atlantic may be the main mechanism for weakening the strong interglacial AMOC (Haskins et al., 2020; Levang & Schmitt, 2020). Modeling studies suggest that freshwater fluxes to the surface of the SPG alone are ineffective in weakening the AMOC for the length of time suggested by paleorecords (Fu et al., 2020; Mecking et al., 2016; Sévellec & Fedorov, 2016). Therefore, the cause and effect relationships connecting subsurface warming, freshwater fluxes and ocean circulation is not yet clear.

Since ocean circulation is of crucial importance for global heat distribution and the maintenance of stable climate patterns, the uncertainty regarding the mechanistic link between subsurface heat and fluctuations in AMOC strength is a major shortcoming of our current understanding of the climate system (IPCC, 2014). Subsurface warming has been detected in the abyssal Atlantic Ocean (Meinen et al., 2020) and interpreted as a consequence of the inferred long-term decline in AMOC strength due to anthropogenic warming (Caesar et al., 2021; Rahmstorf et al., 2015). Therefore, understanding the relationship between high-latitude subsurface warming and oceanic circulation during the deglaciation may provide significant insight regarding how the climate system is projected to respond to climate change.

The aim of this study is, therefore, to advance our understanding of the interaction between upper ocean heat transport and AMOC strength by using a proxy-based assessment of subsurface heat accumulation within the deep thermocline layer of the North Atlantic during the last 30 ka. This period experienced the full range of past AMOC variability as a result of two massive freshwater release events (Heinrich Events 1 and 2), the subsequent deglaciation and the Early Holocene. With this aim, paleotemperature and paleosalinity records from the deep thermocline of Site U1313 were interpreted along bottom and surface water indicators from the same site (Chalk et al., 2019, Lang et al., 2016, Naafs et al., 2013, Smith et al., 2013). The compilation of paleorecords at Site U1313 shows significant accumulation of heat and salt at the deep thermocline between the STG and SPG during HE1, synchronous with the deepening of northern-sourced waters and the return to a modern-like interglacial AMOC state. The available data implies that the variability of northward transport of subtropical waters is intrinsically connected with ice-sheet destabilization during Termination I and a phase of sluggish deep-ocean circulation in the northern and western North Atlantic.

6.2 Hydrography of the dwelling depth of *G. truncatulinoides* (d) at Site U1313

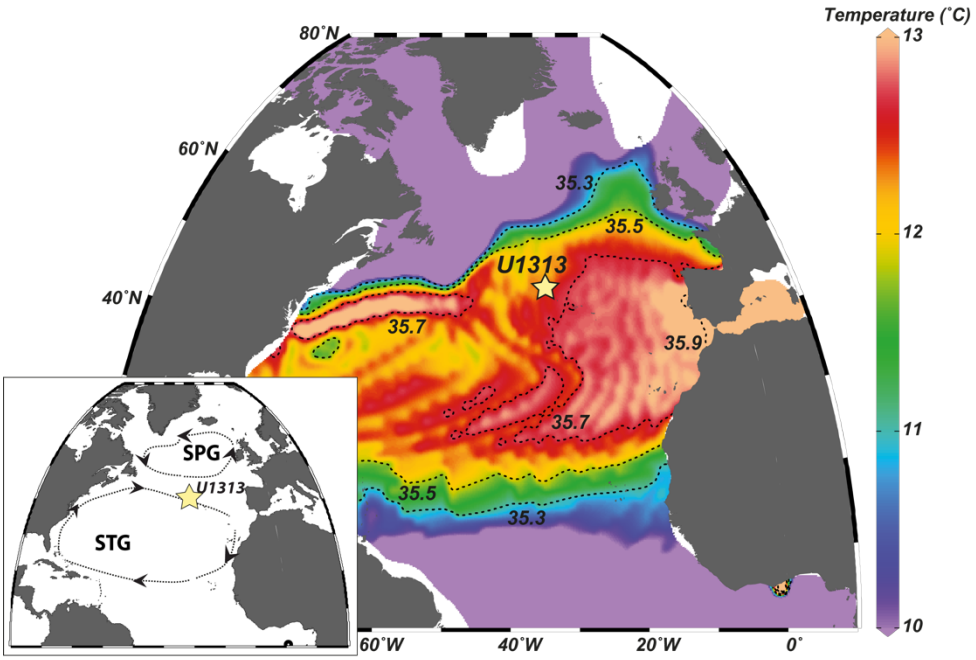

Figure 6.1. (main) Subsurface hydrography at σ_0 = 27.0, located at 450 m water depth at Site U1313. Color shading shows temperatures in °C (Locarnini et al., 2019) and dotted contours indicate isohalines (Zweng et al., 2019). (inset) Location of Site U1313 at the surface in relationship with the subtropical and subpolar gyres (STG and SPG, respectively).

At mid-latitudes *G. truncatulinoides* dextral has been found to calcify at an average water depth of 450 m (Chapter 4.1.1; Cleroux et al., 2013). Nowadays, this depth is within the σ_0=27 density layer (Figure 6.1), very close to the isopycnal with

maximum volume transport between the STG and SPG (Chapter 5; Burkholder & Lozier, 2011), suggesting that this species is able to record changes in northward heat transport across glacial-interglacial transitions and during millennial events in the inter-gyre region. At 450 m water depth above Site U1313, the water column is characterized by the 12ºC Eastern North Atlantic Central Waters (García-Ibáñez et al., 2018), thus between subtropical and subpolar mode waters entrained by MOW (Harvey, 1982).

6.3 Additional materials and methods

6.3.1 Combining records from different holes of Site U1313

The stratigraphies of Holes A, B, C, and D from Site U1313 were initially correlated by their lightness parameter (Naafs et al., 2012). The age model for the upper sections of the primary splice (i.e., Hole B) of Site U1313 was published by Naafs et al. (2013; Chapter 4.3.3). This was based on fine-tuning of Site U1313 XRD-based dolomite/calcite and quartz/calcite ratios to XRF-based Ca/Sr and Si/Sr ratios from Site U1308 (Hodell et al., 2008). This refined age model was later transferred to the upper sections of the secondary splice (in this case, Holes C and D) by matching the dolomite/calcite ratios of the primary splice (Naafs et al., 2013) to the abundancies of detritic carbonate ice-rafted debris (IRD) of the secondary splice (Figure 6.2). As a result, regardless of the uncertainty of this age model in relation to records from other sites, composite depths (in adjusted meters composite depth, amcd) and age models of all records from Site U1313 (this study; Chalk et al., 2019; Jakob, not published; Lang et al., 2016; Naafs et al., 2013; Smith et al., 2013) are comparable without chronostratigraphic uncertainties. This is important because it allows for the interpretation of all records from Site U1313 independently of age model uncertainties (e.g., reservoir corrections). To contextualize the discussion and calculate relative salinity variations (which require ice-volume corrections with independently produced sea-level curves), all records were plotted using the age model of the primary splice (Naafs et al., 2013).

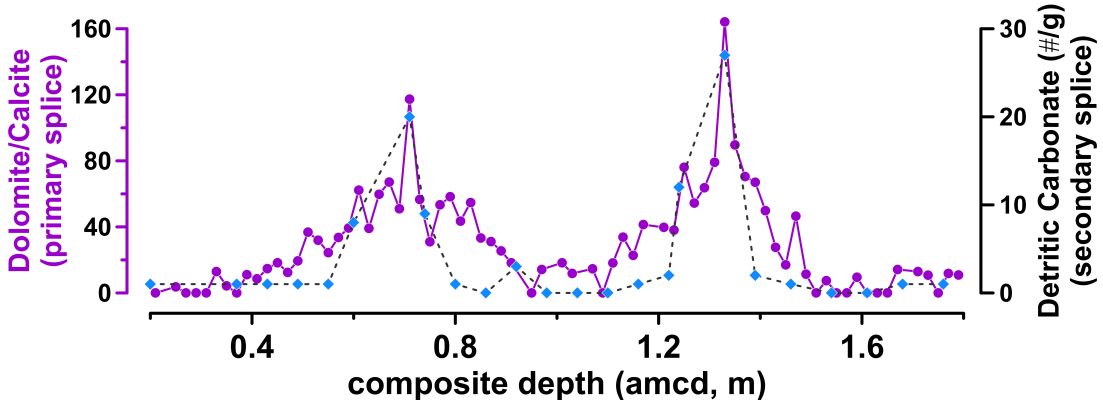

Figure 6.2. Dolomite/calcite ratios of the primary splice (Hole B, purple circles, Naafs et al., 2013) and proportion of detritic carbonate grains of the secondary splice (Holes C and D, blue diamonds, Lang et al., 2016) of Site U1313.

6.3.2 Deep-thermocline temperature uncertainty

The methodology used in Mg/Ca analyses and the paleotemperature equation choice rationale are detailed in chapters 4.3.4 and 4.3.5, respectively. Standard deviation from replicates of trace elements analysis in *G. truncatulinoides* (d) (n=10) was ± 0.13 mmol/mol for Mg/Ca, equivalent to ± 0.95°C using the chosen temperature equation (Cléroux et al., 2008). As this analytical uncertainty is smaller than the 1σ uncertainty of the chosen paleotemperature equation (± 1.4°C), the latter was considered when comparing the relative magnitude of other sources of uncertainties in subsurface estimates (Chapter 6.5.1).

6.4 Results

6.4.1 Compilation of records from Site U1313

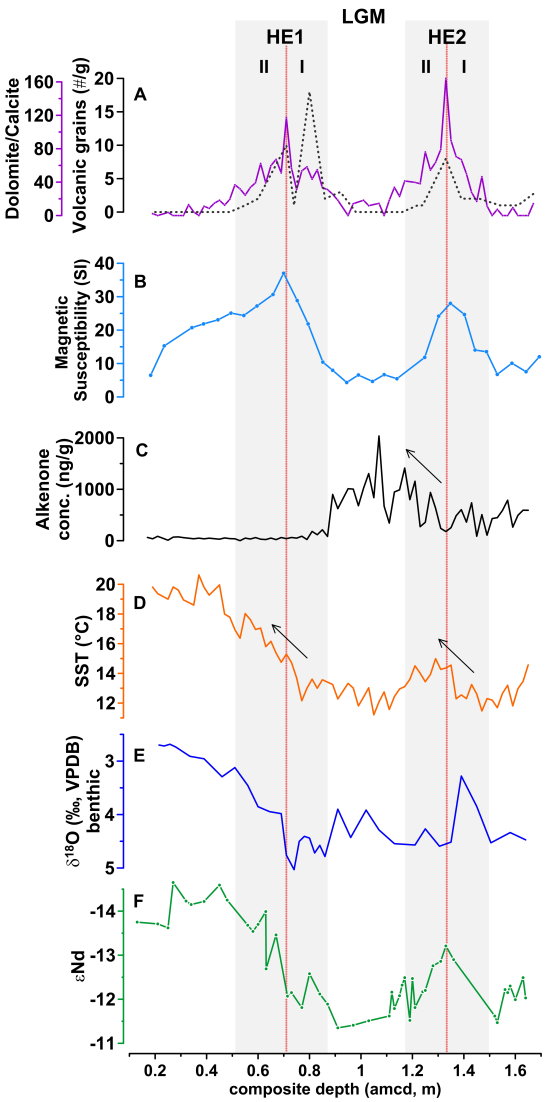

Figure 6.3. Compilation of proxy records from Site U1313. Bold lines show records from the primary splice (Hole B) and the dashed line shows record from the secondary splice (Holes C and D). Tuning between holes was based on lightness parameter (Naafs et al., 2012), refined tuning between dolomite/calcite ratios of Hole B and counts of detritic carbonate grains of the secondary splice (Lang et al., 2016). (A) Dolomite/calcite ratios (purple, Naafs et al., 2013) and proportion of volcanic grains (grey dashed line, Lang et al., 2016). (B) Magnetic susceptibility (light blue, Naafs et al., 2011). (C) Concentration of alkenones in sediments, an indicator of upper ocean biological productivity (black, Naafs et al., 2013). (D) Alkenone-based sea-surface temperatures (orange, Naafs et al., 2013). (E) Cibicidoides wuellerstorfi $\delta^{18}O$ (blue, Jakob, not published). (F) εNd (green, Lippold et al., 2016, Pöppelmeier et al., 2018). Vertical grey bars mark Heinrich Events 1 and 2. The stratigraphic location of peaks in dolomite/calcite ratios are marked by red dotted lines. Early and late sections of Heinrich Events are marked by roman numerals II and I, respectively.

To establish the relationship between upper-level heat transport and the AMOC, upper- and bottom-water circulation proxies at Site U1313 were integrated on their common depth scale (Naafs et al., 2013). The LGM and the deglaciation are arguably the best studied intervals in paleoceanographic research (e.g., Clark & Mix, 2002; Ivanovic et al., 2018; Ng et al., 2018; Oppo & Curry, 2008; Thiagarajan et al., 2014; Yu et al., 2020). Still, significant uncertainties in age models (Stern & Lisiecki, 2013) and diachronous changes in benthic $\delta^{18}O$ (Waelbroeck et al., 2011) preclude a consensus regarding the chronological order of circulation changes in the North Atlantic during the studied period. To address this issue, upper- and deep-water indicators of Site U1313 were compiled (Figure 6.3) according to their common depth-dependent stratigraphy (amcd; Naafs et al., 2012; 2013). At Site U1313, Heinrich Events 2 and 1 (HE2 and HE1) were identified by the typical high abundance of dolomite (i.e., dolomite/calcite ratios, Figure 6.3A, 1.49-1.11 amcd and 0.91-0.49 amcd, respectively; Naafs et al., 2013), which coincide with intervals of increased magnetic susceptibility (Figure 6.3B; Expedition 306 Scientists, 2006). Peak dolomite deposition was found at 1.33 and 0.71 amcd (Figure 6.3A, Naafs et al., 2013) and divide the early and late stages of HE2 (HE2.I and HE2.II) and HE1 (HE1.I and HE1.II), respectively. According to the age model of the primary splice (Hole B; Naafs et al., 2013), HE2-related dolomite deposition had its onset at 26.2 ka, peaked at 24.5 ka and ceased at 22.3 ka. The detritic carbonate deposition associated with HE1 started at 19.5 ka, peaked at 17.4 ka and ceased ca. 15 ka. These intervals are in agreement with the timing and duration of Heinrich Stadials 2 and 1, which are periods of cold atmospheric temperature in the northern North Atlantic with marked ice-sheet destabilization (Bond et al., 1992, Heinrich, 1988), but are here referred to as Heinrich Events because at Site U1313 these are recognized by the typical IRD deposition and characterized by relatively high SSTs (Naafs et al., 2013).

The LGM is the interval between HE1 and HE2, characterized by low SSTs (Figure 6.3D), low IRD deposition (Figure 6.3A), high upper-ocean biological productivity (6.3C; Naafs et al., 2013, Stein et al., 2009) and the highest εNd values (~11.5, Figure 6.3F; Pöppelmeier et al., 2018). Bottom-water εNd end member of northern-sourced waters (NSW) is dependent on the contribution of weathered sediments from the Canadian Shield and/or Greenland (Zhao et al., 2019). Thus, the relatively high εNd between 1.10 - 0.93 amcd during the LGM reflects the decreased input of unradiogenic neodymium to deep waters due to extensive ice-sheet cover of adjacent continental masses. It should be noted that the period characterized here as the LGM (i.e., the episode when global ice volume last reached its maximum and associated sea levels were at their lowest) is not synchronous with maximum benthic oxygen isotope ratios (Figure 6.3E; Jakob, not published). These are classically interpreted to indicate the interval of maximum global ice volume (Shackleton, 1967), but independently dated records show that benthic $\delta^{18}O$ exhibit distinct patterns and significant differences in timing over the last deglaciation depending on water depth and location in the Atlantic Ocean. This diachronicity limits the use of benthic $\delta^{18}O$ as

a stratigraphic marker on millennial time scales and particularly across glacial-interglacial transitions (Waelbroeck et al., 2011, Skinner & Shackleton, 2005). In the age model used here (Naafs et al., 2013), the interval marked as the LGM corresponds to the period between 22.3 and 19.5 ka, which is within the 23-19 ka period strictly defined as the LGM in ocean-based record compilations (e.g., MARGO, 2009) in agreement with most LGM definitions referenced by the general paleoclimate and paleoceanography community (Brady and Otto-Bliesner, 2011; Ezat et al., 2014; He et al., 2020; Marcott et al., 2011; Ng et al., 2018; Otto-Bliesner and Brady, 2010; Weldeab et al., 2016; Yu et al., 2020).

6.4.2 Variability of salinity and temperature at the deep thermocline above Site U1313 between 30 and 5 ka

Trace element and stable isotope records from *G. truncatulinoides* (d) allowed for the reconstruction of deep-thermocline conditions in the North Atlantic across HE2, the LGM, and deglaciation and are shown in Figure 6.4 according to the age model of the primary splice (Naafs et al., 2013). The time interval between 30–5 ka comprises phases of different AMOC states: strong and shallow during the LGM, strong and deep during the Early Holocene and the sluggish "off" AMOC state during HEs (as *per* Böhm et al., 2015) and is therefore well suited for assessing the state of the thermocline heat budget during various ocean-circulation scenarios. *G. truncatulinoides* (d) was present throughout the sampled time interval, allowing for the construction of continuous thermocline temperature and oxygen isotope records with an average temporal resolution of ~340 years.

The oxygen isotope record of *G. truncatulinoides* (d) ($\delta^{18}O_{trunc}$, Figure 6.4A) shows an overall glacial/interglacial amplitude of ~2.3‰. Between 28 ka and 20.5 ka, $\delta^{18}O_{trunc}$ gradually increases from ~1.7‰ to ~3.3‰. Between 19.5 ka and 17.8 ka (Late LGM to Early HE1, before the dolomite/calcite peak), $\delta^{18}O_{trunc}$ remains stable at around ~2.7‰. At 17.8 ka, $\delta^{18}O_{trunc}$ decreases abruptly to ~1.9‰, and plateaus after ~9.7 ka at ~1‰, equivalent to the modern value (Cléroux et al., 2013). Ice-volume corrected $\delta^{18}O_{sw}$ at Site U1313 ($\delta^{18}O_{sw\text{-}ivc}$, Figure 6.4B) has been used as a proxy for salinity. The youngest values in this record are 0.3 ‰ lower than the interpolated $\delta^{18}O_{sw}$ from the database of LeGrande & Schmidt (2006) for Site U1313 at 450 m water depth (0.57‰ SMOW). Nevertheless, the large uncertainty of T_{trunc} (0.95°C) in relation to the uncertainty of $\delta^{18}O$ (0.31‰) results in a large propagated 1σ uncertainty of $\delta^{18}O_{sw\text{-}ivc}$ (±1‰). Thus, $\delta^{18}O_{sw\text{-}ivc}$ should only be interpreted in terms of long-term, high-amplitude fluctuations and trends.

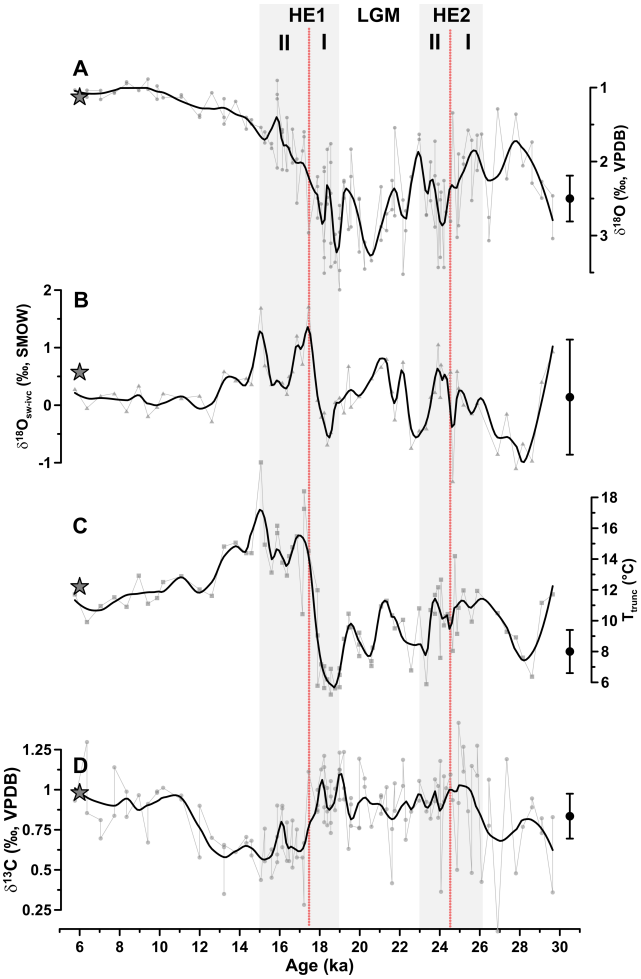

Figure 6.4. Results of stable isotopes and paleothermometry for the deep thermocline above Site U1313 during the time interval 30-5 ka. Stars show modern values for the respective datasets and the error bars to the left show one standard deviation (1σ). (A) G. truncatulinoides (d) $\delta^{18}O$. Reference of modern value: Cléroux et al. (2013). (B) Ice-volume corrected $\delta^{18}O_{sw}$. Reference of modern value: $\delta^{18}O_{sw}$ at 450 m water depth above Site U1313 according to the online database created by LeGrande and Schmidt (2006). Error bar corresponds to the propagated error of the Mg/Ca-based temperatures and $\delta^{18}O$. (C) Mg/Ca-based temperatures for G. truncatulinoides (d). Reference of modern value: temperature at 450 m water depth at Site U1313 from the WOA18, Locarnini et al. (2019). (D) G. truncatulinoides (d) $\delta^{13}C$. Reference of modern value: Cléroux et al., 2013. Original data points are marked as circles for stable isotopes (A and D), triangles for ice-volume corrected $\delta^{18}O_{sw}$ (B), and squares for Mg/Ca-based temperatures (C). Black lines represent LOESS smoothing of the original data points (smoothing factor = 0.1). Vertical grey bars mark Heinrich Events 1 and 2. The stratigraphic location of peaks in dolomite/calcite ratios are marked by red dotted lines. Early and late sections of Heinrich Events are marked by roman numerals II and I, respectively.

The subsurface temperature at Site U1313 (T_{trunc}) shows a remarkable amplitude of ~11°C (Figure 6.4C), ranging between ~6°C at 18.7 ka and ~17°C at 15.0 ka, at the transition between HE1 and the Bølling-Allerød, when deep ocean circulation became stronger (Barker et al., 2009, McManus et al., 2004). From 30 ka to 18.7 ka, T_{trunc} decreases from ~12.3°C to ~6°C and stabilizes at this value until 18 ka. During HE2 (26-23 ka), T_{trunc} was on average 10.4°C, just 1.8°C under the modern subsurface temperatures at 450 m water depth (12.2°C; Locarnini et al., 2019). Minimum thermocline temperatures occurred between 19 and 18 ka during the initial rise in dolomite deposition at Site U1313 (~6.2°C). Starting at 17.8 ka, T_{trunc} recorded an

abrupt ~9°C warming of the subtropical thermocline within only 700 years (~12.8°C/kyr or ~0.12°C/decade), which started ~400 years before the peak in dolomite deposition of HE1. At 16.3 ka the subtropical thermocline cooled by ~2°C and warmed again towards the maximum, ~17°C at 15.0 ka, forming a two-peak shape that is often described for HE1 in continental and oceanic records of the Atlantic realm (e.g., Bond et al., 1992; Bond & Lotti, 1995; Hodell et al., 2017; Strikis et al., 2015). The magnitude of temperature increase at 17.8 ka is unique for this record and implies that a substantial reconfiguration of heat transport in the central North Atlantic, at the subsurface level, took place during HE1. After 15 ka, the thermocline gradually cooled towards modern temperatures.

The carbon isotope record of *G. truncatulinoides* dextral (Figure 6.4D, $\delta^{13}C_{trunc}$) shows an overall amplitude of ~0.7‰. Between 25.5 ka and 17.4 ka and after 11.0 ka $\delta^{13}C_{trunc}$ is relatively stable at 1‰. At 17.4 ka, $\delta^{13}C_{trunc}$ decreased to ~0.55‰ and remained low from mid-HE1 until 12.6 ka, when it gradually rose to 1‰. During the Early Holocene, $\delta^{13}C_{trunc}$ remained relatively stable at 1.0‰, equivalent to modern $\delta^{13}C_{trunc}$ values (Cléroux et al., 2013).

6.5 Discussion

6.5.1 Potential biases in Mg/Ca-based paleotemperature estimates

The incorporation of Mg into tests of foraminifera is commonly used to estimate sea-water temperature in paleoceanographic studies (e.g., Barker et al., 2005; Lear et al., 2002; Schmitt et al., 2019), but its reliability may be affected by seawater [CO_3^{2-}], pH, or salinity during the incorporation of Mg^{2+} into foraminiferal tests (Chapter 4.3.4; Gray et al., 2018; 2019). Post-deposition, Mg/Ca ratios in foraminiferal calcite may also be biased by test exposure to corrosive bottom waters, which preferentially dissolves high-Mg calcite, thus lower temperature estimates (Regenberg et al., 2014).

In the modern upper-level North Atlantic, seawater [CO_3^{2-}] is positively correlated with temperature (Broecker and Peng, 1987), which hinders the independent assessment of the carbonate ion effect on Mg/Ca incorporation in non-cultured tests of foraminifera (Cléroux et al., 2013). Culture studies suggest that Mg/Ca incorporation in planktic foraminifera is negatively correlated to [CO_3^{2-}] and pH but is relatively insensitive to increases above ambient seawater values (Russell et al., 2004; Dueñas-Bohórquez et al., 2009). The pH-dependence of Mg/Ca incorporation in foraminiferal calcite is highly species specific (Gray et al., 2019) and has not been established for *G. truncatulinoides* (d), but its effect is usually assumed to be canceled out by the positive salinity effect on Mg/Ca (Lea et al., 2000). This is justified by the high correlation between salinity and alkalinity in the North Atlantic (r^2=0.83; Olsen et al., 2020) and the opposite effects of pH and salinity in Mg^{2+} incorporation of foraminiferal calcite. Additionally, studies suggest both pH and [CO_3^{2-}] were higher than modern in the upper and intermediate waters of the North Atlantic during the LGM (Russell et al., 2004; Yu et al., 2019). Hence, it is unlikely that paleotemperatures

computed from foraminiferal Mg/Ca during the period studied here were significantly influenced by variations in upper ocean [CO_3^{2-}] or pH.

In high salinity regions (>35 psu) of the world's oceans, such as subtropical gyres of both hemispheres, Mg/Ca-based paleotemperature estimates may be overestimated due to the salinity dependence of Mg/Ca ("excess salinity", Arbuszewski et al., 2010). Thus, relatively high salinities may partially account for the elevated T_{trunc} during HS1. As deviations of the local $\delta^{18}O_{sw}$-salinity during the studied interval are so far impossible to quantify, estimates of the possible salinity effect in T_{trunc} were calculated by applying the salinity-dependence of Mg/Ca estimated from culture studies (4±3% per psu; Gray, 2019), absolute salinity estimated from Equation 5 (Arbuszeski et al., 2010), and a wide range of $\delta^{18}O_{sw}$-salinity sensitivities of different areas in and around the North Atlantic (LeGrande and Schmidt, 2006). The absolute salinity equation by Arbuszeski et al. (2010) was developed specifically for the subtropical Atlantic (35.5 psu < salinity < 37.3 psu) by taking advantage of the opposite effect of salinity in $\delta^{18}O_c$ and Mg/Ca ratios and does not require the conversion of Mg/Ca to temperatures, which results in smaller 1σ uncertainties than using the conventional approach to calculate $\delta^{18}O_{sw}$ (relative salinity) by Bemis et al. (1998). No ice-volume correction was applied as the ~1 psu increase in global ocean salinity during the LGM (Adkins & Schrag, 2003) could also potentially affect Mg/Ca ratios.

(Equation 5) $\text{Salinity (psu)} = 34.28 + 1.97*\ln(\text{Mg/Ca}) + 0.59*\delta^{18}O_c$

The variability in absolute salinity agrees well with seawater $\delta^{18}O_{sw}$ estimates (Figure 6.3A) using the conventional method without global ice volume correction (Chapter 4.3.6). Holocene salinity estimates (35.6 psu) precisely match the modern values at 450 m water depth at Site U1313 (35.6 psu; Zweng et al., 2019). Considering these values as absolute salinities, T_{trunc} was corrected using +1% and +7% Mg/Ca.psu^{-1}, the lowest and highest sensitivities of Mg/Ca to salinity found in culture studies (Figure 6.3B, Grey et al., 2019). In the most conservative scenario (+7% Mg/Ca.psu^{-1}), only 1.1°C in T_{trunc} could be attributed to the 1.3 psu salinity increase between 18.5 ka and 17.4 ka. In all scenarios, the salinity peak at 17.4 ka precedes the associated peak in T_{trunc} by ~350 years (one sample step). The further increase in subsurface salinity at the end of HE1 (15 ka) is synchronous with the rise in T_{trunc}. High salinity at 15 ka may have accounted for an 1.3°C increase in T_{trunc}, but as in the first temperature peak, the salinity effect in subsurface temperatures was smaller than the reported 1σ uncertainty of the paleotemperature equation used (i.e., 1.4°C; Cléroux et al., 2008).

Alternatively, absolute salinity was computed by using a wide range of $\delta^{18}O_{sw}$:salinity relationships found in and around the modern North Atlantic (Figure 6.3C, Table 6.1; LeGrande and Schmidt, 2004; 2006). The $\delta^{18}O_{sw}$:salinity of the

modern NADW yielded the highest absolute salinity estimates and implied on a 3.7 psu increase at deep thermocline levels at the onset of HE1.II (pink curve in Figure 6.3). Deep-thermocline temperatures were then recalculated by assuming that these high salinity values were representative of the salinity variability at above Site U1313 and that Mg/Ca ratios were very sensitive to salinity during the study interval (+7 Mg/Ca.psu^{-1}; Grey et al., 2019). Even then, salinity would have accounted for no more than 1.6°C of the abrupt temperature rise in T_{trunc} between 18 ka and 17 ka (Figure 6.3D). Therefore, although it is possible that deep-thermocline temperatures may be slightly overestimated (by up to 1.3°C) during the coupled salinity and temperature rises of HE1.II, salinity cannot account for the temperature variability recorded in T_{trunc}.

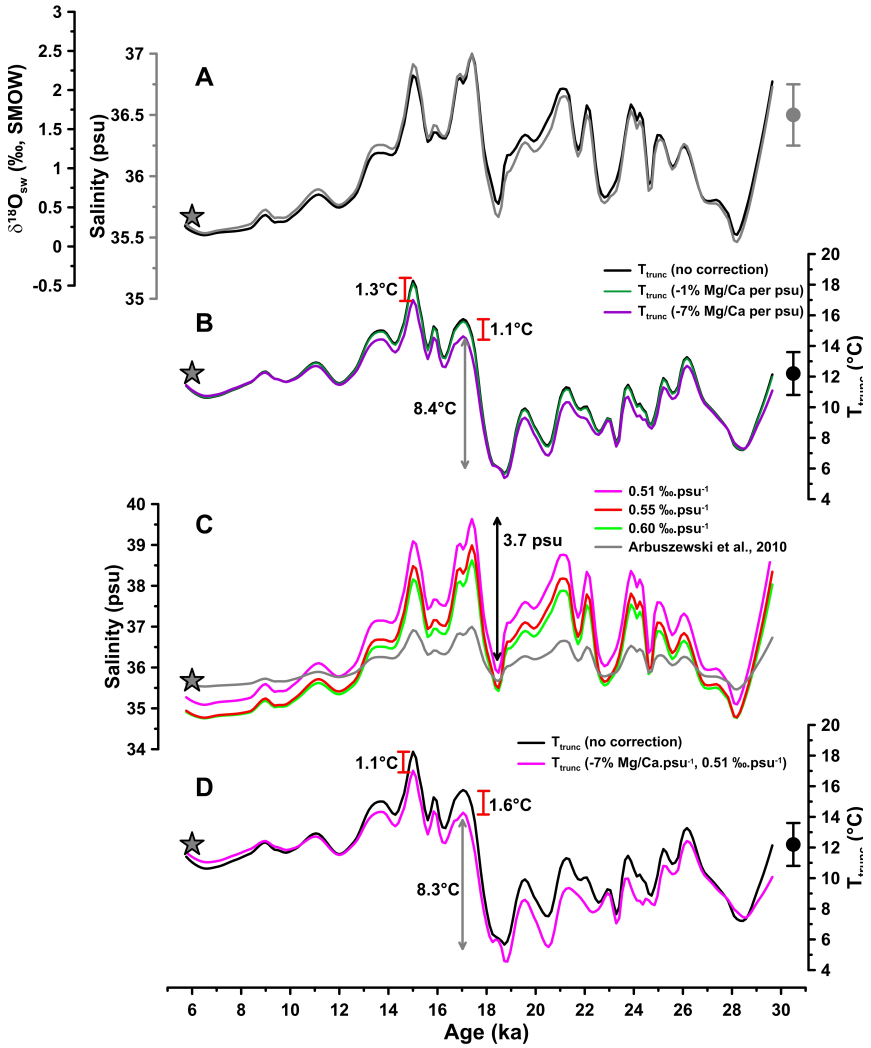

Figure 6.5. (A) Comparison between $\delta^{18}O_{sw}$ (black, calculated using Bemis et al., 1998) and absolute salinity (grey, calculated using Arbuszewski et al., 2010). (B) Salinity-corrected Mg/Ca temperatures for G. truncatulinoides (d). Green and purple lines show T_{trunc} corrected for the salinity dependance of Mg/Ca (1% and 7% Mg/Ca.psu^{-1}, respectively; Gray et al., 2019). (C) Absolute salinity estimated using modern North Atlantic $\delta^{18}O_{sw}$:salinity slopes (LeGrande and Schmidt, 2006). (D) Salinity-corrected Mg/Ca temperatures for G. truncatulinoides (d) using NADW's $\delta^{18}O_{sw}$:salinity (LeGrande & Schmidt, 2006) and 7% Mg/Ca.psu^{-1} (Gray et al., 2019). For comparison, the black line shows non-salinity corrected T_{trunc} in panels B and D. All panels exhibit LOESS smoothed data (smoothing factor = 0.1). Stars show modern values for salinity and temperature at 450 m water depth above Site U1313 (Zweng et al., 2019 and Locarnini et al., 2019, respectively). The error bars show the 1σ uncertainty of the temperature equation (±1.4 ℃, Cléroux et al., 2008).

Table 6.1. Modern $\delta^{18}O_{sw}$:salinity in and around the North Atlantic Ocean.

Salinity = (δ18Osw + Intercept)/Slope (LeGrande & Schmidt, 2004; 2006)				
	Greenland-Iceland-Norwegian Seas	upper North Atlantic Ocean (0 - 1000 m water depth)	North Atlantic (all depths)	North Atlantic Deep Water
Slope (‰/psu)	0.60	0.60	0.55	0.51
Intercept	20.71	20.84	18.98	17.75

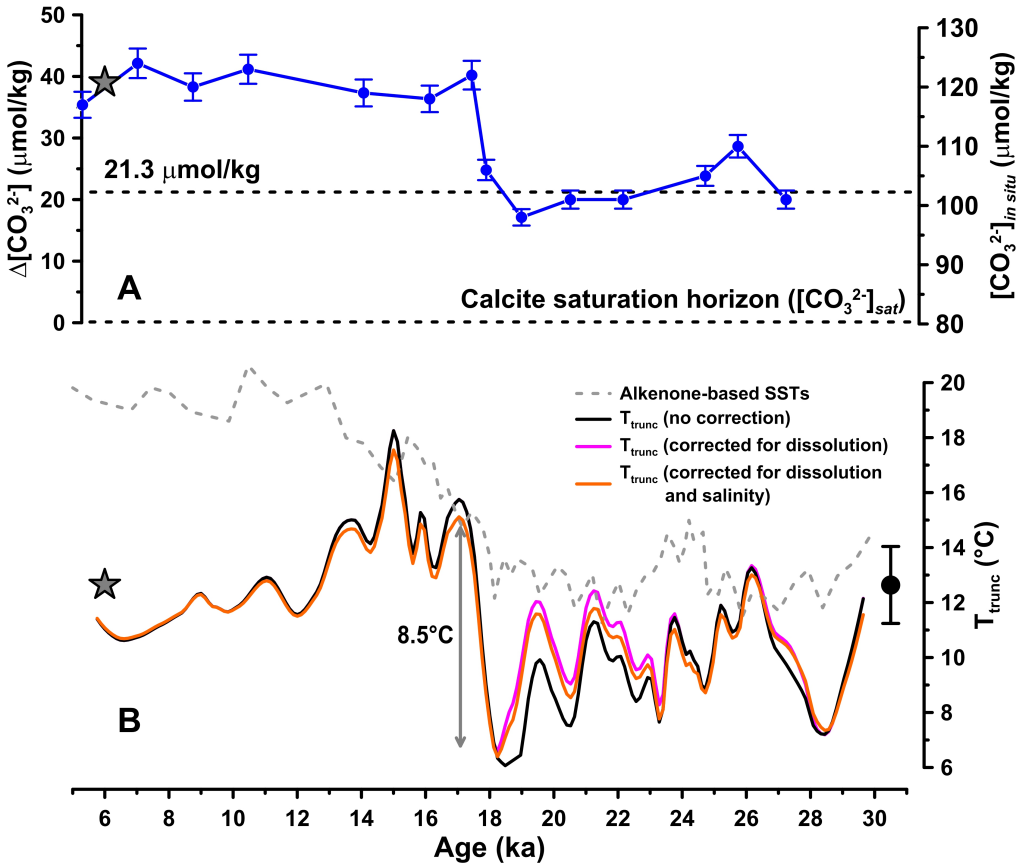

Figure 6.6. (A) Carbonate ion concentration of bottom waters ($[CO_3^{2-}]_{in\ situ}$, left axis, Chalk et al., 2019) and carbonate ion saturation ($\Delta[CO_3^{2-}] = [CO_3^{2-}]_{in\ situ} - [CO_3^{2-}]_{sat}$, Yu et al., 2008) at Site U1313. Dashed lines mark the calcite saturation horizon at 3426 m water depth ($[CO_3^{2-}]_{sat}$; Jansen et al., 2002, Yu et al., 2008) and the calcite saturation threshold ($\Delta[CO_3^{2-}] = 21.3$ μmol/kg; Regenberg et al., 2014), below which planktic foraminifera would be particularly susceptible to dissolution. (B) Alkenone-based sea surface temperatures (light gray dashed line, Naafs et al., 2013), non-corrected subsurface temperatures (T_{trunc}, black line), temperatures corrected for potential high-Mg calcite dissolution (pink line) and for dissolution and salinity (using +4% Mg/Ca.psu^{-1}, orange line). Corrected and non-corrected T_{trunc} in panel B were smoothed using LOESS (smoothing factor = 0.1). Stars show modern values for the respective datasets, subsurface temperature at 450 m water depth (Locarnini et al., 2019) and preindustrial carbonate ion concentration of bottom waters at Site U1313 (Chalk et al., 2019).

The exposure to corrosive bottom waters may also potentially bias Mg/Ca-based temperatures by preferentially dissolving high-Mg calcite in foraminiferal tests, which would result in lower paleotemperatures. This concern was addressed during the foraminifera selection process by specifically avoiding the inclusion of partially dissolved or not fully calcified *G. truncatulinoides* (d) specimens in the samples analyzed for Mg/Ca. Since in the supersaturated waters of the modern North Atlantic, the calcite saturation depth (CSD) is very deep (4600 m water depth, Jansen et al., 2002), at 3426 m water depth, the carbonate sediments of Site U1313 are safe from dissolution. Pre-industrial $[CO_3^{2-}]$ at Site U1313 was ~123 μmol/kg (Chalk et al., 2019), thus 41 μmol/kg higher than the calcite saturation concentration at the same depth ($[CO_3^{2-}]_{sat}$ = 82 μmol/kg; Jansen et al., 2002; Yu et al., 2008). During the LGM (22.3 and 19.6 ka in this age model), the CSD was between 800 m to 1000 m shallower and carbonate ion saturation below 2800 m water depth in the North Atlantic decreased by 20 μmol/kg (Figure 6.4D; Chalk et al., 2019; Yu et al., 2008). At Site U1313, minimum $[CO_3^{2-}]$ during the LGM was still well above the calcite saturation horizon (Figure 6.4A; Chalk et al., 2019) but below the critical threshold concentration for partial dissolution of planktic foraminifera (Regenberg et al., 2014). To assess the potential impact of low $[CO_3^{2-}]$ on subsurface temperatures during the interval between 23 and 18.5 ka, Mg/Ca ratios from *G. truncatulinoides* (d) were corrected using the global Mg/Ca:$\Delta[CO_3^{2-}]$ sensitivity of planktic foraminifera (Figure 6.4B; Regenberg et al., 2014). Carbonate ion saturation concentrations were reconstructed using the B/Ca ratios for the secondary splice of Site U1313 (Chalk et al., 2019) and the local $[CO_3^{2-}]_{sat}$ at 3426 m (Jansen et al., 2002). Subsurface temperatures corrected for dissolution do not differ considerably from non-corrected temperatures in terms of both absolute values and patterns (Figure 6.4B), which supports the interpretation that *G. truncatulinoides* (d) was not significantly affected by low $[CO_3^{2-}]$ at Site U1313 during the LGM. The maximum effect of the dissolution correction was to increase subsurface temperatures during the LGM, which would have been partially compensated by the higher upper ocean salinity during this interval (see T_{trunc} corrected for dissolution and salinity in Figure 6.4B). As the main focus of this research are intervals in which the bottom water $[CO_3^{2-}]$ was higher than the critical threshold (27-23 ka and after 18.5 ka, respectively HE2 and the later portion Heinrich Event 1, HE1.II), it is safe to assume that corrosion did not significantly affect subsurface temperatures and that T_{trunc} is a robust indicator of subsurface temperature variability throughout the discussed intervals.

6.5.2 The North Atlantic water column above Site U1313 between 30 and 5 ka

The compilation of proxy records from Site U1313 (Figure 6.7) provides novel insights into the temporal order and relationship between ocean circulation changes and climatic shifts during the last 30 ka. As all records produced in this thesis derive from samples of the same splice used by Naafs et al. (2013), there is no chronostratigraphic uncertainty between sea-surface and subsurface temperatures,

subsurface salinity and detritic carbonate records, which allowed for the determination of leads and lags between different processes. Maximum deposition of detritic carbonate (i.e., dolomite/calcite, Figure 6.7A) during HE2 and HE1 were preceded by increased subsurface temperatures, accompanied by higher SSTs and followed by a peak in relative subsurface salinity. However, apart from these similarities, both events are markedly different and are preceded by opposite patterns in the upper and deep oceanic circulation branches.

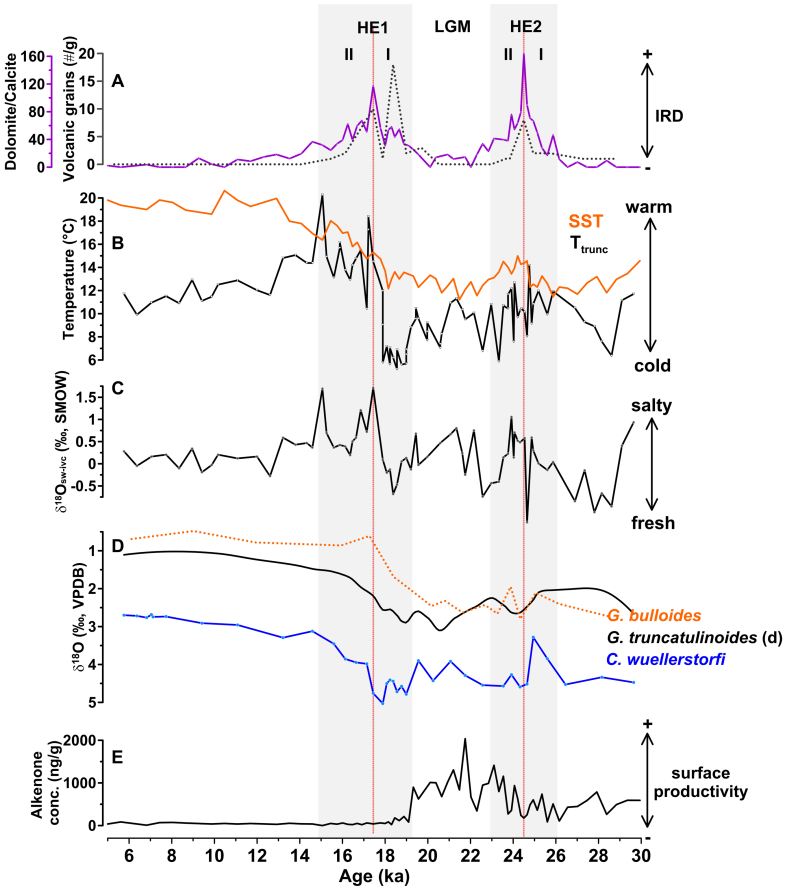

Figure 6.7. Compilation of proxy records from Site U1313. Bold lines show records from the primary splice (Hole B) and dashed lines show records from the secondary splice (Holes C and D) and Hole A. Tuning between holes was based on lightness parameter (Naafs et al., 2012) and tuning between dolomite/calcite ratios of Hole B and counts of detritic carbonate grains of the secondary splice (Lang et al., 2016). (A) Dolomite/calcite ratios (purple, Naafs et al., 2013) and number of volcanic grains per gram of sediment (grey dashed line, Lang et al., 2016). (B) Alkenone-based sea-surface temperatures (orange, Naafs et al., 2013) and Mg/Ca-based subsurface temperatures (T_{trunc}, black, this study). (C) Ice-volume corrected $\delta^{18}O_{sw\text{-}ivc}$ (black, this study). (D) G. bulloides $\delta^{18}O$ (orange dashed line, Schmidt et al., 2013), G. truncatulinoides (d) $\delta^{18}O$ (black, this study, smoothed by a factor of 0.1 using LOESS) and C. wuellerstorfi $\delta^{18}O$ (blue, Jakob, not published). (E) Concentration of alkenones in sediments (black, Naafs et al., 2013). Vertical grey bars mark Heinrich Events 1 and 2. The stratigraphic location of peaks in dolomite/calcite ratios are marked by red dotted lines. Early and late sections of Heinrich Events are marked by roman numerals II and I, respectively.

Heinrich Event 2 took place during full glacial conditions, when density stratification in the upper ocean was minimal (i.e., minimal difference between surface and subsurface planktic foraminiferal $\delta^{18}O$, Figure 6.7D). Deep-thermocline temperatures peaked in the early HE2 (HE2.I) at 11.2°C, just 1°C lower than SSTs

(Figure 6.7B; Naafs et al., 2013). Circum-Atlantic ice sheets were close to their maximum size during HE2 (Toucanne et al., 2015) and high T_{trunc} considerably preceded (by ~ 1.4 kyrs) the peak deposition of IRDs during HE2 at Site U1313, which suggests that increased northward heat transport via the deep thermocline during this interval may have contributed to the destabilization of the European and Laurentide ice sheets upstream. Deep-thermocline temperatures during the late HE2 (HE2.II) began a gradual descent towards minimum values of the early HE1 (HE1.I). After HE2, biological productivity at the surface increased (Figure 6.7E) towards the maximum during the LGM. Cold and highly productive surface waters during the LGM indicate that the surface above Site U1313 was within the domain of the SPG (Chapman and Shackleton, 1998; Chapman and Maslin, 1999). The southward position of the subpolar front during the last glacial stage is corroborated by the high percentages of the foraminifera *Neogloboquadrina pachyderma* across the subpolar North Atlantic during the LGM (Sarnthein et al., 1995, 2003; Pflaumann et al., 2003; Kucera et al., 2005; Eynaud et al., 2009). Paleoceanographic reconstructions indicate that surface ocean circulation during the glacial maximum was more zonal, with the virtual absence of the latitudinal extension of the North Atlantic Current (Chapman and Maslin, 1999). As a consequence, a stark temperature gradient separated the subtropical and subpolar domains of the North Atlantic (DeVernal, 2006, MARGO, 2009) with SSTs north of 45°N being between 8°C and 12°C colder than modern (MARGO, 2009).

At the onset of HE1.II, productivity decreased abruptly (Figure 6.7E), which has been interpreted as a consequence of the abrupt freshening of surface waters above Site U1313 during events of iceberg release and ice-sheet destabilization in the North Atlantic (Stein et al., 2009). This scenario is supported by the increase in upper ocean stratification (i.e., higher difference between surface and subsurface planktic foraminiferal $\delta^{18}O$, Figure 6.7D) and abundant deposition of volcanic grains at the study site (Figure 6.7A; Lang et al., 2016). These were likely sourced from Icelandic or eastern Greenland terrains and indicate the destabilization of ice sheets in northeastern North Atlantic during a precursor event to HE1 (Grousset et al., 1993; Hemming et al., 2004). Similarly to HE2.I, the rise in deep-thermocline temperatures during HE1.I preceded the maximum deposition of dolomite at Site U1313 by ~ 400 yrs and T_{trunc} converged to values similar for the surface (Figure 6.7B). However, in contrast to HE2.II, deep-thermocline temperatures increased abruptly following the rise in subsurface salinity and remained almost as high as SSTs for over 2 kyrs (between 17.4 and 15 ka). Subsurface temperatures only decreased after 15 ka, at the transition between Heinrich Stadial 1 and the Bølling-Allerød/Greenland Interstadial 1 (B-A; Rasmussen, S. et al., 2006). The B-A is characterized by the abrupt 12°C rise of atmospheric temperatures over Greenland (Kindler et al., 2014) and is generally interpreted to mark the disappearance of sea-ice and the onset of deep convection in the Nordic Sea (Rasmussen, T. & Thomsen, 2004, Rasmussen, T. et al., 1993). The continuous increase in SST (Figure 6.7B; Naafs et al., 2013), the high density gradient

between surface and deep thermocline (Figure 6.7D) and the permanently lowered sea surface productivity (Figure 6.7E; Naafs et al., 2013) during HE1.II and towards the Holocene indicates the transition of upper ocean circulation from glacial to modern conditions.

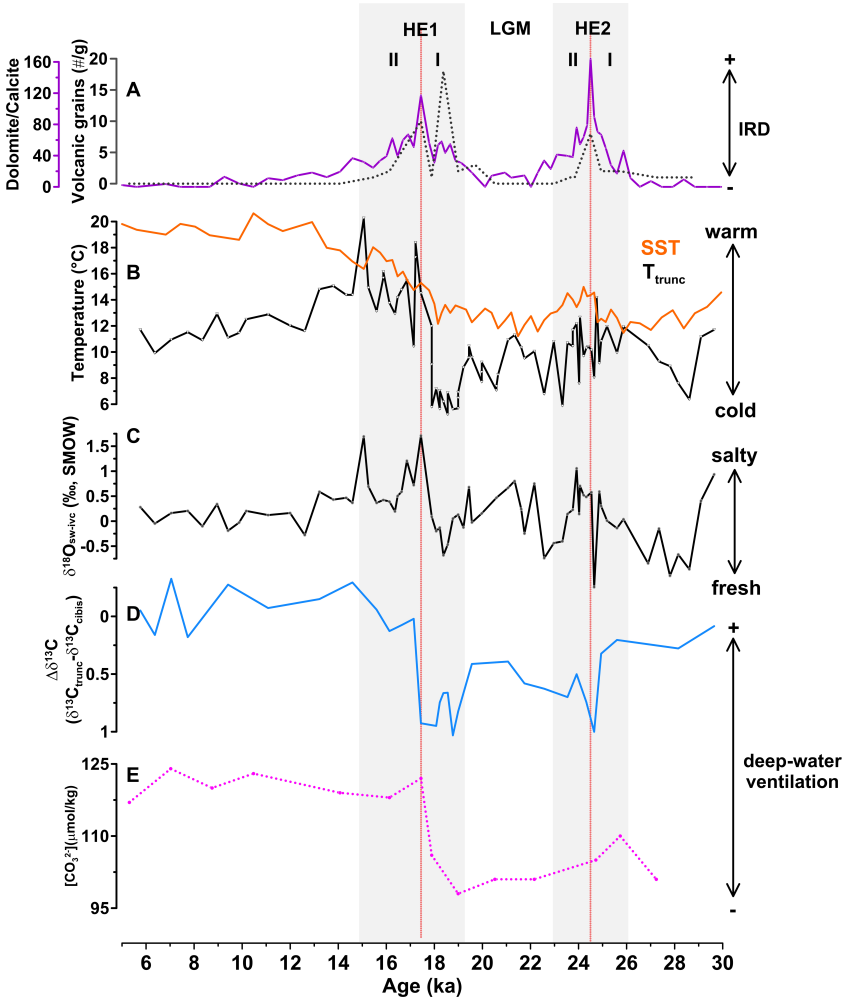

Figure 6.8. Compilation of proxy records from Site U1313. Bold lines show records from the primary splice (Hole B) and dashed lines show records from the secondary splice (Holes C and D) and Hole A. Tuning between holes was based on lightness parameter (Naafs et al., 2012) and tuning between dolomite/calcite ratios of Hole B and counts of detritic carbonate grains of the secondary splice (Lang et al., 2016). (A) Dolomite/calcite ratios (purple, Naafs et al., 2013) and number of volcanic grains per gram of sediment (grey dashed line, Lang et al., 2016). (B) Alkenone-based sea-surface temperatures (orange, Naafs et al., 2013) and Mg/Ca-based subsurface temperatures (T_{trunc}, black, this study). (C) Ice-volume corrected $\delta^{18}O_{sw\text{-}ivc}$ (black, this study). (D) Vertical carbon gradient at Site U1313 ($\Delta\delta^{13}C$, $\delta^{13}C_{trunc}$ - $\delta^{13}C_{cibis}$, light blue, this study and Jakob, not published). (E) Carbonate ion concentration (pink dashed line, Chalk et al., 2019). Vertical grey bars mark Heinrich Events 1 and 2. The stratigraphic location of peaks in dolomite/calcite ratios are marked by red dotted lines. Early and late sections of Heinrich Events are marked by roman numerals II and I, respectively.

The inherently different background conditions of HE2 and HE1 are also reflected in the concurrent changes in deep water ventilation during these events. After HE2 and throughout the LGM, chemical stratification in the North Atlantic increased (indicated by a high vertical carbon gradient, Figure 6.8D) and bottom water carbonate ion saturation further decreased (Figure 6.8E, Chalk et al., 2019). During the glacial

stages of the Late Pleistocene, the water column of the North Atlantic was characterized by a strong chemocline, which separated the well-ventilated upper NSW (i.e., GNAIW) with high $\delta^{13}C$ and $[CO_3^{2-}]$ above ~2800 m water depth from the poorly ventilated bottom waters (lower NSW, with low $\delta^{13}C$ and $[CO_3^{2-}]$; Pöppelmeier et al., 2018, Yu et al., 2008). In contrast, the maximum detritic-carbonate IRD deposition of HE1 coincides with the abrupt increase in deep ocean $[CO_3^{2-}]$ (Chalk et al., 2019) and the decrease in the vertical carbon gradient ($\Delta\delta^{13}C = \delta^{13}C_{trunc}$-$\delta^{13}C_{cibis}$; this study and Jakob, not published). At Site U1313, $[CO_3^{2-}]$ and $\Delta\delta^{13}C$ similar to the modern North Atlantic mark the the disappearance of the glacial chemocline during HE1, showing that the warming and salinification of the deep thermocline also preceded the deepening of the North Atlantic overturning cell. Thus, the data suggest HE1.II marks the transition between the shoaled glacial AMOC state and the modern Atlantic Ocean circulation at the onset of the last deglaciation (Hodell et al., 2016). Therefore, even though HE1 and HE2 are usually referred to as similar, their structure and background conditions are intrinsically different and it may be more accurate to classify HE1 as the onset of Termination I, rather than a stadial period of the last glacial stage.

To address the relationship between northward heat transport and how that may have affected deep-water ventilation, the following Chapter 6.5.3 reviews evidence for subsurface warming during the last 30 ka and Chapter 6.5.4 discusses the link between subsurface warming and the AMOC.

6.5.3 Subsurface warming in the North Atlantic at the onset of the last Termination

Subsurface warming in the deep thermocline and intermediate water levels during the deglaciation has been reported by many proxy-based reconstructions in the North Atlantic Ocean and Nordic Seas (Ezat et al., 2014; Marcott et al., 2011; Poggemann et al., 2018; Thiagarajan et al., 2014; Schmidt et al., 2012; Weldeab et al., 2016), but with different amplitudes and patterns than at observed Site U1313 (Figure 6.9). Records from intermediate water levels (Figures 6.9A, 6.9B and 6.9G; Ezat et al., 2014, Marcott et al., 2011, Poggermann et al., 2018) show an abrupt temperature increase during HE1 (between 2°C and 4°C) and cooling during the B-A, while shallower thermocline records from lower latitudes show either gradual temperature increases after HE1 (Figure 6.9D and 6.9F; Bahr et al., not published, Schmidt et al., 2012) or stable conditions throughout the deglaciation (Figure 6.9E, Reißig et al., 2019). The timing and pattern of the compiled subsurface temperature records suggest that the subsurface warming of HE1 originated in the North Atlantic and that the warming at the intermediate levels and the deep thermocline of the mid-latitudes preceded the gradual warming at shallower depths.

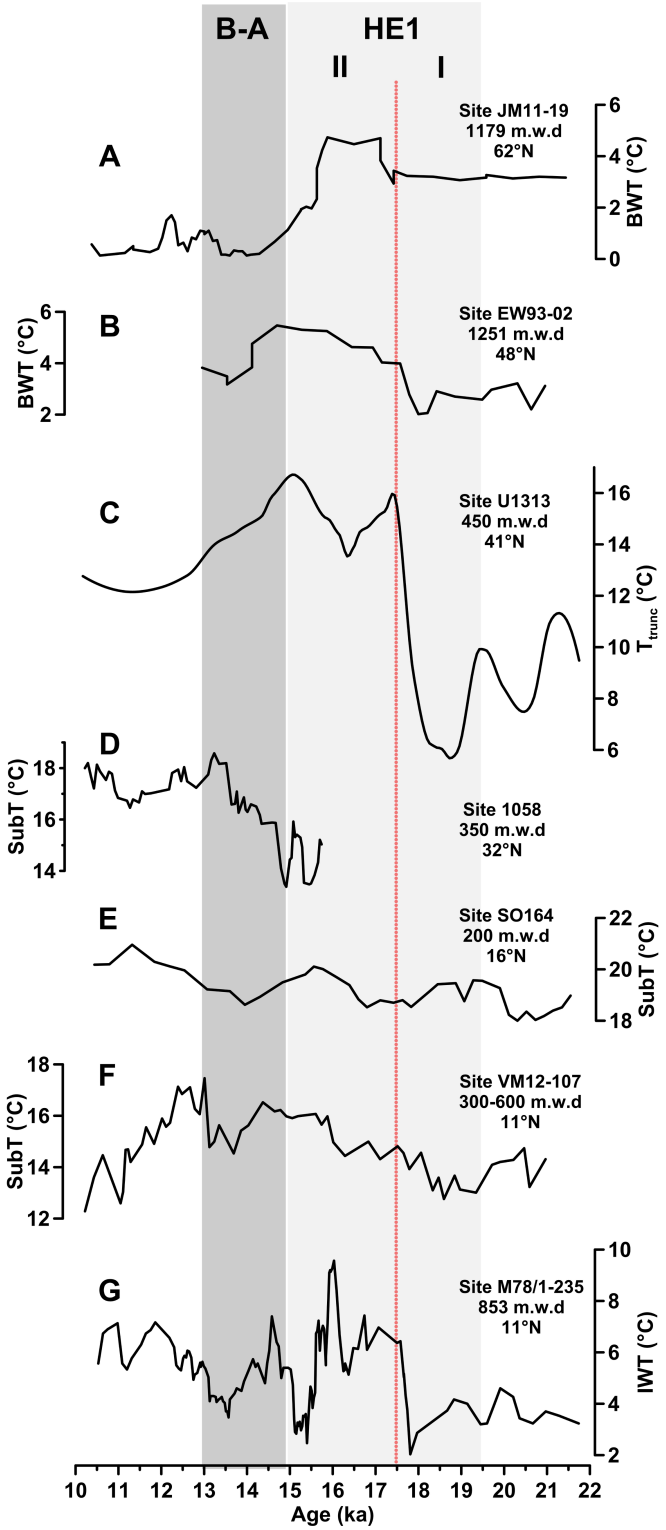

Figure 6.9. Subsurface temperature records in the North Atlantic and the Nordic Seas. (A) Bottom water temperature, BWT, in the Nordic Seas (Ezat et al., 2014, 3pt running average), and (B) in the subpolar North Atlantic (Marcott et al., 2011, 3pt running average). (C) Subsurface temperature from G. truncatulinoides (d) at Site U1313 (this study, smoothed using LOESS by a factor of 0.2). (D) Subsurface temperatures in the Subtropical Gyre (Bahr, not published, 5pt running average). (E) Subsurface temperatures in Central Caribbean (Reißig et al., 2019, 3pt running average). (F) Subsurface and (F) bottom water temperatures in the tropical North Atlantic (Schmidt et al., 2012, Poggemann et al 2018).

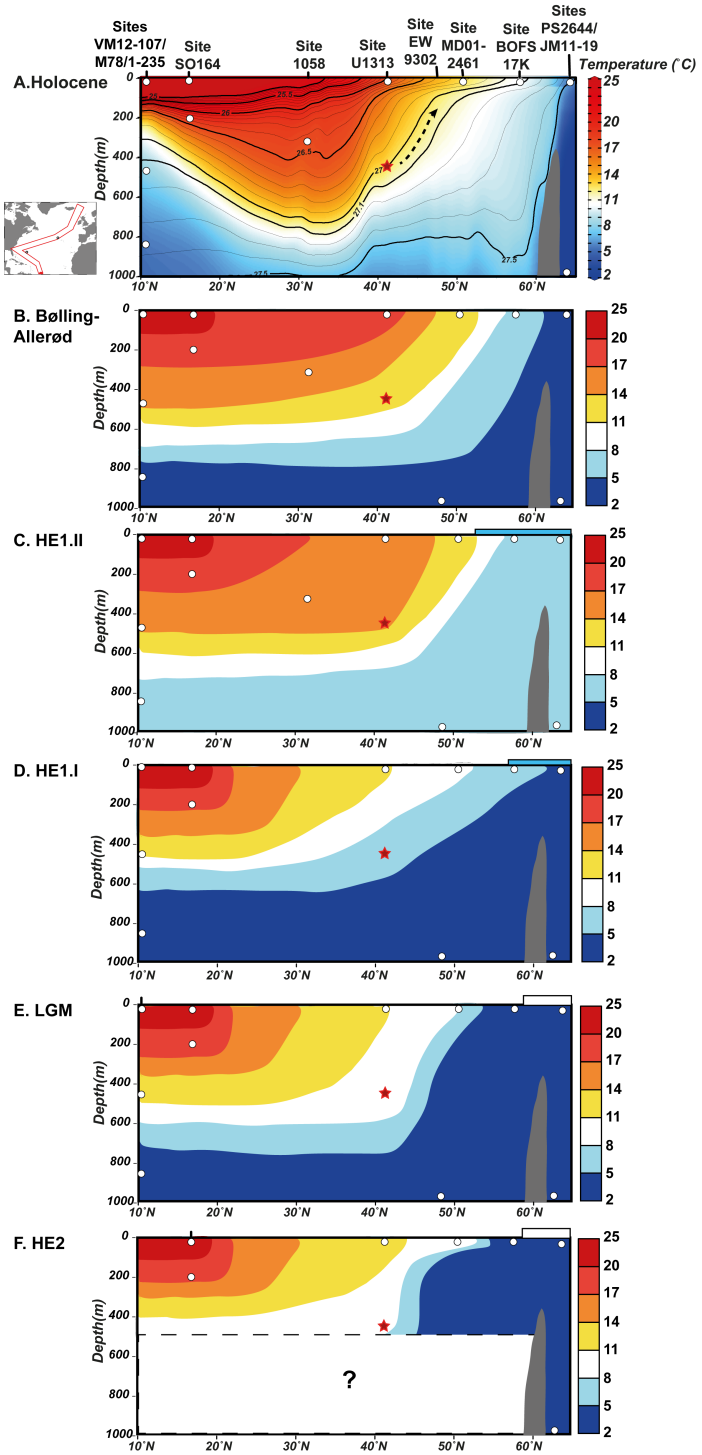

Figure 6.10. (A) Modern temperature and density distribution in the upper North Atlantic. Figure produced using data from the World Ocean Atlas 2018 (Locarnini et al., 2019, Zweng et al., 2019) and the software Ocean Data View (Schlitzer, 2020). Reconstructed temperature distribution in the upper North Atlantic during (B) the Bølling-Allerød (15-12 ka), (C) late and (D) early Heinrich Event (17.5-15 ka and 19-17.5 ka, respectively), (E) Last Glacial Maximum (23-19 ka, MARGO, 2009) and (F) Heinrich Event 2 (26-23 ka). Red star marks temperature as recorded at the deep-thermocline of Site U1313 (this study) and white dots from the records (ordered from low to high latitudes) of sites VM12-107 (surface and subsurface, between 300 and 450 m water depth, Schmidt et al., 2012), M78/1-235 (852 m water depth, Poggemann et al., 2018), SO164-03-4 (surface and subsurface, ca. 200 m water depth, Reißig et al., 2019), 1058 (subsurface, ca. 350 m water depth, Bahr, not published), U1313 (surface, Naafs et al., 2013), EW9302-2JPC (1251 m water depth), MD01-2461 (surface, Peck et al., 2006), JM11-FI-19PC (1179 m water depth, Ezat et al., 2014). Presence of meltwater at the surface was inferred from records of sites BOFS17K (Barker et al., 2004) and PS2644-5 (Voelker et al., 1998).

All the available subsurface records were then used to reconstruct the temperature evolution of the upper 1000 m in the North Atlantic and Nordic Seas across the discussed time intervals (Figures 6.10 and 6.11; starting from the tropical North Atlantic northwards: Site VM12-107, Schmidt et al., 2012; Site M78/1-235, Poggemann et al., 2018; Site SO164-03-4, Reißig et al., 2019; Site 1058, Bahr, not published; Site U1313, Naafs et al., 2013, this study; Site EW9302-2JPC, Marcott et al., 2011; Site MD01-2461, Peck et al., 2006; Site JM11-FI-19PC, Ezat et al., 2014). The presence of meltwater (or warming) at the surface northwards of 50°N was assessed by $\delta^{18}O$ of shallow dwelling foraminifera (Sites BOFS17K, Barker et al., 2004, PS2644-05, Voelker et al., 1998).

The reconstructed scenarios show that heat distribution in the upper 500 m of the North Atlantic during HE2 (26-23 ka, Figure 6.10F) was similar to that of the LGM (23-19.5, Figure 6.10E). The marked latitudinal temperature gradient within the upper North Atlantic water column during the LGM is in agreement with other glacial reconstructions, which show a southward-shifted Subpolar Front and SPG until 18 ka relative to the Holocene (Chapman and Maslin, 1999, MARGO, 2009, Pflaumann et al., 2003, Sarnthein et al., 2003).

At the onset of HE1.I, between 19 and 18 ka, a brief but well-marked SST peak was recorded at Site MD01-2461 (Figure 6.11A), in the northeastern North Atlantic. A similar event is also recorded as low surface $\delta^{18}O$ at Site BOFS17K (Figure 6.11C, Barker et al., 2004). The early HE1 (HE1.I) is marked by high deposition of volcanic grains at Site U1313 (Figure 6.11D) and similar $\delta^{18}O$ values from *G. truncatulinoides* (d) and *G. bulloides* at Sites BOFS17K (Figure 6.11C) and MD01-2461, which suggest the onset of the isopycnal connection between the deep-thermocline at the mid-latitudes and northeastern North Atlantic. In the modern North Atlantic, this density connection is modulated by the MOW, which connects the lower STG and the surface of the SPG (Chapter 5). During the last glacial stage, the MOW settled deeper into the water column of the North Atlantic (Rogerson et al., 2005) and its northwards latitudinal extension was limited (Schönfeld and Zahn, 2000). The gradual upward shift of MOW's northward branch was detected as erosional features in marine sediment cores at the Porcupine Seabight and was interpreted to reach its modern depth after 18 ka. Thus, it's feasible that the renewed intergyre connection at the subsurface aided the destabilization of ice sheets in the eastern North Atlantic during the HE1.I (Figure 6.10D), indicated by the peak in volcanic grains at Site U1313 (Grousset et al., 2000, Lang et al. 2016).

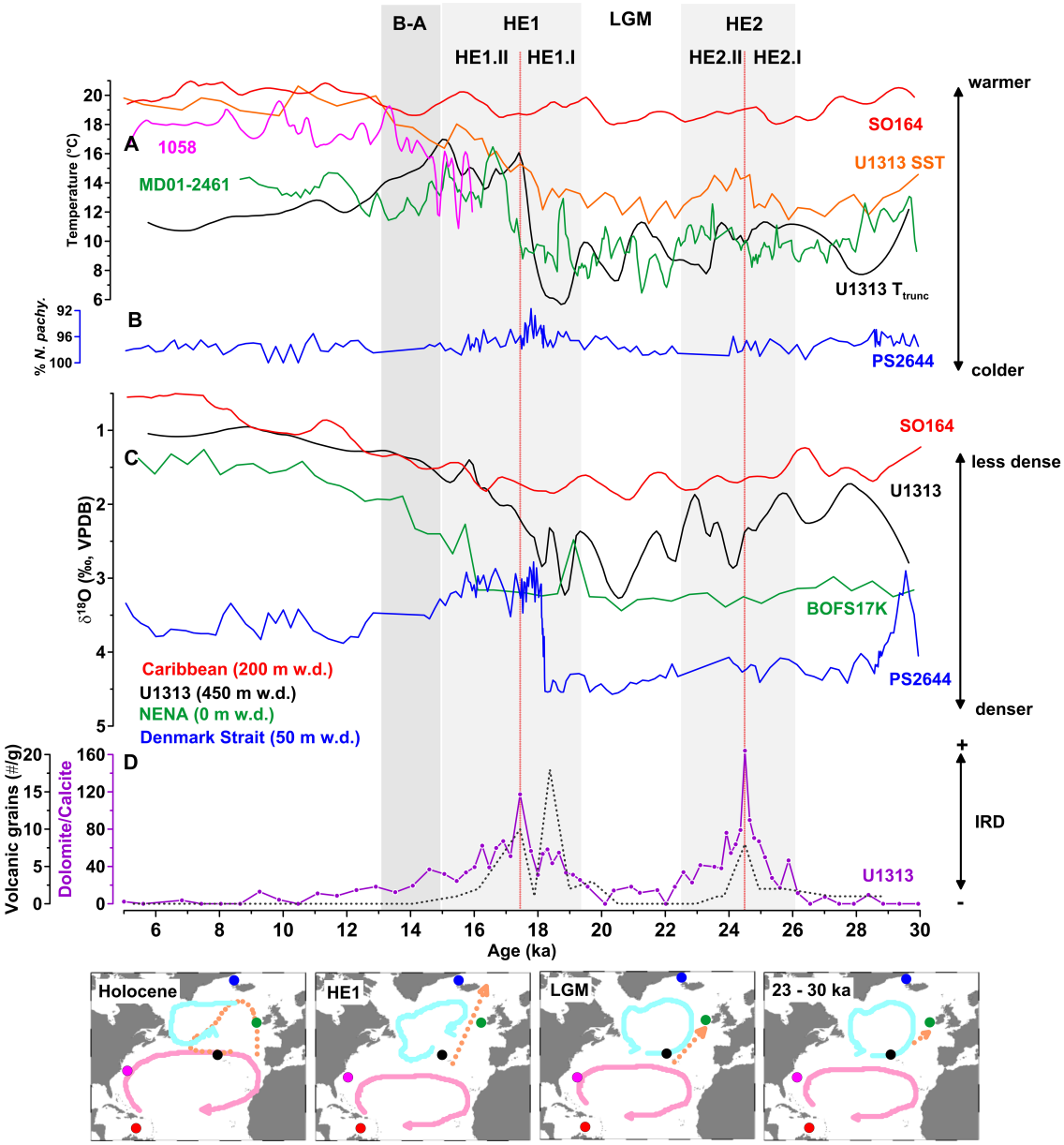

Figure 6.11 (A) Temperature records of: deep thermocline over Site SO164-03 (red, Central Caribbean, smoothed using LOESS by a factor of 0.1; Reißig et al., 2019), deep thermocline over Site 1058 (pink, STG, 3pt running average; Bahr, not published), surface and deep thermocline above Site U1313 (orange, Naafs et al., 2013, and black, smoothed using LOESS by a factor of 0.1, this study, respectively) and the surface at Site MD01-2461 (green, 3pt running average; Peck et al., 2006). (B) Percentage of N. pachyderma at Site PS2644-5 (Voelker et al.1998). (C) $\delta^{18}O$ of G. truncatulinoides (d) from sites SO164-03 (red, Central Caribbean, smoothed using LOESS by a factor of 0.1; Reißig et al., 2019) and U1313 (black, smoothed using LOESS by a factor of 0.1, this study), $\delta^{18}O$ of G. bulloides at Site BOFS17K (green; Barker et al., 2004), $\delta^{18}O$ of N. pachyderma at Site PS2644-5 (blue, Voelker et al., 1998; 2015). (D) Dolomite/calcite ratios and counts of volcanic grains at Site U1313 (purple and grey, respectively; Naafs et al., 2013, Lang et al., 2016). Vertical grey bars mark Heinrich events 1 and 2. The stratigraphic location of peaks in dolomite/calcite ratios are marked by red dotted lines. Sketches at the bottom show the interpreted location of the subtropical (light pink) and subpolar (light blue) gyres in relationship to sites U1313 (black dot), SO164-03 (red dot), 1058 (pink dot) and PS2644-5 (blue dot). Sites MD01-2461 and BOFS17K are represented as a green dot. Orange lines suggest the strength of the subsurface heat transport.

At 17.9 ka, approximately 500 years before the large influx of dolomitic IRD from the western North Atlantic (HE1), subsurface temperatures and relative salinity at the deep thermocline began rising quickly (~0.12°C/decade). Unlike the onset of HE2, salinity and temperature rose synchronously, indicating increased northward advection of density-compensated heat. There is indeed firm evidence that the initial strengthening of the northward heat flux via the deep thermocline recorded at Site U1313 reached the Nordic Seas during HE1.I. High latitude warming is indicated by percentages of the planktic foraminifera *N. pachyderma* at Site PS2644-5, in the Denmark Strait. These briefly but clearly decreased at 18 ka (Figure 6.11B, Voelker et al., 1998), indicating warming. Notably, $\delta^{18}O$ in the shallow thermocline of the Denmark Strait decreased to values similar to $\delta^{18}O_{trunc}$ values at Site U1313 (within 1σ uncertainties, Figure 6.11C) and *G. bulloides* $\delta^{18}O$ values at Site BOFS17K (Barker et al., 2004). This corroborates that the density connectivity between both sites developed precisely when the detected shallow thermocline warming at the Denmark Strait took place, accompanied by a brief IRD peak (Voelker et al., 1998).

Starting during HE1.I and after the brief temperature rise in the Nordic Seas (Figure 6.11B, Voelker et al., 1998), several cores in the eastern SPG and the Nordic Seas show very low $\delta^{18}O$ at the surface and subsurface (e.g., Benway et al, 2010; Maslin et al., 2010; Praetorius et al., 2008; Voelker et al., 1998). This regional $\delta^{18}O$ minimum is usually interpreted as freshening at the surface and, at the subsurface, the overflow of isotopically light brines from the Nordic Seas (Waelbroeck et al., 2011). However, decreasing percentages of *N. pachyderma* and increasing SSTs (estimated using MAT) recorded at the surface of Site 980, at the Rockall Trough, and Site GIK23415, in the northeastern North Atlantic suggest that the widespread low $\delta^{18}O$ must be at least partly due to warming (Benway et al., 2010; Weinelt et al., 2003). Subsurface warming in the northeastern North Atlantic is further supported by the abrupt increase in intermediate water temperatures in the Nordic Seas during HE1.II (Ezat et al., 2014), which are interpreted as a result of the upward shift of the Atlantic Inflow below the glacial halocline. The reported strengthening and upward shift of the Atlantic Inflow corroborate the return of the NAC to the northeastern North Atlantic during HE1, and thus of the intergyre isopycnal connection described in Chapter 5. The subsurface to surface directionality of the northward heat transport along isopycnal pathways (Foukal et al., 2016) would have allowed oceanic heat to "upwell" at the high latitudes where it could melt sea ice and marginal ice sheets from below, causing the $\delta^{18}O$ anomaly at the surface ocean.

The reconstructed upper ocean temperature distribution of the late HE1 (HE1.II) shows that warming occurred throughout the North Atlantic at the subsurface (Figure 6.10C), at the surface of Site U1313 (Naafs et al., 2013) and of northeastern North Atlantic (Site MD01-2461, Figure 6.11A, Peck et al., 2006; Site GIK23415, not shown, Weinelt et al., 2003). Elsewhere at the surface of the North Atlantic, however, the consensus is that the sea surface was cold and fresh (Bond et al.,, 1992; Calvo et

al., 2001; Cayre et al., 2010; Chapman et al. 2000; Chapman & Maslin, 1999; Maslin et al., 1995; Repschläger et al., 2015; Salgueiro et al., 2014). The increased stratification at the surface due to the spreading of meltwater would have hampered air-sea fluxes and may have supported the accumulation of heat at subsurface levels during HE1.II (Hodell et al, 2017). As long as the upper ocean was stratified (fresh and cold at the surface overlaying warm and salty waters), the atmosphere would have remained cold and oceanic heat would have accumulated at the subsurface. As density-compensated heat reached deep western North Atlantic, zonal density gradients at depth would decrease, slowing deep ocean circulation at western and northern North Atlantic (Levang and Schmitt, 2020; McManus et al., 2004, Ng et al., 2018) and triggering the destabilization of the LIS (Alvarez-Solas & Ramstein, 2011; Marcott et al., 2011).

At the onset of the B-A, atmospheric temperatures over Greenland rose abruptly by 13°C within 200 years, intermediate water temperatures in the Nordic Seas decreased abruptly to modern levels and overturning within the basin resumed (Figures 6.9A and 6.10B; Ezat et al., 2014). Concomitantly, deep thermocline temperatures at Site U1313 began a gradual descent (Figure 6.11A and 6.11C), showing that T_{trunc} variability was significantly tied to oceanic heat loss in the SPG.

6.5.4 The connection between freshwater fluxes, northward heat transport and deep ocean circulation as recorded at Site U1313

To explore the relationship between northward heat transport and deep-water ventilation, deep-thermocline and IRD records were compared to the vertical carbon isotope gradient between *G. truncatulinoides* (d) and *C. wuellerstorfi* ($\Delta\delta^{13}C = \delta^{13}C_{trunc} - \delta^{13}C_{cibis}$), here interpreted as a proxy for deep-water ventilation (Hodell et al., 2003, Ziegler et al., 2013). Both species have been previously argued to calcify in equilibrium with DIC of sea water (Curry and Oppo, 2005, Ziegler et al., 2013). Lower (higher) gradients between upper and sea-bottom waters indicate higher (lower) bottom water ventilation. Site U1313 recorded the three episodes of IRD deposition (deemed indicative of freshwater fluxes to the surface of the SPG) during the studied time interval, but each was characterized by different conditions at the deep thermocline of Site U1313 (Figure 6.12).

The delivery of positive buoyancy fluxes to the upper subpolar North Atlantic has long been evoked as the main mechanism for weakening the AMOC (Manabe and Stouffer, 1988; Stommel, 1961), which was supported by circulation proxies such as Pa/Th (Figure 6.12A; McManus, 2004, Böhm, 2015, Ng, 2018). These indicated the near collapse of deep-ocean circulation in the northwestern North Atlantic during HEs, which are mostly associated to the destabilization of the LIS (MacAyeal, 1993; Alley & MacAyeal, 1994). At Site U1313, however, high $\Delta\delta^{13}C$ (i.e., low deep-water ventilation) during HE2 and HE1.I (Figure 6.12E) coincided with abundant deposition

of volcanic grains, associated to destabilization of ice sheets in northeastern North Atlantic. During HE1.II, when the freshwater influx to the subpolar North Atlantic is typically assumed as especially large due to the destabilization of the LIS, deep water ventilation at Site U1313 increased to values similar to the modern. These records therefore imply that meltwater discharges to NENA were more efficient to disrupt deep-ocean ventilation than those to northwestern North Atlantic. The high sensitivity of deep-water formation to freshwater fluxes in northeastern North Atlantic is coherent with monitoring data showing that over 88% of modern deep-water formation in the Atlantic occurs at that location (Lozier et al., 2019).

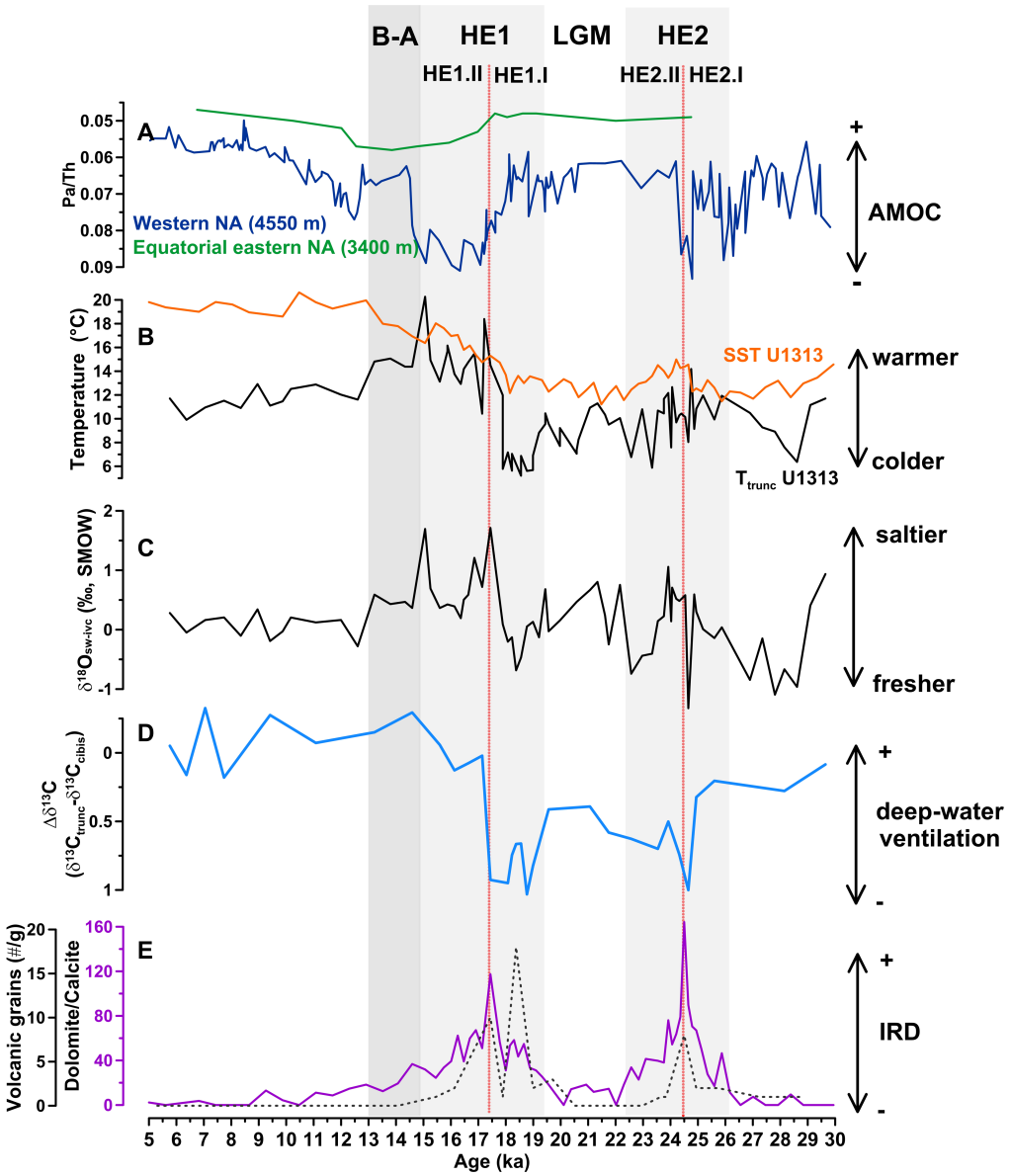

Figure 6.12 (A) Compilation of Pa/Th records from the Bermuda Rise (deep western North Atlantic, dark blue; Böhm et al., 2015, Henry et al., 2016, McManus et al., 2004) and at Sierra Leone Rise (equatorial eastern North Atlantic, green; Ng et al., 2018). (B) Mg/Ca-based subsurface temperatures at Site U1313 (black, this study) and alkenone-based SSTs (orange, Naafs et al., 2013). (C) Ice-volume corrected $\delta^{18}O_{sw\text{-}ivc}$ at the deep-thermocline of Site U1313 (this study). (D) Vertical carbon gradient at Site U1313 ($\Delta\delta^{13}C$, $\delta^{13}C_{trunc}$ - $\delta^{13}C_{cibis}$, light blue, this study and Jakob, not published). (E) Dolomite/calcite ratios and counts of volcanic grains at Site U1313 (purple and grey, respectively; Naafs et al., 2013, Lang et al., 2016).

During the late HE1 (HE1.II), the collection of proxy records at U1313 reveal a paradoxical scenario of hampered overturning in the SPG and active deep-water mass formation at mid latitudes. The 2.5 kyr-long maintenance of subsurface temperatures higher than modern at deep thermocline levels is a robust indicator that oceanic heat loss at high latitudes during this interval was weak, which is supported by Pa/Th ratios close to their production level in the northern and western North Atlantic (Figure 6.12A; Böhm et al., 2015, Henry et al., 2016, McManus et al., 2004). Weak overturning at high latitudes also led to the southward migration of deep-convection to the mid latitudes, as implied by the quasi-continuous overlap of SSTs and T_{trunc} between 17.5 and 15 ka (Figure 6.12B). The low temperature gradient of waters in the upper ocean indicate the development of an extremely deep mixed layer over Site U1313 and may explain the abrupt increase in bottom water ventilation (Figure 6.12D) and [CO_3^{2-}] to modern NADW values despite weak overturning in the subpolar domain. It remains to be tested how strong this overturning cell may have been relative to the modern, because most modelling studies do not account for the increased northwards advection of salinity when forcing a shutdown of the AMOC with freshwater fluxes to the SPG (e.g., Brady & Otto-Bliesner, 2011; He et al., 2020; Liu et al., 2009; Otto-Bliesner & Brady, 2010). The spreading of subtropical waters through the intermediate North Atlantic has been evoked as the dominant mechanism for weakening the AMOC (Haskins et al., 2020, Levang and Schmitt, 2020, Zhang et al., 2017) and may provide a new rationale for explaining prolonged phases of sluggish deep circulation in the subpolar and western North Atlantic which does not require extremely high rates of freshwater fluxes used by many hosing studies.

The occurrence of deep-water formation at mid latitudes during HE1.II is consistent with the different deep-water circulation histories of western and eastern Atlantic sectors reported during the deglaciation (Figure 6.12A, Ng et al., 2018). While in the western and northern North Atlantic, deep ocean circulation came close to a halt during HE1.II, circulation at the low latitudes and in the eastern Atlantic was relatively constant throughout the last deglaciation, with a small decrease in intensity during HE1.II and the B-A. Even as the AMOC was weaker, the accumulation of salt at deep-thermocline levels would have favored the deepening of NSW, leading to the disappearance of the glacial chemocline at indicated both by low $\Delta\delta^{13}C$ (Figure 6.12D) and high [CO_3^{2-}] (Figure 6.8E). The resumption of deep-water ventilation during HE1 has also been reported at intermediate depths in the tropical North Atlantic (Valley et al., 2017) and southwards in the Southern Ocean (Gottschalk et al., 2016; Piotrowski et al., 2004; Skinner et al., 2010; Ziegler et al., 2013), where it has been associated with the atmospheric rise of CO_2 during the deglaciation. Thus, the deepening of NSW upon the return of the NAC to northeastern North Atlantic may have had profound implications for global climate system, not restricted to the North Atlantic realm. The records here discussed indicate the need of modelling studies that consider AMOC dynamics during phases of increased northward transport of subtropical waters.

7 Inter-gyre connectivity and northward heat transport during the MPT

Parts of this chapter have been published in modified form in: Catunda, M.C.A., Bahr, A., Kaboth-Bahr, S., Zhang, X., Foukal, N., Friedrich, O. (2021). Subsurface heat channel drove sea surface warming in the high-latitude North Atlantic during the Mid-Pleistocene Transition. *Geophysical Research Letters*, 48(11), e2020GL091899.

7.1 Introduction

Between 1.2 and 0.6 Ma during the MPT, glacial/interglacial cyclicity shifted from a 40-kyr period to the ~100-kyr saw-toothed cycles characteristic of the Late Pleistocene (Clark et al., 2006; Imbrie et al., 1993; Raymo et al., 1997; Ruddiman et al., 1989). Although there have been numerous studies on the MPT (Chalk et al., 2017; Clark et al., 2006; Hasenfratz et al., 2019; McClymont et al., 2013; Ruddiman et al., 1989), the exact mechanism(s) explaining the shift in glacial-interglacial cyclicity and the increase in precessional pacing in global ice volume records, in the absence of significant changes in the orbital configuration remain(s) elusive (Imbrie et al., 1993; Lisiecki, 2010; Chapter 3).

The most widely accepted explanation for the ice-sheet enlargement during the MPT is the "regolith hypothesis" (Clark & Pollard, 1998; Chapter 3). This cyclicity shift was also marked by the long-term cooling of global sea-surface temperatures due to a decrease in atmospheric pCO_2 (Chalk et al., 2017; Hönisch et al., 2009) and the potential slowdown of the AMOC during the so-called "900 ka event" (Pena & Goldstein, 2014). These processes would have promoted conditions ideally suited for sustaining large continental ice sheets. However, the cooling of global temperatures and the reduction in surface-heat transport in the North Atlantic would have decreased the moisture capacity of the ocean's overlaying air masses, hampering the precipitation over continental ice sheets. Thus, the source of the moisture that fueled the intensification of NH ice-sheet growth across the MPT is also unknown.

The dynamics of the NH ice sheets are intimately linked to variations in ocean circulation on millennial and orbital timescales (Hodell & Channel, 2016; Zhang et al., 2014). The upper ocean is a direct source of heat and moisture to the atmosphere and thus impacts the mass balance of the adjacent ice sheets. Hence, northward heat transport via subsurface routes (Chapter 2 and 5) may have played a so far neglected role in oceanographic processes, including the boundary conditions leading to the MPT.

In this chapter, new mechanisms for North Atlantic meridional heat transport (Chapter 2) are applied to interpret the variability in a deep-thermocline temperature record and are used to trace the potential origin of the moisture source that fueled NH

ice-sheet enlargement during the MPT. To test if enhanced subsurface heat transport into the high-latitude North Atlantic provided moisture for the abrupt increase in NH ice-sheet volume during the MPT, a subsurface temperature record (T_{crass}) from the regions in-between gyres in the North Atlantic was produced for the interval MIS 36 to 14 (~1.2–0.54 Ma). Upper-ocean stratification was assessed by the thermal gradient between alkenone-based sea-surface temperatures (SST) at Site U1313 {Naafs:2012ep} and the newly measured T_{crass} ($\Delta(SST\text{-}T_{crass})$). As vertical temperature gradients determine thermocline stratification in the region, these data allowed to reconstruct the geometric configuration of isopycnals in the upper ocean between the STG and the SPG. The connection between thermocline stratification and northward heat transport across the MPT was further assessed by calculating the sea-surface temperature gradient between Site U1313 and subpolar Site 982 (Lawrence et al., 2010; $\Delta SST_{U1313\text{-}982}$) located in northeastern North Atlantic (NENA). Based on the findings described here, it is proposed that subsurface heat transport played a vital role in enhancing the northward oceanic heat transport during the MPT, which might have helped to shape glacial/interglacial variability during Mid- and Late Pleistocene.

7.2 The dwelling depth of *Globorotalia crassaformis* at Site U1313

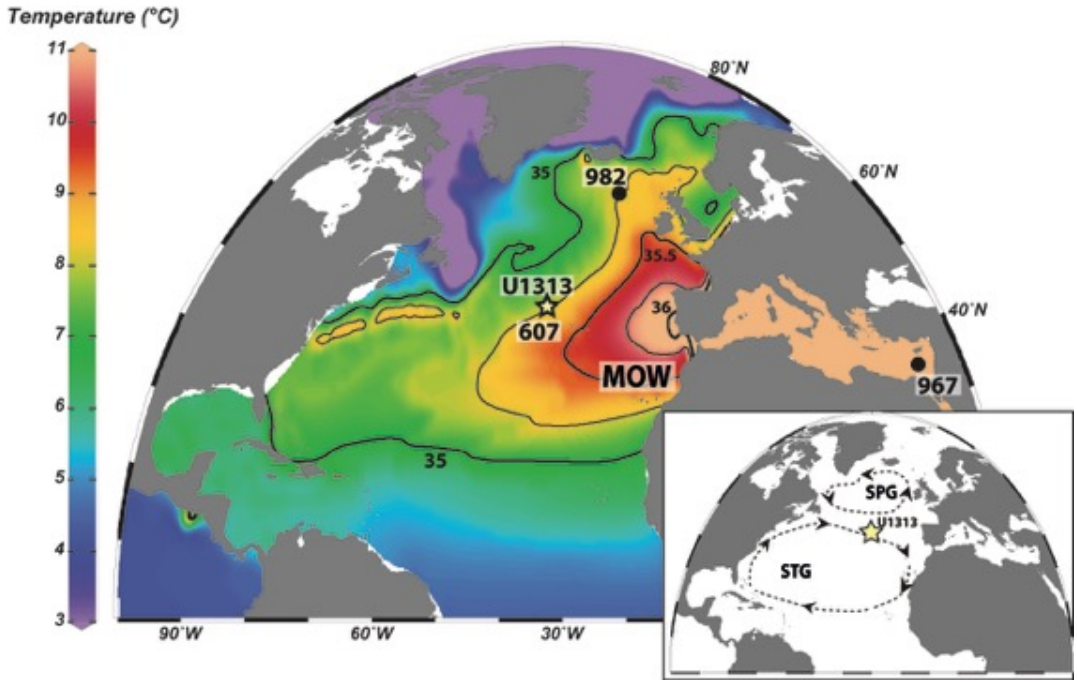

Figure 7.1. Figure 1. (main) Temperature along the σ_0 = 27.45 surface, which intersects Site U1313 (star) at 800 m depth (Locarnini et al., 2019). Black contours indicate isohalines from 35 to 36 psu at 0.25 intervals (Zweng et al., 2019). (inset) Location of Site U1313 (star) relative to the Subtropical Gyre (STG) and the Subpolar Gyre (SPG).

At the mid-latitudes *G. crassaformis* has been found to calcify at 800 m water depth within the zone of minimum oxygen concentration in the upper pycnocline (Cleroux et al., 2013). Nowadays, this depth is within the σ_0=27.45 density layer

(Figure 7.1), very close to the isopycnal of maximum overturning (σ_0=27.53, Chapters 2 and 5), suggesting that this species is able to record the characteristics of waters undergoing overturning further downstream. Figure 7.1 shows the temperature and salinity distribution for the isopycnal level at 800m water depth above Site U1313 (σ_0 = 27.45). Temperature and salinity at this density level covary and radiate from the Gulf of Cadiz, strongly indicating that MOW (Chapter 5.1) modulates temperature distribution at the dwelling depth of *G. crassaformis* in the subtropical North Atlantic.

7.3 Additional methods

7.3.1 Deep-thermocline temperature uncertainty

The methodology used in Mg/Ca analyses and the rationale for the choice of paleotemperature equation are detailed in chapters 4.3.4 and 4.3.5, respectively. Standard deviation from replicated trace element measurements in *G. crassaformis* (d) (n=20) was ± 0.14 mmol/mol for Mg/Ca, which would account for a temperature uncertainty of ± 0.86ºC using the species-specific Equation 2 (Chapter 4.3.5; Cléroux et al., 2013). As this analytical uncertainty is similar but higher than the 1σ uncertainty of the chosen equation (± 0.82°C) the former was considered.

7.3.2 Calculation of temperature gradients

Upper ocean stratification was qualitatively estimated using the temperature gradient between alkenone-based SST and Mg/Ca-based T_{crass} at Site U1313. Both records were produced from the same core sections of the primary splice. As the temporal resolution of the SST record (1 data point every ~0.6 ka) is double that of the SubT record (1 data point every ~1.2 ka), SSTs were linearly interpolated to match the time scale of the SubT record (thereby reducing the resolution of the SST record in half). Deep-thermocline temperatures were then subtracted from SST to produce $\Delta(SST\text{-}T_{crass})$ values. A similar procedure was used to calculate the surface temperature gradients between sites U1313 and 982 (Lawrence et al., 2010). Like the records from site U1313, the age model for the SST record at Site 982 was also produced by tuning benthic oxygen isotopes to the LR04 stack (Lisiecki & Raymo, 2005). As the temporal resolution of the SST record from Site U1313 is higher than the one from Site 982, the U1313 SST record was linearly interpolated to match the 982 record in age. Subpolar SSTs (Site 982) were then subtracted from U1313 SSTs to produce $\Delta SST_{U1313\text{-}982}$ values.

7.3.3 Model description and experimental design

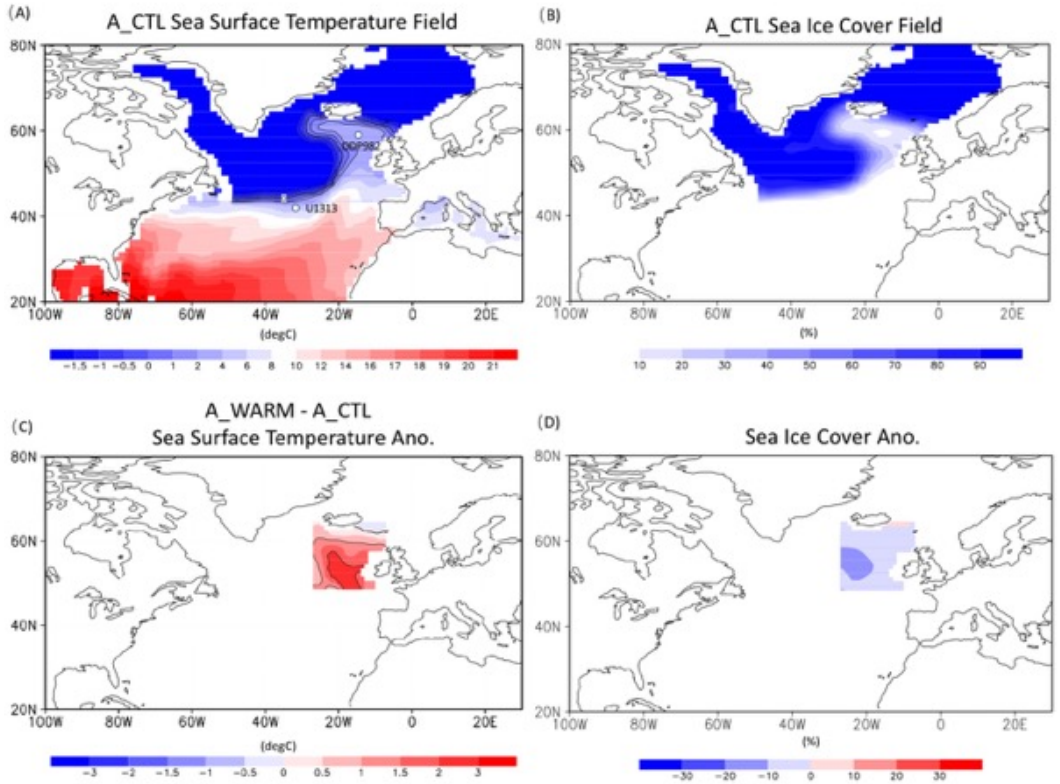

Figure 7.2. Winter sea-surface forcing derived from the modeling experiments. (A) sea-surface temperature (units: ºC) and (B) sea-ice concentration in the control experiment A_CTL/NHIS_0.3s. Contours in (A) represent isothermal lines of -1.5, -1, -0.5, 0, 1, and 2. (C) Sea-surface temperature (units: ºC) and (D) sea-ice cover anomalies between A_CTL and A_WARM.

Two glacial simulations in an Atmosphere General Circulation Model (AGCM), ECHAM5 (Roeckner et al., 2003), were conducted by Prof. Xu Zhang (Langzhou University) to quantify the contributions of preferential warming in the northeastern North Atlantic (NENA) on the mass balance of continental ice sheets in the Atlantic realm during glacial periods. The control experiment (A_CTL) was conducted by applying boundary conditions (including ice-sheet configurations, greenhouse gases, orbital parameters etc.) and sea-surface forcing (i.e., sea-surface temperature, SST, and sea-ice concentration, SIC) from a glacial experiment (NHIS_0.3s) done by a fully coupled atmosphere-ocean model (AOGCM, Zhang et al., 2014). The prescribed global ice volume in NHIS_0.3s equaled a ~50 m sea-level drop. In NHIS_0.3s, NENA was characterized by a perennial open water area, while extensive sea-ice cover was simulated in the southern flank of the North Atlantic subpolar gyre (i.e., north of Site U1313, Figure 7.2). To investigate impacts of the recorded warming on the ice-sheet mass balance, a sensitivity experiment (A_WARM) was conducted in which only the SST in the NENA perennial open water area in A_CTL was substituted by the SST derived from experiment NHIS_0.5 (Zhang et al., 2014), which is 2°C warmer at

NENA than NHIS_0.3s (Figure 7.2). This provides a direct evaluation of sole impacts of NENA warming on the ice-sheet mass balance.

Additional ice-volume growth was calculated based on the precipitation anomaly over the NH ice-sheet area (additional_volume = NH_ice-sheet_area * precipitation_anomaly / ocean_area). Calculated estimates are considered conservative because the simulations do not consider the possible positive feedbacks from a growing ice sheet on ocean circulation, since a larger ice sheet can strengthen the AMOC, leading to an enhancement of precipitation over the ice-sheet area, further increasing its volume (Zhang et al., 2014).

7.4 Results

7.4.1 Subsurface temperature and thermocline variability at Site U1313

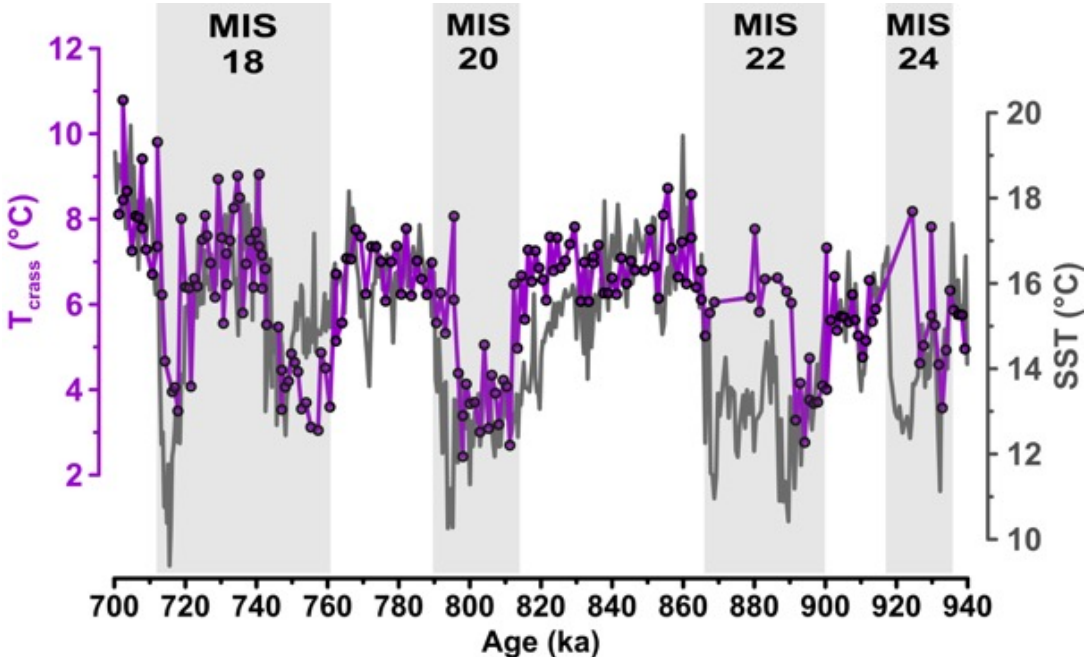

Figure 7.3. Comparison between SST and T_{crass} at Site U1313 between MIS 24 and MIS 18. Mg/Ca-based subsurface temperatures (red line and circles) and alkenone-based SST (grey line). Light gray rectangles denote cold MISs (Lisiecki and Raymo, 2005). Both records were produced from the primary splice from Site U1313 and are plotted using the same updated age model, thus avoiding stratigraphic uncertainties.

The temperature gradient between SST and T_{crass} (Δ(SST-T_{crass}), Figure 7.4C) shows that a steep thermal gradient of 11.2 ± 1.9°C existed at Site U1313 between 1.2 and 0.93 Ma (MIS 36–25), which is higher than the modern mean annual gradient between surface and 800m water depth of ~9.9ºC (Locarnini et al., 2019). Between MIS 24 and 17 (~0.93–0.67 Ma), SSTs cool while SubTs show a long-term warming trend, resulting in a prolonged phase of weaker stratification (9.1 ± 1.5°C). This trend reversed after MIS 17 (~0.67 Ma) when a thermal gradient similar to the modern gradient was re-stablished. Weak upper-ocean stratification between MIS 24–17 (Figure 7.4C) suggests that the thermocline deepened in the mid-latitude North

Atlantic and that heat accumulated at subsurface depths. Minimum upper-ocean stratification occurred during MIS 24 (8.6 ±1.2°C) and MIS 22 (7.4 ±1.6°C, Figure 7.4C), which were crucial stages of ice-sheet build up during the MPT (Ford and Raymo, 2019), particularly for the European Ice Sheet (Berger & Jansen, 1994; Knudsen et al., 2020).

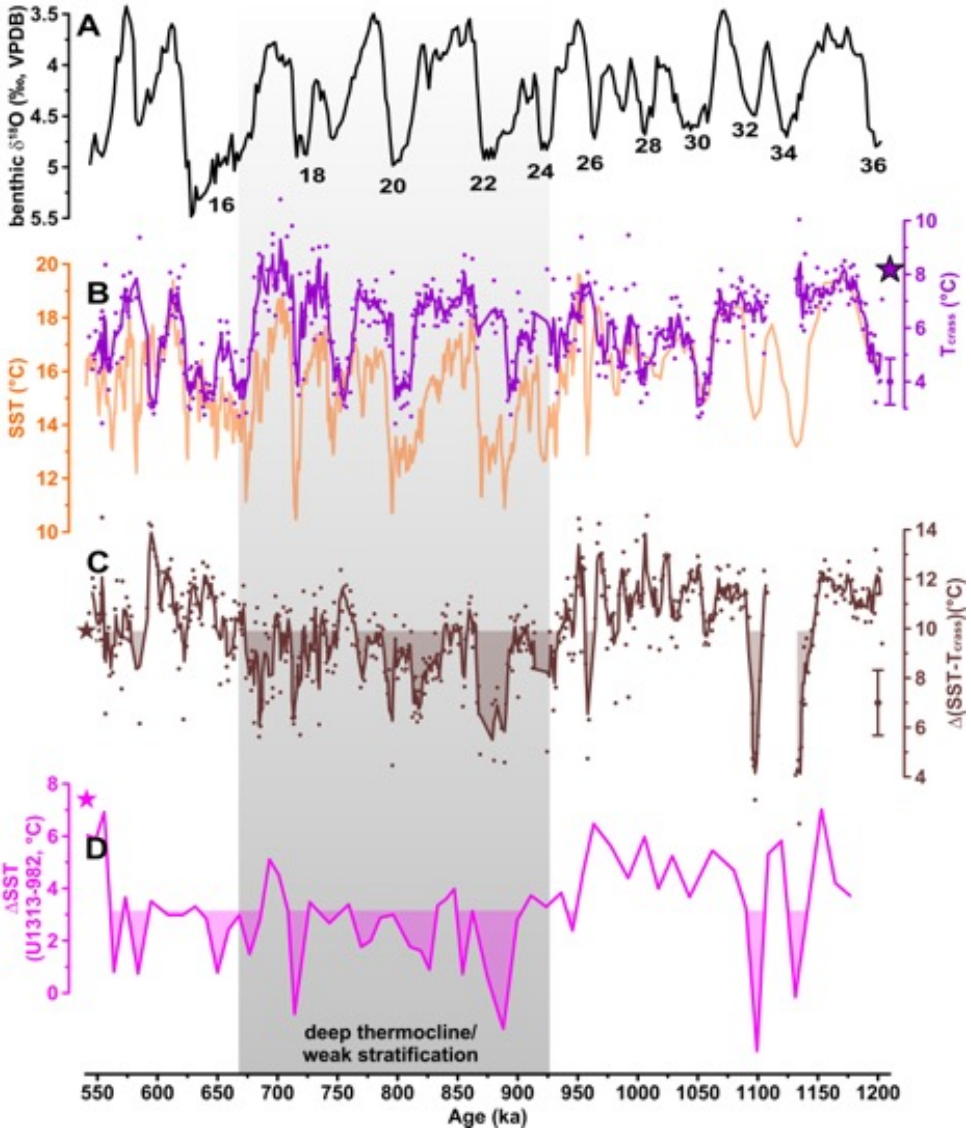

Figure 7.4. (A) U1313 benthic $\delta^{18}O$ record for reference (this study and Ferretti et al., 2015), and numbered cold Marine Isotope Stages (Lisiecki and Raymo, 2005). (B) Alkenone-based sea-surface temperatures (Naafs et al., 2012, SST, orange, 3pt running mean) and Mg/Ca-based subsurface temperatures (purple, this study, original data points and 3pt running mean). Purple star on the left Y-axis marks modern subsurface temperatures at 800 m water depth above Site U1313 (Locarnini et al., 2019). (C) Upper ocean stratification at Site U1313 (Δ(SST-T_{crass}), brown, this study, original data points and 3pt running mean). Light brown filling marks temperature-gradient lower than the modern annual average (~9.9 °C, Locarnini et al., 2019). (D) Temperature gradient between Sites U1313 and 982 (Lawrence et al., 2010). Shading marks $\Delta SST_{U1313\text{-}982}$ lower gradient than the study interval's average (3.2°C). Grey box demarks period of long-term weakening of upper-ocean temperature gradient ("stratification") as indicated by low Δ(SST-T_{crass}).

7.4.2 Heat transfer into the high latitude North Atlantic during the MPT

Net northward heat transport to the eastern SPG was evaluated based on the SST gradient between Site U1313 (Naafs et al., 2012) and the subpolar Site 982 at 58°N ($\Delta SST_{U1313-982}$, Figure 7.3D; Lawrence et al., 2010). Across the studied interval, $\Delta SST_{U1313-982}$ (Figure 7.3D) follows the same trend (Figure 7.3C) and shows a significant correlation to $\Delta(SST-T_{crass})$ changes ($r= 0.69$, $p<0.01$ using the Monte-Carlo-based surrogateCorr script implemented in the *astrochron* package (Meyers et al. 2014) in R). Based on the modern annual SST difference between both sites (~7.2°C; Locarnini et al., 2019), the reduced $\Delta SST_{U1313-982}$ between MIS 24 and 17 suggests increased net northward heat transport between subtropical and subpolar latitudes in the North Atlantic during this interval.

7.5 Discussion

7.5.1 Potential seasonality bias affecting the thermocline temperature gradient of Site U1313

At Site U1313, alkenone-derived SSTs from core-top samples were virtually identical to the modern annual mean SST (18.2°C; Locarnini et al. 2019), supporting the interpretation that the $U_K^{37'}$ SST record at this site reflects mean annual SSTs (Naafs et al., 2012). However, water column and satellite data indicate that most coccolithophorid productivity in subpolar ocean regions occurs from summer to early autumn (Samtleben and Bickert, 1990), biasing alkenone-based SSTs to warm (summer) conditions in locations with surface temperatures below ~15°C (Rosell-Melé et al., 1995). During the time span discussed here, SSTs from Site U1313 dipped below this threshold during cold glacial stages MIS 34, 32, 24, 22, 20 and 16, implying that during these periods, SSTs may have been overestimated. Comparison with SSTs based on planktic foraminiferal assemblages at the same location as Site U1313 (Site V30-97; Ruddiman et al., 1989) supports this interpretation, as $U_K^{37'}$-based temperatures overlap with summer SST estimates during the LGM but fall between winter and summer SSTs during the Holocene (see Naafs et al., 2013).

Subsurface temperatures from *G. crassaformis*, on the other hand, are unlikely to show seasonal biases because the oxygen-depleted niche preferred by this species is stable below the seasonal thermocline depth (see Chapter 4.1.1) and the physically feasible maximum depth reachable by Ekman pumping (~300 m, Talley, 1996). While it is possible that the depth occupied by *G. crassaformis* was influenced by changes in the depth of the pycnocline and/or the shallow oxygen minimum at Site U1313, we infer that the amplitude of shifts in the calcification depth was relatively minor, as abundant proxy records support *G. crassaformis* being a reliable recorder of deep thermocline properties and having a stable habitat (e.g., Bahr et al., 2011; Bolton et al., 2018; Karas et al., 2017). Therefore, during periods in which the sea surface was

warmer, both SST and T_{crass} record annual temperature averages and $\Delta(SST\text{-}T_{crass})$ is a robust indicator of the thermocline thermal gradient. During cold glacial stages, however, the potential summer bias of SST implies that $\Delta(SST\text{-}T_{crass})$ may be overestimated and that the annual thermocline thermal gradient during cold glacial stages MIS 22 and 24 may have been lower (weaker stratification).

Alkenone-based SST estimates from Site 982 likely present summer-biased SSTs throughout the Pleistocene (Lawrence et al., 2010). Core-top SST estimates (13°C, Lawrence et al., 2010) fell in the upper range of the modern annual variability (9–13°C), further supporting the assumption of a warm-season bias. As alkenones from site U1313 and 982 contain the same summer bias during cold glacial stages, the SST gradient between sites U1313 and 982 should be robust during MIS 24, 22 and 20. During interglacials, the SST gradient may be considered a minimum estimate because alkenone-SSTs at Site U1313 are likely reflecting the annual mean temperature (above ~15°C) while Site 982 alkenone-SSTs are summer-biased. Despite these caveats, $\Delta SST_{U1313\text{-}982}$ can be considered a robust indicator of heat transport into the high-latitude North Atlantic, particularly during glacial times. The evaluation of possible seasonal biases in alkenone-based SSTs suggests that these would not negatively impact findings described here, but rather reinforce them.

7.5.2 Subsurface pathway for heat advection to high latitudes during the MPT

The strong correlation between $\Delta SST_{U1313\text{-}982}$ and $\Delta(SST\text{-}T_{crass})$ throughout the MPT ($r= 0.69$, $p<0.01$) suggests that low upper ocean stratification may have facilitated the advection of warmer subtropical waters from the subsurface of the STG to the surface of the eastern SPG (Site 982), particularly during MIS 22. The increased advection of subtropical sourced waters to NENA between MIS 22 and 21 is also supported by the relatively high counts of *G. truncatulinoides* at Site 552, also located in NENA (Kaiser et al., 2019). As this foraminifera species prefers warm waters, they are uncommon at such high latitudes.

As northward heat transport between the STG and SPG in the North Atlantic takes place in the subsurface via the deep thermocline (Chapter 2.1; Foukal and Lozier, 2016), thermocline deepening (decreased stratification) between MIS 25 and 17 may have increased density connectivity between gyres and the subtropical-subpolar flux during the MPT. The location of Site 982 is at the end of the isopycnal pathway described by Burkholder and Lozier (2011) and Foukal and Lozier (2016) and has been previously used to reconstruct climate variability in the high-latitude North Atlantic (Lawrence et al., 2010, Venz et al., 1999). Site 982 is furthermore atmospherically upstream of the European Ice Sheet, which enlarged significantly during MIS 22 (Berger & Jansen, 1994; Knudsen et al., 2020). The relatively mild and higher than average temperatures at Site 982 particularly during MIS 22 (Figure 7.5A) are notably at odds with the concurrent intrusion of subpolar waters in the mid-latitude North Atlantic as reflected by the high abundance of *N. pachyderma* within sediments of Site

607 (adjacent to Site U1313, Figure 7.5D; Ruddiman et al., 1989) and SST cooling at Site U1313 (Figure 7.5A; Naafs et al., 2012). This indicates that the heat giving rise to mild SST at Site 982 between MIS 24 and 17 was not transferred along a surface trajectory, but rather via a subsurface pathway.

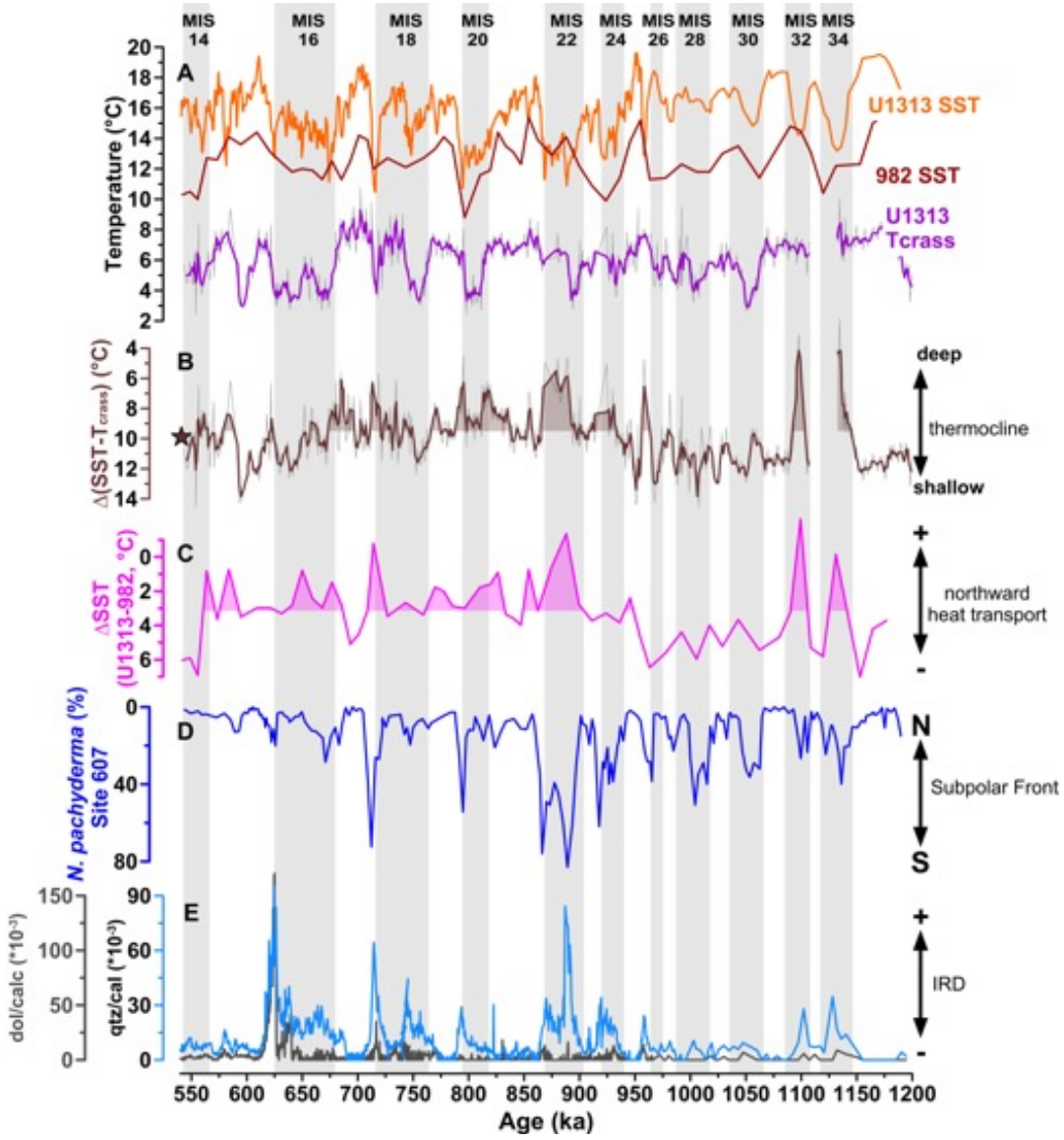

Figure 7.5. (A) Alkenone-based SSTs at sites U1313 (orange, 3pt running mean; Naafs et al., 2012) and 982 (red; Lawrence et al., 2010) and Mg/Ca-based T_{crass} at Site U1313 (original data shown as a light grey line and 3pt running mean shown as a purple line). (B) Thermocline stratification ($\Delta(SST-T_{crass})$) at Site U1313 (original data shown as a light grey line and 3pt running mean shown as a brown line). Brown shading marks stratification weaker (deeper thermocline) than the modern (9.9ºC, Locarnini et al., 2019). (C) Temperature gradient between Sites U1313 and 982. Shading marks $\Delta SST_{U1313-982}$ lower gradient than the study interval's average (3.2ºC). (D) Percentage of Neogloboquadrina pachyderma (Ruddiman et al., 1989) at Site 607. (E) Quartz/calcite (light blue line and Y-axis) and dolomite/calcite ratios (dark grey line and Y-axis) at Site U1313 (Naafs et al., 2012). All records of Site U1313 not produced in this study are plotted on the updated age model for this site (Chapter 4.3.3). Grey bars in the background mark cold Marine Isotope Stages (Lisiecki and Raymo, 2005).

7.5.3 Did shifts in the Subpolar Front and/or variations in AMOC strength cause the subsurface warming between MIS 24–17?

Temperature fluctuations in the upper ocean of the mid-latitude North Atlantic thermocline are typically attributed to spatial shifts of the Subpolar Front, which may also explain the minimum thermocline stratification during MIS 22 and 24 (Figure 7.5B and 7.5D). However, such frontal shifts should generate synchronous fluctuations of SST and T_{crass} as expansion (retreat) of the front would decrease (increase) the influence of the STG above Site U1313, thereby cooling (warming) the entire upper water column. Particularly during MIS 24 and the end of MISs 22 and 20, T_{crass} warmed while SST remained cold (Figures 7.3 and 7.5A), arguing against frontal shifts as a driver of the T_{crass} increases during these intervals.

The increased warming at depth relative to the surface might instead be the consequence of a weakened AMOC (Lopes dos Santos et al., 2010). In particular, during MIS 22, very high percentages of *N. pachyderma* at Site 607 (Figure 7.5D; Ruddiman et al., 1989) and quartz/dolomite ratios at Site U1313 (Figure 7.5E; Naafs et al., 2012) suggest this stage was marked by both prominent development and long-term instability of the European Ice Sheets (i.e., quartz IRDs are usually associated with EIS instability; Hodell et al., 2017, Naafs et al., 2012). As the NENA is nowadays an important *locus* of deep-water formation (Lozier et al., 2019), high IRD deposition and surface freshening could also be indicative of a long-term disruption of overturning in the SPG. Weakened overturning in the SPG due to freshwater influx (as suggested by abundant *N. pachyderma* and IRDs at sites 607 and U1313; Naafs et al., 2012, Ruddiman et al., 1989) could potentially hamper intergyre heat transport, leading to the accumulation of heat and reduced thermal stratification in the subtropical upper ocean during MIS 22. However, although weak overturning in the SPG may have co-occurred with subsurface warming at Site U1313, the cause and effect relationship between subsurface warming in the mid-latitudes and the strength of the AMOC is unclear, even over short timescales (Lozier et al., 2010).

Subsurface warming at the mid- to high- latitudes of the North Atlantic is considered a product of the two competing effects of surface freshening over deep convection regions (He et al., 2020): (1) surface freshening reduces the mixing of warm subsurface and cold surface water masses, resulting in anomalous subsurface warming and (2) surface freshening also weakens the AMOC which reduces ocean heat transport into northern North Atlantic and results in subsurface cooling (Sgubin et al., 2017, He et al., 2020). Thus, although it is possible that overturning in the SPG could result in subsurface warming in the northern North Atlantic at millennial timescales, over the glacial-interglacial timescales of this study, a weak AMOC would more likely have resulted in cooling of the deep thermocline. Furthermore, if thermocline stratification in the subtropics was modulated by AMOC strength on orbital time scales, the spectral signal of $\Delta(SST\text{-}T_{crass})$ would be expected to peak in the obliquity band (Lisiecki et al, 2008, Rutberg & Broccoli, 2019). Yet, $\Delta(SST\text{-}T_{crass})$

variability is dominated by a peak in the precession frequency, without any obliquity imprint (Figure 7.6). Thus, this finding suggests that AMOC strength was not the primary driver of the temperature gradient in the subtropical North Atlantic during the MPT.

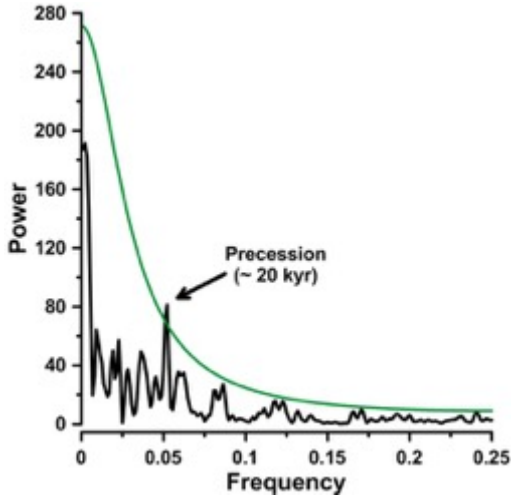

Figure 7.6. Power spectrum of Δ(SST-T_{crass}) at Site U1313 computed with the interpolated and detrended data using the program REDFIT (Schulz and Mudelsee. 2002) implemented in the software PAST (version 3.18, Hammer et al., 2001). The green line marks the 99% chi squared confidence limit.

7.5.4 The connection between the thermocline in central North Atlantic and eastern Mediterranean

Here it is argued that the influence of the MOW on the deep-thermocline waters at Site U1313 is primarily responsible for both the T_{crass} warming during MIS 24–17 and the precession modulation of the Δ(SST-T_{crass}) record. The MOW is a particularly suitable candidate to explain the good agreement between thermocline warming and increased northward heat transport to the SPG because it affects temperature and salinity at the deep-thermocline and upper-intermediate levels of both the subtropical and subpolar North Atlantic (Potter & Lozier, 2004), thus playing a crucial role in determining upper-ocean stratification (Feucher et al., 2016; Chapter 5).

During the MPT, the occurrence of pronounced and widespread erosion within the Gulf of Cadiz suggests that the outflow was particularly strong (Hernandez-Molina et al. 2014). This is supported by the high abundance of epibenthic foraminifera, directly associated with the presence of the MOW, between MIS 30 and MIS 18 (Site U1391, 1085 m water depth; Guo et al., 2020). The presence of the MOW at intermediate levels of the slope of the Gulf of Cadiz was mostly paced by obliquity for the last 1.3 Ma, but developed a strong precession pacing between 0.7 and 0.9 Ma (Guo et al., 2020). The precession pacing of the MOW during the Late Pleistocene is derived from the relationship between Eastern Mediterranean aridity and the convection of Levantine Intermediate Water (LIW; Rohling et al., 2015), the main component of the modern outflow (Bryden and Stommel 1982, Parrilla et al.1986).

Aridity in the East Mediterranean, in its turn, is driven by the strength of the African Monsoon (Rohling et al. 2015). During phases of low precession and increased NH insolation, the ITCZ migrates northward and strengthens the monsoon (Rohling et al. 2002). The strengthening leads to increased freshwater outflow by the River Nile and consequent decreased surface salinity and buoyancy loss at the source region of LIW (Rohling et al. 2015). Inversely, southward shifts of the ITCZ and weakening of the African Monsoon leads to reduced continental freshwater runoff and, likely, intensification of buoyancy loss in eastern Mediterranean (Bahr et al. 2015). During the MPT, the eastern Mediterranean experienced diminished runoff from the River Nile which, favored continuous LIW formation, as suggested by scarcity of sapropels (i.e. organic matter-rich layers formed during periods of low bottom water ventilation by LIW, citation) in Mediterranean sedimentary records (Konijnendijk et al. 2014).

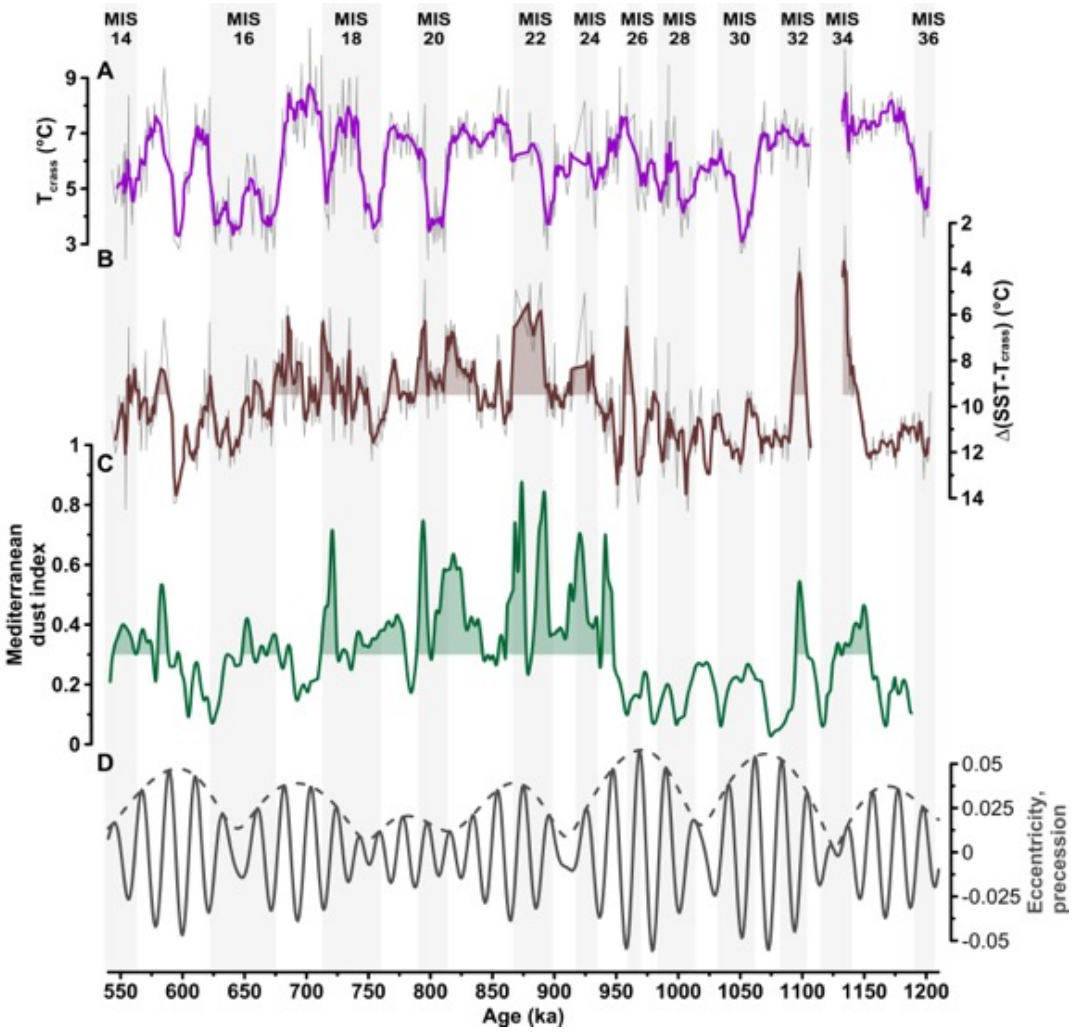

Figure 7.7. (A) Mg/Ca-based T_{crass} at Site U1313 (original data shown as a light grey line and 3pt running mean shown as a purple line).(B) Thermocline stratification (Δ(SST-T_{crass})) at Site U1313 (original data shown as a light grey line and 3pt running mean shown as a brown line). Brown shading marks stratification weaker (deeper thermocline) than the modern (9.5°C, Locarnini et al., 2019). (C) Mediterranean dust index at Site 967 (IRM strength, Larrasoana et al., 2003). (D) Eccentricity (dashed line) and precession parameters (solid line) as calculated by Laskar et al., 2004. Grey bars and numbers highlight cold marine isotope stages according to the LR04 benthic $\delta^{18}O$ stack (Lisiecki and Raymo, 2005).

To indirectly assess LIW (thus, MOW) production during the MPT, Δ(SST-T_{crass}) was compared to an eastern Mediterranean aridity proxy (Figure 7.7). Isothermal Remanent Magnetization (IRM) at ODP Site 967 indicates variations in hematite concentration in the eastern Mediterranean, at the formation site of LIW. High hematite concentrations (high IRM values) at this site are inferred to represent enhanced Saharan dust supply(Larrasoaña et al. 2003). As dust input reflects wet and arid cycles in the Sahara (Trauth et al. 2009) and annual moisture availability in this region is related to intensity of the African Monsoon, increased IRM at this site indicates a weakened North African monsoonal system, which allowed for increased dust formation and transport to the eastern Mediterranean. Between MIS 25 and MIS 17, high dust deposition in the eastern Mediterranean Sea suggests the prevalence of arid conditions during these stages (Larrasoaña et al. 2003; Konijnendijk et al. 2014). The long-term covariations in both the aridity index and thermocline depth may also suggest that the MOW is a long-standing modulator of subsurface heat and thermocline depth along the subtropical North Atlantic (Figure 7.7). The most pronounced peaks of IRM at Site 967 also correspond to decreased thermohaline stratification in central North Atlantic (Figure 7.7). Pronounced aridity in eastern Mediterranean may have predisposed convection of the LIW, which would have resulted in a shallower-settling and a warmer and possibly stronger MOW (Cacho et al., 2000, Guo et al., 2020, Rohling et al., 2015, Sierro et al., 2020). The entrainment and mixing between the shallower and warmer MOW would preferentially warm the lower thermocline of the subtropical North Atlantic, thereby decreasing the upper ocean stratification at Site U1313 during MIS 24 to 17.

The shoaling of the MOW during this interval also coincides with a period of flourishing cold-water coral reefs at the Irish Margin after a 600 kyr-long hiatus (Kano et al., 2007). These corals depend on the high-energy pycnocline between the MOW and the central waters for nutrient mobilization and larval dispersal, serving as indicators of the presence of the northward branch of the MOW along the eastern European margins (Wienberg et al., 2020). The enhanced MOW production between MIS 25 and 17 is likely the result of progressively smaller amplitudes of the precessional cycle associated with the transition towards the minimum of the ~2.4 Myr eccentricity cycle from ~930 ka onwards (Fig. 7.5D). Low eccentricity reduced precession amplitudes and weakened the African Monsoon, and thus favored conditions ideally suited to sustain strong intermediate water formation (LIW) in the eastern Mediterranean. This, in turn, would have kept the deep thermocline in the subtropical North Atlantic relatively warm even during times of decreasing atmospheric pCO_2 (Hönisch et al., 2009) and global surface-water cooling (McClymont et al., 2013). Increased subsurface heat advection to the SPG, counteracting surface cooling, would have led to weaker thermocline stratification in the central and northeastern North Atlantic, thus, creating a subsurface channel for latitudinal heat transport via the deep thermocline.

7.5.5 Implications: impact of the subsurface heat channel on ice-sheet growth

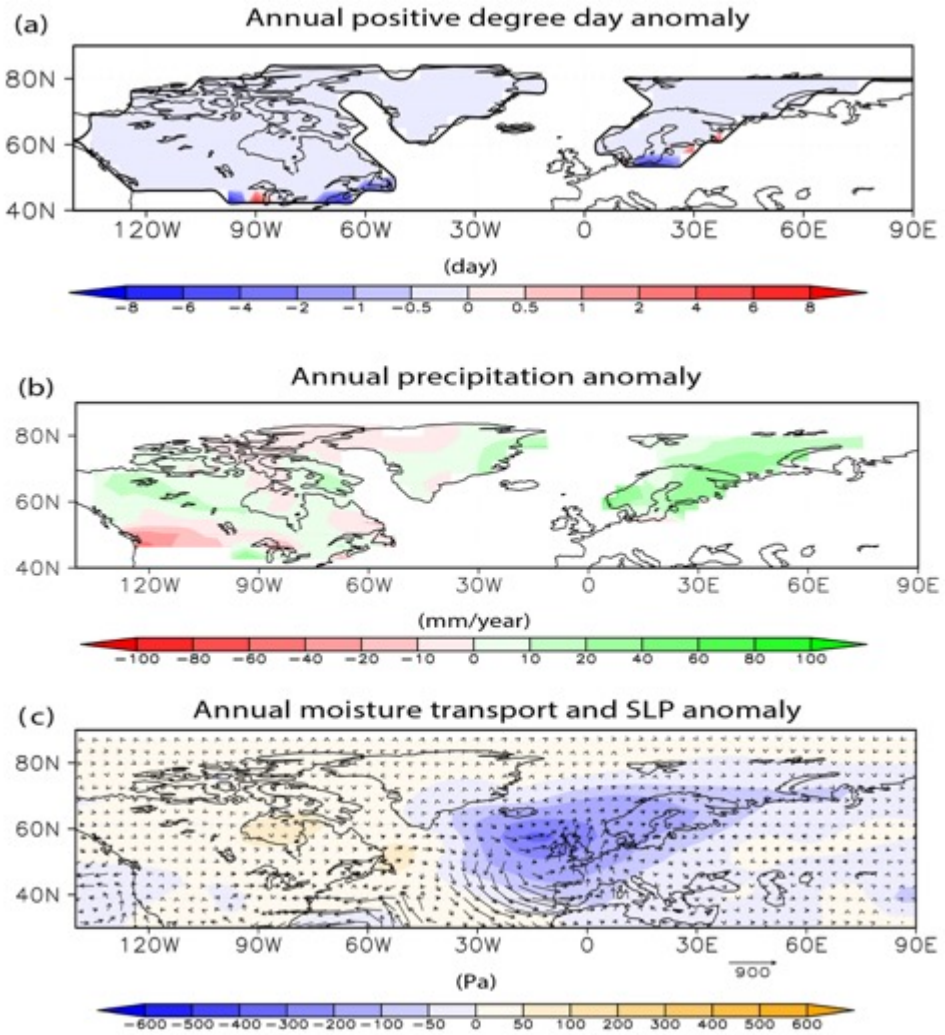

Figure 7.8. Changes in (A) simulated changes in the annual mean positive degree days (units: day), (B) the annual mean precipitation (units: mm/year), (C) sea-level pressure (SLP, shaded, units: Pa), and vertical integrated moisture transport (vector, units: kg.m^{-1}.s^{-1}) in response to sea-surface warming in the northeastern North Atlantic in the climate model (Figure 7.2).

Subsurface transport of warm waters to the eastern SPG has the potential to impact the adjacent ice sheets. During glacial stages with intermediate-sized ice sheets, warming of the eastern SPG could provide the moisture necessary for promoting ice-sheet build up. To evaluate if the anomalously strong subsurface heat transport into the high latitudes during the MPT could provide additional moisture and thus enhance NH ice-sheet growth, two glacial simulations with an atmospheric global-circulation model were conducted by Dr. Xu Zhang (Lanzhou University). The initial settings of both control (A_CTL) and experiment (A_WARM) simulations reflected intermediate glacial conditions with global ice-sheet volumes consistent with pre-MIS 22 glaciations (~65 m sea level equivalent, Chapter 7.3.3 and Figure 7.2; Zhang et al. 2014). The experiment run was forced with a 2°C higher mean SST at NENA. This 2°C warming is the average SST difference at Site 982 between the glacial interval with lowest net northward heat transport (MIS 26; ~11°C, Lawrence et al., 2010) and

the glacial with maximum subsurface warming and maximum northward heat transport (MIS 22; ~13°C). According to the model output, warming of the subpolar North Atlantic by 2°C during intermediate glacial conditions boosts atmospheric absolute humidity and stimulates a low-pressure anomaly across the NENA (Figure 7.8C). This, in turn, leads to enhanced moisture transport and a salient increase in annual mean precipitation over the Eurasian Ice Sheets (Figure 7.8B) without evident changes in ice-sheet surface melting (Figure 7.8A). Based on this precipitation increase, the model output suggests that SST warming in the NENA would have led to at least the equivalent of a 3 meter rise in sea level of additional ice-volume growth. This is a conservative estimate because ice-sheet volumes were fixed in these simulations.

The increased northward subsurface heat transport against the cold atmospheric background associated with decreased glacial atmospheric pCO_2 (Hönisch et al., 2009) and intermediate-sized ice sheets ultimately provided a potent moisture source, as evidenced by model results, and acted as an amplifier for NH ice-sheet growth over the strongly eroded regolith (Clark et al., 2006; Clark and Pollard, 1998). The resultant ice-sheet enlargement may have helped the cryosphere system to cross the critical threshold that enabled the full establishment of the large Late Pleistocene ice sheets after ~700 ka BP.

7.6 Conclusions

Vertical temperature gradients between the surface and the deep thermocline in the mid-latitude North Atlantic may be used to assess the influence of MOW in the upper water column and to develop a new precession-paced mechanism for the subsurface transport of warm waters to the eastern SPG during the MPT. Strong outflow from the Mediterranean Sea during the MPT deepened the thermocline in subtropical North Atlantic and led to the return of the northward branch of the MOW to the eastern SPG, connecting the gyres along density layers. Increased inter-gyre connectivity allowed for the advection of warm waters to the NENA at a time of presumably lower atmospheric temperatures, due to decreased glacial atmospheric pCO_2 (Hönisch et al., 2009) and global sea-surface cooling (McClymont et al., 2013). During glacial stages with intermediate-sized ice-sheets, a warming of the eastern SPG could have provided the moisture necessary to promote precipitation over the downstream ice-sheets, particularly the European Ice Sheets. As the advection of subtropical waters into the North Atlantic was essentially driven by orbital precession via the MOW, the combination of both the intrinsic obliquity forcing of ice-sheet feedbacks (Imbrie et al., 1993) and the precession-paced changes in North Atlantic stratification might explain the average 100-kyr cyclicity that characterizes the post-MPT world (Feng and Bailer-Jones, 2015).

8 Modulation of North Atlantic upper ocean circulation by the interplay between oceanic heat transport and the cryosphere across the Mid-Pleistocene Transition

8.1 Introduction

Ocean circulation during glacial stages of the Late Pleistocene was drastically different from modern ocean circulation and was characterized by the development of a strong chemocline between the upper and lower northern sourced waters (NSW; Oppo and Lehman, 1993). Contrasting ventilation conditions in the upper and lower waters have been classically attributed to a shoaling of the North Atlantic's overturning cell (Gebbie, 2014) or enhanced formation of upper NSW relative to lower NSW (Oppo and Lehman, 1993). Shoaled NSW are classically termed Glacial North Atlantic Intermediate Water (GNAIW) and has been characterized by low-nutrient concentrations and high-$\delta^{13}C$ (Boyle and Keigwin, 1987; Zahn et al., 1987; Oppo and Lehman, 1993), similar to the modern NADW. The shoaling of NSW would have resulted in a poorly ventilated ocean below ~2500 m water depth which then allowed for the accumulation of "light" remineralized carbon on the sea floor of the North Atlantic during glacial stages (Gebbie, 2014). Glacial $\delta^{13}C$ minima occurred in the deep North Atlantic during the MPT (in particular during MIS 24 and 22) and have been associated with the abrupt drawdown of atmospheric carbon during this interval, which facilitated the enlargement of polar ice caps and fostered the prolongation of glacial stages of the Late Pleistocene (Chalk, 2019; Farmer 2019). Therefore, the shoaling of the northern overturning cell (i.e., the formation of GNAIW) is considered a critical aspect of the Late Pleistocene glacial stages and is linked to the evolution of the Northern Hemisphere cryosphere through CO_2 feedbacks.

Despite its relevance, little is known about the characteristics and evolution of upper NSW during glacial stages and the origins of GNAIW are still controversial (Sarnthein et al., 1994). Suggested sources for GNAIW formation include subtropical thermocline waters through rapid, open ocean circulation (Boyle and Keigwin, 1987), subpolar northeastern Atlantic (Veum et al., 1992; Oppo and Lehman, 1993), and Mediterranean Sea Outflow (Zahn et al., 1987), but a consensus has not yet been reached. Here, the changing ocean circulation patterns associated with the dramatic decrease in deep water ventilation during the MPT were assessed using planktic and benthic stable isotope records from Site U1313 and subpolar North Atlantic. The thermocline of the North Atlantic is the passageway which transports subtropical waters upstream to undergo overturning and become components of NADW. Additionally, since the dwelling level of *G. crassaformis* is the pycnocline (i.e., the interface between upper and intermediate water masses), changes in the characteristic

of upper NADW may have been recorded in the test of this foraminifera. In Chapter 8.3.1, the *G. crassaformis* $\delta^{13}C$ record of the deep-thermocline was compared to *C, wuellerstorfi* $\delta^{13}C$ from sediment cores in northeastern North Atlantic that tracked upper and lower NSW during the MPT to assess how deep-thermocline waters may have responded to or recorded glacial-interglacial variability. Controlled culture investigations on the fractionation of carbon isotopes in *G. crassaformis* are few, but suggest that the $\delta^{13}C$ of this species is not biased by species specific vital effects (Ravelo & Fairbanks, 1995). To then reconstruct upper ocean circulation patterns during the study interval, in Chapter 8.3.2, the $\delta^{18}O$ gradients between *G. crassaformis* Site U1313 and *C. wuellerstorfi* from Site 982 (the benchmark location for monitoring the GNAIW; Venz et al., 1999) were interpreted as density gradients. As oceanographic flows are directed primarily along isopycnals, low density and $\delta^{18}O$ gradients may indicate where isopycnals passing through the deep thermocline outcropped and thus, the direction of flow during glacial and interglacial stages between MIS 36 and 14. Together, carbon and oxygen isotopes from the deep thermocline recorded upper ocean circulation patterns during the MPT and traced the origins of GNAIW.

8.2 Results

The oxygen isotopic signature of *G. crassaformis* ($\delta^{18}O_{crass}$, Figure 8.2A, purple) varied between 3.6 and 1.6 ‰, broadly in parallel with the *C. wuellerstorfi* benthic $\delta^{18}O$ ($\delta^{18}O_{cibis}$) record from the same site (Figure 8.2A, pink). This epibenthic species is believed to calcify its test in equilibrium with sea water oxygen (Bemis et al., 1998, Marchitto et al., 2014, Zahn et a., 1986), thus for the purpose of this study $\delta^{18}O_{cibis}$ was not corrected (as it was done for the updating the age model for Site U1313 in Chapter 4.3.3). Both $\delta^{18}O_{crass}$ and $\delta^{18}O_{cibis}$ display pronounced glacial-interglacial cyclicity, with increased amplitude and glacial length from MIS 21 onwards. Interglacial $\delta^{18}O_{crass}$ after MIS 21 was consistent with the modern value of $\delta^{18}O_{crass}$ (1.88‰), obtained from the uppermost samples available from Site U1313 (dated ca. 5 ka, Chapter 6). The modern values of $\delta^{18}O_{cibis}$ (2.74‰) and $\delta^{13}C_{cibis}$ (0.95‰) were also obtained from core-top samples from Site U1313 (Jakob, not published).

Stable carbon isotopes from the benthic foraminifera *C. wuellerstorfi* ($\delta^{13}C_{cibis}$, Figure 8.1B, gray) show a glacial-interglacial pattern, with low values between 0 and -0.6‰ during glacials and high values approaching those of modern NADW during interglacials (~1‰, Schmittner et al., 2013) Stable carbon isotope values of *G. crassaformis* ($\delta^{13}C_{crass}$, Figure 8.1B, orange) were stable relative to $\delta^{13}C_{cibis}$ and averaged 1.04‰ between MIS 36 and MIS 14, also similar to the modern $\delta^{13}C$ of NADW {Schmittner:2013hq}. Throughout the record, sharp $\delta^{13}C_{crass}$ decreases of up to 0.6‰ marked glacial to interglacial transitions in the oxygen isotope records.

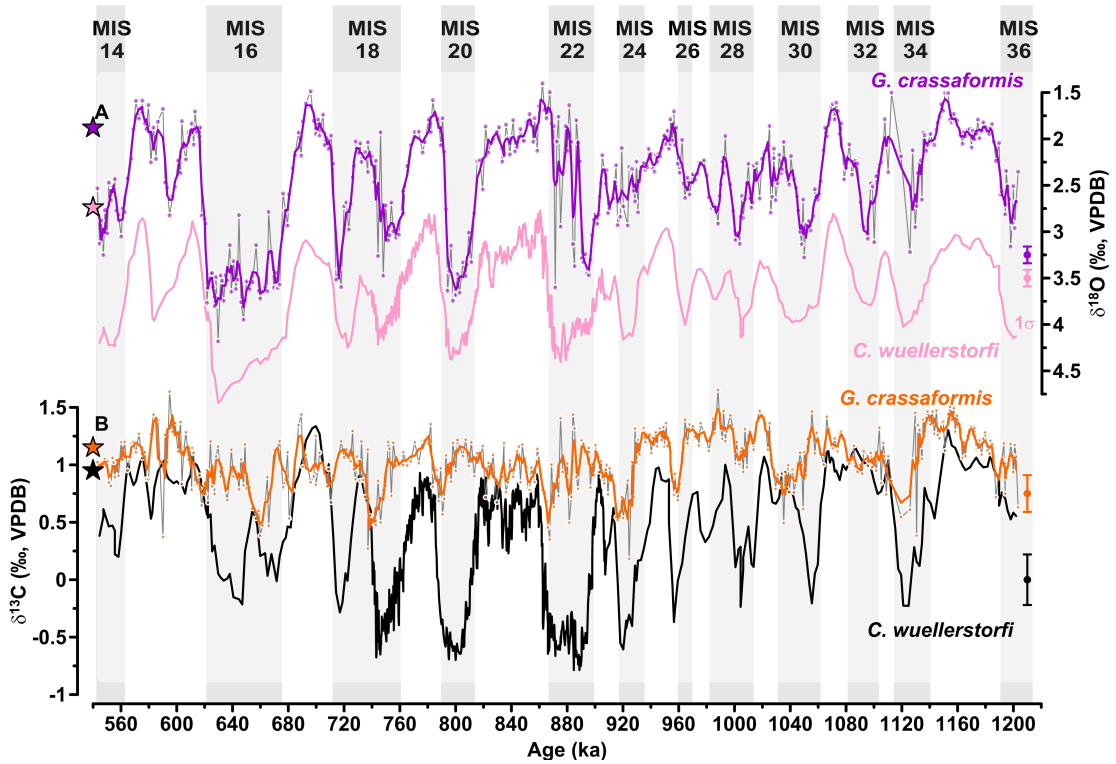

Figure 8.1. Stable isotope records from the deep thermocline and bottom water at Site U1313 spanning the interval between MIS 36 and MIS 14. Stars show modern values for the respective datasets and the error bars to the left show one standard deviation (1σ). (A) $\delta^{18}O$ values from G. crassaformis ($\delta^{18}O_{crass}$, purple, 3pt running average) and $\delta^{18}O$ values from C. wuellerstorfi ($\delta^{18}O_{cibis}$, pink, 3pt running average; this study and Ferretti et al., 2015). (B) $\delta^{13}C$ values from C. wuellerstorfi ($\delta^{13}C_{cibis}$, black, 3pt running average; this study and Ferretti et al., 2015). Stars on the left indicate modern values for all records obtained either from core-top samples in the case of C. wullerstorfi (Jakob, not published) or from the top most sample of the first section of Site U1313, in the case of G. crassaformis (this study). Original data points are marked as circles for stable isotopes of G. crassaformis. Cold Marine Isotope Stages (MIS) are indicated as light gray rectangles according to Lisiecki and Raymo (2005).

8.3 Discussion

8.3.1 Was the deep-water ventilation in the North Atlantic controlled by deep water formation in the Nordic Seas or around Antarctica?

To assess the relationship between deep thermocline records and GNAIW $\delta^{13}C_{crass}$ was compared to the $\delta^{13}C$ of the epibenthic foraminifera *C. wuellerstorfi* from Site 982 (982- $\delta^{13}C_{Cw}$, 16°W, 58°N, 1145 m, Figure 8.3A; Raymo et al., 2004, Venz et al., 1999), considered the benchmark site for the characterization of intermediate waters in the subpolar North Atlantic. Site 982 is located eastwards of Site 984, at the Rockall Bank, and bathed mainly by LSW with a secondary influence of the MOW's northward branch (Figure 8.2). The general matching values of $\delta^{13}C_{crass}$ and 982-$\delta^{13}C_{Cw}$ support the assumption that deep thermocline waters were under the domain of

upper NSW, thus records based on *G. crassaformis* could serve as a monitor of GNAIW (Figure 8.3A).

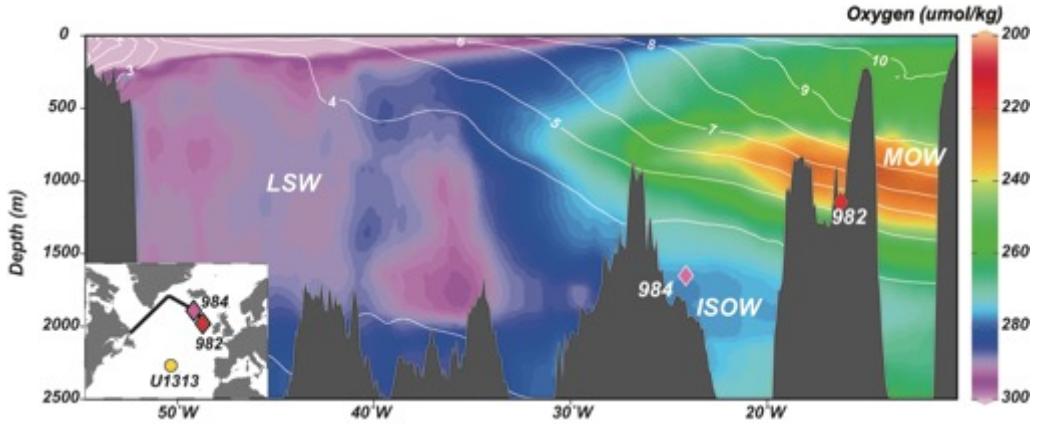

Figure 8.2. Longitudinal section across the main loci of deep- and intermediate- mass formation in the SPG. Colors show oxygen concentration, superposed by isotherms. Sites 984 and 982 are referred in the text and the main water masses in this section are marked by their acronyms: LSW (Labrador Sea Water), MOW (Mediterranean Outflow Water) and ISOW (Iceland-Scotland Overflow). Figure prepared using the software Ocean Data View with data from the World Ocean Atlas 2018 (Locarnini et al., 2019).

The concept of glacial shoaling of NSW (i.e., GNAIW formation) arose due to low deep-water ventilation in the Atlantic Ocean below approx. 2000 m water depth, as indicated by the consistently low $\delta^{13}C$ of benthic foraminifera in the Atlantic Ocean during glacial stages ($\delta^{13}O_{cibis}$, Figure 8.3B; Raymo, 1997). Progressive depletion in benthic $\delta^{13}C$ during glacial stages have been classically interpreted as northward excursions of southern-sourced waters (SSW) either as a compensatory mechanism due to due to sluggish formation of lower NSW (i.e., NSOW) or increased deep-water formation around Antarctica. However, the increased contribution of deep-water formation in the Nordic Seas or in the Southern Ocean to deep ocean ventilation (and the shoaling of NSW to form GNAIW) have been questioned based on two lines of evidence.

A compilation of vertical $\delta^{13}C$ profiles from deep cores located at the northeastern North Atlantic (NENA) showed that during the MPT and at least until MIS 16, the relative volumetric importance of water originating in the Nordic Seas versus the Labrador Sea did not change significantly from glacial to interglacial stages. The carbon and oxygen isotopic composition of NSOW was stable across glacial-interglacial intervals and formed a plume of low $\delta^{13}C$ (~0.2‰) and relatively high $\delta^{18}O$ water at NENA centered at ~1500 m water depth and extending downwards to at least ~2500m (Raymo et al., 2004). The persistent low $\delta^{13}C$ of NSOW during the early-mid- Pleistocene led to the interpretation that the Nordic Seas were mostly covered by sea ice, which is supported by the lack of carbonate preservation within the basin between 2.8 and 0.5 Ma (Kellogg, 1980; Baumann & Huber, 1999). Perennial sea-ice cover would have suppressed surface water productivity, convection and deep-water ventilation, leading to the accumulation of low-$\delta^{13}C$ and preformed nutrient-rich waters in this basin. Episodic inflow of warm Atlantic waters may have contributed to

further decreasing NSOW's $\delta^{13}C$ by leading to gas hydrate instability and local methane seeping under glacial lower sea-level conditions (Millo et al., 2005). Thus, the Nordic Seas was an endogenous source of low-$\delta^{13}C$ waters to the North Atlantic during glacial stages (Bauch et al., 2001; Raymo et al., 2004). The low $\delta^{13}C$ signature from the Nordic Seas has been detected on samples from Site 984 (61°N, 24°W, 1650 m water depth), nowadays located along the pathway of ISOW. This water mass is a significant component of NEADW and low-$\delta^{13}C$ values from Site 984 correspond to the glacial $\delta^{13}C_{cibis}$ at Site U1313 between MIS 36 to 25 and the end of MIS 16 (Figure 8.3B), suggesting that Site U1313 was already bathed by the glacial equivalent of ISOW during glacials before the MIS 25. Nevertheless, as $\delta^{13}C$ of Site 984, was equally low during glacials and interglacials, the role of ISOW in ventilating the deep North Atlantic before MIS 25, must have been secondary to another source of well-ventilated deep waters. As NSOW (mainly ISOW) is considered the main component of lower NSW at present (Chapter 2.1.3), their passive role to deep waters ventilation before the MPT was surprising (Raymo et al., 2004).

It has also been suggested that the decrease in deep ocean ventilation in the North Atlantic may be related to increased deep-water formation around Antarctica (Raymo et al., 2004, Pena & Goldstein, 2014), particularly during the MPT. Southern-sourced Waters are denser than NSW and are thus capable of displacing the entire water column upward. Increased formation of deep SSW relative to NSW was inferred as a mechanism for the glacial shoaling of NSW based on the relatively radiogenic εNd of sediments in the Southern Ocean during the "900-kyr event" (MIS 24 to 22; Pena and Goldstein, 2014). However, this model conflicts with the new evidence regarding the effects of extensive ice-sheet cover over the εNd-end member of NSW during glacial stages (see Chapter 6; Zhao et al., 2019). Specifically, the relatively radiogenic NSW signal found at southern sites during glacial stages after MIS 24 (and interglacial MIS 23) could also be argued to be a consequence of ice-sheet enlargement in the northern hemisphere and decreased contribution of unradiogenic weathering sediments to NSW during glacial stages after MIS 24 (Tachikawa et al., 2021). Tachikawa et al. (2021) produced a εNd record from 3400 m water depth in the eastern North Atlantic, which showed that during MIS 24 and 22 εNd-signature of deep waters were still reflective of NSW, albeit with a more radiogenic endmember (~-10.5), similar to LGM values (Chapter 6; Pöppelmeier et al., 2020, Zhao et al., 2019). Based also on model results, Tachikawa et al. (2021) suggested that the low glacial $\delta^{13}C$ and radiogenic εNd of Atlantic waters below 2000 m water depth in the North Atlantic is consistent with the combination of a weak overturning circulation in the Atlantic, and increased ice-sheet cover of the European and North American landmasses during mid-MPT glacial stages. Consequently, deep-water ventilation in the North Atlantic during the MPT was likely a result of interactions between the cryosphere and deep-water formation in the North Atlantic but outside of the Nordic Seas. Thus, the appearance of GNAIW during glacial stages after MIS 25 was more likely dependent on overturning

variability at other sites of deep-water mass formation, such as the Iceland and Irminger basins.

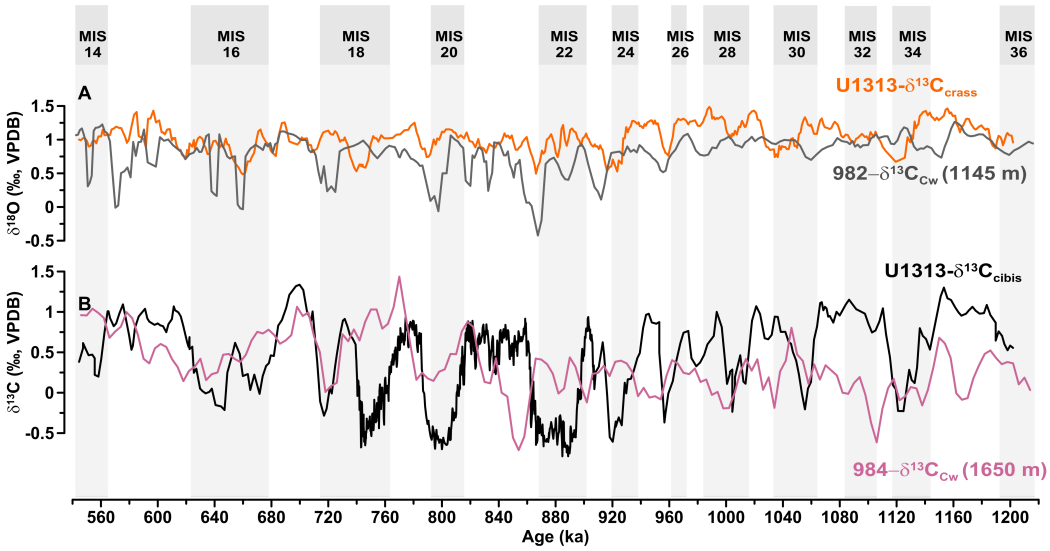

Figure 8.3. (A) $\delta^{13}C$ values from C. wuellerstorfi at Site U1313 ($\delta^{13}C_{cibis}$, black, 3pt running average; this study and Ferretti et al., 2015) and at Site 984 (984-$\delta^{13}C_{Cw}$, pink, 3pt running average, Raymo et al., 2004). (B) $\delta^{13}C$ values from G. crassaformis from Site U1313 ($\delta^{13}C_{crass}$, orange, 3pt running average; this study) and at Site 982 (982-$\delta^{13}C_{Cw}$, pink, 3pt running average, Raymo et al., 2004). Cold Marine Isotope Stages (MIS) are indicated as light gray rectangles according to Lisiecki and Raymo (2005).

8.3.2 Assessing the variability in upper NSW based on isopycnal connectivity with the deep thermocline of Site U1313

Oceanographic flows are directed primarily along isopycnals and their outcropping location indicate the geographical location where subsurface waters exchange properties with the atmosphere and therefore density records can be used to infer circulatory pathways in the upper ocean. To establish the baseline upper ocean circulation during glacial and interglacial stages during the MPT, $\delta^{18}O$ of *G. crassaformis* was first compared to the upper ocean $\delta^{18}O$ signature of the northeastern North Atlantic (Figure 8.4). The $\delta^{18}O$ of surface waters above Site 982 is available until 1 Ma from a record based on *Globorotalia bulloides* ($\delta^{18}O_{Gb}$, 16°N, 58°W, 1145 m water depth; Venz et al., 1999). This species has been shown to calcify in in equilibrium with the oxygen composition of the upper 200 m of the water column in a monitoring study done with samples collected from the northern North Atlantic (Irminger Sea; Jonkers et al., 2013). The deep thermocline of Site U1313 is currently occupied by North Atlantic central waters entrained by the MOW (Chapter 5) and intercepts density layers that occupy similar depths (approx. 800 m) in the northeastern North Atlantic. There, these density layers bend steeply upwards in response to convection driven by oceanic heat loss (Ferrari et al., 2014) and enter the Nordic Seas. Thus, a modern-like upper ocean circulation pattern should imply a relatively warm deep thermocline in the mid-latitudes and low $\delta^{18}O$ gradients between *G. crassaformis* and upper ocean dwelling foraminifera of above Site 982. This scenario occurred

during MIS 25 (Figure 8.5). During all other warm phases (until 1 Ma), matching $\delta^{18}O_{Gb}$ and $\delta^{18}O_{crass}$ and high T_{crass} suggest that waters from the deep thermocline of the central North Atlantic upwelled in the NENA (interglacials MIS 15, 17, 19 and 21 and during a warm interval of MIS 18, Figure 8.5).

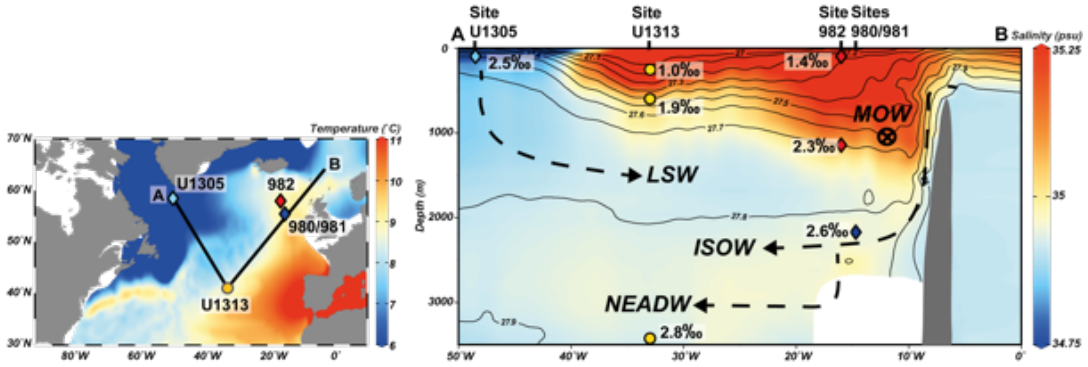

Figure 8.5. (Left panel) Temperature distribution at the density level σ_0=27.45, that intersects Site U1313 at 800 m water depth, and location of sites discussed within the text. (Right panel) Salinity and density distribution along the section A-B, shown in the left panel. Longitude of sites U1305, U1313, 982 and 980/981 are marked above the panel. Blue diamond marks the dwelling depth of N. pachyderma (upper 200 m, Jonkers et al., 2013). Yellow circles mark the dwelling depth of G. crassaformis above Site U1313 (~800 m water depth, Cléroux et al. 2013) and the corresponding depth of the record based on C. wuellerstorfi (3426 m water depth, Expedition 306 Scientists, 2006). Red diamonds mark the depth correspondent to the records from Site 982, based on G. bulloides (upper 200 m; Jonkers et al., 2013) and C. wuellerstorfi (1145 m water depth, Jansen et al., 1996). Dark blue diamond marks the depth of sites 980 and 981, records based on C. wuellerstorfi of these sites were spliced to generate the record referred as of Site 980/981 (2171 m water depth, Jansen et al.. 1996, Raymo et al., 2004). Black numbers marked close to diamonds and circles refer to the youngest $\delta^{18}O$ values available from each record (Hillaire-Marcel et al., 2011, Jakob, not published, this study, Raymo et al., 2004, Venz et al., 1999).

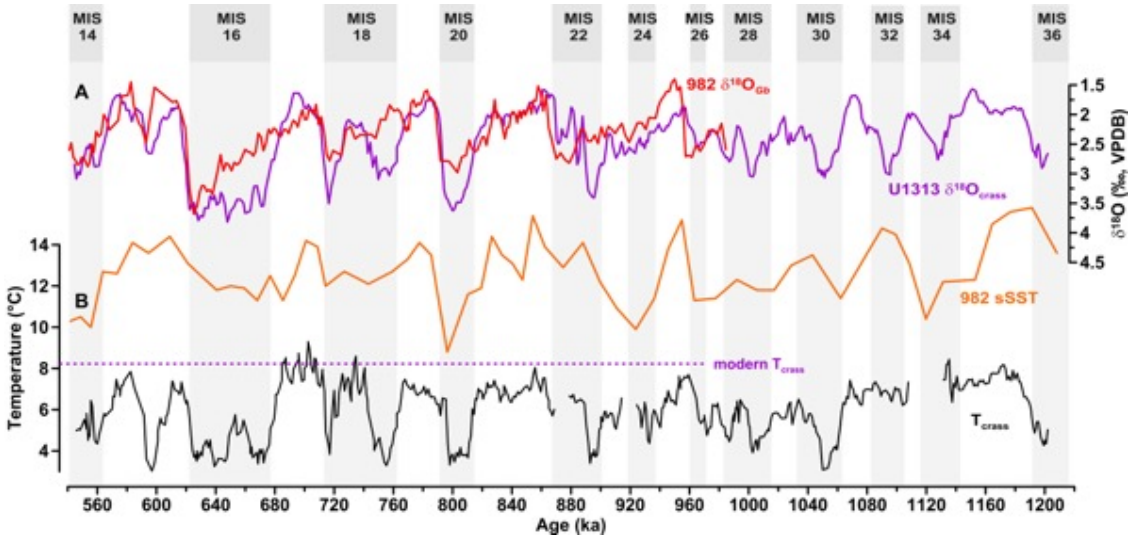

Figure 8.5. (A) Stable oxygen isotope ratios from G. crassaformis at Site U1313 (purple, 3pt running average) and G. bulloides at Site 982 (red, Venz et al., 1999). (B) Mg/Ca-based subsurface temperatures from G. crassaformis at Site U1313 (T_{crass}, black, 3pt running average) and alkenone-based summer SSTs at Site 982 (orange, Lawrence et al., 2010). Purple dashed line marks the modern subsurface temperature at the deep thermocline of Site U1313 (8.1 ℃, Locarnini et al., 2019). Light gray bars denote cold Marine Isotopic Stages (Lisiecki and Raymo, 2005).

The second half of MIS 22 was exceptional, with lower $\delta^{18}O_{crass}$ than $\delta^{18}O_{Gb}$ indicating that surface waters at Site 982 occupied denser isopycnals than the ones intercepting the dwelling depth of *G. crassaformis* in the mid latitudes. As this occurred while SSTs at the northern site were warm and thermocline at Site U1313 was deep (Chapter 7), the 0.64‰ difference between the two records between 884 ka and 870 ka indicates that the surface of Site 982 was occupied by relatively saline waters that were transported northwards via density layers located below the dwelling depth of *G. crassaformis*. Together, the comparisons between the SST, T_{crass} and $\delta^{18}O$ records from sites 982 and U1313 corroborate the scenario delineated by Kaiser et al. (2019) and discussed in Chapter 7 for the second half of MIS 22. Given that it was a glacial stage, the second half of MIS 22 was marked by an anomalous northward advection of subtropical waters to NENA, via deep density layers and due to the outpour of MOW from the Gulf of Cadiz (Chapter 7).

Interestingly, after MIS 25 high gradients between $\delta^{18}O_{crass}$ and $\delta^{18}O_{Gb}$ occurred during periods in which the deep thermocline was markedly cold (early MIS 22, MIS 20, early and late MIS 18, and MIS 16), indicating that density layers intercepting the deep thermocline contained denser (colder and/or saltier) waters than the surface layer above Site 982. During these intervals, density layers crossing the deep thermocline at Site U1313 would have either outcropped northwards of Site 982 (e.g. in the Nordic Seas) or were influenced by waters that interacted with the atmosphere near the Labrador Sea. To trace changes in the geographical source of water masses occupying the central North Atlantic, $\delta^{18}O_{crass}$ (Site U1313) was then compared to $\delta^{18}O$ of the upper thermocline dweller *Neogloboquadrina pachyderma* from Site U1305 ($\delta^{18}O_{Np}$, 58.5°N, 48.5°W, {HillaireMarcel:2011cb}), located southeastwards of Greenland within the downwelling zone of LSW. The lack of species-specific offsets of this species in regard to its oxygen isotope signature was validated by Jonkers et al. (2013) using samples collected close to the location of Site U1305.

Matching $\delta^{18}O_{crass}$ and $\delta^{18}O_{Np}$ occurred episodically throughout the studied interval, but most often coincided with cold T_{crass} after MIS 23 (Figure 8.6; early MIS 22, MIS 20, late MIS 18, early MIS 16 and mid MIS 15). Matching $\delta^{18}O_{crass}$, $\delta^{18}O_{Np}$ and low T_{crass} is a robust indicator that intermediate waters that occupied the deep thermocline during those post-MIS 23 glacial stages were very similar to the modern LSW. Periods of matching $\delta^{18}O_{crass}$, $\delta^{18}O_{Np}$ and warm T_{crass} occurred only during interglacials after MIS 30. The prolonged phase of overlap between $\delta^{18}O_{crass}$ and $\delta^{18}O_{Np}$ during MIS 31, 32 and 34, when deep-thermocline waters were warm, indicates that surface waters in northwestern North Atlantic were also warm during those intervals even though MIS 32 and 34 were glacial stages. As the northward branch of the MOW did not extend northwards before ca. 1 Ma (Kano et al., 2007) and the

northern ice sheets were still intermediate in size, it is possible that the warm surface in northwestern North Atlantic was the *status quo* before the MPT.

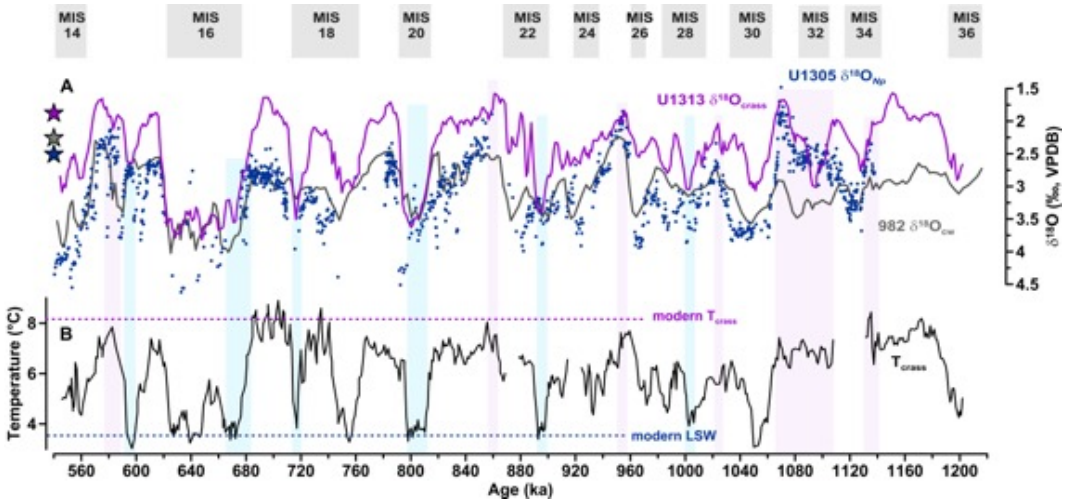

Figure 8.6. (A) Stable oxygen isotope ratios from G. crassaformis at Site U1313 (purple, 3pt running average), N. pachyderma from Site 1305 (dark blue dotsHillaire-Marcel, 2011) and C. wuellerstorfi from Site 982 (blue, 3pt running mean, Venz et al., 1999, Raymo et al., 2004). (B) Mg/Ca-based subsurface temperatures from G. crassaformis at Site U1313 (T_{crass}, green, 3pt running average). Blue dashed line marks modern temperature of LSW (3.5 ℃, Talley and McCartney, 1982). Blue bars mark periods of low T_{crass} (panel B) and coincident $\delta^{18}O_{crass}$, 982-$\delta^{18}O_{cibis}$ and U1305- $\delta^{18}O_{pachy}$ (panel A). Light gray bars denote cold Marine Isotopic Stages (Lisiecki and Raymo, 2005).

The significance of the interplay between of subpolar and subtropical waters for the characterization of GNAIW is clarified by analyzing the oxygen composition of *N. pachyderma* and *G. crassaformis* in comparison with the $\delta^{18}O$ of the epibenthic foraminifera *C. wuellerstorfi* from Site 982 (Figure 8.6, $\delta^{18}O_{cw}$; Venz, 1999, Raymo, 2004). At 1145 m water depth, *C. wuellerstorfi* from Site 982 were permanently bathed by upper NSW/GNAIW (Venz et al., 1999). The comparison between $\delta^{18}O_{cw}$ at Site 982 and $\delta^{18}O_{Np}$ of Site U1305 (a planktic and a benthic) is justified based on the current hydrography of LSW and density distribution in the northern North Atlantic (Figure 8.4). In its modern state, the role of overturning (i.e., sea-water densification) to the formation of LSW is secondary to Eulerian downwelling (e.g., Georgiou et al., 2019, Lozier et al., 2019). The formation of deep waters that sink westward of Greenland to form LSW take place upstream, in the Irminger Sea and Iceland Basin. Densified waters (i.e., deep waters) then flow westward and sink into the water column maintaining their density characteristics, that afterward change only via mixing. Thus, in settings similar to the modern, the density of waters at the surface of Site U1305 is quasi-conservative and stable until LSW is not mixed with other water masses, which occurs eastwards by entrainment of ISOW and northern MOW and southwards upon the encounter with MOW's westward branch (Chapters 2 and 5, Talley et al., 2011). After sinking LSW occupies between 1000 m and 2000 m in the SPG and is the dominant water mass bathing the sea floor over Site 982 (Figure 8.7). Thus, matching values of $\delta^{18}O_{cw}$ and $\delta^{18}O_{Np}$ indicate that Site 982 was occupied by LSW-like waters, originated in northwestward North Atlantic.

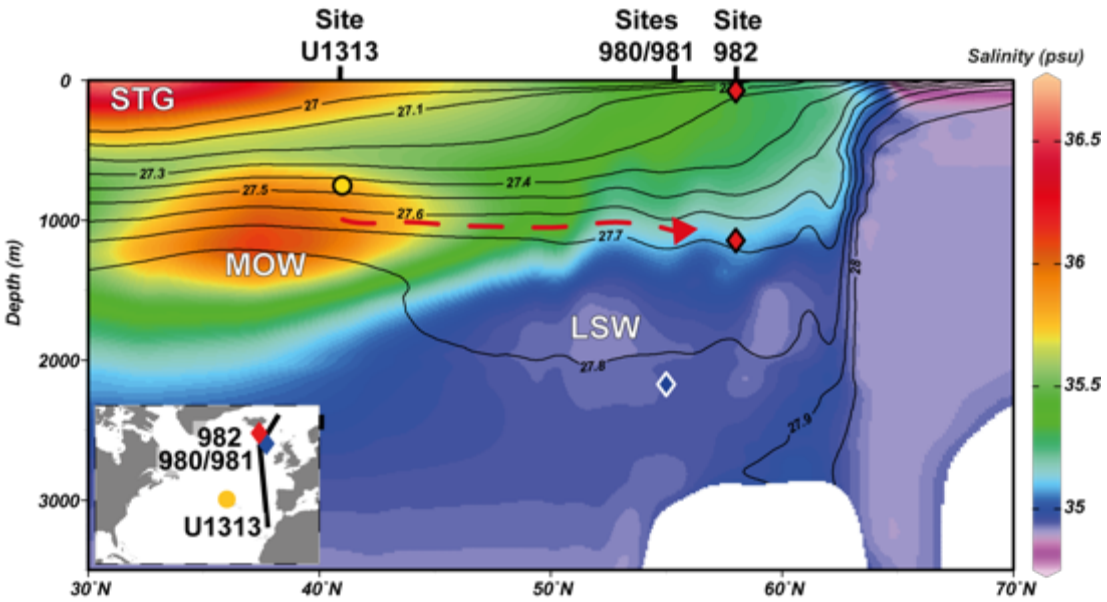

Figure 8.7. Salinity and density distribution along a latitudinal transect connecting the Gulf of Cadiz and the Nordic Seas. Location and depth of records discussed in the text are marked as symbols.

Based the above description, the comparison of $\delta^{18}O$ records shows that ocean circulation in the SPG during MIS 34, 32 and 31 was indeed markedly different from modern ocean circulation. $\delta^{18}O$ at the surface of Site U1305 coincided with $\delta^{18}O_{crass}$, showing that deep-thermocline waters above Site U1313 interacted with the atmosphere in the northwestern North Atlantic. As both $\delta^{18}O_{crass}$ and $\delta^{18}O_{Np}$ were up to 1.3‰ lower than $\delta^{18}O_{cw}$, it's robust to interpret that during these stages, the *loci* of deep-water formation were distributed differently in the SPG (e.g., overturning may have taken in the Labrador Seas). Unfortunately, lack of data from the surface of the NENA, prevents further conclusions. Commencing with MIS 30, matching $\delta^{18}O_{Np}$ and $\delta^{18}O_{cw}$ indicate that the Labrador Sea became a *locus* of intermediate mass downwelling and continued to be so during most of the studied time interval, without distinction between glacials or interglacials. Furthermore, matching $\delta^{18}O_{crass}$ and $\delta^{18}O_{cw}$ (and cold T_{crass}) show that especially after the MPT (MIS 22, MIS 20, early and late MIS 18 and MIS 16) GNAIW reached deep-thermocline waters at mid-latitudes episodically during glacial stages. It had similar temperature and origin as the modern LSW and was also subjected to heat transport from the MOW (e.g., mid-MIS 16, Figure 8.8). During interglacial stages the deep thermocline records show that LSW was mixed with MOW, forming upper NADW.

The fact that the Labrador Sea became a *locus* of intermediate mass downwelling and continued to be so without distinction between glacials or interglacials from MIS 30 onwards (i.e., matching $\delta^{18}O_{cw}$ at Site 982 and $\delta^{18}O_{Np}$ of Site U1305, Figure 8.6) suggests the that deep-ocean ventilation was also not dependent on downwelling in northwestern North Atlantic. Rather, the data suggests that upper-ocean circulation and deep-ocean ventilation are dependent on the strength of the meridional flux of subtropical waters to northeastern North Atlantic. The variability pattern of $\delta^{13}C_{cibis}$ at Site U1313 is the most similar to that of deep-thermocline temperatures at the same

site (T_{crass}, Figure 8.8). Both records were generated from the same samples, so there's no chronostratigraphic uncertainty between them. The rise in deep-thermocline temperatures at the end of glacial stages preceded the rise in benthic $\delta^{13}C$ at the same site between MIS 25 and 18, indicating that increased northward heat transport preceded the rise in deep-water ventilation. This observation is coherent with the suggestion that overturning is mainly responsive to upper ocean property changes instead of their driver (Lozier et al., 2010). By extension, as upper ocean properties in northeastern North Atlantic reflect the shoaling and extension of the northward MOW branch to the Rockall Trough (Chapter 5), the arrival of subtropical waters to that region may be intrinsically connected to deep-water mass formation in the North Atlantic.

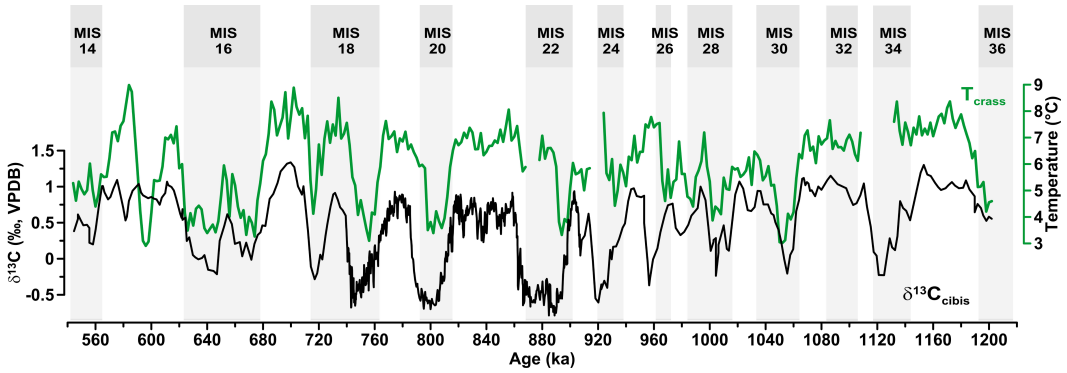

Figure 8.8. Mg/Ca-based subsurface temperatures from G. crassaformis *at Site U1313 (green, 3pt running average) and stable carbon isotope ratios of* C. wuellerstorfi *from Site U1313 (black, 3pt running average).*

9 Conclusions and outlook

In the framework of this thesis, materials from deep-sea sediment cores of IODP Site U1313 were investigated. New proxy records of stable isotopes ($\delta^{18}O$ and $\delta^{13}C$) and Mg/Ca ratios were generated from planktic and benthic foraminiferal tests from the time intervals 5–30 ka (Last Glacial Maximum, LGM, and Termination I, TI) and 540–1200 ka (Mid-Pleistocene Transition). This final chapter summarizes research results and discussions of Chapters 6 to 8 and explores the main conclusions of the research presented in this thesis. In the outlook, implications of this work are discussed in a societal context and future work to refine scientific understanding on the topics here discussed are suggested.

9.1 Conclusion

The first question addressed in this thesis concerned the dynamics of northward heat transport in the North Atlantic during the last glacial maximum and deglaciation and its relationship with the demise of northern hemispheric ice sheets (Chapter 6). Northward heat transport between 5 and 30 ka was assessed using stable isotopes and Mg/Ca ratios to estimate temperature and salinity at the ocean's subsurface in between the subtropical and subpolar gyres. These were then compiled with all other available records from the same core site, which included the proportion of terrigenous carbonate, an indicator of the deposition of ice-rafted debris transported by icebergs. The lack of chronostratigraphic uncertainties between records of Site U1313 allowed the recognition that subsurface warming preceded peak IRD deposition at Site U1313 during Heinrich Events 1 and 2, and therefore likely contributed to ice-sheet destabilization of the European and Laurentide ice sheets during Termination I. Subsurface temperatures at Site U1313 between 17.5–15 ka (i.e., the second phase of HE1, here termed "HE1.II") were as high as sea-surface temperatures and suggest that the center of deep-water convection in the North Atlantic moved southwards to the mid latitudes. Synchronous warming at the deep thermocline of Site U1313 and in northeastern North Atlantic show that HE1 coincided and may have been triggered by the resumption of northwards heat advection via the subsurface, of which the surface expression is referred to as the North Atlantic Current. The accumulation of heat and salt at deep-thermocline levels between both gyres during the late HE1 (HE1.II) happened synchronously to the deepening of the North Atlantic overturning cell. However, the convected deep waters had a lower than modern $\delta^{13}C_{DIC}$ (~0.5 ‰), which may have prevented its identification as NADW thus far and led to the previous attribution to southern-sourced waters.

Therefore, the data produced within the context of Chapter 6 suggest that subsurface heat transport was intrinsically connected with the demise of northern hemisphere ice sheets during the end of the last glacial stage. The initial destabilization

of the European Ice Sheets began at 25 ka (Toucanne et al., 2015), 1.4 kyrs after a rise in subsurface temperatures and when northern summer insolation was close to its minimum. The destabilization of EIS, adjacent to the main sites of deep-water convection, may have hampered northward heat transport between 25 and 18 ka but also supplied freshwater to the North Atlantic, which decreased the density of upper ocean waters. After a major pulse of freshwaters to the ocean during early HE1 (i.e., "HE1.I"), meltwaters possibly entered in the Mediterranean Sea (Sierro et al., 2020), which would have decreased the density of the MOW and the Mediterranean-Atlantic density gradient. A lower density gradient across the Gulf of Cadiz would have caused the plume of warm and salty MOW to shoal, reconnecting the subtropical and subpolar gyres via density layers at the subsurface and intensifying the northward transport of heat. Nevertheless, heat release by the ocean in the subpolar gyre would have been hampered by the combined effects of the meltwater flux to the surface of the subpolar gyre and the northward advance of density-compensated subtropical waters (Haskins et al. 2020). The superposition of these two effects would have maintained the stratification in the Subpolar Gyre and favored the prolonged accumulation of heat at subsurface levels of the North Atlantic and Nordic Seas during HE1.II (Ezat et al., 2014, Marcott et al., 2011, Poggemann et al., 2019, Thiagarajan et al., 2014). The stratification in the subpolar gyre would have weakened subpolar overturning during HE1.II, but deep-water formation may have taken place by convection at mid latitudes and by the mixing of subtropical and subpolar waters at the subsurface. Deep-water formation via mixing is indeed the most likely explanation for the resumption of deep-water ventilation in the North Atlantic at 17.5 ka (onset of HE1.II). This may have had significant global impacts by driving deep upwelling in the Southern Ocean and flushing the CO_2 that was previously stored throughout the deep Atlantic and Southern oceans (Ziegler et al., 2013), in agreement with the deglacial rise in atmospheric CO_2 that has also been dated at 17.5 ka using Antarctic ice cores (Buizert et al., 2014, Marcott et al., 2014, Köhler et al., 2016).

The second question addressed in this thesis concerned potential changes in ocean circulation during the Mid-Pleistocene Transition and its relationship between the variability in northward heat transport to the glacial-interglacial cyclicity shift that occurred during this interval (Chapters 7 and 8). Northward heat transport between 540 and 1200 ka was assessed using Mg/Ca ratios of deep-dwelling foraminifera to estimate temperature at the ocean's subsurface (Chapter 7). Combined records of subsurface temperatures and stable isotopes were then used to infer the density connectivity and circulatory pathways between the subtropical and subpolar gyres (Chapter 8).

In Chapter 7, the comparison between subsurface temperatures with sea-surface temperatures produced from Site U1313 led to the conclusion that vertical temperature gradients in the upper North Atlantic Ocean at mid-latitudes may be used to assess the lateral heat advection from the Mediterranean Sea. Between Marine Isotope Stages 25 and 17 (936–676 ka), strong and sustained mixing of MOW into North Atlantic central

waters kept the deep thermocline in the subtropical North Atlantic relatively warm even during times of decreasing atmospheric pCO_2 (Hönisch et al., 2009) and global sea-surface cooling (McClymont et al., 2013). Minimum upper-ocean stratification (i.e., temperature gradients at Site U1313) occurred during MIS 24 and MIS 22, crucial stages of ice-sheet build up during the MPT (Ford and Raymo, 2019). Thus, it has been inferred that increased mixing of warm Mediterranean waters into the central waters of the North Atlantic deepened the permanent thermocline, thereby increasing northward heat advection into the SPG during the MPT. Glacial simulations in an atmospheric global circulation model indicate that strong subsurface heat transport into the high latitudes during the MPT may have contributed to ice-sheet growth in the northern hemisphere. In the model experiment, warmer SSTs in the eastern North Atlantic against a cold atmospheric background and intermediate glacial conditions (consistent with pre-MIS 22 glaciations) boosted atmospheric absolute humidity and stimulated a low-pressure anomaly across northeastern North Atlantic (Catunda et al., 2021). This in turn lead to enhanced moisture transport and a prominent increase in annual mean precipitation over the European Ice Sheets. The resultant ice-sheet enlargement may have accelerated erosion of the regolith and boosted the cryosphere system across the critical threshold that enabled the full establishment of the Late Pleistocene ice sheets after ~0.70 Ma. As the advection of subtropical waters into the North Atlantic was essentially driven by orbital precession via the MOW, the combination of the intrinsic obliquity forcing of northward heat transport via latitudinal insolation gradients (Maslin and Brierley, 2015) and the MOW-led precession-paced changes in North Atlantic stratification may have contributed to glacial-interglacial cyclicity shift of the post-MPT world (Feng and Bailer-Jones, 2015).

In Chapter 8, stable oxygen and carbon isotope data were used to reconstruct ocean circulation at intermediate levels of the North Atlantic during the MPT. These showed that *loci* of deep-water formation and dynamics of the northern-formed water masses were radically different during MIS 34–31 relative to the rest of the studied interval (MIS 30-14). Waters sinking in the Labrador Sea occupied intermediate levels of the northeastern North Atlantic commencing from MIS 30. The upward and southward shift of cold intermediate waters became a typical feature of thermocline records during glacial stages after MIS 23, possibly due to the enlargement of northern ice sheets between MIS 24 and 22. Larger northern ice sheets would have strengthened the northern westerly winds and favored the shoaling and southward shift of the cold waters from the Labrador Sea to the deep thermocline at mid-latitudes. During glacials after MIS 22, intervals of low bottom water ventilation coincided with the surfacing of Labrador Sea-like waters to the deep-thermocline, meaning that waters referred to as Glacial North Atlantic Intermediate Waters had similar temperature (3.5°C) and subducting location as modern LSW. During interglacial stages and phases in which the deep thermocline was relatively warm, LSW interacted with MOW forming upper NADW, analogously to the modern circulation patterns of intermediate levels of the North Atlantic

All datasets within this thesis provide support to the predominant role of density connectivity between the subtropical and subpolar gyres in driving heat transport northwards. The interplay between heat transport and freshwater fluxes from ice sheets would then modulate deep-water formation at high latitudes of the North Atlantic. This represents a reversal of the concept that northward heat transport is driven by overturning and testifies to the importance developing oceanic models that can resolve the effects of narrow outflows (e.g., MOW and ISOW) to large-scale ocean dynamics across time.

9.2 Outlook – The oceanic mechanisms propelling glacial-interglacial cyclicity -Potential implications and future perspectives

For decades, northward heat transport in the North Atlantic has been considered to be driven by overturning at high latitudes. However, if this was the case deep thermocline waters should have been the coldest during periods of reported weakening of the AMOC. Rather, during crucial climate transitions when freshwater from melting ice sheets stratified the upper ocean, the deep subtropical thermocline was unexpectedly warm. Similar inconsistencies have been found also on short timescales, for which continuous monitoring data of the AMOC is available (Lozier et al., 2010). These authors analyzed continuous ocean monitoring data and were puzzled by warming (cooling) of the subtropical thermocline during phases of weak (strong) overturning in the subpolar gyre. The data shown in this thesis are consistent with modern observations and model studies, which point out that northward heat transport is not driven by subpolar overturning (Levang & Schmitt, 2020).

A potential solution to understand the driving forces of northward heat transport is to consider that property transport across isopycnals is secondary to transport along density layers (Kuhlbrodt et al., 2007). In this case, as the MOW is a subsurface source of heat (Chapter 5), vertical shifts on its settling depth may modulate the temperature gradients along isopycnals outcropping in the northern North Atlantic. This mechanism requires numerical confirmation, which may be done by varying the settling depth of the MOW in an eddy permitting ocean model with fixed atmospheric conditions and tracking temperature variability in the surface and subsurface of the subpolar gyre. If true, shoaling (deepening) of the MOW would connect the surface of the SPG to warmer (colder) density layers within the STG, strengthening (weakening) the northward heat transport and warming (cooling) the subpolar gyre. This process may then impact overturning, because deep-water formation is primarily driven by oceanic heat loss. Thus, more (less) heat loss in the SPG would result in higher (lower) rates of overturning and stronger (weaker) circulation in the deep ocean. Coupled ocean and ice-sheet models may also be used to test the influence of additional heat and moisture supply on ice-sheet sizes for different boundary conditions, particularly those expected in the near future.

Redefining feedbacks between northward heat transport and deep-water formation has far-reaching implications for our understanding of the mechanisms driving oceanic storage and release of CO_2 during climate transitions. For example, the generation of subsurface, sea-surface temperature and stable isotope records without chronostratigraphic uncertainties (from the same samples) from sites close to the southern subtropical front could be used to verify leads and lags between different processes related to the degassing of CO_2 from the ocean (e.g., subsurface warming, strength of upwelling in the Southern Ocean). Together with IRD counts and the determination of εNd from sea-bottom sediments, the variability between records can be used to test if the strengthening of NSW's εNd signal in the Southern Ocean coincided with subsurface warming and preceded CO_2 release to the atmosphere during deglaciations.

10 References

Adkins, J. F., & Schrag, D. P. (2003). Reconstructing Last Glacial Maximum bottom water salinities from deep-sea sediment pore fluid profiles. *Earth and Planetary Science Letters,* 216(1–2), 109–123. https://doi.org/10.1016/s0012-821x(03)00502-8

Adkins, J. F., McIntyre, K., & Schrag, D. P. (2002). The salinity, temperature, and delta 18O of the glacial deep ocean. *Science,* 298(5599), 1769–1773. https://doi.org/10.1126/Science.1076252

Aken, H. M. van. (2000). The hydrography of the mid-latitude Northeast Atlantic Ocean II: The intermediate water masses. *Deep Sea Research Part I: Oceanographic Research Papers,* 47(5), 789–824. https://doi.org/10.1016/s0967-0637(99)00112-0

Alley, R. B., & MacAyeal, D. R. (1994). Ice-rafted debris associated with binge/purge oscillations of the Laurentide Ice Sheet. *Paleoceanography*, 9(4), 503–511. https://doi.org/10.1029/94pa01008

Alvarez-Solas, J., Carreño, R. B., Robinson, A. J., Redondo, M. L. M., Carreño, R. B., Robinson, A. J., & Redondo, M. L. M. (2019). Ocean-driven millennial-scale variability of the Eurasian ice sheet during the last glacial period simulated with a hybrid ice-sheet-shelf model. *Climate of the Past, 15*(3), 957–979. https://doi.org/10.5194/cp-15-957-2019

Alvarez-Solas, J., & Ramstein, G. (2011). On the triggering mechanism of Heinrich events. *Proceedings of the National Academy of Sciences, 108*(50), E1359–E1360. https://doi.org/10.1073/pnas.1116575108

Anand, P., Elderfield, H., & Conte, M. H. (2003). Calibration of Mg/Ca thermometry in planktonic foraminifera from a sediment trap time series. *Paleoceanography*, *18*(2), 1050(1-15). https://doi.org/10.1029/2002pa000846

Arbuszewski, J., deMenocal, P., Kaplan, A., & Farmer, E. C. (2010). On the fidelity of shell-derived δ 18O seawater estimates. *Earth and Planetary Science Letters, 300*(3–4), 185–196. https://doi.org/10.1016/j.epsl.2010.10.035

Armi, L., & Zenk, W. (1984). Large Lenses of Highly Saline Mediterranean Water. *Journal of Physical Oceanography*, 14(10), 1560–1576.

Bahr, A. et al., 2015. Persistent monsoonal forcing of Mediterranean Outflow Water dynamics during the late Pleistocene. *Geology,* 43(11), 951–954.

Baringer, M. O., & Price, J. F. (1999). A review of the physical oceanography of the Mediterranean outflow. *Marine Geology, 155*(1–2), 63–82. https://doi.org/10.1016/s0025-3227(98)00141-8

Barker, S., Cacho, I., Benway, H., & Tachikawa, K. (2005). Planktonic foraminiferal Mg/Ca as a proxy for past oceanic temperatures: a methodological overview and data compilation for the Last Glacial Maximum. *Quaternary Science Reviews, 24*(7–9), 821–834. https://doi.org/10.1016/j.quascirev.2004.07.016

Barker, S., Diz, P., Vautravers, M. J., Pike, J., Knorr, G., Hall, I. R., & Broecker, W. S. (2009). Interhemispheric Atlantic seesaw response during the last deglaciation. *Nature,* 457(7233), 1097–1102. https://doi.org/10.1038/Nature07770

Barker, S., Kiefer, T., & Elderfield, H. (2004). Temporal changes in North Atlantic circulation constrained by planktonic foraminiferal shell weights. *Paleoceanography*, 19(3). https://doi.org/10.1029/2004pa001004

Bauch, H. A., Erlenkeuser, H., Jung, S. J. A., & Thiede, J. (2000). surface and deep water changes in the subpolar North Atlantic during Termination II and the Last Interglaciation. *Paleoceanography*, *15*(1), 76–84. https://doi.org/10.1029/1998pa000343

Baumann, K.-H., & Huber, R. (1999). Proceedings of the Ocean Drilling Program, 162 Scientific Results. *Proceedings of the Ocean Drilling Program*. https://doi.org/10.2973/odp.proc.sr.162.014.1999

Bemis, B. E., Spero, H. J., Bijma, J., & Lea, D. W. (1998). Reevaluation of the oxygen isotopic composition of planktonic foraminifera: Experimental results and revised paleotemperature equations. *Paleoceanography*, *13*(2), 150–160. https://doi.org/10.1029/98pa00070

Bennett, A.F., 1976. Poleward heat fluxes in southern hemisphere oceans. *Journal of Physical Oceanography,* 8, 785-789.

Benway, H. M., McManus, J. F., Oppo, D. W., & Cullen, J. L. (2010). Hydrographic changes in the eastern subpolar North Atlantic during the last deglaciation. *Quaternary Science Reviews,* 29(23–24), 3336–3345. https://doi.org/10.1016/j.quascirev.2010.08.013

Berger, W. H., & Jansen, E. (1994). Mid-Pleistocene climate shift-the Nansen connection. In: *The polar oceans and their role in shaping the global environment*, 85(4), 295–311.

Boer, B. de, Lourens, L. J., & Wal, R. S. W. van de. (2014). Persistent 400,000-year variability of Antarctic ice volume and the carbon cycle is revealed throughout the Plio-Pleistocene. *Nature Communications,* 5(2999). https://doi.org/10.1038/ncomms3999

Böhm, E., Lippold, J., Gutjahr, M., Frank, M., Blaser, P., Antz, B., Fohlmeister, J., Frank, N., Andersen, M. B., & Deininger, M. (2015). Strong and deep Atlantic meridional overturning circulation during the last glacial cycle. *Nature,* 517(7532), 73–76. https://doi.org/10.1038/Nature14059

Bond, G. C., & Lotti, R. (1995). Iceberg Discharges into the North Atlantic on Millennial Time Scales During the Last Glaciation. *Science,* 267(5200), 1005–1010. https://doi.org/10.1126/Science.267.5200.1005

Bond, G., Heinrich, H., Broecker, W. S., & Labeyrie, L. (1992). Evidence for massive discharges of icebergs into the North Atlantic Ocean during the last glacial period. *Nature,* 360(6401), 245–249. https://doi.org/10.1038/360245a0

Boyle, E. A., & Keigwin, L. (1987). North-Atlantic Thermohaline Circulation During the Past 20,000 Years Linked to High-Latitude Surface-Temperature. *Nature*, *330*(6143), 35–40. https://doi.org/10.1038/330035a0

Bower, A. S., Armi, L., & Ambar, I. (1997). Lagrangian Observations of Meddy Formation during A Mediterranean Undercurrent Seeding Experiment*. *Journal of Physical Oceanography*, 27(12), 2545–2575. https://doi.org/10.1175/1520-0485(1997)027

Bower, A., Lozier, S., Biastoch, A., Drouin, K., Foukal, N., Furey, H., Lankhorst, M., Rühs, S., & Zou, S. (2019). Lagrangian Views of the Pathways of the Atlantic Meridional Overturning Circulation. *Journal of Geophysical Research: Oceans*, 124(8), 5313–5335. https://doi.org/10.1029/2019jc015014

Brady, E. C., & Otto-Bliesner, B. (2011). The role of meltwater-induced subsurface ocean warming in regulating the Atlantic meridional overturning in glacial climate simulations. *Climate Dynamics*.

Brambilla, E., & Talley, L. D. (2008). Subpolar Mode Water in the northeastern Atlantic: 1. Averaged properties and mean circulation. *Journal of Geophysical Research*, 113(C4), 109. https://doi.org/10.1029/2006jc004062

Broecker, W. S. (1982). Glacial to interglacial changes in ocean chemistry. *Progress in Oceanography*, 11(2), 151–197. https://doi.org/10.1016/0079-6611(82)90007-6

Broecker, W. S., & Peng, T. (1987). The role of CaCO3 compensation in the glacial to interglacial atmospheric CO2 change. *Proceedings of the National Academy of Sciences,* 1(1), 15–29. https://doi.org/10.1029/gb001i001p00015

Broecker, W. S., & Reimer, E. M. (1992). The influence of air and sea exchange on the carbon isotope distribution in the sea. *Proceedings of the National Academy of Sciences,* 6(3), 315–320. https://doi.org/10.1029/92gb01672

Broeker, W.S. (1991). The Great Ocean Conveyor. *Oceanography*, 4(2), 79–89. https://doi.org/10.5670/oceanog.1991.07

Buckley, M. W., & Marshall, J. (2016). Observations, inferences, and mechanisms of the Atlantic Meridional Overturning Circulation: A review. *Reviews of Geophysics,* 54(1), 5–63. https://doi.org/10.1002/2015rg000493

Burkholder, K. C., & Lozier, M. S. (2011). Mid-depth Lagrangian pathways in the North Atlantic and their impact on the salinity of the eastern subpolar gyre. *Deep-Sea Research Part I*, 58(12), 1196–1204. https://doi.org/10.1016/j.dsr.2011.08.007

Burkholder, K. C., & Lozier, M. S. (2014). Tracing the pathways of the upper limb of the North Atlantic Meridional Overturning Circulation. *Geophysical Research Letters,* 41(12), 4254–4260. https://doi.org/10.1002/2014gl060226

Bylinskaya, M. E. (2005). Range and stratigraphic significance of the Globorotalia crassaformis plexus. *Journal of Iberian Geology,* 31, 51-63.

Caesar, L., McCarthy, G. D., Thornalley, D. J. R., Cahill, N., & Rahmstorf, S. (2021). Current Atlantic Meridional Overturning Circulation weakest in last millennium. *Nature Geoscience*, 14(3), 118–120. https://doi.org/10.1038/s41561-021-00699-z

Calvo, E., Villanueva, J., Grimalt, J. O., Boelaert, A., & Labeyrie, L. (2001). New insights into the glacial latitudinal temperature gradients in the North Atlantic. Results from UK′37 sea surface temperatures and terrigenous inputs. *Earth and Planetary Science Letters,* 188(3–4), 509–519. https://doi.org/10.1016/s0012-821x(01)00316-8

Catunda, M.C.A, Bahr, A., Kaboth-Bahr, S., Zhang, X., Foukal, N., Friedrich, O. (2021). Subsurface heat channel drove sea surface warming in the high-latitude North Atlantic during the Mid-Pleistocene Transition. *Geophysical Research Letters*, 48(11), e2020GL091899

Cayre, O., Lancelot, Y., Vincent, E., & Hall, M. A. (1999). Paleoceanographic reconstructions from planktonic foraminifera off the Iberian Margin: Temperature, salinity, and Heinrich events. *Paleoceanography*, 14(3), 384–396. https://doi.org/10.1029/1998pa900027

Chalk, T. B., Foster, G. L., & Wilson, P. A. (2019). Dynamic storage of glacial CO2 in the Atlantic Ocean revealed by boron [CO 32−] and pH records. *Earth and Planetary Science Letters,* 510, 1–11. https://doi.org/10.1016/j.epsl.2018.12.022

Chalk, T. B., Hain, M. P., Foster, G. L., Rohling, E. J., Sexton, P. F., Badger, M. P. S., Cherry, S. G., Hasenfratz, A. P., Haug, G. H., Jaccard, S. L., Martínez-García, A., Pälike, H., Pancost, R. D., & Wilson, P. A. (2017). Causes of ice age intensification across the Mid-Pleistocene Transition. *Proceedings of the National Academy of Sciences,* 114(50), 13114–13119. https://doi.org/10.1073/pnas.1702143114

Chapman, M. R., & Maslin, M. A. (1999). Low latitude forcing of meridional temperature and salinity gradients in the subpolar North Atlantic and the growth of glacial ice sheets. *Geology,* 27(10), 875. https://doi.org/10.1130/0091-7613

Chapman, M. R., & Shackleton, N. J. (1998). Millennial-scale fluctuations in North Atlantic heat flux during the last 150,000 years. *Earth and Planetary Science Letters,* 159(1–2), 57–70. https://doi.org/10.1016/s0012-821x(98)00068-5

Chapman, M. R., Shackleton, N. J., & Duplessy, J.-C. (2000). Sea surface temperature variability during the last glacial–interglacial cycle: assessing the magnitude and pattern of climate change in the North Atlantic. *Palaeogeography, Palaeoclimatology, Palaeoecology,* 157(1–2), 1–25. https://doi.org/10.1016/s0031-0182(99)00168-6

Clark, P. U., & Mix, A. C. (2002). Ice sheets and sea level of the Last Glacial Maximum. *Quaternary Science Reviews, 21*(1-3), 1-7.

Clark, P. U., & Pollard, D. (1998). Origin of the middle Pleistocene transition by ice sheet erosion of regolith. *Paleoceanography*, 13(1), 1–9. https://doi.org/10.1029/97pa02660

Clark, P. U., Archer, D., Pollard, D., Blum, J. D., Rial, J. A., Brovkin, V., Mix, A. C., Pisias, N. G., & Roy, M. (2006). The middle Pleistocene transition: characteristics, mechanisms, and implications for long-term changes in atmospheric pCO2. *Quaternary Science Reviews,* 25(23–24), 3150–3184. https://doi.org/10.1016/j.quascirev.2006.07.008

Clark, P. U., Pisias, N. G., Pisias, N. G., Stocker, T. F., Stocker, T. F., Weaver, A. J., & Weaver, A. J. (2002). The role of the thermohaline circulation in abrupt climate change. *Nature,* 415(6874), 863–869. https://doi.org/10.1038/415863a

Cléroux, C., Cortijo, E., Anand, P., Labeyrie, L., Bassinot, F., Caillon, N., & Duplessy, J. C. (2008). Mg/Ca and Sr/Ca ratios in planktonic foraminifera: Proxies for upper water column temperature reconstruction. *Paleoceanography*, 23(3), https://doi.org/10.1029/2007pa001505

Cléroux, C., deMenocal, P., Arbuszewski, J., & Linsley, B. (2013). Reconstructing the upper water column thermal structure in the Atlantic Ocean. *Paleoceanography*, 28(3), 503–516. https://doi.org/10.1002/palo.20050

Cunningham, S. A., Kanzow, T., Rayner, D., Baringer, M. O., Johns, W. E., Marotzke, J., Longworth, H. R., Grant, E. M., Hirschi, J. J.-M., Beal, L. M., Meinen, C. S., & Bryden, H. L. (2007). Temporal Variability of the Atlantic Meridional Overturning Circulation at 26.5°N. *Science,* 317(5840), 935–938. https://doi.org/10.1126/Science.1141304

Curry, W. B., & Oppo, D. W. (2005). Glacial water mass geometry and the distribution of δ13C of ΣCO2 in the western Atlantic Ocean. *Paleoceanography and Paleoclimatology,* 20(1), n/a-n/a. https://doi.org/10.1029/2004pa001021

Daniault, N., Mazé, J. P., & Arhan, M. (1994). Circulation and mixing of Mediterranean Water west of the Iberian Peninsula. *Deep Sea Research Part I: Oceanographic Research Papers,* 41(11–12), 1685–1714. https://doi.org/10.1016/0967-0637(94)90068-x

Deplazes, G., Lückge, A., Peterson, L. C., Timmermann, A., Hamann, Y., Hughen, K. A., Röhl, U., Laj, C., Cane, M. A., Sigman, D. M., & Haug, G. H. (2013). Links between tropical rainfall and North Atlantic climate during the last glacial period. *Nature Geoscience,* 6(3), 213–217. https://doi.org/10.1038/ngeo1712

Dueñas-Bohórquez, A., Rocha, R. E. da, Kuroyanagi, A., Bijma, J., & Reichart, G.-J. (2009). Effect of salinity and seawater calcite saturation state on Mg and Sr incorporation in cultured planktonic foraminifera. *Marine Micropaleontology,* 73(3–4), 178–189. https://doi.org/10.1016/j.marmicro.2009.09.002

Duplessy, J. C., Shackleton, N. J., Fairbanks, R. G., Labeyrie, L. D., Oppo, D. W., & Kallel, N. (1988). Deepwater source variations during the last climatic cycle and their impact on the global deepwater circulation. *Paleoceanography*, 3(3), 343–360. https://doi.org/10.1029/pa003i003p00343

Duplessy, J. C., Shackleton, N. J., Matthews, R. K., Prell, W., Ruddiman, W. F., Caralp, M., & Hendy, C. H. (1984). 13C Record of benthic foraminifera in the last interglacial ocean: Implications for the carbon cycle and the global deep water circulation. *Quaternary Research,* 21(2), 225–243. https://doi.org/10.1016/0033-5894(84)90099-1

Elderfield, H., Ferretti, P., Greaves, M., Crowhurst, S., McCave, I. N., Hodell, D., & Piotrowski, A. M. (2012). Evolution of Ocean Temperature and Ice Volume Through the Mid-Pleistocene Climate Transition. *Science,* 337(6095), 704–709. https://doi.org/10.1126/Science.1221294

Elderfield, H., Vautravers, M., & Cooper, M. (2002). The relationship between shell size and Mg/Ca, Sr/Ca, δ18O, and δ13C of species of planktonic foraminifera. *Geochemistry, Geophysics, Geosystems,* 3(8), 1–13. https://doi.org/10.1029/2001gc000194

Emiliani, C. (1955). Pleistocene temperatures. The Journal of geology, 63(6), 538-578

Eynaud, F., Abreu, L. de, Voelker, A., Schönfeld, J., Salgueiro, E., Turon, J., Penaud, A., Toucanne, S., Naughton, F., Goñi, M. F. S., Malaizé, B., & Cacho, I. (2009). Position of the Polar Front along the western Iberian margin during key cold episodes of the last 45 ka. *Geochemistry, Geophysics, Geosystems,* 10(7), https://doi.org/10.1029/2009gc002398

Expedition Scientists (2005). North Atlantic climate 2. *IODP Preliminary Report*, 306. doi:10.2204/iodp.pr.306.2005

Ezat, M. M., Rasmussen, T. L., & Groeneveld, J. (2014). Persistent intermediate water warming during cold stadials in the southeastern Nordic seas during the past 65 ky. *Geology,* https://doi.org/10.1130/g35579.1

Fairbanks, R. G., Wiebe, P. H., & Bé, A. W. H. (1980). Vertical Distribution and Isotopic Composition of Living Planktonic Foraminifera in the Western North Atlantic. *Science,* 207(4426), 61–63. https://doi.org/10.1126/Science.207.4426.61

Farmer, J. R., Hönisch, B., Haynes, L. L., Kroon, D., Jung, S., Ford, H. L., ... & Kim, J. (2019). Deep Atlantic Ocean carbon storage and the rise of 100,000-year glacial cycles. *Nature Geoscience,* 12(5), 355-360, 1–9. https://doi.org/10.1038/s41561-019-0334-6

Feely, R. A., Sabine, C. L., Schlitzer, R., Bullister, J. L., Mecking, S., & Greeley, D. (2004). Oxygen utilization and organic carbon remineralization in the upper water column of the Pacific Ocean. *Journal of Oceanography,* 60(1), 45–52.

Feldmeijer, W., Metcalfe, B., Brummer, G. J. A., & Ganssen, G. M. (2015). Reconstructing the depth of the permanent thermocline through the morphology and geochemistry of the deep dwelling planktonic foraminifer Globorotalia truncatulinoides. *Paleoceanography*, 30(1), 1–22. https://doi.org/10.1002/2014pa002687

Feng, F., & Bailer-Jones, C. A. L. (2015). Obliquity and precession as pacemakers of Pleistocene deglaciations. *Quaternary Science Reviews,* 122, 166–179. https://doi.org/10.1016/j.quascirev.2015.05.006

Ferrari, R., Jansen, M. F., Adkins, J. F., Burke, A., Stewart, A. L., & Thompson, A. F. (2014). Antarctic sea ice control on ocean circulation in present and glacial climates. *Proceedings of the National Academy of Sciences*, *111*(24), 201323922–201328758. https://doi.org/10.1073/pnas.1323922111

Ferretti, P., Crowhurst, S. J., Naafs, B. D. A., & Barbante, C. (2015). The Marine Isotope Stage 19 in the mid-latitude North Atlantic Ocean: astronomical sigNature and intra-interglacial variability. *Quaternary Science Reviews,* 108, 95–110. https://doi.org/10.1016/j.quascirev.2014.10.024

Feucher, C., Maze, G., & Mercier, H. (2016). Mean Structure of the North Atlantic Subtropical Permanent Pycnocline from In Situ Observations. *Journal of Atmospheric and Oceanic Technology,* 33(6), 1285–1308. https://doi.org/10.1175/jtech-d-15-0192.1

Ford, H. L., & Raymo, M. E. (2019). Regional and global signals in seawater δ18O records across the mid-Pleistocene transition. *Geology,* 48(2), 113–117. https://doi.org/10.1130/g46546.1

Foukal, N. P., & Lozier, M. S. (2016). No inter-gyre pathway for sea-surface temperature anomalies in the North Atlantic. *Nature Communications,* 7(11333), 1–6. https://doi.org/10.1038/ncomms11333

Freeman, K. H., & Hayes, J. M. (1992). Fractionation of carbon isotopes by phytoplankton and estimates of ancient CO 2levels. *Proceedings of the National Academy of Sciences,* 6(2), 185–198. https://doi.org/10.1029/92gb00190

Friedrich, O., Schiebel, R., Wilson, P. A., Weldeab, S., Beer, C. J., Cooper, M. J., & Fiebig, J. (2012). Influence of test size, water depth, and ecology on Mg/Ca, Sr/Ca, δ18O and δ13C in nine modern species of planktic foraminifers. *Earth and Planetary Science Letters,* 319–320, 133–145. https://doi.org/10.1016/j.epsl.2011.12.002

Fu, Y., Li, F., Karstensen, J., & Wang, C. (2020). A stable Atlantic Meridional Overturning Circulation in a changing North Atlantic Ocean since the 1990s. *Science Advances,* 6(48), eabc7836. https://doi.org/10.1126/sciadv.abc7836

Ganachaud, A., & Wunsch, C. (2000). Improved estimates of global ocean circulation, heat transport and mixing from hydrographic data. *Nature,* 408(6811), 453–457. https://doi.org/10.1038/35044048

García-Ibáñez, M. I., Pérez, F. F., Lherminier, P., Zunino, P., Mercier, H., & Tréguer, P. (2018). Water mass distributions and transports for the 2014 GEOVIDE cruise in the North Atlantic. *Biogeosciences,* 15(7), 2075–2090. https://doi.org/10.5194/bg-15-2075-2018

Gebbie, G. (2014). How much did Glacial North Atlantic Water shoal? *Paleoceanography and Paleoclimatology*, *29*(3), 190–209. https://doi.org/10.1002/2013pa002557

Gent, P. R. (2011). The Gent–McWilliams parameterization: 20/20 hindsight. *Ocean Modelling*, *39*(1-2), 2-9.

Georgiou, S., Boog, C. G. van der, Brüggemann, N., Ypma, S. L., Pietrzak, J. D., & Katsman, C. A. (2019). On the interplay between downwelling, deep convection and mesoscale eddies in the Labrador Sea. *Ocean Modelling*, *135*, 56–70. https://doi.org/10.1016/j.ocemod.2019.02.004

Gherardi, J. M., Labeyrie, L., Nave, S., Francois, R., McManus, J. F., & Cortijo, E. (2009). Glacial-interglacial circulation changes inferred from 231Pa/230Th sedimentary record in the North Atlantic region. *Paleoceanography*, 24(2), n/a-n/a. https://doi.org/10.1029/2008pa001696

Gibbard, P. L., Head, M. J., & Walker, M. J. C. (2010). Formal ratification of the Quaternary System/Period and the Pleistocene Series/Epoch with a base at 2.58 Ma. *Journal of Quaternary Science,* 25(2), 96–102. https://doi.org/10.1002/jqs.1338

Gnanadesikan, A. (1999). A Simple Predictive Model for the Structure of the Oceanic Pycnocline. *Science,* 283(5410), 2077–2079. https://doi.org/10.1126/Science.283.5410.2077

Gooday, A. J. (2003). Benthic foraminifera (protista) as tools in deep-water palaeoceanography: Environmental influences on faunal characteristics. *Advances in Marine Biology,* 46, pp. 1–90. https://doi.org/10.1016/s0065-2881(03)46002-1

Gottschalk, J., Skinner, L. C., Lippold, J., Vogel, H., Frank, N., Jaccard, S. L., & Waelbroeck, C. (2016). Biological and physical controls in the Southern Ocean on past millennial-scale atmospheric CO_2 changes. *Nature Communications,* 7(1), 11539. https://doi.org/10.1038/ncomms11539

Gowing, M. M., & Wishner, K. F. (1998). Feeding ecology of the copepod Lucicutia aff. L. grandis near the lower interface of the Arabian Sea oxygen minimum zone. *Deep Sea Research Part II: Topical Studies in Oceanography,* 45(10–11), 2433–2459. https://doi.org/10.1016/s0967-0645(98)00077-0

Gray, W. R., & Evans, D. (2019). Nonthermal Influences on Mg/Ca in Planktonic Foraminifera: A Review of Culture Studies and Application to the Last Glacial Maximum. *Paleoceanography and Paleoclimatology,* 34(3), 306–315. https://doi.org/10.1029/2018pa003517

Gray, W. R., Weldeab, S., Lea, D. W., Rosenthal, Y., Gruber, N., Donner, B., & Fischer, G. (2018). The effects of temperature, salinity, and the carbonate system on Mg/Ca in Globigerinoides ruber (white): A global sediment trap calibration. *Earth and Planetary Science Letters,* 482, 607–620. https://doi.org/10.1016/j.epsl.2017.11.026

Greaves, M., Caillon, N., Rebaubier, H., Bartoli, G., Bohaty, S., Cacho, I., Clarke, L., Cooper, M., Daunt, C., Delaney, M., deMenocal, P., Dutton, A., Eggins, S., Elderfield, H., Garbe-Schoenberg, D., Goddard, E., Green, D., Groeneveld, J., Hastings, D., … Wilson, P. A. (2008). Interlaboratory comparison study of calibration standards for foraminiferal Mg/Ca thermometry. *Geochemistry, Geophysics, Geosystems,* 9(8), 1–27. https://doi.org/10.1029/2008gc001974

GRID-Arendal (2014). GRID-Arendal: Board Report 2013. https://www.grida.no/resources/5885

Grousset, F. E., Labeyrie, L., Sinko, J. A., Cremer, M., Bond, G., Duprat, J., Cortijo, E., & Huon, S. (1993). Patterns of Ice-Rafted Detritus in the Glacial North Atlantic (40–55°N). *Paleoceanography*, 8(2), 175–192. https://doi.org/10.1029/92pa02923

Hanawa, K., & Talley, L. D. (2001). Chapter 5.4 Mode waters. *International Geophysics*, 77, 373–386. https://doi.org/10.1016/s0074-6142(01)80129-7

Harvey, J. (1982). θ-S relationships and water masses in the eastern North Atlantic. *Deep Sea Research Part A: Oceanographic Research Papers,* 29(8), 1021–1033. https://doi.org/10.1016/0198-0149(82)90025-5

Hasenfratz, A. P., Jaccard, S. L., Martínez-Garcia, A., Sigman, D. M., Hodell, D. A., Vance, D., Bernasconi, S. M., Kleiven, H. K. F., Haumann, F. A., & Haug, G. H. (2019). The residence time of Southern Ocean surface waters and the 100,000-year ice age cycle. *Science,* 363(6431), 1080–1084. https://doi.org/10.1126/Science.aat7067

Haskins, R. K., Oliver, K. I. C., Jackson, L. C., Wood, R. A., & Drijfhout, S. S. (2020). Temperature domination of AMOC weakening due to freshwater hosing in two GCMs. *Climate Dynamics,* 54(1), 273–286. https://doi.org/10.1007/s00382-019-04998-5

Hayes, D. R., Schroeder, K., Poulain, P.-M., Testor, P., Mortier, L., Bosse, A., & Madron, X. du. (2019). Mediterranean Cold-Water Corals: Past, Present and Future. *Coral Reefs of the World,* 195–211. https://doi.org/10.1007/978-3-319-91608-8_18

He, C., Liu, Z., Zhu, J., Zhang, J., Gu, S., Otto-Bliesner, B. L., Brady, E., Zhu, C., Jin, Y., & Sun, J. (2020). North Atlantic subsurface temperature response controlled by effective freshwater input in "Heinrich" events. *Earth and Planetary Science Letters,* 539, 116247. https://doi.org/10.1016/j.epsl.2020.116247

Hecht, M., Holland, W., Artale, V., & Pinardi, N. (1997). North Atlantic model sensitivity to Mediterranean waters. *Assessing Climate Change: Results from the Model Evaluation Consortium for Climate Assessment.* 169, 191.

Heinrich, H. (2021). Origin and Consequences of Cyclic Ice Rafting in the Northeast Atlantic Ocean During the Past 130,000 Years. *Quaternary Research,* 29(2), 142–152. https://doi.org/10.1016/0033-5894(88)90057-9

Hemleben, C., Spindler, M., Breitinger, I., & Deuser, W. G. (1985). Field and laboratory studies on the ontogeny and ecology of some globorotaliid species from the Sargasso Sea off Bermuda. *Journal of Foraminiferal Research*.

Hemming, S. R. (2004). Heinrich events: Massive late Pleistocene detritus layers of the North Atlantic and their global climate imprint. *Reviews of Geophysics,* 42(1). https://doi.org/10.1029/2003rg000128

Hernández-Almeida, I., Sierro, F. J., Cacho, I., & Flores, J. A. (2015). Subsurface North Atlantic warming as a trigger of rapid cooling events: evidence from the early Pleistocene (MIS 31–19). *Climate of the Past,* 11(4), 687–696. https://doi.org/10.5194/cp-11-687-2015

Hernandez-Molina, F.J. et al., 2014. Onset of Mediterranean outflow into the North Atlantic. *Science,* 344(6189), pp.1244–1250.

Hodell, D. A., Channell, J. E. T., Curtis, J. H., Romero, O. E., & Röhl, U. (2008). Onset of "Hudson Strait" Heinrich events in the eastern North Atlantic at the end of the middle Pleistocene transition (~640 ka)? *Paleoceanography and Paleoclimatology,* 23(4), n/a-n/a. https://doi.org/10.1029/2008pa001591

Hodell, D. A., Nicholl, J. A., Bontognali, T. R. R., Danino, S., Dorador, J., Dowdeswell, J. A., Einsle, J., Kuhlmann, H., Martrat, B., Mleneck-Vautravers, M. J., Rodríguez-Tovar, F. J., & Röhl, U. (2017). Anatomy of Heinrich Layer 1 and its role in the last deglaciation. *Paleoceanography and Paleoclimatology,* 32(3), 284–303. https://doi.org/10.1002/2016pa003028

Hodell, D. A., Venz, K. A., Charles, C. D., & Ninnemann, U. S. (2003). Pleistocene vertical carbon isotope and carbonate gradients in the South Atlantic sector of the Southern Ocean. *Geochemistry, Geophysics, Geosystems,* 4(1), 1–19. https://doi.org/10.1029/2002gc000367

Hodell, D., & Channell, J. E. T. (2016). Mode transitions in Northern Hemisphere glaciation: co-evolution of millennial and orbital variability in Quaternary climate. *Climate of the Past,* 12, 1805–1828. https://doi.org/10.17863/cam.6210

Hodell, D.A., & Channell, J. E. T. (2016). Mode transitions in Northern Hemisphere glaciation: co-evolution of millennial and orbital variability in Quaternary climate. *Climate of the Past,* 12, 1805–1828. https://doi.org/10.17863/cam.6210

Hogg, A. M., & Gayen, B. (2020). Ocean Gyres Driven by Surface Buoyancy Forcing. *Geophysical Research Letters,* 47(16), e2020GL088539. https://doi.org/10.1029/2020gl088539

Hönisch, B., Hemming, N. G., Archer, D., Siddall, M., & McManus, J. F. (2009). Atmospheric carbon dioxide concentration across the Mid-Pleistocene Transition. *Science,* 324(5934), 1551–1554. https://doi.org/10.1126/Science.1171477

Imbrie, J., Berger, A., Boyle, E. A., Clemens, S. C., Duffy, A., Howard, W. R., Kukla, G., Kutzbach, J., Martinson, D. G., McIntyre, A., Mix, A. C., Molfino, B., Morley, J. J., Peterson, L. C., Pisias, N.

G., Prell, W. L., Raymo, M. E., Shackleton, N. J., & Toggweiler, J. R. (1993). On the structure and origin of major glaciation cycles 2. The 100,000-year cycle. *Paleoceanography*, 8(6), 699–735. https://doi.org/10.1029/93pa02751

Imbrie, J., Boyle, E. A., Clemens, S. C., Duffy, A., Howard, W. R., Kukla, G., Kutzbach, J., Martinson, D. G., McIntyre, A., Mix, A. C., Molfino, B., Morley, J. J., Peterson, L. C., Pisias, N. G., Prell, W. L., Raymo, M. E., Shackleton, N. J., & Toggweiler, J. R. (1992). On the Structure and Origin of Major Glaciation Cycles 1. Linear Responses to Milankovitch Forcing. *Paleoceanography*, 7(6), 701–738. https://doi.org/10.1029/92pa02253

Intergovernmental Panel on Climate Change. (2009). Climate Change 2013 - *The Physical Science Basis*. https://doi.org/10.1017/cbo9781107415324

Iorga, M. C., & Lozier, M. S. (1999). SigNatures of the Mediterranean outflow from a North Atlantic climatology: 2. Diagnostic velocity fields. *Journal of Geophysical Research: Oceans*, 104(C11), 26011–26029. https://doi.org/10.1029/1999jc900204

IPCC, 2014: Climate Change 2014: Synthesis Report. *Contribution of Working Groups I, II and III to the Fifth Assessment Report of the Intergovernmental Panel on Climate Change* [Core Writing Team, R.K. Pachauri and L.A. Meyer (eds.)]. IPCC, Geneva, Switzerland, 151 pp.

Ivanovic, R. F., Gregoire, L. J., Burke, A., Wickert, A. D., Valdes, P. J., Ng, H. C., ... & Dentith, J. E. (2018). Acceleration of northern ice sheet melt induces AMOC slowdown and northern cooling in simulations of the early last deglaciation. *Paleoceanography and Paleoclimatology, 33*(7), 807-824.

Jansen, H., Zeebe, R. E., & Wolf-Gladrow, D. A. (2002). Modeling the dissolution of settling CaCO3 in the ocean. *Proceedings of the National Academy of Sciences,* 16(2), 11-1-11–16. https://doi.org/10.1029/2000gb001279

Jia, Y., Coward, A. C., Cuevas, B. A. de, Webb, D. J., & Drijfhout, S. S. (2007). A Model Analysis of the Behavior of the Mediterranean Water in the North Atlantic. *Journal of Physical Oceanography*, 37(3), 764–786. https://doi.org/10.1175/jpo3020.1

Johns, W. E., Baringer, M. O., Beal, L. M., Cunningham, S. A., Kanzow, T., Bryden, H. L., Hirschi, J. J. M., Marotzke, J., Meinen, C. S., Shaw, B., & Curry, R. (2011). Continuous, Array-Based Estimates of Atlantic Ocean Heat Transport at 26.5°N. *Journal of Climate,* 24(10), 2429–2449. https://doi.org/10.1175/2010jcli3997.1

Johnson, H. L., Cessi, P., Marshall, D. P., Schloesser, F., & Spall, M. A. (2019). Recent Contributions of Theory to Our Understanding of the Atlantic Meridional Overturning Circulation. *Journal of Geophysical Research: Oceans*, 124(8), 5376–5399. https://doi.org/10.1029/2019jc015330

Jonkers, L., Heuven, S. van, Zahn, R., & Peeters, F. J. C. (2013). Seasonal patterns of shell flux, δ18O and δ13C of small and large N. pachyderma (s) and G. bulloides in the subpolar North Atlantic. *Paleoceanography*, *28*(1), 164–174. https://doi.org/10.1002/palo.20018

Keigwin, L. D., Jones, G. A., Lehman, S. J., & Boyle, E. A. (1991). Deglacial meltwater discharge, North Atlantic Deep Circulation, and abrupt climate change. *Journal of Geophysical Research,* 96(C9), 16811. https://doi.org/10.1029/91jc01624

Kellogg, T. B. (1980). Paleoclimatology and paleo-oceanography of the Norwegian and Greenland seas: glacial-interglacial contrasts. *Boreas*, *9*(2), 115–137. https://doi.org/10.1111/j.1502-3885.1980.tb01033.x

Kemle-von-Mücke, S., & Oberhänsli, H. (1999). The Distribution of Living Planktic Foraminifera in Relation to Southeast Atlantic Oceanography. In: *Use of proxies in paleoceanography*, 53(2), pp. 91–115. https://doi.org/10.1007/978-3-642-58646-0_3

Kender, S., Ravelo, A. C., Worne, S., Swann, G. E. A., Leng, M. J., Asahi, H., Becker, J., Detlef, H., Aiello, I. W., Andreasen, D., & Hall, I. R. (2018). Closure of the Bering Strait caused Mid-Pleistocene Transition cooling. *Nature Communications,* 9(1), 173. https://doi.org/10.1038/s41467-018-07828-0

Kim, S.-T., & O'Neil, J. R. (1997). Equilibrium and nonequilibrium oxygen isotope effects in synthetic carbonates. *Geochimica et Cosmochimica Acta*, 61(16), 3461–3475. https://doi.org/10.1016/s0016-7037(97)00169-5

Kinder, T. H., & Parrilla, G. (1987). Yes, some of the Mediterranean outflow does come from great depth. *Journal of Geophysical Research: Oceans* (1978–2012), 92(C3), 2901–2906. https://doi.org/10.1029/jc092ic03p02901

Kindler, P., Guillevic, M., Baumgartner, M., Schwander, J., Landais, A., & Leuenberger, M. (2014). Temperature reconstruction from 10 to 120 kyr b2k from the NGRIP ice core. *Climate of the Past,* 10(2), 887–902. https://doi.org/10.5194/cp-10-887-2014

Knutti, R., Flückiger, J., Stocker, T. F., & Timmermann, A. (2004). Strong hemispheric coupling of glacial climate through freshwater discharge and ocean circulation. *Nature,* 430(7002), 851–856. https://doi.org/10.1038/Nature02786

Konijnendijk, T.Y.M., Ziegler, M. & Lourens, L.J., 2014. Chronological constraints on Pleistocene sapropel depositions from high-resolution geochemical records of ODP Sites 967 and 968. *Newsletters on Stratigraphy*, 47(3), pp.263–282.

Kroopnick, P. M. (1985). The distribution of 13C of ΣCO2 in the world oceans. *Deep Sea Research Part A: Oceanographic Research Papers*, 32(1), 57–84. https://doi.org/10.1016/0198-0149(85)90017-2

Kucera, M., Weinelt, M., Kiefer, T., Pflaumann, U., Hayes, A., Weinelt, M., Chen, M.-T., Mix, A. C., Barrows, T. T., Cortijo, E., Duprat, J., Juggins, S., & Waelbroeck, C. (2005). Reconstruction of sea-surface temperatures from assemblages of planktonic foraminifera: multi-technique approach based on geographically constrained calibration data sets and its application to glacial Atlantic and Pacific Oceans. *Quaternary Science Reviews,* 24(7–9), 951–998. https://doi.org/10.1016/j.quascirev.2004.07.014

Kuhlbrodt, T., Griesel, A., Montoya, M., Levermann, A., Hofmann, M., & Rahmstorf, S. (2007). On the driving processes of the Atlantic meridional overturning circulation. *Reviews of Geophysics,* 45(2), RG2001. https://doi.org/10.1029/2004rg000166

Kutzbach, J. E. (1981). Monsoon Climate of the Early Holocene: Climate Experiment with the Earth's Orbital Parameters for 9000 Years Ago. *Science,* 214(4516), 59–61. https://doi.org/10.1126/Science.214.4516.59

Lafuente, J. G., Fanjul, E. Á., Vargas, J. M., & Ratsimandresy, A. W. (2002). Subinertial variability in the flow through the Strait of Gibraltar. *Journal of Geophysical Research: Oceans* (1978–2012), 107(C10), 32-1-31–39. https://doi.org/10.1029/2001jc001104

Lambeck, K., Rouby, H., Purcell, A., Sun, Y., & Sambridge, M. (2014). Sea level and global ice volumes from the Last Glacial Maximum to the Holocene. *Proceedings of the National Academy of Sciences*, 111(43), 15296–15303. https://doi.org/10.1073/pnas.1411762111

Lang, D. C., Bailey, I., Wilson, P. A., Chalk, T. B., Foster, G. L., & Gutjahr, M. (2016). Incursions of southern-sourced water into the deep North Atlantic during late Pliocene glacial intensification. *Nature Geoscience,* 9(5), 375–379. https://doi.org/10.1038/ngeo2688

Larrasoaña, J.C. et al., 2003. Three million years of monsoon variability over the northern Sahara. *Climate Dynamics*, 21(7-8), pp.689–698.

Lawrence, K. T., Sosdian, S., White, H. E., & Rosenthal, Y. (2010). North Atlantic climate evolution through the Plio-Pleistocene climate transitions. *Earth and Planetary Science Letters,* 300(3–4), 329–342. https://doi.org/10.1016/j.epsl.2010.10.013

Lea, D. W., Pak, D. K., & Spero, H. J. (2000). Climate impact of late Quaternary equatorial Pacific sea surface temperature variations. *Science, 289*(5485), 1719-1724.

Lear, C. H., Rickaby, R. E. M., Billups, K., Mawbey, E. M., Diester-Haass, L., & Sosdian, S. M. (2016). Breathing more deeply: Deep ocean carbon storage during the mid-Pleistocene climate transition. *Geology,* 44(12), 1035–1038. https://doi.org/10.1130/g38636.1

Lear, C. H., Rosenthal, Y., & Slowey, N. (2002). Benthic foraminiferal Mg/Ca-paleothermometry: a revised core-top calibration. *Geochimica et Cosmochimica Acta*, 66(19), 3375–3387. https://doi.org/10.1016/s0016-7037(02)00941-9

Ledwell, J. R., Watson, A. J., & Law, C. S. (1993). Evidence for slow mixing across the pycnocline from an open-ocean tracer-release experiment. *Nature,* 364(6439), 701–703.

LeGrande, A. N., & Schmidt, G. A. (2006). Global gridded data set of the oxygen isotopic composition in seawater. *Geophysical Research Letters,* 33(12), 15833–15835. https://doi.org/10.1029/2006gl026011

LeGrande, A. N., Stieglitz, J. L., & Farmer, E. C. (2004). Oxygen isotopic composition of Globorotalia truncatulinoides as a proxy for intermediate depth density. *Paleoceanography*, 19(4), n/a-n/a. https://doi.org/10.1029/2004pa001045

Lehman, S. J., & Keigwin, L. D. (1992). Sudden changes in North Atlantic circulation during the last deglaciation. *Nature,* 356(6372), 757–762. https://doi.org/10.1038/356757a0

Levang, S. J., & Schmitt, R. W. (2020). What Causes the AMOC to Weaken in CMIP5? *Journal of Climate,* 33(4), 1535–1545. https://doi.org/10.1175/jcli-d-19-0547.1

Lippold, J., Gutjahr, M., Blaser, P., Christner, E., Ferreira, M. L. de C., Mulitza, S., Christl, M., Wombacher, F., Böhm, E., Antz, B., Cartapanis, O., Vogel, H., & Jaccard, S. L. (2016). Deep water provenance and dynamics of the (de)glacial Atlantic meridional overturning circulation. *Earth and Planetary Science Letters,* 445, 68–78. https://doi.org/10.1016/j.epsl.2016.04.013

Lisiecki, L. E. (2010). Links between eccentricity forcing and the 100,000-year glacial cycle. *Nature Geoscience,* 3(5), 349–352. https://doi.org/10.1038/ngeo828

Lisiecki, L. E., & Raymo, M. E. (2005). A Pliocene-Pleistocene stack of 57 globally distributed benthic δ18O records. *Paleoceanography*, 20(1). https://doi.org/10.1029/2004pa001071

Liu, Z., Otto-Bliesner, B. L., He, F., He, F., Brady, E. C., Tomas, R., Clark, P. U., Clark, P. U., Carlson, A. E., Lynch-Stieglitz, J., Curry, W. B., Brook, E. J., Erickson, D., Jacob, R., Kutzbach, J., & Cheng, J. (2009). Transient Simulation of Last Deglaciation with a New Mechanism for Bolling-Allerod Warming. *Science,* 325(5938), 310–314. https://doi.org/10.1126/Science.1171041

Locarnini et al., 2013. *World Ocean Atlas 2013, Volume 1: Temperature* S. Levitus & A. V. Mishonov, eds.,

Lohmann, G. P. (1992). Increasing seasonal upwelling in the subtropical South Atlantic over the past 700,000 yrs: Evidence from deep-living planktonic foraminifera. *Marine Micropaleontology,* 19(1–2), 1–12.

Lozier, M. S. (2012). Overturning in the North Atlantic. *Annual Review of Marine Science,* 4(1), 291–315. https://doi.org/10.1146/annurev-marine-120710-100740

Lozier, M. S., & Stewart, N. M. (2008). On the temporally varying northward penetration of Mediterranean Overflow Water and eastward penetration of Labrador Sea water. *Journal of Physical Oceanography*, 38(9), 2097–2103. https://doi.org/10.1175/2008jpo3908.1

Lozier, M. S., Bacon, S., Bower, A. S., Cunningham, S. A., Jong, M. F. de, Steur, L. de, deYoung, B., Fischer, J., Gary, S. F., Greenan, B. J. W., Heimbach, P., Holliday, N. P., Houpert, L., Inall, M. E., Johns, W. E., Johnson, H. L., Karstensen, J., Li, F., Lin, X., … Zika, J. D. (2016). Overturning in the Subpolar North Atlantic Program: a new international ocean observing system. *Bulletin of the American Meteorological Society*, 98(4), 737–752. https://doi.org/10.1175/bams-d-16-0057.1

Lozier, M. S., Li, F., Bacon, S., Bahr, F., Bower, A. S., Cunningham, S. A., Jong, M. F. de, Steur, L. de, deYoung, B., Fischer, J., Gary, S. F., Greenan, B. J. W., Holliday, N. P., Houk, A., Houpert, L., Inall, M. E., Johns, W. E., Johnson, H. L., Johnson, C., … Zhao, J. (2019). A sea change in our view of overturning in the subpolar North Atlantic. *Science,* 363(6426), 516–521. https://doi.org/10.1126/Science.aau6592

Lozier, M. S., Roussenov, V., Reed, M. S. C., & Williams, R. G. (2010). Opposing decadal changes for the North Atlantic meridional overturning circulation. *Nature Geoscience,* 3(10), 728–734. https://doi.org/10.1038/ngeo947

Lynch-Stieglitz, J., Curry, W. B., & Slowey, N. (1999). A geostrophic transport estimate for the Florida Current from the oxygen isotope composition of benthic foraminifera. *Paleoceanography*, 14(3), 360–373. https://doi.org/10.1029/1999pa900001

Lynch-Stieglitz, J., Curry, W. B., Oppo, D. W., Ninneman, U. S., Charles, C. D., & Munson, J. (2006). Meridional overturning circulation in the South Atlantic at the last glacial maximum. *Geochemistry, Geophysics, Geosystems,* 7(10), 14. https://doi.org/10.1029/2005gc001226

MacAyeal, D. R. (1993). Binge/purge oscillations of the Laurentide Ice Sheet as a cause of the North Atlantic's Heinrich events. *Paleoceanography*, 8(6), 775–784. https://doi.org/10.1029/93pa02200

Marchitto, T. M., Curry, W. B., Lynch-Stieglitz, J., Bryan, S. P., Cobb, K. M., & Lund, D. C. (2014). Improved oxygen isotope temperature calibrations for cosmopolitan benthic foraminifera. *Geochimica et Cosmochimica Acta*, *130*, 1–11. https://doi.org/10.1016/j.gca.2013.12.034

McClymont, E.L. et al., 2013. Pleistocene sea-surface temperature evolution: Early cooling, delayed glacial intensification, and implications for the mid-Pleistocene climate transition. *Earth-Science Reviews*, 123, pp.173–193.

Manabe, S., & Stouffer, R. J. (1988). Two Stable Equilibria of a Coupled Ocean-Atmosphere Model. *Journal of Climate,* 1(9), 841–866. https://doi.org/10.1175/1520-0442(1988)001<0841:tseoac>2.0.co;2

Marchitto, T. M., Curry, W. B., Lynch-Stieglitz, J., Bryan, S. P., Cobb, K. M., & Lund, D. C. (2014). Improved oxygen isotope temperature calibrations for cosmopolitan benthic foraminifera. *Geochimica et Cosmochimica Acta*, 130, 1–11. https://doi.org/10.1016/j.gca.2013.12.034

Marcott, S. A., Clark, P. U., Padman, L., Klinkhammer, G. P., Springer, S. R., Liu, Z., Otto-Bliesner, B. L., Carlson, A. E., Ungerer, A., Padman, J., He, F., Cheng, J., & Schmittner, A. (2011). Ice-shelf collapse from subsurface warming as a trigger for Heinrich events. *Proceedings of the National Academy of Sciences,* 108(33), 13415–13419. https://doi.org/10.1073/pnas.1104772108

Martin, P. A., & Lea, D. W. (2002). A simple evaluation of cleaning procedures on fossil benthic foraminiferal Mg/Ca. *Geochemistry, Geophysics, Geosystems,* 3(10), 1–8. https://doi.org/10.1029/2001gc000280

Maslin, M. A., & Brierley, C. M. (2015). The role of orbital forcing in the Early Middle Pleistocene Transition. *Quaternary International*, 389, 47–55. https://doi.org/10.1016/j.quaint.2015.01.047

Maslin, M. A., Shackleton, N. J., & Pflaumann, U. (1995). Surface water temperature, salinity, and density changes in the northeast Atlantic during the last 45,000 years: Heinrich events, deep water formation, and climatic rebounds. *Paleoceanography*, 10(3), 527–544. https://doi.org/10.1029/94pa03040

Mazé, J. P., Arhan, M., & Mercier, H. (1997). Volume budget of the eastern boundary layer off the Iberian Peninsula. *Deep-Sea Research Part I*, 44(9–10), 1543–1574. https://doi.org/10.1016/s0967-0637(97)00038-1

McCartney, M. S. (1982). The subtropical recirculation of Mode Waters. *Journal of Marine Research*, 40, 427–464.

McClymont, E. L., Sosdian, S. M., Rosell-Melé, A., & Rosenthal, Y. (2013). Pleistocene sea-surface temperature evolution: Early cooling, delayed glacial intensification, and implications for the mid-Pleistocene climate transition. *Earth-Science Reviews*, 123, 173–193. https://doi.org/10.1016/j.earscirev.2013.04.006

McDowell, S. E., & Rossby, H. T. (1978). Mediterranean Water: An Intense Mesoscale Eddy off the Bahamas. *Science,* 202(4372), 1085–1087. https://doi.org/10.1126/Science.202.4372.1085

McGee, D., Donohoe, A., Marshall, J., & Ferreira, D. (2014). Changes in ITCZ location and cross-equatorial heat transport at the Last Glacial Maximum, Heinrich Stadial 1, and the mid-Holocene. *Earth and Planetary Science Letters,* 390, 69–79. https://doi.org/10.1016/j.epsl.2013.12.043

McKay, R., Naish, T., Powell, R., Barrett, P., Scherer, R., Talarico, F., Kyle, P., Monien, D., Kuhn, G., Jackolski, C., & Williams, T. (2012). Pleistocene variability of Antarctic Ice Sheet extent in the Ross

Embayment. *Quaternary Science Reviews,* 34, 93–112. https://doi.org/10.1016/j.quascirev.2011.12.012

McManus, J. F., Francois, R., Gherardi, J. M., Keigwin, L. D., & Brown-Leger, S. (2004). Collapse and rapid resumption of Atlantic meridional circulation linked to deglacial climate changes. *Nature,* 428(6985), 834–837. https://doi.org/10.1038/Nature02494

Mecking, J. V., Drijfhout, S. S., Jackson, L. C., & Graham, T. (2016). Stable AMOC off state in an eddy-permitting coupled climate model. *Climate Dynamics*, 47(7–8), 2455–2470. https://doi.org/10.1007/s00382-016-2975-0

Meinen, C. S., Perez, R. C., Dong, S., Piola, A. R., & Campos, E. (2020). Observed Ocean Bottom Temperature Variability at Four Sites in the Northwestern Argentine Basin: Evidence of Decadal Deep/Abyssal Warming Amidst Hourly to Interannual Variability During 2009–2019. *Geophysical Research Letters,* 47(18). https://doi.org/10.1029/2020gl089093

Menviel, L. C., Spence, P., Skinner, L. C., Tachikawa, K., Friedrich, T., Missiaen, L., & Yu, J. (2020). Enhanced Mid-depth Southward Transport in the Northeast Atlantic at the Last Glacial Maximum Despite a Weaker AMOC. *Paleoceanography and Paleoclimatology,* 35(2). https://doi.org/10.1029/2019pa003793

Millo, C., Sarnthein, M., Erlenkeuser, H., & Frederichs, T. (2005). Methane-driven late Pleistocene δ13C minima and overflow reversals in the southwestern Greenland Sea. *Geology*, *33*(11), 873–876. https://doi.org/10.1130/g21790.1

Millot, C. (2009). Another description of the Mediterranean Sea outflow. *Progress in Oceanography*, 82(2), 101–124. https://doi.org/10.1016/j.pocean.2009.04.016

Mimura, N. (2013). Sea-level rise caused by climate change and its implications for society. *Proceedings of the Japan Academy*, Series B, 89(7), 281–301. https://doi.org/10.2183/pjab.89.281

Mook, W. G., Bommerson, J. C., & Staverman, W. H. (1974). Carbon Isotope Fractionation Between Dissolved Bicarbonate and Gaseous Carbon-Dioxide. *Earth and Planetary Science Letters,* 22(2), 169–176.

Naafs, B. D. A., Hefter, J., Acton, G., Haug, G. H., Martínez-Garcia, A., Pancost, R., & Stein, R. (2012). Strengthening of North American dust sources during the late Pliocene (2.7Ma). *Earth and Planetary Science Letters,* 317–318, 8–19. https://doi.org/10.1016/j.epsl.2011.11.026

Naafs, B. D. A., Hefter, J., Ferretti, P., Stein, R., & Haug, G. H. (2011). Sea surface temperatures did not control the first occurrence of Hudson Strait Heinrich Events during MIS 16. *Paleoceanography*, 26(4). https://doi.org/10.1029/2011pa002135

Naafs, B. D. A., Hefter, J., Grutzner, J., & Stein, R. (2013). Warming of surface waters in the mid-latitude North Atlantic during Heinrich events. *Paleoceanography and Paleoclimatology,* 28(1), 153–163. https://doi.org/10.1029/2012pa002354

Ng, H. C., Robinson, L. F., McManus, J. F., Mohamed, K. J., Jacobel, A. W., Ivanovic, R. F., Gregoire, L. J., & Chen, T. (2018). Coherent deglacial changes in western Atlantic Ocean circulation. *Nature Communications,* 9(1), 1–10. https://doi.org/10.1038/s41467-018-05312-3

Nürnberg, D., Bijma, J., & Hemleben, C. (1996). Assessing the reliability of magnesium in foraminiferal calcite as a proxy for water mass temperatures. *Geochimica et Cosmochimica Acta*, 60(5), 803–814. https://doi.org/10.1016/0016-7037(95)00446-7

Olsen, A., Lange, N., Key, R. M., Tanhua, T., Bittig, H. C., Kozyr, A., Àlvarez, M., Azetsu-Scott, K., Becker, S., Brown, P. J., Carter, B. R., Cunha, L. C. da, Feely, R. A., Heuven, S. van, Hoppema, M., Ishii, M., Jeansson, E., Jutterström, S., Landa, C. S., … Woosley, R. J. (2020). GLODAPv2.2020 – the second update of GLODAPv2. *Earth System Science Data Discussions*, 2020, 1–41. https://doi.org/10.5194/essd-2020-165

Oppo, D. W., Curry, W. B., & McManus, J. F. (2015). What do benthic δ13C and δ18O data tell us about Atlantic circulation during Heinrich Stadial 1? *Paleoceanography* and Paleoclimatology. https://doi.org/10.1002/(issn)1944-9186

Oppo, D. W., & Lehman, S. J. (1993). Mid-Depth Circulation of the Subpolar North Atlantic During the Last Glacial Maximum. *Science*, *259*(5098), 1148–1152. https://doi.org/10.1126/science.259.5098.1148

Otto-Bliesner, B. L., & Brady, E. C. (2010). The sensitivity of the climate response to the magnitude and location of freshwater forcing: last glacial maximum experiments. *Quaternary Science Reviews,* 29(1–2), 56–73. https://doi.org/10.1016/j.quascirev.2009.07.004

Paillard, D., Labeyrie, L., & Yiou, P. (2011). Macintosh Program performs time-series analysis. *Eos, Transactions*, American Geophysical Union, 77(39), 379–379. https://doi.org/10.1029/96eo00259

Paul, D., Skrzypek, G., & Fórizs, I. (2007). Normalization of measured stable isotopic compositions to isotope reference scales – a review. *Rapid Communications in Mass Spectrometry*, 21(18), 3006–3014. https://doi.org/10.1002/rcm.3185

Peck, V. L., Hall, I. R., Zahn, R., Elderfield, H., Grousset, F., Hemming, S. R., & Scourse, J. D. (2006). High resolution evidence for linkages between NW European ice sheet instability and Atlantic Meridional Overturning Circulation. *Earth and Planetary Science Letters,* 243(3–4), 476–488. https://doi.org/10.1016/j.epsl.2005.12.023

Pena, L. D., & Goldstein, S. L. (2014). Thermohaline circulation crisis and impacts during the mid-Pleistocene transition. *Science,* 345(6194), 318–322. https://doi.org/10.1126/Science.1249770

Pflaumann, U., Sarnthein, M., Chapman, M., d'Abreu, L., Funnell, B., Huels, M., Kiefer, T., Maslin, M., Schulz, H., Swallow, J., Kreveld, S. van, Vautravers, M., Vogelsang, E., & Weinelt, M. (2003). Glacial North Atlantic: Sea-surface conditions reconstructed by GLAMAP 2000. *Paleoceanography*, 18(3) https://doi.org/10.1029/2002pa000774

Piotrowski, A. M., Goldstein, S. L., Hemming, S. R. & Fairbanks, R. G. (2004). Intensification and variability of ocean thermohaline circulation through the last deglaciation. *Earth and Planetary Science Letters*, 225(1–2), 205–220. https://doi.org/10.1016/j.epsl.2004.06.002

Poggemann, D. W., Nurnberg, D., Hathorne, E. C., Frank, M., Rath, W., Reißig, S., & Bahr, A. (2018). Deglacial Heat Uptake by the Southern Ocean and Rapid Northward Redistribution Via Antarctic Intermediate Water. *Paleoceanography and Paleoclimatology,* 33(11), 1292–1305. https://doi.org/10.1029/2017pa003284

Pöppelmeier, F., Gutjahr, M., Blaser, P., Keigwin, L. D., & Lippold, J. (2018). Origin of Abyssal NW Atlantic Water Masses Since the Last Glacial Maximum. *Paleoceanography and Paleoclimatology,* 33(5), 530–543. https://doi.org/10.1029/2017pa003290

Potter, R. A., & Lozier, M. S. (2004). On the warming and salinification of the Mediterranean outflow waters in the North Atlantic. *Geophysical Research Letters,* 31(1(L01202)), 1–4. https://doi.org/10.1029/2003gl018161

Praetorius, S. K., McManus, J. F., Oppo, D. W., & Curry, W. B. (2008). Episodic reductions in bottom-water currents since the last ice age. *Nature,* 1(7), 449–452. https://doi.org/10.1038/ngeo227

Price, J. F., Baringer, M. O., Lueck, R. G., Johnson, G. C., Ambar, I., Parrilla, G., Cantos, A., Kennelly, M. A., & Sanford, T. B. (1993). Mediterranean Outflow Mixing and Dynamics. *Science,* 259(5099), 1277–1282. https://doi.org/10.1126/Science.259.5099.1277

Rahmstorf, S. (2002). Ocean circulation and climate during the past 120,000 years. *Nature,* 419(6903), 207–214. https://doi.org/10.1038/Nature01090

Rahmstorf, S., & Willebrand, J. (1995). The Role of Temperature Feedback in Stabilizing the Thermohaline Circulation. *Journal of Physical Oceanography*, 25(5), 787–805. https://doi.org/10.1175/1520-0485(1995)025<0787:trotfi>2.0.co;2

Rahmstorf, S., Box, J. E., Feulner, G., Mann, M. E., Robinson, A., Rutherford, S., & Schaffernicht, E. J. (2015). Exceptional twentieth-century slowdown in Atlantic Ocean overturning circulation. *Nature Climate Change*, 5(5), 475–480. https://doi.org/10.1038/nclimate2554

Rasmussen, S. O., Andersen, K. K., Svensson, A. M., Steffensen, J. P., Vinther, B. M., Clausen, H. B., Siggaard-Andersen, M. L., Johnsen, S. J., Larsen, L. B., Dahl-Jensen, D., Bigler, M., Röthlisberger, R., Fischer, H., Goto-Azuma, K., Hansson, M. E., & Ruth, U. (2006). A new Greenland ice core

chronology for the last glacial termination. *Journal of Geophysical Research: Oceans*, 111(D6), D06102-16. https://doi.org/10.1029/2005jd006079

Rasmussen, T. L., & Thomsen, E. (2004). The role of the North Atlantic Drift in the millennial timescale glacial climate fluctuations. *Palaeogeography, Palaeoclimatology, Palaeoecology,* 210(1), 101–116. https://doi.org/10.1016/j.palaeo.2004.04.005

Rasmussen, T. L., Thomsen, E., & Moros, M. (2016). North Atlantic warming during Dansgaard-Oeschger events synchronous with Antarctic warming and out-of-phase with Greenland climate. *Scientific Reports,* 6(1), 1–12. https://doi.org/10.1038/srep20535

Ravelo, A. C., & Fairbanks, R. G. (1995). Carbon isotopic fractionation in multiple species of planktonic foraminifera from core-tops in the tropical Atlantic. *Oceanographic Literature Review,* 10(42), 854.

Raymo, M. E. (1997). The timing of major climate terminations. *Paleoceanography*, 12(4), 577–585. https://doi.org/10.1029/97pa01169

Raymo, M. E., Oppo, D. W., Flower, B. P., Hodell, D. A., McManus, J. F., Venz, K. A., Kleiven, K. F., & McIntyre, K. (2004). Stability of North Atlantic water masses in face of pronounced climate variability during the Pleistocene. *Paleoceanography and Paleoclimatology*, *19*(2), n/a-n/a. https://doi.org/10.1029/2003pa000921

Raymo, M. E., Lisiecki, L. E., & Nisancioglu, K. H. (2006). Plio-Pleistocene Ice Volume, Antarctic Climate, and the Global δ18O Record. *Science,* 313(5786), 492–495. https://doi.org/10.1126/Science.1123296

Raymo, M. E., Ruddiman, W. F., Shackleton, N. J., & Oppo, D. W. (1990). Evolution of Atlantic-Pacific δ13C gradients over the last 2.5 my. *Earth and Planetary Science Letters,* 97(3–4), 353–368. https://doi.org/10.1016/0012-821x(90)90051-x

Regenberg, M., Regenberg, A., Schönberg, D. G., & Lea, D. W. (2014). Global dissolution effects on planktonic foraminiferal Mg/Ca ratios controlled by the calcite-saturation state of bottom waters. *Paleoceanography*, 29(3), 127–142. https://doi.org/10.1002/2013pa002492

Regenberg, M., Steph, S., Nürnberg, D., Tiedemann, R., & Garbe-Schönberg, D. (2009). Calibrating Mg/Ca ratios of multiple planktonic foraminiferal species with δ18O-calcification temperatures: Paleothermometry for the upper water column. *Earth and Planetary Science Letters,* 278(3–4), 324–336. https://doi.org/10.1016/j.epsl.2008.12.019

Reid, J. L. (1979). On the contribution of the Mediterranean Sea outflow to the Norwegian-Greenland Sea. *Deep Sea Research Part A: Oceanographic Research Papers*, 26(11), 1199–1223. https://doi.org/10.1016/0198-0149(79)90064-5

Reid, J. L. (1994). On the total geostrophic circulation of the North Atlantic Ocean: Flow patterns, tracers, and transports. *Progress in Oceanography*, 33(1), 1–92. https://doi.org/10.1016/0079-6611(94)90014-0

Reißig, S., Nurnberg, D., Bahr, A., Poggemann, D. W., & Hoffmann, J. (2019). Southward displacement of the North Atlantic Subtropical Gyre circulation system during North Atlantic cold spells. *Paleoceanography and Paleoclimatology,* 2018PA003376-40. https://doi.org/10.1029/2018pa003376

Repschläger, J., Weinelt, M., Kinkel, H., Andersen, N., Garbe-Schönberg, D., & Schwab, C. (2015). Response of the subtropical North Atlantic surface hydrography on deglacial and Holocene AMOC changes. *Paleoceanography and Paleoclimatology,* 30(5), 456–476. https://doi.org/10.1002/2014pa002637

Richardson, P. L., McCartney, M. S., & Maillard, C. (1991). A search for meddies in historical data. *Dynamics of Atmospheres and Oceans*, 15(3–5), 241–265. https://doi.org/10.1016/0377-0265(91)90022-8

Richardson, P. L., Price, J. F., Walsh, D., Armi, L., & Schröder, M. (1989). Tracking Three Meddies with SOFAR Floats. *Journal of Physical Oceanography*, 19(3), 371–383. https://doi.org/10.1175/1520-0485(1989)019<0371:ttmwsf>2.0.co;2

Rogerson, M., Rohling, E. J., Bigg, G. R., & Ramirez, J. (2012). Paleoceanography of the Atlantic-Mediterranean exchange: Overview and first quantitative assessment of climatic forcing. *Reviews of Geophysics,* 50(2), 46–32. https://doi.org/10.1029/2011rg000376

Rogerson, M., Rohling, E. J., Weaver, P. P. E., & Murray, J. W. (2005). Glacial to interglacial changes in the settling depth of the Mediterranean Outflow plume. *Paleoceanography and Paleoclimatology,* 20(3), n/a-n/a. https://doi.org/10.1029/2004pa001106

Rohling, E. J., & Cooke, S. (1999). Stable oxygen and carbon isotopes in foraminiferal carbonate shells. In: *Modern Foraminifera*, B. K. S. Gupta, pp. 239–258. Kluwer Academic Publishers. https://doi.org/10.1007/0-306-48104-9_14

Rohling, E. J., Foster, G. L., Grant, K. M., Marino, G., Roberts, A. P., Tamisiea, M. E., & Williams, F. (2014). Sea-level and deep-sea-temperature variability over the past 5.3 million years. *Nature,* 508(7497), 477–482. https://doi.org/10.1038/Nature13230

Ruddiman, W. F., & McIntyre, A. (1981). Oceanic Mechanisms for Amplification of the 23,000-Year Ice-Volume Cycle. *Science,* 212(4495), 617–627. https://doi.org/10.1126/Science.212.4495.617

Ruddiman, W. F., Raymo, M. E., Martinson, D. G., Clement, B. M., & Backman, J. (1989). Pleistocene evolution: Northern Hemisphere ice sheets and North Atlantic Ocean. *Paleoceanography*, 4(4), 353–412.

Rühlemann, C., Mulitza, S., Lohmann, G., Paul, A., Prange, M., & Wefer, G. (2004). Intermediate depth warming in the tropical Atlantic related to weakened thermohaline circulation: Combining paleoclimate data and modeling results for the last deglaciation. *Paleoceanography*, 19(1), https://doi.org/10.1029/2003pa000948

Russell, A. D., Hönisch, B., Spero, H. J., & Lea, D. W. (2004). Effects of seawater carbonate ion concentration and temperature on shell U, Mg, and Sr in cultured planktonic foraminifera. *Geochimica et Cosmochimica Acta*, 68(21), 4347–4361. https://doi.org/10.1016/j.gca.2004.03.013

Salgueiro, E., Naughton, F., Voelker, A. H. L., Abreu, L. de, Alberto, A., Rossignol, L., Duprat, J., Magalhães, V. H., Vaqueiro, S., Turon, J.-L., & Abrantes, F. (2014). Past circulation along the western Iberian margin: a time slice vision from the Last Glacial to the Holocene. *Quaternary Science Reviews,* 106, 316–329. https://doi.org/10.1016/j.quascirev.2014.09.001

Sarnthein, M., Winn, K., Jung, S. J. A., Duplessy, J., Labeyrie, L., Erlenkeuser, H., & Ganssen, G. (1994). Changes in East Atlantic Deepwater Circulation over the last 30,000 years: Eight time slice reconstructions. *Paleoceanography*, *9*(2), 209–267. https://doi.org/10.1029/93pa03301

Sarnthein, M., Jansen, E., Weinelt, M., Arnold, M., Duplessy, J. C., Erlenkeuser, H., Flatøy, A., Johannessen, G., Johannessen, T., Jung, S., Koc, N., Labeyrie, L., Maslin, M., Pflaumann, U., & Schulz, H. (1995). Variations in Atlantic surface ocean *Paleoceanography*, 50°-80°N: A time-slice record of the last 30,000 years. *Paleoceanography*, 10(6), 1063–1094. https://doi.org/10.1029/95pa01453

Sarnthein, M., Pflaumann, U., & Weinelt, M. (2003). Past extent of sea ice in the northern North Atlantic inferred from foraminiferal paleotemperature estimates. *Paleoceanography*, 18(2), n/a-n/a. https://doi.org/10.1029/2002pa000771

Schiebel, R., & Hemleben, C. (2017). Planktic Foraminifers in the Modern Ocean. 177–207. https://doi.org/10.1007/978-3-662-50297-6_6

Schmidt, M. W., Chang, P., Hertzberg, J. E., Them, T. R. I., Link, J., & Otto-Bliesner, B. L. (2012). Impact of abrupt deglacial climate change on tropical Atlantic subsurface temperatures. *Proceedings of the National Academy of Sciences,* 109(36), 14348–14352. https://doi.org/10.1073/pnas.1207806109

Schmitt, A., Elliot, M., Thirumalai, K., La, C., Bassinot, F., Petersen, J., Movellan, A., Jorry, S. J., & Borgomano, J. (2019). Single foraminifera Mg/Ca analyses of past glacial-interglacial temperatures derived from G. ruber sensu stricto and sensu lato morphotypes. *Chemical Geology,* 511, 510–520. https://doi.org/10.1016/j.chemgeo.2018.11.007

Schmittner, A., Gruber, N., Mix, A. C., Key, R. M., Tagliabue, A., & Westberry, T. K. (2013). Biology and air–sea gas exchange controls on the distribution of carbon isotope ratios ($\delta^{13}C$) in the ocean. *Biogeosciences*, *10*(9), 5793–5816. https://doi.org/10.5194/bg-10-5793-2013

Seo, I., Lee, Y. I., Kim, W., Yoo, C. M., & Hyeong, K. (2015). Movement of the Intertropical Convergence Zone during the mid-pleistocene transition and the response of atmospheric and surface ocean circulations in the central equatorial Pacific. *Geochemistry, Geophysics, Geosystems,* 16(11), 3973–3981. https://doi.org/10.1002/2015gc006077

Sévellec, F., & Fedorov, A. V. (2016). AMOC sensitivity to surface buoyancy fluxes: Stronger ocean meridional heat transport with a weaker volume transport? *Climate Dynamics*, 47(5–6), 1497–1513. https://doi.org/10.1007/s00382-015-2915-4

Sévellec, F., Verdiére, A. C. de, & Ollitrault, M. (2017). Evolution of Intermediate Water Masses Based on Argo Float Displacements. *Journal of Physical Oceanography*, 47(7), 1569–1586. https://doi.org/10.1175/jpo-d-16-0182.1

Shackelton, N. (1967). Oxygen Isotope Analyses and Pleistocene Temperatures Re-assessed. *Nature,* 215(5096), 15–17. https://doi.org/10.1038/215015a0

Shackleton, N. J. (1974). Attainment of isotopic equilibrium between ocean water and the benthonic foraminifera genus Uvigerina: isotopic changes in the ocean during the last glacial. *Colloques Internationaux du C.R.N.S.*, 219

Shackleton, N. J., & Opdyke, N. D. (1973). Oxygen isotope and palaeomagnetic stratigraphy of Equatorial Pacific core V28-238: Oxygen isotope temperatures and ice volumes on a 105 year and 106 year scale. *Quaternary Research,* 3(1), 39–55. https://doi.org/10.1016/0033-5894(73)90052-5

Shackleton, N. J., Berger, A., & Peltier, W. R. (1990). An alternative astronomical calibration of the lower Pleistocene timescale based on ODP Site 677. *Transactions of the Royal Society of Edinburgh: Earth Sciences,* 81(4), 251–261. https://doi.org/10.1017/s0263593300020782

Shakun, J. D., Raymo, M. E., & Lea, D. W. (2016). An early Pleistocene Mg/Ca-δ 18O record from the Gulf of Mexico: Evaluating ice sheet size and pacing in the 41-kyr world. *Paleoceanography*, 31(7), 1011–1027. https://doi.org/10.1002/2016pa002956

Sigman, D. M., & Boyle, E. A. (2000). Glacial/Interglacial variations in atmospheric carbon dioxide. *Nature,* 407, 859–869.

Skinner, L. C., & Shackleton, N. J. (2005). An Atlantic lead over Pacific deep-water change across Termination I: implications for the application of the marine isotope stage stratigraphy. *Quaternary Science Reviews,* 24(5–6), 571–580. https://doi.org/10.1016/j.quascirev.2004.11.008

Skinner, L. C., Fallon, S., Waelbroeck, C., Michel, E., & Barker, S. (2010). Ventilation of the deep Southern Ocean and deglacial CO2 rise. *Science* (New York, N.Y.), 328(5982), 1147–1151. https://doi.org/10.1126/Science.1183627

Skliris, N. (2013). The Mediterranean Sea, Its history and present challenges. 29–48. https://doi.org/10.1007/978-94-007-6704-1_3

Smith, M., Glick, E., Lodestro, S., & Rashid, H. (2013). Data report: Oxygen isotopes and foraminifer abundance record for the last glacial–interglacial cycle and marine isotope stage 6 at IODP Site U1313 (J. E. T. Channel, T Kanamatsu, T Sato, Ruediger Stein, Carlos A Alvarez Zarikian, M J Malone, & E. 303/306 Scientists, Eds.; Vol. 303/306). Integrated Ocean Drilling Program Management International. https://doi.org/doi:10.2204/iodp.proc.303306.216.2013

Soto-Navarro, J., Somot, S., Sevault, F., Beuvier, J., Criado-Aldeanueva, F., García-Lafuente, J., & Béranger, K. (2015). Evaluation of regional ocean circulation models for the Mediterranean Sea at the Strait of Gibraltar: volume transport and thermohaline properties of the outflow. *Climate Dynamics*, 44(5), 1277–1292. https://doi.org/10.1007/s00382-014-2179-4

Spall, M. A. (1999). A simple model of the large-scale circulation of Mediterranean Water and Labrador Sea Water. *Deep Sea Research Part II: Topical Studies in Oceanography*, 46(1–2), 181–204. https://doi.org/10.1016/s0967-0645(98)00105-2

Speich, S., Reverdin, G., Mercier, H., Jeandel, C. (2017). Ocean, heat reservoir, ocean-climate.org pp. 1-12, retrieved from site: https://www.ocean-climate.org/wp-content/uploads/2017/03/ocean-heat-reservoir.pdf.

Spero, H. J., Bijma, J., Lea, D. W., & Bemis, B. E. (1997). Effect of seawater carbonate concentration on foraminiferal carbon and oxygen isotopes. *Nature,* 390(6659), 497–500.

Spratt, R. M., & Lisiecki, L. E. (2016). A Late Pleistocene sea level stack. *Climate of the Past,* 12(4), 1079–1092. https://doi.org/10.5194/cp-12-1079-2016

Stein, R., Hefter, J., Grützner, J., Voelker, A., & Naafs, B. D. A. (2009). Variability of surface water characteristics and Heinrich-like events in the Pleistocene midlatitude North Atlantic Ocean: Biomarker and XRD records from IODP Site U1313 (MIS 16-9). *Paleoceanography and Paleoclimatology,* 24(2), PA2203 (1-13). https://doi.org/10.1029/2008pa001639

Stern, J. V., & Lisiecki, L. E. (2013). North Atlantic circulation and reservoir age changes over the past 41,000 years. *Geophysical Research Letters,* 40(14), 3693–3697. https://doi.org/10.1002/grl.50679

Stocker, T. F., & Johnsen, S. J. (2003). A minimum thermodynamic model for the bipolar seesaw: THERMAL BIPOLAR SEESAW. *Paleoceanography*, 18(4), n/a-n/a. https://doi.org/10.1029/2003pa000920

Stommel, H. (1961). Thermohaline Convection with Two Stable Regimes of Flow. *Tellus B,* 13(2). https://doi.org/10.3402/tellusb.v13i2.12985

Stríkis, N. M., Chiessi, C. M., Cruz, F. W., Vuille, M., Cheng, H., Barreto, E. A. de S., Mollenhauer, G., Karsten, S., Karmann, I., Edwards, R. L., Bernal, J. P., & Sales, H. dos R. (2015). Timing and structure of Mega-SACZ events during Heinrich Stadial 1. *Geophysical Research Letters,* 42, 1–8. https://doi.org/10.1002/(issn)1944-8007

Sutton, R. T., & Allen, M. R. (1997). Decadal predictability of North Atlantic sea surface temperature and climate. *Nature,* 388(6642), 563–567. https://doi.org/10.1038/41523

Tachikawa, K., Rapuc, W., Vidal, L., Dubois-Dauphin, Q., Westerhold, T., Guihou, A., Bickert, T., Pérez-Asensio, J. N., Deschamps, P., & Skonieczny, C. (2021). Eastern Atlantic deep-water circulation and carbon storage inferred from neodymium and carbon isotopic compositions over the past 1.1 million years. *Quaternary Science Reviews*, *252*, 106752. https://doi.org/10.1016/j.quascirev.2020.106752

Talley, L. D. (2008). Freshwater transport estimates and the global overturning circulation: Shallow, deep and throughflow components. *Progress in Oceanography*, 78(4), 257–303. https://doi.org/10.1016/j.pocean.2008.05.001

Talley, L. D. (2011). Descriptive physical oceanography: an introduction. Academic Press.

Talley, L. D., & McCartney, M. S. (1982). Distribution and circulation of Labrador Sea water. *Journal of Physical Oceanography*, 12, 1189–1205.

Thiagarajan, N., Subhas, A. V., Southon, J. R., Eiler, J. M., & Adkins, J. F. (2014). Abrupt pre-Bølling–Allerød warming and circulation changes in the deep ocean. *Nature,* 511(7507), 75–78. https://doi.org/10.1038/Nature13472

Thiede, J., Jessen, C., Knutz, P., Kuijpers, A., Mikkelsen, N., & Spielhagen, R. F. (2011). Millions of years of Greenland Ice Sheet history recorded in ocean sediments. Polarforschung, 80(3), 141-159.

Timmermann, A., Knies, J., Timm, O. E., Ouchi, A. A., & Friedrich, T. (2010). Promotion of glacial ice sheet buildup 60–115 kyr B.P. by precessionally paced Northern Hemispheric meltwater pulses. *Paleoceanography*, 25(4), PA4208. https://doi.org/10.1029/2010pa001933

Todd, R. E., Rudnick, D. L., Mazloff, M. R., Cornuelle, B. D., & Davis, R. E. (2012). Thermohaline structure in the California Current System: Observations and modeling of spice variance. *Journal of Geophysical Research: Oceans*, *117*(C2).

Toucanne, S., Soulet, G., Freslon, N., Jacinto, R. S., Dennielou, B., Zaragosi, S., Eynaud, F., Bourillet, J.-F., & Bayon, G. (2015). Millennial-scale fluctuations of the European Ice Sheet at the end of the

last glacial, and their potential impact on global climate. *Quaternary Science Reviews,* 123, 113–133. https://doi.org/10.1016/j.quascirev.2015.06.010

Trauth, M.H., Larrasoana, J.C. & Mudelsee, M., 2009. Trends, rhythms and events in Plio-Pleistocene African climate. *Quaternary Science Reviews,* 28(5-6), pp.399–411.

Tsuchiya, M., Talley, L. D., & McCartney, M. S. (1992). An eastern Atlantic section from Iceland southward across the equator. *Deep Sea Research Part A: Oceanographic Research Papers*, 39(11–12), 1885–1917. https://doi.org/10.1016/0198-0149(92)90004-d

Valley, S., Lynch-Stieglitz, J., & Marchitto, T. M. (2017). Timing of Deglacial AMOC Variability From a High-Resolution Seawater Cadmium Reconstruction. *Paleoceanography and Paleoclimatology,* 32(11), 1195–1203. https://doi.org/10.1002/2017pa003099

Van Dijk, J., Ziegler, M., De Nooijer, L. J., Reichart, G. J., Xuan, C., Ducassou, E., ... & Lourens, L. J. (2018). A saltier glacial mediterranean outflow. *Paleoceanography and Paleoclimatology,* 33(2), 179-197. https://doi.org/10.1002/2017pa003228

Vernal, A. de, Rosell-Melé, A., Kucera, M., Hillaire-Marcel, C., Eynaud, F., Weinelt, M., Dokken, T., & Kageyama, M. (2006). Comparing proxies for the reconstruction of LGM sea-surface conditions in the northern North Atlantic. *Quaternary Science Reviews,* 25(21–22), 2820–2834. https://doi.org/10.1016/j.quascirev.2006.06.006

Veum, T., Jansen, E., Arnold, M., Beyer, I., & Duplessy, J.-C. (1992). Water mass exchange between the North Atlantic and the Norwegian Sea during the past 28,000 years. *Nature*, *356*(6372), 783–785. https://doi.org/10.1038/356783a0

Voelker, A. H. L., Sarnthein, M., Grootes, P. M., Erlenkeuser, H., Laj, C., Mazaud, A., Nadeau, M.-J., & Schleicher, M. (1998). Correlation of Marine 14C Ages from the Nordic Seas with the GISP2 Isotope Record: Implications for 14C Calibration Beyond 25 ka BP. *Radiocarbon*, 40(1), 517–534. https://doi.org/10.1017/s0033822200018397

Voelker, A., Lebreiro, S., Schonfeld, J., Cacho, I., Erlenkeuser, H., & Abrantes, F. (2006). Mediterranean outflow strengthening during northern hemisphere coolings: A salt source for the glacial Atlantic? *Earth and Planetary Science Letters,* 245(1–2), 39–55. https://doi.org/10.1016/j.epsl.2006.03.014

Waelbroeck, C., Labeyrie, L., Michel, E., Duplessy, J. C., McManus, J. F., Lambeck, K., Balbon, E., & Labracherie, M. (2002). Sea-level and deep water temperature changes derived from benthic foraminifera isotopic records. *Quaternary Science Reviews,* 21, 295–305.

Waelbroeck, C., Skinner, L. C., Labeyrie, L., Duplessy, J. C., Michel, E., Riveiros, N. V., Gherardi, J. M., & Dewilde, F. (2011). The timing of deglacial circulation changes in the Atlantic. *Paleoceanography and Paleoclimatology,* 26(3), n/a-n/a. https://doi.org/10.1029/2010pa002007

Weinelt, M., Vogelsang, E., Kucera, M., Pflaumann, U., Sarnthein, M., Voelker, A., Erlenkeuser, H., & Malmgren, B. A. (2003). Variability of North Atlantic heat transfer during MIS 2. *Paleoceanography*, 18(3). https://doi.org/10.1029/2002pa000772

Weldeab, S., Friedrich, T., Timmermann, A., & Schneider, R. R. (2016). Strong middepth warming and weak radiocarbon imprints in the equatorial Atlantic during Heinrich 1 and Younger Dryas. *Paleoceanography*, 31(8), 1070–1082. https://doi.org/10.1002/2016pa002957

Wüst, G., 1957. Wissenschaftliche Ergebnisse der deutschen atlantischen Expedition “Meteor”, vol. 6. Walter de Gruyter, Berlin, part 2, pp. 1e208 (in German)

Yu, J., & Elderfield, H. (2008). Mg/Ca in the benthic foraminifera Cibicidoides wuellerstorfi and Cibicidoides mundulus: Temperature versus carbonate ion saturation. *Earth and Planetary Science Letters,* 276(1–2), 129–139. https://doi.org/10.1016/j.epsl.2008.09.015

Yu, J., Menviel, L., Jin, Z. D., Anderson, R. F., Jian, Z., Piotrowski, A. M., Ma, X., Rohling, E. J., Zhang, F., Marino, G., & McManus, J. F. (2020). Last glacial atmospheric CO2 decline due to widespread Pacific deep-water expansion. *Nature,* 1–18. https://doi.org/10.1038/s41561-020-0610-5

Yu, J., Yu, J., Menviel, L., Jin, Z. D., *Nature,* D. T., & 2019. (2019). More efficient North Atlantic carbon pump during the Last Glacial Maximum. *Nature Communications*, 10(1), 554. https://doi.org/10.1038/s41467-019-10028-z.

Zahn, R., Sarnthein, M., & Erlenkeuser, H. (1987). Benthic isotope evidence for changes of the Mediterranean outflow during the Late Quaternary. *Paleoceanography*, *2*(6), 543–559. https://doi.org/10.1029/pa002i006p00543

Zahn, R., Winn, K., & Sarnthein, M. (1986). Benthic foraminiferal δ13C and accumulation rates of organic carbon: Uvigerina peregrina group and Cibicidoides wuellerstorfi. *Paleoceanography*.

Zavatarielli, M., & Mellor, G. L. (1995). A Numerical Study of the Mediterranean Sea Circulation. *Journal of Physical Oceanography*, 25(6), 1384–1414. https://doi.org/10.1175/1520-0485(1995)025

Zhang, X., Lohmann, G., Knorr, G., & Purcell, C. (2014). Abrupt glacial climate shifts controlled by ice sheet changes. *Nature,* 512(7514), 290–294. https://doi.org/10.1038/Nature13592

Zhao, N., Oppo, D. W., Huang, K.-F., Howe, J. N. W., Blusztajn, J., & Keigwin, L. D. (2019). Glacial–interglacial Nd isotope variability of North Atlantic Deep Water modulated by North American ice sheet. *Nature Communications,* 10(1), 1–10. https://doi.org/10.1038/s41467-019-13707-z

Ziegler, M., Diz, P., Hall, I. R., & Zahn, R. (2013). Millennial-scale changes in atmospheric CO 2 levels linked to the Southern Ocean carbon isotope gradient and dust flux. *Nature,* 6(6), 457–461. https://doi.org/10.1038/ngeo1782

Agradecimentos

I'm thankful to everyone that came along on this journey with me and the list has to start with my very patient supervisors, André Bahr and Oliver Friedrich. Thank you for the opportunities, the scientific discussions and everything else, you are great! I'd also like to acknowledge all my wonderful colleagues and friends that made me company throughout these years and provided a lot of help, both in keeping my sanity and in finishing this thesis. Thank you Lisa Egger, Swaantje Brzerlinski, Polina Vakhrameeva, Alicia Hou, Tobias Fischer, Martina Vannacci, Andreas Koutsodendris. For the great scientific discussions and insights, I'd like to thank my coauthors Nick Foukal and Xu Zhang, but also Finn Süfke, Frerk Pöppelmeier, and Patrick Blaser.

Eu também preciso muito agradecer aos meus amigos do outro lado do oceano, que me ajudaram a trazer comigo um pedaço de casa. Lugar, sem seu apoio meu bem, essa tese quase que não sai. Gemida, Piroca, Dani, Camila, Xumaço, Mihang, Luís, Cammy e Bárbara, por favor continuem comigo pra onde quer que eu vá. Quero citar meus irmãos também porque eles muito supimpas, Gustavo e Arthur. Mãe e pai, amo vocês. E pro Daniel, meu companheiro de vida, obrigada por estar comigo em todos os momentos, pela sua paciência e por ter mantido alimentados eu e Uli durante todos esses meses loucos de final de tese. Obrigada também pelo brilho dos meus olhos, Ulisses.

Data Appendix

Table A1. Tie points between LR04 and Site U1313 on the amcd depth scale.

Depth (amcd)	Age (ka)
27.72	562.3
28.58	580.8
29.66	602.8
30.63	621.1
34.87	713.5
36.52	743.7
37.32	758.3
38.44	790.1
39.10	805.9
40.07	825.7
41.63	866.8
42.94	900.1
43.83	917.5
46.22	968.0
47.27	991.4
48.49	1014.2
49.21	1032.2
50.75	1064.9
51.69	1086.1
52.90	1116.0
54.07	1138.3
56.11	1189.7

Table A2. All other data produced within the framework of this thesis (next page)

Sample Label	Laboratory ID	Age (ka)	Comp. depth (m, MCD)	Adjusted MCD (m, AMCD)	$\delta^{18}O$ (‰, VPDB)	$\delta^{13}C$ (‰, VPDB)	Mg/Ca (mmol/mol)	Fe/Ca (mmol/mol)	Mn/Ca (mmol/mol)	SubT (°C)	$\delta 18O_{sw\text{-}ivc}$ (‰, VPDB)	Species
306-U1313B-1H-1W,4.5-6.5	E52	5.76	0.22	0.22	1.88	1.15						*G. crassaformis*
306-U1313B-1H-1W,4.5-6.5	E1	5.76	0.22	0.22	1.03	0.93	1.42	0.01	0.01	11.70	0.28	*G. truncatulinoides (d)*
306-U1313B-1H-1W,6.5-7.5	D92	6.37	0.24	0.24	1.13	1.30	1.24	0.00	0.00	9.91	-0.05	*G. truncatulinoides (d)*
306-U1313B-1H-1W,6.5-7.5	D92	6.37	0.24	0.24	1.04	0.85						*G. truncatulinoides (d)*
306-U1313B-1H-1W,8.75-10.75	D80	7.05	0.26	0.26	1.04	0.81	1.34	0.00	0.00	10.95	0.16	*G. truncatulinoides (d)*
306-U1313B-1H-1W,8.75-10.75	D80	7.05	0.26	0.26	1.16	0.70						*G. truncatulinoides (d)*
306-U1313B-1H-1A,11-13	E2	7.74	0.28	0.28	1.06	0.84	1.40	0.01	0.01	11.52	0.21	*G. truncatulinoides (d)*
306-U1313B-1H-1A,11-13	E2	7.74	0.28	0.28	1.08	1.14						*G. truncatulinoides (d)*
306-U1313B-1H-1W,13-15	D81	8.35	0.30	0.30	0.95	0.99	1.34	0.00	0.00	10.90	-0.10	*G. truncatulinoides (d)*
306-U1313B-1H-1W,13-15	D81	8.35	0.30	0.30	0.92	0.83						*G. truncatulinoides (d)*
306-U1313B-1H-1W,15-17	E3	8.96	0.32	0.32	1.04	0.97	1.56	0.01	0.01	12.92	0.34	*G. truncatulinoides (d)*
306-U1313B-1H-1W,16.5-18.5	D82	9.41	0.34	0.34	0.89	0.67	1.36	0.00	0.00	11.10	-0.19	*G. truncatulinoides (d)*
306-U1313B-1H-1W,16.5-18.5	D82	9.41	0.34	0.34	1.02	0.91						*G. truncatulinoides (d)*
306-U1313B-1H-1W,18-19	E4	9.87	0.35	0.35	1.16	0.98	1.40	0.02	0.01	11.47	-0.03	*G. truncatulinoides (d)*
306-U1313B-1H-1W,18-19	E4	9.87	0.35	0.35	0.98	0.99						*G. truncatulinoides (d)*
306-U1313B-1H-1A,19-21	E5	10.17	0.36	0.36	1.14	1.01	1.51	0.03	0.01	12.51	0.20	*G. truncatulinoides (d)*
306-U1313B-1H-1W,22-24	D83	11.08	0.39	0.39	1.13	0.94	1.55	0.00	0.00	12.88	0.12	*G. truncatulinoides (d)*
306-U1313B-1H-1W,22-24	D83	11.08	0.39	0.39	1.10	0.96						*G. truncatulinoides (d)*
306-U1313B-1H-1A,25-27	E6	12.00	0.42	0.42	1.40	0.58	1.46	0.02	0.01	12.03	0.16	*G. truncatulinoides (d)*
306-U1313B-1H-1A,25-27	E6	12.00	0.42	0.42	1.37	0.90						*G. truncatulinoides (d)*
306-U1313B-1H-1W,27-29	D64	12.61	0.44	0.44	1.07	0.70	1.41	0.05	0.00	11.61	-0.28	*G. truncatulinoides (d)*
306-U1313B-1H-1W,29-32	D84	13.22	0.46	0.46	1.40	0.64	1.80	0.00	0.00	14.81	0.59	*G. truncatulinoides (d)*
306-U1313B-1H-1W,29-32	D84	13.22	0.46	0.46	1.15	0.35						*G. truncatulinoides (d)*
306-U1313B-1H-1W,29-32	D84	13.22	0.46	0.46	1.49	0.66						*G. truncatulinoides (d)*
306-U1313B-1H-1A,31-33	E7	13.80	0.48	0.48	1.19	0.61	1.83	0.05	0.01	15.06	0.43	*G. truncatulinoides (d)*
306-U1313B-1H-1W,33-34	D61	14.33	0.50	0.50	1.56	0.71	1.74	0.00	0.00	14.38	0.47	*G. truncatulinoides (d)*
306-U1313B-1H-1W,33-34	D61	14.33	0.50	0.50	1.40	0.67						*G. truncatulinoides (d)*

Sample Label	Laboratory ID	Age (ka)	Comp. depth (m, MCD)	Adjusted MCD (m, AMCD)	$\delta^{18}O$ (‰, VPDB)	$\delta^{13}C$ (‰, VPDB)	Mg/Ca (mmol/mol)	Fe/Ca (mmol/mol)	Mn/Ca (mmol/mol)	SubT (°C)	$\delta 18O_{sw\text{-}ivc}$ (‰, VPDB)	Species
306-U1313B-1H-1W,34-35.5	E8	14.59	0.51	0.51	1.44	0.68	1.74	0.03	0.01	14.38	0.37	*G. truncatulinoides (d)*
306-U1313B-1H-1W,34-35.5	E8	14.59	0.51	0.51	1.49	0.59						*G. truncatulinoides (d)*
306-U1313B-1H-1A,36-38	E9	15.06	0.53	0.53	1.54	0.44	2.70	0.06	0.01	20.27	1.70	*G. truncatulinoides (d)*
306-U1313B-1H-1W,37-39	D85	15.26	0.54	0.54	1.75	0.76	1.81	0.00	0.00	14.93	0.69	*G. truncatulinoides (d)*
306-U1313B-1H-1W,37-39	D85	15.26	0.54	0.54	1.60	0.55						*G. truncatulinoides (d)*
306-U1313B-1H-1W,39-41	E10	15.60	0.56	0.56	1.82	0.63	1.58	0.02	0.01	13.12	0.36	*G. truncatulinoides (d)*
306-U1313B-1H-1W,39-41	E10	15.60	0.56	0.56	1.76	0.45						*G. truncatulinoides (d)*
306-U1313B-1H-1A,41-43	E11	15.88	0.58	0.58	2.09	0.55	1.92	0.02	0.01	15.68	0.42	*G. truncatulinoides (d)*
306-U1313B-1H-1W,41-43	D59	15.88	0.58	0.58	0.90	0.90	1.99	0.00	0.00	16.16	0.42	*G. truncatulinoides (d)*
306-U1313B-1H-1A,41-43	E11	15.88	0.58	0.58	1.15	0.60						*G. truncatulinoides (d)*
306-U1313B-1H-1W,41-43	D59	15.88	0.58	0.58	1.09	0.71						*G. truncatulinoides (d)*
306-U1313B-1H-1A,43-45	E12	16.13	0.60	0.60	1.60	0.88	1.66	0.02	0.01	13.76	0.39	*G. truncatulinoides (d)*
306-U1313B-1H-1A,43-45	E12	16.13	0.60	0.60	2.11	0.90						*G. truncatulinoides (d)*
306-U1313B-1H-1A,43-45	E12	16.13	0.60	0.60	1.57	0.64						*G. truncatulinoides (d)*
306-U1313B-1H-1W,45-47	D86	16.36	0.62	0.62	2.12	0.56	1.56	0.00	0.00	12.93	0.19	*G. truncatulinoides (d)*
306-U1313B-1H-1W,45-47	D86	16.36	0.62	0.62	1.41	0.80						*G. truncatulinoides (d)*
306-U1313B-1H-1A,46-48	E13	16.47	0.63	0.63	1.82	0.55	1.71	0.01	0.01	14.18	0.50	*G. truncatulinoides (d)*
306-U1313B-1H-1W,47.5-49.5	D87	16.64	0.65	0.65	2.02	0.81	1.79	0.00	0.00	14.77	0.59	*G. truncatulinoides (d)*
306-U1313B-1H-1W,47.5-49.5	D87	16.64	0.65	0.65	1.56	0.51						*G. truncatulinoides (d)*
306-U1313B-1H-1A,49.5-51.5	E14	16.86	0.67	0.67	1.97	0.75	1.89	0.02	0.02	15.47	1.21	*G. truncatulinoides (d)*
306-U1313B-1H-1A,49.5-51.5	E14	16.86	0.67	0.67	2.56	0.58						*G. truncatulinoides (d)*
306-U1313B-1H-1A,52-55	E15	17.14	0.69	0.69	1.86	0.58	1.29	0.02	0.02	10.43	0.72	*G. truncatulinoides (d)*
306-U1313B-1H-1W,52.5-54.5	D77	17.22	0.70	0.70	1.66	0.28	2.15	0.07	0.00	17.25		*G. truncatulinoides (d)*
306-U1313B-1H-1W,52.5-54.5	D77	17.22	0.70	0.70	1.60	0.67	2.35	0.06	0.00	18.39		*G. truncatulinoides (d)*
306-U1313B-1H-1W,54-57	D41	17.44	0.71	0.71	2.96	1.11	1.75	0.10	0.01	14.51	1.71	*G. truncatulinoides (d)*
306-U1313B-1H-1W,57-59	D34	17.89	0.74	0.74	2.20	0.86	1.45	0.00	0.00	11.98	0.09	*G. truncatulinoides (d)*
306-U1313B-1H-1A,57-59	E16	17.89	0.74	0.74	2.34	0.87	1.17	0.03	0.01	9.04	0.09	*G. truncatulinoides (d)*

Sample Label	Laboratory ID	Age (ka)	Comp. depth (m, MCD)	Adjusted MCD (m, AMCD)	$\delta^{18}O$ (‰, VPDB)	$\delta^{13}C$ (‰, VPDB)	Mg/Ca (mmol/mol)	Fe/Ca (mmol/mol)	Mn/Ca (mmol/mol)	SubT (°C)	$\delta 18O_{sw\text{-}ivc}$ (‰, VPDB)	Species
306-U1313B-1H-1W,57-59	D34	17.89	0.74	0.74								*G. truncatulinoides (d)*
306-U1313B-1H-1A,57-59	E16	17.89	0.74	0.74	2.76	0.90	0.91	0.05	0.00	5.78	0.09	*G. truncatulinoides (d)*
306-U1313B-1H-1A,57-59	E16	17.89	0.74	0.74	2.50	1.00						*G. truncatulinoides (d)*
306-U1313B-1H-1W,59-61	E17	18.08	0.76	0.76	2.57	1.13	1.01	0.06	0.01	7.17	-0.20	*G. truncatulinoides (d)*
306-U1313B-1H-1W,61-63	D43	18.23	0.78	0.78	3.30	1.21	0.90	0.00	0.00	5.63	-0.13	*G. truncatulinoides (d)*
306-U1313B-1H-1W,61-63	D43	18.23	0.78	0.78	3.51	1.02	1.00	0.12	0.00	7.05	-0.13	*G. truncatulinoides (d)*
306-U1313B-1H-1A,61-63	E18	18.23	0.78	0.78	2.13	0.89						*G. truncatulinoides (d)*
306-U1313B-1H-1A,61-63	E18	18.23	0.78	0.78	2.08	0.80						*G. truncatulinoides (d)*
306-U1313B-1H-1W,61-63	D43	18.23	0.78	0.78	3.07	1.14						*G. truncatulinoides (d)*
306-U1313B-1H-1A,63-65	E19	18.38	0.80	0.80	2.48	1.01	0.94	0.01	0.01	6.19	-0.68	*G. truncatulinoides (d)*
306-U1313B-1H-1A,63-65	E19	18.38	0.80	0.80	2.57	0.78						*G. truncatulinoides (d)*
306-U1313B-1H-1A,63-65	E19	18.38	0.80	0.80	1.84	0.86						*G. truncatulinoides (d)*
306-U1313B-1H-1W,65-67	E20	18.56	0.82	0.82	1.76	0.89	0.87	0.01	0.01	5.21	-0.47	*G. truncatulinoides (d)*
306-U1313B-1H-1W,65-67	D88	18.56	0.82	0.82	3.10	0.79	0.99	0.00	0.00	6.87	-0.47	*G. truncatulinoides (d)*
306-U1313B-1H-1W,65-67	E20	18.56	0.82	0.82	2.43	1.05						*G. truncatulinoides (d)*
306-U1313B-1H-1W,65-67	E20	18.56	0.82	0.82	2.01	0.73						*G. truncatulinoides (d)*
306-U1313B-1H-1W,65-67	D88	18.56	0.82	0.82	3.42	0.96						*G. truncatulinoides (d)*
306-U1313B-1H-1A,67-69	E21	18.77	0.84	0.84	3.36	0.87	0.90	0.00	0.01	5.61	0.05	*G. truncatulinoides (d)*
306-U1313B-1H-1A,67-69	E21	18.77	0.84	0.84	2.98	1.01						*G. truncatulinoides (d)*
306-U1313B-1H-1W,69-71	D46	18.99	0.86	0.86	3.73	1.12	0.90	0.04	0.01	5.68	0.13	*G. truncatulinoides (d)*
306-U1313B-1H-1W,69-71	D46	18.99	0.86	0.86	3.47	0.94	0.96	0.00	0.00	6.48	0.13	*G. truncatulinoides (d)*
306-U1313B-1H-1A,69-71	E22	18.99	0.86	0.86	2.59	1.23	0.99	0.00	0.01	6.91	0.13	*G. truncatulinoides (d)*
306-U1313B-1H-1A,69-71	E22	18.99	0.86	0.86	2.95	1.10						*G. truncatulinoides (d)*
306-U1313B-1H-1A,69-71	E22	18.99	0.86	0.86	2.77	1.13						*G. truncatulinoides (d)*
306-U1313B-1H-1A,71-72.5	E23	19.21	0.88	0.88	2.26	1.24	1.15	0.02	0.03	8.82	-0.13	*G. truncatulinoides (d)*
306-U1313B-1H-1A,71-72.5	E23	19.21	0.88	0.88	2.49	0.94						*G. truncatulinoides (d)*
306-U1313B-1H-1A,71-72.5	E23	19.21	0.88	0.88	2.28	1.01						*G. truncatulinoides (d)*

Sample Label	Laboratory ID	Age (ka)	Comp. depth (m, MCD)	Adjusted MCD (m, AMCD)	$\delta^{18}O$ (‰, VPDB)	$\delta^{13}C$ (‰, VPDB)	Mg/Ca (mmol/mol)	Fe/Ca (mmol/mol)	Mn/Ca (mmol/mol)	SubT (°C)	$\delta 18O_{sw\text{-}ivc}$ (‰, VPDB)	Species
306-U1313B-1H-1W,73-75	D70	19.44	0.90	0.90	2.92	0.63	1.21	0.03	0.01	9.55	0.68	*G. truncatulinoides (d)*
306-U1313B-1H-1W,73-75	D70	19.44	0.90	0.90			1.30	0.00	0.00	10.46		*G. truncatulinoides (d)*
306-U1313B-1H-1A,74-76	E24	19.56	0.91	0.91	2.20	0.91	1.21	0.01	0.03	9.58	-0.03	*G. truncatulinoides (d)*
306-U1313B-1H-1A,74-76	E24	19.56	0.91	0.91	2.88	0.95						*G. truncatulinoides (d)*
306-U1313B-1H-1A,74-76	E24	19.56	0.91	0.91	1.83	0.77						*G. truncatulinoides (d)*
306-U1313B-1H-1W,77-79	D47	19.97	0.94	0.94			1.05	0.00	0.00	7.71		*G. truncatulinoides (d)*
306-U1313B-1H-1W,77-79	D47	19.97	0.94	0.94	3.22	0.76	1.11	0.04	0.01	8.46	0.16	*G. truncatulinoides (d)*
306-U1313B-1H-1A,77-79	E25	19.97	0.94	0.94	2.50	0.76	1.18	0.01	0.01	9.22	0.16	*G. truncatulinoides (d)*
306-U1313B-1H-1A,77-79	E25	19.97	0.94	0.94	2.51	1.19						*G. truncatulinoides (d)*
306-U1313B-1H-1A,79-81	E26	20.25	0.96	0.96	3.45	1.07						*G. truncatulinoides (d)*
306-U1313B-1H-1A,79-81	E26	20.25	0.96	0.96	3.09	1.02						*G. truncatulinoides (d)*
306-U1313B-1H-1W,81.5-83.5	D35	20.58	0.99	0.99	3.34	0.77	1.00	0.05	0.01	7.06	0.47	*G. truncatulinoides (d)*
306-U1313B-1H-1W,81.5-83.5	D35	20.58	0.99	0.99			1.03	0.00	0.00	7.38		*G. truncatulinoides (d)*
306-U1313B-1H-1A,82-84	E27	20.65	0.99	0.99			1.10	0.07	0.02	8.25		*G. truncatulinoides (d)*
306-U1313B-1H-1W,85-87	D89	21.07	1.02	1.02	2.34	0.95	1.34	0.05	0.00	10.93	0.67	*G. truncatulinoides (d)*
306-U1313B-1H-1W,85-87	D89	21.07	1.02	1.02	3.06	0.96						*G. truncatulinoides (d)*
306-U1313B-1H-1W,85-87	D89	21.07	1.02	1.02	2.88	0.85						*G. truncatulinoides (d)*
306-U1313B-1H-1W,87-89	E28	21.34	1.04	1.04	2.93	1.02	1.38	0.03	0.04	11.30	0.80	*G. truncatulinoides (d)*
306-U1313B-1H-1W,87-89	E28	21.34	1.04	1.04	2.71	0.88						*G. truncatulinoides (d)*
306-U1313B-1H-1W,89-91	D90	21.62	1.06	1.06	2.65	0.42	1.28	0.00	0.00	10.35	0.24	*G. truncatulinoides (d)*
306-U1313B-1H-1W,89-91	D90	21.62	1.06	1.06	2.26	0.75						*G. truncatulinoides (d)*
306-U1313B-1H-1A,90-92	E29	21.75	1.07	1.07	2.73	1.04	1.21	0.02	0.03	9.51	-0.25	*G. truncatulinoides (d)*
306-U1313B-1H-1A,90-92	E29	21.75	1.07	1.07	1.54	0.87						*G. truncatulinoides (d)*
306-U1313B-1H-1W,93-95	D49	22.16	1.10	1.10	2.52	1.02	1.26	0.00	0.00	10.06	0.75	*G. truncatulinoides (d)*
306-U1313B-1H-1W,93-95	D49	22.16	1.10	1.10	3.52	1.19						*G. truncatulinoides (d)*
306-U1313B-1H-1A,94-96	E30	22.30	1.11	1.11	2.93	0.81						*G. truncatulinoides (d)*
306-U1313B-1H-1A,94-96	E30	22.30	1.11	1.11	2.67	0.69						*G. truncatulinoides (d)*

Sample Label	Laboratory ID	Age (ka)	Comp. depth (m, MCD)	Adjusted MCD (m, AMCD)	$\delta^{18}O$ (‰, VPDB)	$\delta^{13}C$ (‰, VPDB)	Mg/Ca (mmol/mol)	Fe/Ca (mmol/mol)	Mn/Ca (mmol/mol)	SubT (°C)	$\delta 18O_{sw\text{-}ivc}$ (‰, VPDB)	Species
306-U1313B-1H-1W,96-98	D91	22.57	1.13	1.13	2.21	0.86	0.98	0.00	0.00	6.77	-0.74	*G. truncatulinoides (d)*
306-U1313B-1H-1W,99-102	E31	22.97	1.16	1.16	1.70	0.93	1.33	0.03	0.04	10.80	-0.44	*G. truncatulinoides (d)*
306-U1313B-1H-1W,99-102	E31	22.97	1.16	1.16	1.63	1.05						*G. truncatulinoides (d)*
306-U1313B-1H-1W,102-104	D51	23.33	1.19	1.19	2.73	0.92	0.92	0.00	0.00	5.88	-0.40	*G. truncatulinoides (d)*
306-U1313B-1H-1W,102-104	D51	23.33	1.19	1.19	2.72	0.86						*G. truncatulinoides (d)*
306-U1313B-1H-1W,104-106	E32	23.54	1.21	1.21	2.00	0.91	1.32	0.05	0.04	10.69	0.14	*G. truncatulinoides (d)*
306-U1313B-1H-1W,104-106	E32	23.54	1.21	1.21	2.53	0.82						*G. truncatulinoides (d)*
306-U1313B-1H-1W,106-108	D36	23.76	1.23	1.23	2.89	0.93	1.29	0.00	0.00	10.45	0.23	*G. truncatulinoides (d)*
306-U1313B-1H-1A,106-108	E33	23.76	1.23	1.23	1.72	0.96	1.42	0.05	0.04	11.67	0.23	*G. truncatulinoides (d)*
306-U1313B-1H-1W,106-108	D36	23.76	1.23	1.23	2.19	1.06						*G. truncatulinoides (d)*
306-U1313B-1H-1W,108-109.5	E34	23.92	1.25	1.25	3.43	1.02	1.47	0.09	0.01	12.17	1.06	*G. truncatulinoides (d)*
306-U1313B-1H-1W,108-109.5	E34	23.92	1.25	1.25	2.31	0.82						*G. truncatulinoides (d)*
306-U1313B-1H-1W,109.5-111.5	D53	24.03	1.27	1.27	3.29	1.18	1.04	0.00	0.00	7.58	0.14	*G. truncatulinoides (d)*
306-U1313B-1H-1W,109.5-111.5	D53	24.03	1.27	1.27	2.52	0.90						*G. truncatulinoides (d)*
306-U1313B-1H-1W,110-112	E35	24.06	1.27	1.27	2.41	0.36	1.53	0.09	0.03	12.66	0.71	*G. truncatulinoides (d)*
306-U1313B-1H-1W,112-113.5	E36	24.21	1.29	1.29	3.43	1.08	1.22	0.06	0.03	9.69	0.52	*G. truncatulinoides (d)*
306-U1313B-1H-1W,112-113.5	E36	24.21	1.29	1.29	2.26	0.93						*G. truncatulinoides (d)*
306-U1313B-1H-1W,113.5-114.5	D37	24.32	1.31	1.31	2.68	1.01	1.28	0.00	0.00	10.29	0.48	*G. truncatulinoides (d)*
306-U1313B-1H-1W,114.5-116	E37	24.40	1.32	1.32			1.29	0.03	0.01	10.43		*G. truncatulinoides (d)*
306-U1313B-1H-1W,116.5-118.5	E38	24.54	1.34	1.34	2.81	1.09	1.27	0.05	0.02	10.14	0.58	*G. truncatulinoides (d)*
306-U1313B-1H-1W,118-120	D55	24.65	1.35	1.35	1.34	0.94	1.08	0.00	0.00	8.04	-1.32	*G. truncatulinoides (d)*
306-U1313B-1H-1W,119.5-121	E39	24.76	1.37	1.37			1.71	0.05	0.03	14.19		*G. truncatulinoides (d)*
306-U1313B-1H-1W,121-123	D38	24.87	1.38	1.38	3.03	0.50	1.17	0.00	0.00	9.15	0.59	*G. truncatulinoides (d)*
306-U1313B-1H-1A,122-124	E40	24.94	1.39	1.39	1.90	0.92	1.33	0.03	0.05	10.83	0.30	*G. truncatulinoides (d)*
306-U1313B-1H-1A,122-124	E40	24.94	1.39	1.39	2.87	1.42						*G. truncatulinoides (d)*
306-U1313B-1H-1A,124.5-126	E41	25.19	1.42	1.42	2.03	1.11	1.45	0.05	0.03	11.96	0.01	*G. truncatulinoides (d)*
306-U1313B-1H-1A,124.5-126	E41	25.19	1.42	1.42	1.94	1.27						*G. truncatulinoides (d)*

Sample Label	Laboratory ID	Age (ka)	Comp. depth (m, MCD)	Adjusted MCD (m, AMCD)	$\delta^{18}O$ (‰, VPDB)	$\delta^{13}C$ (‰, VPDB)	Mg/Ca (mmol/mol)	Fe/Ca (mmol/mol)	Mn/Ca (mmol/mol)	SubT (°C)	$\delta 18O_{sw\text{-}ivc}$ (‰, VPDB)	Species
306-U1313B-1H-1W,126.5-128.5	D57	25.41	1.44	1.44	1.57	0.87						*G. truncatulinoides (d)*
306-U1313B-1H-1W,128-129.5	E42	25.60	1.45	1.45	1.71	0.48	1.25	0.03	0.06	9.94	-0.14	*G. truncatulinoides (d)*
306-U1313B-1H-1W,128-129.5	E42	25.60	1.45	1.45	2.53	1.15						*G. truncatulinoides (d)*
306-U1313B-1H-1A,130-132	E43	25.87	1.47	1.47	1.64	1.09	1.45	0.04	0.02	11.93	0.04	*G. truncatulinoides (d)*
306-U1313B-1H-1A,130-132	E43	25.87	1.47	1.47	2.12	1.27						*G. truncatulinoides (d)*
306-U1313B-1H-1W,131.5-133.5	D79	26.09	1.49	1.49	1.63	0.43						*G. truncatulinoides (d)*
306-U1313B-1H-1W,133.5-135.5	E44	26.45	1.51	1.51	2.76	0.78						*G. truncatulinoides (d)*
306-U1313B-1H-1W,133.5-135.5	E44	26.45	1.51	1.51	3.07	1.06						*G. truncatulinoides (d)*
306-U1313B-1H-1W,135.5-137	E45	26.90	1.53	1.53	1.29	0.12	1.30	0.11	0.02	10.49	-0.85	*G. truncatulinoides (d)*
306-U1313B-1H-1W,137.5-139.5	E46	27.35	1.55	1.55	2.23	1.19	1.19	0.05	0.02	9.27	-0.15	*G. truncatulinoides (d)*
306-U1313B-1H-1W,139.5-141	E47	27.81	1.57	1.57	1.36	0.48	1.15	0.04	0.05	8.92	-1.09	*G. truncatulinoides (d)*
306-U1313B-1H-1W,141-143	E48	28.15	1.58	1.58	2.06	0.77	1.05	0.03	0.03	7.60	-0.67	*G. truncatulinoides (d)*
306-U1313B-1H-1W,143-145	E49	28.61	1.60	1.60	1.74	0.89	0.95	0.04	0.01	6.37	-0.96	*G. truncatulinoides (d)*
306-U1313B-1H-1W,143-145	E49	28.61	1.60	1.60	2.29	0.95						*G. truncatulinoides (d)*
306-U1313B-1H-1W,145-147	E50	29.10	1.62	1.62	2.49	0.73	1.37	0.04	0.02	11.15	0.41	*G. truncatulinoides (d)*
306-U1313B-1H-1W,145-147	E50	29.10	1.62	1.62	2.27	0.82						*G. truncatulinoides (d)*
306-U1313B-1H-1W,147-149.5	E51	29.65	1.64	1.64	2.46	0.36	1.42	0.04	0.03	11.70	0.94	*G. truncatulinoides (d)*
306-U1313B-1H-1W,147-149.5	E51	29.65	1.64	1.64	3.04	0.83						*G. truncatulinoides (d)*
306-U1313C-4H-2W,82-84	A255	543.1	26.82	26.90	2.53	1.02	1.32	0.00	0.00	5.68		*G. crassaformis*
306-U1313C-4H-2W,82-84	A1184	543.1	26.82	26.90	4.30	0.37						*C. wuellerstorfi*
306-U1313C-4H-2W,89-91	A1185	544.6	26.89	26.98	4.36	0.09						*C. wuellerstorfi*
306-U1313C-4H-2W,95-97	A258	545.9	26.95	27.04	2.88	1.01	1.13	0.00	0.00	4.45		*G. crassaformis*
306-U1313C-4H-2W,102-104	A259	547.4	27.02	27.11	3.25	1.00	1.19	0.00	0.00	4.82		*G. crassaformis*
306-U1313C-4H-2W,102-104	A1186	547.4	27.02	27.11	3.93	0.69						*C. wuellerstorfi*
306-U1313C-4H-2W,107-109	A260	548.5	27.07	27.17	2.77	1.05	1.35	0.00	0.00	5.88		*G. crassaformis*
306-U1313C-4H-2W,111-113	A1187	549.4	27.11	27.21	4.20	0.28						*C. wuellerstorfi*
306-U1313C-4H-2W,120-122	A263	551.3	27.20	27.30	2.47	0.85	1.12	0.00	0.00	4.34		*G. crassaformis*

Sample Label	Laboratory ID	Age (ka)	Comp. depth (m, MCD)	Adjusted MCD (m, AMCD)	$\delta^{18}O$ (‰, VPDB)	$\delta^{13}C$ (‰, VPDB)	Mg/Ca (mmol/mol)	Fe/Ca (mmol/mol)	Mn/Ca (mmol/mol)	SubT (°C)	$\delta 18O_{sw\text{-}ivc}$ (‰, VPDB)	Species
306-U1313C-4H-2W,120-122	A1188	551.3	27.20	27.30	4.20	0.46						*C. wuellerstorfi*
306-U1313C-4H-2W,127-129	A264	552.8	27.27	27.38	2.66	0.82	1.43	0.00	0.00	6.35		*G. crassaformis*
306-U1313C-4H-2W,127-129	A264	552.8	27.27	27.38	2.66	0.82	1.14	0.02	0.01	4.49		*G. crassaformis*
306-U1313C-4H-2W,132-134	A265	553.9	27.32	27.43	2.52	1.06	1.47	0.03	0.04	6.62		*G. crassaformis*
306-U1313C-4H-2W,132-134	A265	553.9	27.32	27.43	2.52	1.06	0.89	0.00	0.00	2.44		*G. crassaformis*
306-U1313C-4H-2W,132-134	A1189	553.9	27.32	27.43	4.27	0.66						*C. wuellerstorfi*
306-U1313C-4H-2W,136-138	A266	554.7	27.36	27.47	2.54	1.02	1.28	0.00	0.00	5.47		*G. crassaformis*
306-U1313C-4H-2W,140-142	A267	555.6	27.40	27.52	2.43	0.89	1.39	0.19	0.00	6.11		*G. crassaformis*
306-U1313C-4H-2W,140-142	A267	555.6	27.40	27.52	2.43	0.89	1.19	0.07	0.04	4.85		*G. crassaformis*
306-U1313C-4H-2W,140-142	A1190	555.6	27.40	27.52	4.18	0.30						*C. wuellerstorfi*
306-U1313C-4H-2W,145-147	A268	556.7	27.45	27.57	2.77	1.04	1.82	0.00	0.00	8.36		*G. crassaformis*
306-U1313C-4H-2W,145-147	A268	556.7	27.45	27.57	2.77	1.04	1.26	0.13	0.13	5.30		*G. crassaformis*
306-U1313C-4H-3W,2-4	A269	558.2	27.52	27.64	2.82	0.90	1.16	0.00	0.00	4.62		*G. crassaformis*
306-U1313C-4H-3W,2-4	A1191	558.2	27.52	27.64	4.07	0.04						*C. wuellerstorfi*
306-U1313C-4H-3W,7-9	A270	559.3	27.57	27.70			1.03	0.06	0.05	3.69		*G. crassaformis*
306-U1313C-4H-3W,11-13	A271	560.1	27.61	27.74	3.05	1.20	1.19	0.00	0.00	4.85		*G. crassaformis*
306-U1313C-4H-3W,11-13	A1192	560.1	27.61	27.74	3.97	0.23						*C. wuellerstorfi*
306-U1313C-4H-3W,16-18	A272	561.2	27.66	27.79	2.75	1.04	1.14	0.02	0.09	4.52		*G. crassaformis*
306-U1313C-4H-3W,22-24	A273	562.5	27.72	27.85	2.79	1.20	1.22	0.00	0.00	5.03		*G. crassaformis*
306-U1313C-4H-3W,22-24	A1193	562.5	27.72	27.85	3.79	0.96						*C. wuellerstorfi*
306-U1313C-4H-3W,32-34	A275	564.7	27.82	27.96	2.42	0.95	1.34	0.04	0.00	5.85		*G. crassaformis*
306-U1313C-4H-3W,32-34	A1194	564.7	27.82	27.96	3.56	1.06						*C. wuellerstorfi*
306-U1313C-4H-3W,35-37	A276	565.3	27.85	27.99			1.46	0.06	0.15	6.56		*G. crassaformis*
306-U1313C-4H-3W,35-37	A1195	565.3	27.85	27.99	3.30	1.01						*C. wuellerstorfi*
306-U1313C-4H-3W,40-42	A277	566.4	27.90	28.04	2.22	1.07	1.16	0.00	0.07	4.68		*G. crassaformis*
306-U1313C-4H-3W,40-42	A1305	566.4	27.90	28.04	3.24	0.96						*C. wuellerstorfi*
306-U1313C-4H-3W,52-54	A279	569.0	28.02	28.17	1.89	1.20	1.38	0.02	0.07	6.05		*G. crassaformis*

Sample Label	Laboratory ID	Age (ka)	Comp. depth (m, MCD)	Adjusted MCD (m, AMCD)	$\delta^{18}O$ (‰, VPDB)	$\delta^{13}C$ (‰, VPDB)	Mg/Ca (mmol/mol)	Fe/Ca (mmol/mol)	Mn/Ca (mmol/mol)	SubT (°C)	$\delta 18O_{sw\text{-}ivc}$ (‰, VPDB)	Species
306-U1313C-4H-3W,52-54	A1196	569.0	28.02	28.17	3.38	0.80						*C. wuellerstorfi*
306-U1313C-4H-3W,57-59	A280	570.1	28.07	28.22			1.57	0.08	0.08	7.14		*G. crassaformis*
306-U1313C-4H-3W,60-62	A281	570.7	28.10	28.24	1.59	1.11	1.19	0.04	0.04	4.88		*G. crassaformis*
306-U1313C-4H-3W,60-62	A1197	570.7	28.10	28.24	3.13	0.71						*C. wuellerstorfi*
306-U1313C-4H-3W,65-67	A282	571.8	28.15	28.28			1.73	0.20	0.07	7.95		*G. crassaformis*
306-U1313C-4H-3W,70-72	A283	572.9	28.20	28.32	1.78	1.27	1.55	0.03	0.11	7.04		*G. crassaformis*
306-U1313C-4H-3W,70-72	A1198	572.9	28.20	28.32	2.76	1.06						*C. wuellerstorfi*
306-U1313C-4H-3W,76.5-78.5	A284	574.3	28.27	28.37	1.67	1.14	1.63	0.11	0.12	7.41		*G. crassaformis*
306-U1313C-4H-3W,81.5-83.5	A285	575.4	28.32	28.41	1.59	1.06	1.47	0.04	0.06	6.58		*G. crassaformis*
306-U1313C-4H-3W,81.5-83.5	A285	575.4	28.32	28.41	1.59	1.06	1.54	0.06	0.10	6.99		*G. crassaformis*
306-U1313C-4H-3W,81.5-83.5	A1199	575.4	28.32	28.41	2.82	1.16						*C. wuellerstorfi*
306-U1313C-4H-3W,85-87	A286	576.1	28.35	28.44			1.44	0.09	0.10	6.41		*G. crassaformis*
306-U1313C-4H-3W,90-92	A287	577.2	28.40	28.48	1.83	1.11	1.76	0.07	0.16	8.06		*G. crassaformis*
306-U1313C-4H-3W,90-92	A1200	577.2	28.40	28.48	2.98	1.06						*C. wuellerstorfi*
306-U1313C-4H-3W,95-97	A288	578.3	28.45	28.52	1.89	0.88	1.55	0.04	0.19	7.03		*G. crassaformis*
306-U1313C-4H-3W,101.5-103.5	A1201	579.7	28.52	28.58	2.92	0.62						*C. wuellerstorfi*
306-U1313C-4H-3W,110-112	A1202	581.5	28.60	28.66	3.84	0.46						*C. wuellerstorfi*
306-U1313C-4H-3W,115-117	A708	582.5	28.65	28.71			1.57	0.00	0.17	7.13		*G. crassaformis*
306-U1313C-4H-3W,115-117	A1203	582.5	28.65	28.71	4.00	0.52						*C. wuellerstorfi*
306-U1313C-4H-3W,122-124	A1204	583.9	28.72	28.79	3.94	0.77						*C. wuellerstorfi*
306-U1313C-4H-3W,128-130	A295	585.1	28.78	28.85	2.22	1.40	2.06	0.16	0.09	9.37		*G. crassaformis*
306-U1313C-4H-3W,135-137	A1205	586.6	28.85	28.92	3.29	1.10						*C. wuellerstorfi*
306-U1313C-4H-4W,7-9	A1206	591.0	29.07	29.16	3.65	0.95						*C. wuellerstorfi*
306-U1313C-4H-4W,10-12	A299	591.6	29.10	29.19	2.47	1.26	1.16	0.02	0.04	4.64		*G. crassaformis*
306-U1313C-4H-4W,15-17	A1207	592.6	29.15	29.24	3.55	1.06						*C. wuellerstorfi*
306-U1313C-4H-4W,17.5-19.5	A301	593.1	29.18	29.27	2.53	1.02	0.97	0.00	0.00	3.14		*G. crassaformis*
306-U1313C-4H-4W,22-24	A1208	594.1	29.22	29.31	3.79	0.75						*C. wuellerstorfi*

Sample Label	Laboratory ID	Age (ka)	Comp. depth (m, MCD)	Adjusted MCD (m, AMCD)	$\delta^{18}O$ (‰, VPDB)	$\delta^{13}C$ (‰, VPDB)	Mg/Ca (mmol/mol)	Fe/Ca (mmol/mol)	Mn/Ca (mmol/mol)	SubT (°C)	$\delta 18O_{sw\text{-}ivc}$ (‰, VPDB)	Species
306-U1313C-4H-4W,26-28	A303	594.9	29.26	29.35	2.83	1.64	0.95	0.02	0.00	3.04		*G. crassaformis*
306-U1313C-4H-4W,36-38	A305	596.9	29.36	29.46	2.62	1.29	0.93	0.00	0.00	2.80		*G. crassaformis*
306-U1313C-4H-4W,40-42	A1210	597.7	29.40	29.50	3.58	0.83						*C. wuellerstorfi*
306-U1313C-4H-4W,45-47	A307	598.7	29.45	29.55	2.52	1.37	0.98	0.00	0.03	3.23		*G. crassaformis*
306-U1313C-4H-4W,51-53	A308	599.9	29.51	29.62			1.10	0.04	0.07	4.22		*G. crassaformis*
306-U1313C-4H-4W,51-53	A1211	599.9	29.51	29.62	3.42	0.94						*C. wuellerstorfi*
306-U1313C-4H-4W,56-58	A309	601.0	29.56	29.67	2.23	1.12	1.15	0.01	0.05	4.56		*G. crassaformis*
306-U1313C-4H-4W,56-58	A309	601.0	29.56	29.67	2.23	1.12	1.17	0.00	0.06	4.69		*G. crassaformis*
306-U1313C-4H-4W,60-62	A310	601.8	29.60	29.71			1.30	0.04	0.09	5.58		*G. crassaformis*
306-U1313C-4H-4W,60-62	A1212	601.8	29.60	29.71	3.50	0.80						*C. wuellerstorfi*
306-U1313C-4H-4W,65-67	A311	602.7	29.65	29.76	2.37	1.37	1.29	0.02	0.08	5.54		*G. crassaformis*
306-U1313C-4H-4W,70-72	A312	603.7	29.70	29.82	1.81	0.84	1.31	0.05	0.05	5.65		*G. crassaformis*
306-U1313C-4H-4W,70-72	A1213	603.7	29.70	29.82	3.15	0.76						*C. wuellerstorfi*
306-U1313C-4H-4W,76.5-78.5	A313	604.9	29.77	29.89	2.09	1.12	1.18	0.02	0.09	4.80		*G. crassaformis*
306-U1313C-4H-4W,81.5-83.5	A314	605.9	29.82	29.94			1.28	0.03	0.10	5.45		*G. crassaformis*
306-U1313C-4H-4W,81.5-83.5	A1214	605.9	29.82	29.94	3.21	0.91						*C. wuellerstorfi*
306-U1313C-4H-4W,85-87	A315	606.5	29.85	29.97	2.22	1.29	1.29	0.02	0.07	5.55		*G. crassaformis*
306-U1313C-4H-4W,90-92	A316	607.5	29.90	30.03			1.38	0.02	0.07	6.04		*G. crassaformis*
306-U1313C-4H-4W,90-92	A1215	607.5	29.90	30.03	3.37	0.58						*C. wuellerstorfi*
306-U1313C-4H-4W,95-97	A317	608.4	29.95	30.08	1.93	1.05	1.33	0.01	0.07	5.75		*G. crassaformis*
306-U1313C-4H-4W,103-105	A318	609.9	30.03	30.16	1.95	1.14	1.49	0.06	0.05	6.69		*G. crassaformis*
306-U1313C-4H-4W,103-105	A1216	609.9	30.03	30.16	2.78	1.06						*C. wuellerstorfi*
306-U1313C-4H-4W,107-109	A319	610.7	30.07	30.19	1.83	0.78	1.76	0.03	0.10	8.07		*G. crassaformis*
306-U1313C-4H-4W,110-112	A320	611.2	30.10	30.22	1.91	1.15	1.62	0.05	0.11	7.40		*G. crassaformis*
306-U1313C-4H-4W,110-112	A1217	611.2	30.10	30.22	2.92	1.10						*C. wuellerstorfi*
306-U1313C-4H-4W,115-117	A321	612.2	30.15	30.26	2.06	1.10	1.45	0.02	0.10	6.47		*G. crassaformis*
306-U1313C-4H-4W,115-117	A1218	612.2	30.15	30.26	2.29	0.67						*C. wuellerstorfi*

Sample Label	Laboratory ID	Age (ka)	Comp. depth (m, MCD)	Adjusted MCD (m, AMCD)	$\delta^{18}O$ (‰, VPDB)	$\delta^{13}C$ (‰, VPDB)	Mg/Ca (mmol/mol)	Fe/Ca (mmol/mol)	Mn/Ca (mmol/mol)	SubT (°C)	$\delta 18O_{sw\text{-}ivc}$ (‰, VPDB)	Species
306-U1313C-4H-4W,120-122	A322	613.1	30.20	30.30	1.70	0.82	1.57	0.08	0.11	7.11		*G. crassaformis*
306-U1313C-4H-4W,127-129	A323	614.4	30.27	30.36	1.93	0.84	1.59	0.03	0.14	7.21		*G. crassaformis*
306-U1313C-4H-4W,127-129	A1219	614.4	30.27	30.36	2.95	0.91						*C. wuellerstorfi*
306-U1313C-4H-4W,132-134	A324	615.4	30.32	30.41			1.43	0.02	0.11	6.38		*G. crassaformis*
306-U1313C-4H-4W,136-138	A325	616.1	30.36	30.44	1.98	0.91	1.48	0.01	0.13	6.65		*G. crassaformis*
306-U1313C-4H-4W,136-138	A1220	616.1	30.36	30.44	3.26	1.02						*C. wuellerstorfi*
306-U1313C-4H-4W,140-142	A326	616.9	30.40	30.47	1.88	0.79	1.64	0.06	0.16	7.48		*G. crassaformis*
306-U1313C-4H-4W,145-147	A327	617.8	30.45	30.52	2.83	0.65	1.72	0.03	0.08	7.88		*G. crassaformis*
306-U1313C-4H-4W,145-147	A1221	617.8	30.45	30.52	3.36	0.91						*C. wuellerstorfi*
306-U1313C-4H-5W,6.5-8.5	A328	620.0	30.57	30.62	2.86	0.84	1.28	0.00	0.07	5.45		*G. crassaformis*
306-U1313C-4H-5W,10-12	A329	620.7	30.60	30.65	2.91	0.75	1.29	0.01	0.07	5.55		*G. crassaformis*
306-U1313C-4H-5W,10-12	A1222	620.7	30.60	30.65	3.61	0.57						*C. wuellerstorfi*
306-U1313C-4H-5W,15-17	A330	621.7	30.65	30.69	3.77	0.95	1.81	0.06	0.01	8.31		*G. crassaformis*
306-U1313C-4H-5W,15-17	A1312	621.7	30.65	30.69	4.59	0.39						*C. wuellerstorfi*
306-U1313C-4H-5W,18-20	A331	622.3	30.68	30.71	3.60	0.67	1.11	0.00	0.04	4.30		*G. crassaformis*
306-U1313C-4H-5W,18-20	A1223	622.3	30.68	30.71	3.34	0.94						*C. wuellerstorfi*
306-U1313C-4H-5W,26.5-28.5	A332	624.2	30.77	30.79	3.45	1.20	1.09	0.00	0.00	4.17		*G. crassaformis*
306-U1313C-4H-5W,26.5-28.5	A1313	624.2	30.77	30.79	4.70	-0.05						*C. wuellerstorfi*
306-U1313C-4H-5W,32-34	A333	625.4	30.82	30.83	3.45	0.81	1.05	0.00	0.00	3.83		*G. crassaformis*
306-U1313C-4H-5W,32-34	A1224	625.4	30.82	30.83	3.95	0.82						*C. wuellerstorfi*
306-U1313C-4H-5W,35-37	A334	626.0	30.85	30.86	3.59	0.97	0.96	0.04	0.02	3.07		*G. crassaformis*
306-U1313C-4H-5W,40-42	A335	627.1	30.90	30.90	3.80	0.75	1.13	0.02	0.01	4.47		*G. crassaformis*
306-U1313C-4H-5W,40-42	A335	627.1	30.90	30.90	3.80	0.75	0.95	0.03	0.00	2.97		*G. crassaformis*
306-U1313C-4H-5W,40-42	A1225	627.1	30.90	30.90	4.83	-0.03						*C. wuellerstorfi*
306-U1313C-4H-5W,45-47	A336	628.2	30.95	30.95	3.49	1.07	1.15	0.02	0.04	4.55		*G. crassaformis*
306-U1313C-4H-5W,51.5-53.5	A337	629.6	31.02	31.01	4.18	1.16	0.99	0.00	0.00	3.37		*G. crassaformis*
306-U1313C-4H-5W,51.5-53.5	A1226	629.6	31.02	31.01	4.88	0.10						*C. wuellerstorfi*

Sample Label	Laboratory ID	Age (ka)	Comp. depth (m, MCD)	Adjusted MCD (m, AMCD)	$\delta^{18}O$ (‰, VPDB)	$\delta^{13}C$ (‰, VPDB)	Mg/Ca (mmol/mol)	Fe/Ca (mmol/mol)	Mn/Ca (mmol/mol)	SubT (°C)	$\delta 18O_{sw\text{-}ivc}$ (‰, VPDB)	Species
306-U1313C-4H-5W,56.5-58.5	A338	630.7	31.07	31.06			1.06	0.02	0.02	3.90		*G. crassaformis*
306-U1313C-4H-5W,60-62	A339	631.5	31.10	31.09	3.47	0.90	1.07	0.00	0.00	4.00		*G. crassaformis*
306-U1313C-4H-5W,60-62	A1227	631.5	31.10	31.09	4.84	0.08						*C. wuellerstorfi*
306-U1313C-4H-5W,65-67	A340	632.6	31.15	31.13	3.53	0.97	1.17	0.02	0.04	4.70		*G. crassaformis*
306-U1313C-4H-5W,70-72	A341	633.7	31.20	31.18	3.75	0.89	1.11	0.00	0.08	4.31		*G. crassaformis*
306-U1313C-4H-5W,70-72	A1228	633.7	31.20	31.18	4.75	-0.13						*C. wuellerstorfi*
306-U1313C-4H-5W,76-78	A342	635.0	31.26	31.24	3.47	0.77	1.14	0.03	0.12	4.54		*G. crassaformis*
306-U1313C-4H-5W,81.5-83.5	A343	636.2	31.32	31.29	3.53	0.69	1.03	0.00	0.00	3.64		*G. crassaformis*
306-U1313C-4H-5W,81.5-83.5	A1229	636.2	31.32	31.29	4.68	0.02						*C. wuellerstorfi*
306-U1313C-4H-5W,85-87	A344	637.0	31.35	31.32			1.27	0.03	0.05	5.41		*G. crassaformis*
306-U1313C-4H-5W,90-92	A345	638.0	31.40	31.36	3.14	0.90	0.96	0.00	0.03	3.06		*G. crassaformis*
306-U1313C-4H-5W,90-92	A1230	638.0	31.40	31.36	4.67	0.14						*C. wuellerstorfi*
306-U1313C-4H-5W,95-97	A346	639.1	31.45	31.41	3.65	1.13	0.92	0.01	0.01	2.76		*G. crassaformis*
306-U1313C-4H-5W,102-104	A347	640.7	31.52	31.47	3.32	0.90	1.06	0.00	0.00	3.93		*G. crassaformis*
306-U1313C-4H-5W,102-104	A1231	640.7	31.52	31.47	4.64	-0.01						*C. wuellerstorfi*
306-U1313C-4H-5W,106.5-108.5	A348	641.6	31.57	31.52			1.02	0.02	0.05	3.58		*G. crassaformis*
306-U1313C-4H-5W,110-112	A349	642.4	31.60	31.55	3.62	0.92	0.99	0.00	0.10	3.37		*G. crassaformis*
306-U1313C-4H-5W,115-117	A350	643.5	31.65	31.59	3.52	0.93	1.06	0.02	0.06	3.87		*G. crassaformis*
306-U1313C-4H-5W,120-122	A351	644.6	31.70	31.64	2.82	0.79	1.02	0.00	0.00	3.61		*G. crassaformis*
306-U1313C-4H-5W,120-122	A1233	644.6	31.70	31.64	4.58	-0.59						*C. wuellerstorfi*
306-U1313C-4H-5W,127-129	A352	646.1	31.77	31.71	3.76	1.05	0.99	0.00	0.04	3.32		*G. crassaformis*
306-U1313C-4H-5W,131-133	A353	647.0	31.81	31.75			1.01	0.01	0.02	3.51		*G. crassaformis*
306-U1313C-4H-5W,131-133	A1234	647.0	31.81	31.75	4.61	0.09						*C. wuellerstorfi*
306-U1313C-4H-5W,135-137	A354	647.9	31.85	31.80	3.95	0.82	1.05	0.03	0.03	3.82		*G. crassaformis*
306-U1313C-4H-5W,140-142	A355	649.0	31.90	31.85	3.74	1.18	1.09	0.00	0.00	4.13		*G. crassaformis*
306-U1313C-4H-5W,140-142	A1235	649.0	31.90	31.85	4.53	-0.14						*C. wuellerstorfi*
306-U1313B-4H-2W,110-112	A1	652.2	32.05	32.05	3.62	0.80	1.41	0.09	0.12	6.26		*G. crassaformis*

Sample Label	Laboratory ID	Age (ka)	Comp. depth (m, MCD)	Adjusted MCD (m, AMCD)	$\delta^{18}O$ (‰, VPDB)	$\delta^{13}C$ (‰, VPDB)	Mg/Ca (mmol/mol)	Fe/Ca (mmol/mol)	Mn/Ca (mmol/mol)	SubT (°C)	$\delta 18O_{sw\text{-}ivc}$ (‰, VPDB)	Species
306-U1313B-4H-2W,110-112	A1236	652.2	32.05	32.05	4.39	0.80						*C. wuellerstorfi*
306-U1313B-4H-2W,114.5-116.5	A2	653.2	32.10	32.10			1.33	0.06	0.10	5.79		*G. crassaformis*
306-U1313B-4H-2W,120-122	A3	654.4	32.15	32.15	3.54	0.62	1.24	0.04	0.07	5.21		*G. crassaformis*
306-U1313B-4H-2W,120-122	A1237	654.4	32.15	32.15	4.35	0.70						*C. wuellerstorfi*
306-U1313B-4H-2W,131.5-133.5	A4	656.9	32.27	32.27	3.14	0.53	0.99	0.04	0.07	3.31		*G. crassaformis*
306-U1313B-4H-2W,135-137	A5	657.7	32.30	32.30			1.41	0.03	0.13	6.23		*G. crassaformis*
306-U1313B-4H-2W,135-137	A1238	657.7	32.30	32.30	4.46	0.34						*C. wuellerstorfi*
306-U1313B-4H-2W,140-142	A6	658.8	32.35	32.35	3.64	0.60	1.34	0.06	0.07	5.81		*G. crassaformis*
306-U1313B-4H-2W,145-147	A1239	659.9	32.40	32.40	4.30	0.39						*C. wuellerstorfi*
306-U1313B-4H-3W,2.5-4.5	A8	661.5	32.48	32.48	3.64	0.47	1.13	0.07	0.00	4.43		*G. crassaformis*
306-U1313B-4H-3W,11-13	A9	663.4	32.56	32.56	3.60	0.67	1.09	0.03	0.00	4.14		*G. crassaformis*
306-U1313B-4H-3W,11-13	A9	663.4	32.56	32.56	3.60	0.67	1.11	0.05	0.05	4.26		*G. crassaformis*
306-U1313B-4H-3W,11-13	A1240	663.4	32.56	32.56	4.52	-0.12						*C. wuellerstorfi*
306-U1313B-4H-3W,15-17	A10	664.2	32.60	32.60			0.97	0.04	0.01	3.19		*G. crassaformis*
306-U1313B-4H-3W,19-20	A11	665.0	32.64	32.64	3.64	0.89	1.23	0.00	0.00	5.11		*G. crassaformis*
306-U1313B-4H-3W,19-20	A1241	665.0	32.64	32.64	4.28	0.42						*C. wuellerstorfi*
306-U1313B-4H-3W,32-33	A13	667.8	32.77	32.77	3.23	0.82	0.92	0.02	0.00	2.71		*G. crassaformis*
306-U1313B-4H-3W,32-33	A1242	667.8	32.77	32.77	4.36	-0.20						*C. wuellerstorfi*
306-U1313B-4H-3W,35-37	A14	668.6	32.80	32.80			1.06	0.04	0.02	3.95		*G. crassaformis*
306-U1313B-4H-3W,40-42	A15	669.7	32.85	32.85	3.60	1.13	1.00	0.03	0.00	3.46		*G. crassaformis*
306-U1313B-4H-3W,40-42	A1243	669.7	32.85	32.85	4.73							*U. peregrina*
306-U1313B-4H-3W,45-47	A16	670.8	32.90	32.90	3.44	1.11	1.18	0.04	0.11	4.79		*G. crassaformis*
306-U1313B-4H-3W,49-50	A17	671.5	32.94	32.94			1.00	0.03	0.02	3.39		*G. crassaformis*
306-U1313B-4H-3W,49-50	A1244	671.5	32.94	32.94	4.18	0.45						*C. wuellerstorfi*
306-U1313B-4H-3W,52-54	A18	672.3	32.97	32.97	3.61	1.14	1.08	0.00	0.00	4.05		*G. crassaformis*
306-U1313B-4H-3W,59-61	A19	673.8	33.04	33.04	3.57	1.21	0.93	0.04	0.00	2.83		*G. crassaformis*
306-U1313B-4H-3W,59-61	A1245	673.8	33.04	33.04	4.22	-0.29						*C. wuellerstorfi*

Sample Label	Laboratory ID	Age (ka)	Comp. depth (m, MCD)	Adjusted MCD (m, AMCD)	$\delta^{18}O$ (‰, VPDB)	$\delta^{13}C$ (‰, VPDB)	Mg/Ca (mmol/mol)	Fe/Ca (mmol/mol)	Mn/Ca (mmol/mol)	SubT (°C)	$\delta 18O_{sw\text{-}ivc}$ (‰, VPDB)	Species
306-U1313B-4H-3W,70-72	A21	676.2	33.15	33.15	2.59	0.81	1.19	0.02	0.05	4.89		*G. crassaformis*
306-U1313B-4H-3W,70-72	A1246	676.2	33.15	33.15	4.18	0.46						*C. wuellerstorfi*
306-U1313B-4H-3W,73-75	A22	676.9	33.18	33.18			1.24	0.04	0.15	5.18		*G. crassaformis*
306-U1313B-4H-3W,79-80	A23	678.1	33.24	33.24	2.77	0.87	1.24	0.00	0.06	5.19		*G. crassaformis*
306-U1313B-4H-3W,79-80	A1247	678.1	33.24	33.24	4.01	0.83						*C. wuellerstorfi*
306-U1313B-4H-3W,81.5-83.5	A24	678.7	33.27	33.27			1.28	0.04	0.14	5.48		*G. crassaformis*
306-U1313B-4H-3W,85-87	A25	679.5	33.30	33.30	2.94	1.11	1.29	0.05	0.13	5.53		*G. crassaformis*
306-U1313B-4H-3W,85-87	A1248	679.5	33.30	33.30	4.24	-0.19						*C. wuellerstorfi*
306-U1313B-4H-3W,90-92	A26	680.6	33.35	33.35	2.60	0.53	1.32	0.09	0.04	5.70		*G. crassaformis*
306-U1313B-4H-3W,90-92	A26	680.6	33.35	33.35	2.60	0.53	1.72	0.11	0.23	7.90		*G. crassaformis*
306-U1313B-4H-3W,95-97	A27	681.7	33.40	33.40			1.47	0.03	0.20	6.60		*G. crassaformis*
306-U1313B-4H-3W,95-97	A1249	681.7	33.40	33.40	3.40	0.75						*C. wuellerstorfi*
306-U1313B-4H-3W,101.5-103.5	A28	683.1	33.47	33.47	2.32	0.78	1.33	0.02	0.12	5.78		*G. crassaformis*
306-U1313B-4H-3W,109-111	A29	684.7	33.54	33.54	2.17	0.96	1.91	0.00	0.00	8.75		*G. crassaformis*
306-U1313B-4H-3W,109-111	A29	684.7	33.54	33.54	2.17	0.96	1.70	0.16	0.05	7.78		*G. crassaformis*
306-U1313B-4H-3W,109-111	A1250	684.7	33.54	33.54	3.51	0.81						*C. wuellerstorfi*
306-U1313B-4H-3W,114.5-116.5	A30	685.9	33.60	33.60			1.81	0.05	0.10	8.30		*G. crassaformis*
306-U1313B-4H-3W,121-123	A31	687.4	33.66	33.66	1.93	1.34	1.88	0.09	0.02	8.60		*G. crassaformis*
306-U1313B-4H-3W,121-123	A31	687.4	33.66	33.66	1.93	1.34	1.89	0.16	0.21	8.65		*G. crassaformis*
306-U1313B-4H-3W,121-123	A1251	687.4	33.66	33.66	3.27	0.94						*C. wuellerstorfi*
306-U1313B-4H-3W,130-132	A32	689.3	33.75	33.75	2.18	1.44	1.54	0.00	0.11	6.99		*G. crassaformis*
306-U1313B-4H-3W,135-137	A33	690.4	33.80	33.80	1.81	0.98	1.54	0.02	0.12	6.97		*G. crassaformis*
306-U1313B-4H-3W,135-137	A1252	690.4	33.80	33.80	3.04	0.95						*C. wuellerstorfi*
306-U1313B-4H-3W,140.5-142.5	A34	691.6	33.86	33.86			1.78	0.11	0.11	8.17		*G. crassaformis*
306-U1313B-4H-3W,145-147	A35	692.6	33.90	33.90	1.62	1.09	1.48	0.02	0.09	6.65		*G. crassaformis*
306-U1313B-4H-3W,145-147	A1253	692.6	33.90	33.90	3.08	1.27						*C. wuellerstorfi*
306-U1313B-4H-4W,10.5-12.5	A36	696.0	34.06	34.06	1.49	0.85	2.00	0.07	0.12	9.13		*G. crassaformis*

Sample Label	Laboratory ID	Age (ka)	Comp. depth (m, MCD)	Adjusted MCD (m, AMCD)	$\delta^{18}O$ (‰, VPDB)	$\delta^{13}C$ (‰, VPDB)	Mg/Ca (mmol/mol)	Fe/Ca (mmol/mol)	Mn/Ca (mmol/mol)	SubT (°C)	$\delta 18O_{sw\text{-}ivc}$ (‰, VPDB)	Species
306-U1313B-4H-4W,10.5-12.5	A36	696.0	34.06	34.06	1.49	0.85	2.10	0.12	0.20	9.50		*G. crassaformis*
306-U1313B-4H-4W,15.5-17.5	A37	697.1	34.11	34.11			1.66	0.03	0.16	7.58		*G. crassaformis*
306-U1313B-4H-4W,15.5-17.5	A1254	697.1	34.11	34.11	3.16	1.41						*C. wuellerstorfi*
306-U1313B-4H-4W,21-23	A38	698.3	34.16	34.16	1.81	0.90	1.45	0.03	0.14	6.46		*G. crassaformis*
306-U1313B-4H-4W,28-30	A39	699.8	34.23	34.23	1.89	1.25	1.77	0.03	0.14	8.10		*G. crassaformis*
306-U1313B-4H-4W,28-30	A39	699.8	34.23	34.23	1.89	1.25	1.70	0.06	0.16	7.78		*G. crassaformis*
306-U1313B-4H-4W,28-30	A1255	699.8	34.23	34.23	3.30	1.27						*C. wuellerstorfi*
306-U1313B-4H-4W,35-37	A40	701.3	34.30	34.30	1.79	0.95	1.77	0.02	0.13	8.11		*G. crassaformis*
306-U1313B-4H-4W,40-42	A41	702.4	34.35	34.35	1.97	1.11	1.84	0.10	0.16	8.45		*G. crassaformis*
306-U1313B-4H-4W,40-42	A41	702.4	34.35	34.35	1.97	1.11	2.45	0.12	0.25	10.79		*G. crassaformis*
306-U1313B-4H-4W,40-42	A1256	702.4	34.35	34.35	3.33	1.32						*C. wuellerstorfi*
306-U1313B-4H-4W,45-47	A42	703.5	34.40	34.40			1.89	0.04	0.15	8.65		*G. crassaformis*
306-U1313B-4H-4W,51.5-53.5	A43	704.9	34.47	34.47	1.74	0.98	1.59	0.02	0.12	7.26		*G. crassaformis*
306-U1313B-4H-4W,51.5-53.5	A1257	704.9	34.47	34.47	3.22	1.21						*C. wuellerstorfi*
306-U1313B-4H-4W,56.5-58.5	A44	706.0	34.52	34.52	2.07	0.98	1.76	0.04	0.18	8.07		*G. crassaformis*
306-U1313B-4H-4W,56.5-58.5	A1307	706.0	34.52	34.52	3.44	0.47						*C. wuellerstorfi*
306-U1313B-4H-4W,60.5-62.5	A45	706.9	34.56	34.56			1.75	0.03	0.12	8.03		*G. crassaformis*
306-U1313B-4H-4W,65-67	A46	707.9	34.60	34.60	1.99	0.81	2.07	0.14	0.22	9.41		*G. crassaformis*
306-U1313B-4H-4W,65-67	A46	707.9	34.60	34.60	1.99	0.81	1.70	0.05	0.16	7.80		*G. crassaformis*
306-U1313B-4H-4W,65-67	A1306	707.9	34.60	34.60	3.36	1.20						*C. wuellerstorfi*
306-U1313B-4H-4W,70-72	A47	709.0	34.65	34.65	2.11	0.96	1.60	0.03	0.10	7.29		*G. crassaformis*
306-U1313B-4H-4W,70-72	A1259	709.0	34.65	34.65	3.27	1.00						*C. wuellerstorfi*
306-U1313B-4H-4W,78-80	A48	710.7	34.73	34.73	1.96	0.67	1.49	0.00	0.10	6.71		*G. crassaformis*
306-U1313B-4H-4W,84.5-86.5	A49	712.1	34.80	34.80	2.27	0.91	1.61	0.03	0.06	7.35		*G. crassaformis*
306-U1313B-4H-4W,84.5-86.5	A49	712.1	34.80	34.80	2.27	0.91	2.18	0.00	0.07	9.81		*G. crassaformis*
306-U1313B-4H-4W,84.5-86.5	A1260	712.1	34.80	34.80	3.37	0.82						*C. wuellerstorfi*
306-U1313B-4H-4W,91-93	A50	713.5	34.86	34.86			1.41	0.00	0.00	6.23		*G. crassaformis*

Sample Label	Laboratory ID	Age (ka)	Comp. depth (m, MCD)	Adjusted MCD (m, AMCD)	$\delta^{18}O$ (‰, VPDB)	$\delta^{13}C$ (‰, VPDB)	Mg/Ca (mmol/mol)	Fe/Ca (mmol/mol)	Mn/Ca (mmol/mol)	SubT (°C)	$\delta 18O_{sw\text{-}ivc}$ (‰, VPDB)	Species
306-U1313B-4H-4W,95-97	A51	714.3	34.90	34.90	3.52	1.02	1.16	0.06	-0.01	4.67		*G. crassaformis*
306-U1313B-4H-4W,95-97	A1261	714.3	34.90	34.90	4.10	-0.68						*C. wuellerstorfi*
306-U1313B-4H-4W,106.5-108.5	A52	716.4	35.02	35.02	3.40	1.09	1.07	0.00	0.00	3.95		*G. crassaformis*
306-U1313B-4H-4W,110-112	A53	717.0	35.05	35.05			1.08	0.06	0.00	4.05		*G. crassaformis*
306-U1313B-4H-4W,110-112	A1262	717.0	35.05	35.05	4.35	-0.46						*C. wuellerstorfi*
306-U1313B-4H-4W,115-117	A54	717.9	35.10	35.10	3.60	1.21	1.01	0.00	0.00	3.50		*G. crassaformis*
306-U1313B-4H-4W,120-122	A55	718.8	35.15	35.15			1.75	0.00	0.00	8.02		*G. crassaformis*
306-U1313B-4H-4W,120-122	A1263	718.8	35.15	35.15	3.80	0.30						*C. wuellerstorfi*
306-U1313B-4H-4W,126.5-128.5	A56	720.0	35.22	35.22	2.72	1.06	1.44	0.02	0.11	6.41		*G. crassaformis*
306-U1313B-4H-4W,131.5-133.5	A57	720.9	35.27	35.27			1.43	0.02	0.13	6.39		*G. crassaformis*
306-U1313B-4H-4W,131.5-133.5	A1264	720.9	35.27	35.27	4.28	-0.43						*C. wuellerstorfi*
306-U1313B-4H-4W,135-137	A58	721.6	35.30	35.30	2.69	1.13	1.08	0.00	0.05	4.08		*G. crassaformis*
306-U1313B-4H-4W,140-142	A59	722.5	35.35	35.35			1.47	0.00	0.07	6.61		*G. crassaformis*
306-U1313B-4H-4W,140-142	A1265	722.5	35.35	35.35	4.19	0.30						*C. wuellerstorfi*
306-U1313B-4H-4W,145-147	A60	723.4	35.40	35.40	2.98	1.05	1.44	0.00	0.06	6.42		*G. crassaformis*
306-U1313B-4H-5W,2.5-4.5	A61	724.7	35.48	35.48	2.70	1.03	1.65	0.03	0.18	7.52		*G. crassaformis*
306-U1313B-4H-5W,2.5-4.5	A1266	724.7	35.48	35.48	4.27	0.10						*C. wuellerstorfi*
306-U1313B-4H-5W,7-9	A62	725.6	35.52	35.52			1.76	0.10	0.12	8.08		*G. crassaformis*
306-U1313B-4H-5W,10-12	A63	726.1	35.55	35.55	2.41	1.30	1.66	0.05	0.16	7.61		*G. crassaformis*
306-U1313B-4H-5W,10-12	A1267	726.1	35.55	35.55	4.05	0.59						*C. wuellerstorfi*
306-U1313B-4H-5W,15-17	A64	727.0	35.60	35.60	2.29	0.96	1.54	0.00	0.06	6.96		*G. crassaformis*
306-U1313B-4H-5W,22-24	A65	728.3	35.67	35.67	2.03	0.87	1.40	0.02	0.10	6.17		*G. crassaformis*
306-U1313B-4H-5W,22-24	A1268	728.3	35.67	35.67	3.87	0.77						*C. wuellerstorfi*
306-U1313B-4H-5W,27-29	A66	729.2	35.72	35.72	2.11	1.07	1.96	0.09	0.24	8.94		*G. crassaformis*
306-U1313B-4H-5W,32.5-34.5	A67	730.2	35.78	35.78			1.66	0.03	0.20	7.57		*G. crassaformis*
306-U1313B-4H-5W,32.5-34.5	A1269	730.2	35.78	35.78	3.48	0.81						*C. wuellerstorfi*
306-U1313B-4H-5W,35-37	A68	730.7	35.80	35.80	2.15	1.03	1.30	0.00	0.10	5.56		*G. crassaformis*

Sample Label	Laboratory ID	Age (ka)	Comp. depth (m, MCD)	Adjusted MCD (m, AMCD)	$\delta^{18}O$ (‰, VPDB)	$\delta^{13}C$ (‰, VPDB)	Mg/Ca (mmol/mol)	Fe/Ca (mmol/mol)	Mn/Ca (mmol/mol)	SubT (°C)	$\delta 18O_{sw\text{-}ivc}$ (‰, VPDB)	Species
306-U1313B-4H-5W,40-42	A69	731.6	35.85	35.85	2.05	0.86	1.58	0.02	0.14	7.19		*G. crassaformis*
306-U1313B-4H-5W,40-42	A69	731.6	35.85	35.85	2.05	0.86	1.45	0.01	0.12	6.46		*G. crassaformis*
306-U1313B-4H-5W,40-42	A1270	731.6	35.85	35.85	3.55	1.10						*C. wuellerstorfi*
306-U1313B-4H-5W,45-47	A70	732.5	35.90	35.90	2.25	1.20	1.64	0.03	0.16	7.50		*G. crassaformis*
306-U1313B-4H-5W,51.5-52.5	A71	733.6	35.97	35.97	2.17	0.87	1.80	0.11	0.18	8.26		*G. crassaformis*
306-U1313B-4H-5W,51.5-52.5	A1271	733.6	35.97	35.97	3.40	0.83						*C. wuellerstorfi*
306-U1313B-4H-5W,57-59	A72	734.7	36.02	36.02			1.98	0.03	0.10	9.01		*G. crassaformis*
306-U1313B-4H-5W,60-62	A73	735.2	36.05	36.05	2.14	0.72	1.86	0.00	0.14	8.50		*G. crassaformis*
306-U1313B-4H-5W,60-62	A1272	735.2	36.05	36.05	3.80	0.52						*C. wuellerstorfi*
306-U1313B-4H-5W,65-67	A74	736.1	36.10	36.10			1.33	0.02	0.11	5.80		*G. crassaformis*
306-U1313B-4H-5W,70-72	A75	737.0	36.15	36.15	2.36	1.13	1.54	0.04	0.12	6.95		*G. crassaformis*
306-U1313B-4H-5W,70-72	A1273	737.0	36.15	36.15	3.58	0.79						*C. wuellerstorfi*
306-U1313B-4H-5W,76.5-78.5	A76	738.2	36.22	36.22	2.19	0.56	1.64	0.08	0.17	7.51		*G. crassaformis*
306-U1313B-4H-5W,81.5-83.5	A77	739.1	36.27	36.27			1.44	0.03	0.16	6.41		*G. crassaformis*
306-U1313B-4H-5W,81.5-83.5	A1274	739.1	36.27	36.27	3.66	0.71						*C. wuellerstorfi*
306-U1313B-4H-5W,85-87	A78	739.8	36.30	36.30	2.19	0.49	1.68	0.10	0.09	7.69		*G. crassaformis*
306-U1313B-4H-5W,90-92	A79	740.7	36.35	36.35			1.98	0.05	0.17	9.05		*G. crassaformis*
306-U1313C-5H-1W,61-63	A357	740.7	36.35	36.35			1.62	0.04	0.21	7.36		*G. crassaformis*
306-U1313B-4H-5W,90-92	A1275	740.7	36.35	36.35	3.77	0.54						*C. wuellerstorfi*
306-U1313B-4H-5W,95-97	A80	741.6	36.40	36.40	2.47	0.54	1.43	0.00	0.00	6.37		*G. crassaformis*
306-U1313C-5H-1W,66-68	A358	741.6	36.40	36.40			1.57	0.03	0.14	7.15		*G. crassaformis*
306-U1313B-4H-5W,95-97	A1276	741.6	36.40	36.40	3.72	0.62						*C. wuellerstorfi*
306-U1313C-5H-1W,71-73	A359	742.5	36.45	36.45			1.51	0.00	0.13	6.83		*G. crassaformis*
306-U1313C-5H-1W,71-73	A1277	742.5	36.45	36.45	3.77	-0.19						*C. wuellerstorfi*
306-U1313B-4H-5W,101.5-103.5	A81	742.8	36.47	36.47	2.23	0.48	1.29	0.02	0.09	5.53		*G. crassaformis*
306-U1313C-5H-1W,76.5-78.5	A1278	743.5	36.51	36.40	3.69	0.56						*C. wuellerstorfi*
306-U1313B-4H-5W,110-112	A1279	744.3	36.55	36.43	4.32	-0.72						*C. wuellerstorfi*

Sample Label	Laboratory ID	Age (ka)	Comp. depth (m, MCD)	Adjusted MCD (m, AMCD)	$\delta^{18}O$ (‰, VPDB)	$\delta^{13}C$ (‰, VPDB)	Mg/Ca (mmol/mol)	Fe/Ca (mmol/mol)	Mn/Ca (mmol/mol)	SubT (°C)	$\delta 18O_{sw\text{-}ivc}$ (‰, VPDB)	Species
306-U1313B-4H-5W,115-117	A1280	745.3	36.60	36.48	4.25	-0.94						*C. wuellerstorfi*
306-U1313C-5H-1W,91-93	A363	746.2	36.65	36.55	1.93	0.50	1.28	0.04	0.00	5.47		*G. crassaformis*
306-U1313B-4H-5W,120-122	A1281	746.2	36.65	36.55	4.09	-0.74						*C. wuellerstorfi*
306-U1313B-4H-5W,125-127	A86	747.1	36.70	36.61			1.01	0.03	0.06	3.54		*G. crassaformis*
306-U1313C-5H-1W,96-98	A364	747.1	36.70	36.61			1.13	0.05	0.01	4.46		*G. crassaformis*
306-U1313B-4H-5W,125-127	A1282	747.1	36.70	36.61	4.26	-0.07						*C. wuellerstorfi*
306-U1313C-5H-1W,101.5-103.5	A365	748.1	36.76	36.67	3.48	0.78	1.08	0.00	0.00	4.06		*G. crassaformis*
306-U1313C-5H-1W,101.5-103.5	A1283	748.1	36.76	36.67	4.31	-0.31						*C. wuellerstorfi*
306-U1313C-5H-1W,106.5-108.5	A366	749.0	36.81	36.73			1.10	0.02	0.07	4.20		*G. crassaformis*
306-U1313C-5H-1W,111-113	A367	749.8	36.85	36.77	2.72	0.82	1.19	0.00	0.00	4.84		*G. crassaformis*
306-U1313C-5H-1W,111-113	A1284	749.8	36.85	36.77	4.32	-0.32						*C. wuellerstorfi*
306-U1313C-5H-1W,116-118	A368	750.7	36.90	36.82			1.16	0.01	0.05	4.64		*G. crassaformis*
306-U1313C-5H-1W,121-123	A369	751.6	36.95	36.87	3.09	1.20	1.13	0.00	0.00	4.42		*G. crassaformis*
306-U1313C-5H-1W,121-123	A1285	751.6	36.95	36.87	4.79							*U. peregrina*
306-U1313C-5H-1W,126.5-128.5	A370	752.6	37.01	36.94	3.04	1.14	1.01	0.04	0.00	3.55		*G. crassaformis*
306-U1313C-5H-1W,133.5-135.5	A371	753.9	37.08	37.01	2.68	0.73	1.03	0.00	0.00	3.70		*G. crassaformis*
306-U1313C-5H-1W,133.5-135.5	A1286	753.9	37.08	37.01	3.75	-0.48						*C. wuellerstorfi*
306-U1313C-5H-1W,141-143	A373	755.3	37.15	37.08	3.00	1.19	0.96	0.00	0.00	3.12		*G. crassaformis*
306-U1313C-5H-1W,141-143	A1287	755.3	37.15	37.08	3.98	0.04						*C. wuellerstorfi*
306-U1313C-5H-2W,2-4	A375	757.3	37.26	37.17	3.06	0.99	0.95	0.00	0.00	3.05		*G. crassaformis*
306-U1313C-5H-2W,2-4	A1288	757.3	37.26	37.17	4.14	-0.14						*C. wuellerstorfi*
306-U1313C-5H-2W,6.5-8.5	A376	758.1	37.31	37.21			1.19	0.03	0.06	4.87		*G. crassaformis*
306-U1313C-5H-2W,11-13	A377	759.3	37.35	37.25	3.03	1.01	1.14	0.00	0.03	4.51		*G. crassaformis*
306-U1313C-5H-2W,11-13	A1289	759.3	37.35	37.25	4.71							*U. peregrina*
306-U1313C-5H-2W,15.5-17.5	A378	760.6	37.40	37.28			1.02	0.02	0.01	3.59		*G. crassaformis*
306-U1313C-5H-2W,21.5-23.5	A379	762.3	37.46	37.33	2.56	1.00	1.49	0.05	0.01	6.71		*G. crassaformis*
306-U1313C-5H-2W,21.5-23.5	A379	762.3	37.46	37.33	2.56	1.00	1.23	0.03	0.03	5.14		*G. crassaformis*

Sample Label	Laboratory ID	Age (ka)	Comp. depth (m, MCD)	Adjusted MCD (m, AMCD)	$\delta^{18}O$ (‰, VPDB)	$\delta^{13}C$ (‰, VPDB)	Mg/Ca (mmol/mol)	Fe/Ca (mmol/mol)	Mn/Ca (mmol/mol)	SubT (°C)	$\delta 18O_{sw\text{-}ivc}$ (‰, VPDB)	Species
306-U1313C-5H-2W,21.5-23.5	A1290	762.3	37.46	37.33	3.53	-0.19						*C. wuellerstorfi*
306-U1313C-5H-2W,27.5-29.5	A380	764.0	37.52	37.40			1.30	0.02	0.06	5.57		*G. crassaformis*
306-U1313C-5H-2W,32-34	A381	765.3	37.56	37.47	2.29	0.99	1.56	0.01	0.10	7.08		*G. crassaformis*
306-U1313C-5H-2W,32-34	A1291	765.3	37.56	37.47	3.85	0.56						*C. wuellerstorfi*
306-U1313C-5H-2W,36-38	A382	766.5	37.60	37.52			1.56	0.10	0.08	7.06		*G. crassaformis*
306-U1313C-5H-2W,41-43	A383	767.9	37.65	37.60	2.07	1.03	1.69	0.00	0.12	7.75		*G. crassaformis*
306-U1313C-5H-2W,41-43	A1292	767.9	37.65	37.60	3.70	0.27						*C. wuellerstorfi*
306-U1313C-5H-2W,46-48	A384	769.3	37.70	37.67			1.66	0.03	0.17	7.59		*G. crassaformis*
306-U1313C-5H-2W,51-53	A385	770.7	37.75	37.74	1.92	1.20	1.41	0.04	0.11	6.24		*G. crassaformis*
306-U1313C-5H-2W,51-53	A1293	770.7	37.75	37.74	3.37	1.00						*C. wuellerstorfi*
306-U1313C-5H-2W,56.5-58.5	A386	772.3	37.81	37.81			1.61	0.04	0.13	7.36		*G. crassaformis*
306-U1313C-5H-2W,61-63	A387	773.6	37.85	37.85	1.92	1.01	1.61	0.01	0.09	7.35		*G. crassaformis*
306-U1313C-5H-2W,61-63	A1294	773.6	37.85	37.85	3.23	0.52						*C. wuellerstorfi*
306-U1313C-5H-2W,66-68	A388	775.0	37.90	37.90			1.55	0.06	0.11	7.01		*G. crassaformis*
306-U1313C-5H-2W,70.5-72.5	A389	776.3	37.95	37.96	2.15	1.21	1.38	0.02	0.12	6.08		*G. crassaformis*
306-U1313C-5H-2W,70.5-72.5	A1295	776.3	37.95	37.96	3.23	0.17						*C. wuellerstorfi*
306-U1313C-5H-2W,76-78	A390	777.9	38.00	38.01	2.03	1.22	1.55	0.05	0.13	7.00		*G. crassaformis*
306-U1313C-5H-2W,81.5-83.5	A391	779.4	38.06	38.07			1.62	0.05	0.18	7.37		*G. crassaformis*
306-U1313C-5H-2W,81.5-83.5	A1296	779.4	38.06	38.07	3.12	1.15						*C. wuellerstorfi*
306-U1313C-5H-2W,86-88	A392	780.7	38.10	38.12	1.79	1.18	1.41	0.00	0.11	6.23		*G. crassaformis*
306-U1313C-5H-2W,91-93	A393	782.1	38.15	38.17	1.93	1.36	1.70	0.03	0.14	7.78		*G. crassaformis*
306-U1313C-5H-2W,91-93	A1297	782.1	38.15	38.17	3.05	0.99						*C. wuellerstorfi*
306-U1313C-5H-2W,96-98	A394	783.6	38.20	38.22	1.58	0.81	1.40	0.02	0.11	6.20		*G. crassaformis*
306-U1313C-5H-2W,101.5-103.5	A395	785.1	38.26	38.28	1.75	0.93	1.55	0.07	0.13	7.02		*G. crassaformis*
306-U1313C-5H-2W,101.5-103.5	A1298	785.1	38.26	38.28	2.93	0.84						*C. wuellerstorfi*
306-U1313C-5H-2W,106-108	A396	786.4	38.30	38.33	1.79	0.96	1.47	0.00	0.08	6.59		*G. crassaformis*
306-U1313C-5H-2W,111-113	A397	787.8	38.35	38.38	1.78	0.68	1.41	0.01	0.13	6.23		*G. crassaformis*

Sample Label	Laboratory ID	Age (ka)	Comp. depth (m, MCD)	Adjusted MCD (m, AMCD)	$\delta^{18}O$ (‰, VPDB)	$\delta^{13}C$ (‰, VPDB)	Mg/Ca (mmol/mol)	Fe/Ca (mmol/mol)	Mn/Ca (mmol/mol)	SubT (°C)	$\delta 18O_{sw\text{-}ivc}$ (‰, VPDB)	Species
306-U1313C-5H-2W,111-113	A1299	787.8	38.35	38.38	2.99	-0.06						*C. wuellerstorfi*
306-U1313C-5H-2W,116-118	A398	789.3	38.40	38.43	2.07	0.97	1.54	0.00	0.10	6.98		*G. crassaformis*
306-U1313C-5H-2W,121-123	A399	790.6	38.45	38.49	1.78	0.57	1.30	0.00	0.05	5.57		*G. crassaformis*
306-U1313C-5H-2W,121-123	A1300	790.6	38.45	38.49	3.61	-0.33						*C. wuellerstorfi*
306-U1313C-5H-2W,126-128	A400	791.8	38.50	38.54	2.14	0.70	1.41	0.00	0.00	6.27		*G. crassaformis*
306-U1313C-5H-2W,131.5-133.5	A401	793.1	38.56	38.60	2.76	1.08	1.26	0.00	0.00	5.32		*G. crassaformis*
306-U1313C-5H-2W,131.5-133.5	A1301	793.1	38.56	38.60	4.14	-0.63						*C. wuellerstorfi*
306-U1313C-5H-2W,141.5-143.5	A403	795.5	38.66	38.71	3.42	1.01	1.76	0.02	0.05	8.07		*G. crassaformis*
306-U1313C-5H-2W,141.5-143.5	A403	795.5	38.66	38.71	3.42	1.01	1.39	0.11	0.00	6.11		*G. crassaformis*
306-U1313C-5H-2W,141.5-143.5	A1302	795.5	38.66	38.71	4.40	-0.28						*C. wuellerstorfi*
306-U1313C-5H-2W,146.5-148.5	A404	796.7	38.71	38.76	3.15	0.85	1.12	0.00	0.00	4.38		*G. crassaformis*
306-U1313C-5H-3W,2-4	A405	798.1	38.76	38.81	3.74	1.19	0.89	0.00	0.00	2.43		*G. crassaformis*
306-U1313C-5H-3W,2-4	A405	798.1	38.76	38.81	3.74	1.19	1.00	0.01	0.01	3.39		*G. crassaformis*
306-U1313C-5H-3W,2-4	A1303	798.1	38.76	38.81	4.11	-0.61						*C. wuellerstorfi*
306-U1313C-5H-3W,6-8	A406	799.0	38.80	38.85			1.09	0.04	0.04	4.13		*G. crassaformis*
306-U1313C-5H-3W,10.5-12.5	A407	800.1	38.85	38.89	3.68	0.95	1.03	0.04	0.00	3.68		*G. crassaformis*
306-U1313C-5H-3W,10.5-12.5	A1304	800.1	38.85	38.89	4.36	-0.83						*C. wuellerstorfi*
306-U1313C-5H-3W,15.5-17.5	A408	801.3	38.90	38.94	3.45	1.22	1.03	0.00	0.04	3.71		*G. crassaformis*
306-U1313C-5H-3W,22-24	A409	802.9	38.96	39.00	3.66	1.16	0.95	0.00	0.00	3.01		*G. crassaformis*
306-U1313C-5H-3W,27-29	A410	804.1	39.01	39.05			1.22	0.02	0.12	5.05		*G. crassaformis*
306-U1313C-5H-3W,32-34	A411	805.3	39.06	39.10	3.33	1.08	0.96	0.00	0.00	3.09		*G. crassaformis*
306-U1313C-5H-3W,36-38	A412	806.2	39.10	39.14			1.12	0.04	0.08	4.34		*G. crassaformis*
306-U1313C-5H-3W,41-43	A413	807.2	39.15	39.19	3.48	1.22	1.06	0.04	0.02	3.92		*G. crassaformis*
306-U1313C-5H-3W,45.5-47.5	A414	808.1	39.20	39.24	3.35	1.13	0.97	0.00	0.00	3.18		*G. crassaformis*
306-U1313C-5H-3W,52-54	A415	809.4	39.26	39.30	3.01	0.99	1.10	0.00	0.00	4.22		*G. crassaformis*
306-U1313C-5H-3W,56.5-58.5	A416	810.4	39.31	39.35			1.08	0.03	0.07	4.08		*G. crassaformis*
306-U1313C-5H-3W,61-63	A417	811.3	39.35	39.39	3.33	1.20	0.91	0.00	0.04	2.70		*G. crassaformis*

Sample Label	Laboratory ID	Age (ka)	Comp. depth (m, MCD)	Adjusted MCD (m, AMCD)	$\delta^{18}O$ (‰, VPDB)	$\delta^{13}C$ (‰, VPDB)	Mg/Ca (mmol/mol)	Fe/Ca (mmol/mol)	Mn/Ca (mmol/mol)	SubT (°C)	$\delta 18O_{sw\text{-}ivc}$ (‰, VPDB)	Species
306-U1313C-5H-3W,66.5-68.5	A418	812.4	39.41	39.45			1.45	0.09	0.20	6.47		*G. crassaformis*
306-U1313C-5H-3W,71-73	A419	813.3	39.45	39.49	2.80	0.90	1.21	0.00	0.05	4.97		*G. crassaformis*
306-U1313C-5H-3W,76.5-78.5	A420	814.4	39.51	39.55			1.49	0.05	0.09	6.67		*G. crassaformis*
306-U1313C-5H-3W,81.5-83.5	A421	815.5	39.56	39.60	2.24	1.10	1.31	0.00	0.08	5.65		*G. crassaformis*
306-U1313C-5H-3W,86-88	A422	816.4	39.60	39.64			1.60	0.10	0.14	7.28		*G. crassaformis*
306-U1313C-5H-3W,91-93	A423	817.4	39.65	39.69	2.23	1.05	1.46	0.00	0.08	6.54		*G. crassaformis*
306-U1313C-5H-3W,96-98	A424	818.4	39.70	39.74			1.59	0.02	0.13	7.25		*G. crassaformis*
306-U1313C-5H-3W,101-103	A425	819.4	39.75	39.79	2.55	1.17	1.52	0.00	0.14	6.86		*G. crassaformis*
306-U1313C-5H-3W,106.5-108.5	A426	820.6	39.81	39.85			1.47	0.04	0.16	6.58		*G. crassaformis*
306-U1313C-5H-3W,111-113	A427	821.5	39.85	39.89	1.87	0.72	1.38	0.00	0.08	6.10		*G. crassaformis*
306-U1313C-5H-3W,116-118	A428	822.5	39.90	39.94			1.66	0.03	0.12	7.58		*G. crassaformis*
306-U1313C-5H-3W,121-123	A429	823.5	39.95	39.99	2.15	1.02	1.51	0.00	0.10	6.79		*G. crassaformis*
306-U1313C-5H-3W,126-128	A430	824.5	40.00	40.04			1.66	0.11	0.14	7.57		*G. crassaformis*
306-U1313C-5H-3W,131-133	A431	825.6	40.05	40.09	2.01	0.92	1.52	0.02	0.08	6.86		*G. crassaformis*
306-U1313C-5H-3W,136-138	A432	826.8	40.10	40.14	2.00	1.09	1.55	0.00	0.12	7.03		*G. crassaformis*
306-U1313C-5H-3W,141-143	A433	828.1	40.15	40.19			1.62	0.04	0.08	7.41		*G. crassaformis*
306-U1313C-5H-3W,146-148	A434	829.5	40.20	40.24	1.93	0.68	1.71	0.02	0.14	7.82		*G. crassaformis*
306-U1313C-5H-4W,2.5-4.5	A435	831.2	40.27	40.31	1.87	0.84	1.38	0.02	0.08	6.07		*G. crassaformis*
306-U1313C-5H-4W,6.5-8.5	A436	832.2	40.31	40.35			1.54	0.03	0.13	6.99		*G. crassaformis*
306-U1313C-5H-4W,11-13	A437	833.4	40.35	40.39	2.25	0.90	1.38	0.00	0.12	6.07		*G. crassaformis*
306-U1313C-5H-4W,16-18	A438	834.7	40.40	40.44	2.14	1.19	1.54	0.04	0.12	6.96		*G. crassaformis*
306-U1313C-5H-4W,16-18	A438	834.7	40.40	40.44	2.14	1.19	1.57	0.01	0.16	7.12		*G. crassaformis*
306-U1313C-5H-4W,21.5-23.5	A439	836.1	40.46	40.50	1.85	0.76	1.62	0.03	0.14	7.39		*G. crassaformis*
306-U1313C-5H-4W,27-29	A440	837.6	40.51	40.55	1.99	0.85	1.41	0.00	0.12	6.27		*G. crassaformis*
306-U1313C-5H-4W,32-34	A441	838.9	40.56	40.60	2.17	1.04	1.41	0.02	0.12	6.26		*G. crassaformis*
306-U1313C-5H-4W,36-38	A442	840.0	40.60	40.64	1.99	0.95	1.48	0.03	0.16	6.62		*G. crassaformis*
306-U1313C-5H-4W,41-43	A443	841.3	40.65	40.70	1.80	0.90	1.41	0.00	0.08	6.24		*G. crassaformis*

Sample Label	Laboratory ID	Age (ka)	Comp. depth (m, MCD)	Adjusted MCD (m, AMCD)	$\delta^{18}O$ (‰, VPDB)	$\delta^{13}C$ (‰, VPDB)	Mg/Ca (mmol/mol)	Fe/Ca (mmol/mol)	Mn/Ca (mmol/mol)	SubT (°C)	$\delta 18O_{sw\text{-}ivc}$ (‰, VPDB)	Species
306-U1313C-5H-4W,46-48	A444	842.6	40.70	40.75	2.13	1.00	1.56	0.00	0.09	7.09		*G. crassaformis*
306-U1313C-5H-4W,51.5-53.5	A445	844.0	40.76	40.81	2.09	1.12	1.45	0.02	0.13	6.48		*G. crassaformis*
306-U1313C-5H-4W,56.5-58.5	A446	845.3	40.81	40.86	1.98	1.16	1.55	0.03	0.14	7.02		*G. crassaformis*
306-U1313C-5H-4W,61-63	A447	846.5	40.85	40.90	1.89	0.85	1.51	0.00	0.12	6.80		*G. crassaformis*
306-U1313C-5H-4W,66-68	A1068	847.8	40.90	40.95	3.53	0.29						*C. wuellerstorfi*
306-U1313C-5H-4W,71-73	A449	849.1	40.95	41.00	2.02	1.03	1.51	0.00	0.11	6.80		*G. crassaformis*
306-U1313C-5H-4W,77-79	A450	850.7	41.01	41.06	1.83	0.98	1.70	0.03	0.13	7.76		*G. crassaformis*
306-U1313C-5H-4W,77-79	A1069	850.7	41.01	41.06	3.29	0.33						*C. wuellerstorfi*
306-U1313C-5H-4W,81.5-83.5	A451	851.9	41.06	41.11	1.84	0.79	1.52	0.03	0.11	6.89		*G. crassaformis*
306-U1313C-5H-4W,86-88	A452	853.1	41.10	41.15	1.73	0.78	1.39	0.00	0.07	6.14		*G. crassaformis*
306-U1313C-5H-4W,86-88	A1070	853.1	41.10	41.15	3.07	0.81						*C. wuellerstorfi*
306-U1313C-5H-4W,91-93	A453	854.4	41.15	41.20	1.80	0.98	1.77	0.03	0.10	8.09		*G. crassaformis*
306-U1313C-5H-4W,91-93	A1009	854.4	41.15	41.20	3.40	0.59						*C. wuellerstorfi*
306-U1313C-5H-4W,96-98	A454	855.7	41.20	41.25	2.03	0.90	1.91	0.06	0.07	8.72		*G. crassaformis*
306-U1313C-5H-4W,99.5-101.5	A455	856.6	41.24	41.29	1.78	0.85	1.61	0.00	0.08	7.32		*G. crassaformis*
306-U1313C-5H-4W,99.5-101.5	A1026	856.6	41.24	41.29	3.22	0.80						*C. wuellerstorfi*
306-U1313C-5H-4W,107-109	A456	858.6	41.31	41.36	2.13	1.14	1.48	0.00	0.08	6.64		*G. crassaformis*
306-U1313C-5H-4W,107-109	A962	858.6	41.31	41.36	3.18	0.93						*C. wuellerstorfi*
306-U1313C-5H-4W,111-113	A457	859.6	41.35	41.40	1.65	1.06	1.64	0.03	0.09	7.46		*G. crassaformis*
306-U1313C-5H-4W,116-118	A458	860.9	41.40	41.45	1.68	0.92	1.45	0.00	0.06	6.49		*G. crassaformis*
306-U1313C-5H-4W,116-118	A1027	860.9	41.40	41.45	2.72	0.56						*C. wuellerstorfi*
306-U1313C-5H-4W,121-123	A459	862.3	41.45	41.51	1.40	0.78	1.87	0.00	0.08	8.58		*G. crassaformis*
306-U1313C-5H-4W,121-123	A459	862.3	41.45	41.51	1.40	0.78	1.66	0.05	0.13	7.56		*G. crassaformis*
306-U1313C-5H-4W,126.5-128.5	A460	863.7	41.51	41.57	1.69	0.76	1.44	0.02	0.09	6.40		*G. crassaformis*
306-U1313C-5H-4W,126.5-128.5	A963	863.7	41.51	41.57	2.68	0.61						*C. wuellerstorfi*
306-U1313C-5H-4W,132-134	A461	865.1	41.56	41.62	1.78	0.68	1.39	0.00	0.07	6.11		*G. crassaformis*
306-U1313C-5H-4W,132-134	A461	865.1	41.56	41.62	1.78	0.68	1.51	0.03	0.11	6.79		*G. crassaformis*

Sample Label	Laboratory ID	Age (ka)	Comp. depth (m, MCD)	Adjusted MCD (m, AMCD)	$\delta^{18}O$ (‰, VPDB)	$\delta^{13}C$ (‰, VPDB)	Mg/Ca (mmol/mol)	Fe/Ca (mmol/mol)	Mn/Ca (mmol/mol)	SubT (°C)	$\delta 18O_{sw\text{-}ivc}$ (‰, VPDB)	Species
306-U1313C-5H-4W,136-138	A462	866.2	41.60	41.66	1.70	0.46	1.25	0.03	0.04	5.26		*G. crassaformis*
306-U1313C-5H-4W,136-138	A1028	866.2	41.60	41.66	3.99	-0.77						*C. wuellerstorfi*
306-U1313C-5H-4W,141-143	A463	867.5	41.65	41.71	1.49	0.35	1.34	0.00	0.00	5.80		*G. crassaformis*
306-U1313C-5H-5W,11-13	A955	867.5	41.65	41.71	5.06							*U. peregrina*
306-U1313C-5H-5W,11-13	A956	867.5	41.65	41.71	4.54	0.13						*C. wuellerstorfi*
306-U1313C-5H-4W,146-148	A464	868.8	41.70	41.76	1.84	1.00	1.38	0.02	0.05	6.05		*G. crassaformis*
306-U1313C-5H-4W,146-148	A964	868.8	41.70	41.76	3.41	-0.05						*C. wuellerstorfi*
306-U1313C-5H-5W,2.5-4.5	A1045	870.4	41.77	41.83	3.99	-0.34						*C. wuellerstorfi*
306-U1313C-5H-5W,6.5-8.5	A1029	871.4	41.81	41.87	4.42	-0.75						*C. wuellerstorfi*
306-U1313C-5H-5W,21.5-23.5	A1030	875.2	41.96	42.01	4.51	-0.36						*C. wuellerstorfi*
306-U1313C-5H-5W,31.5-33.5	A967	877.8	42.06	42.11	4.96							*U. peregrina*
306-U1313C-5H-5W,36-38	A472	878.9	42.10	42.14	1.86	0.90	1.40	0.00	0.00	6.16		*G. crassaformis*
306-U1313C-5H-5W,36-38	A1046	878.9	42.10	42.14	4.43	-0.37						*C. wuellerstorfi*
306-U1313C-5H-5W,41-43	A473	880.2	42.15	42.19	2.13	1.01	1.70	0.00	0.00	7.77		*G. crassaformis*
306-U1313C-5H-5W,41-43	A1031	880.2	42.15	42.19	4.40	-0.21						*C. wuellerstorfi*
306-U1313C-5H-5W,46-48	A474	881.5	42.20	42.24	1.64	0.50	1.34	0.10	0.09	5.82		*G. crassaformis*
306-U1313C-5H-5W,52-54	A475	883.0	42.26	42.30	2.03	0.72	1.47	0.00	0.00	6.59		*G. crassaformis*
306-U1313C-5H-5W,52-54	A968	883.0	42.26	42.30	4.14	0.13						*C. wuellerstorfi*
306-U1313C-5H-5W,61-63	A1032	885.3	42.35	42.38	4.22	0.29						*C. wuellerstorfi*
306-U1313C-5H-5W,66-68	A478	886.5	42.40	42.43	1.80	0.90	1.48	0.04	0.12	6.62		*G. crassaformis*
306-U1313C-5H-5W,71-73	A969	887.8	42.45	42.48	4.27	-0.43						*C. wuellerstorfi*
306-U1313C-5H-5W,76-78	A480	889.1	42.50	42.53	2.24	1.04	1.42	0.00	0.00	6.30		*G. crassaformis*
306-U1313C-5H-5W,81-83	A481	890.4	42.55	42.58	3.29	1.21	1.37	0.04	0.01	6.03		*G. crassaformis*
306-U1313C-5H-5W,81-83	A1071	890.4	42.55	42.58	4.20	-0.91						*C. wuellerstorfi*
306-U1313C-5H-5W,86-88	A482	891.6	42.60	42.62	3.33	1.19	0.98	0.02	0.00	3.28		*G. crassaformis*
306-U1313C-5H-5W,91-93	A483	892.9	42.65	42.67	3.24	1.10	1.09	0.03	0.00	4.15		*G. crassaformis*
306-U1313C-5H-5W,91-93	A1072	892.9	42.65	42.67	4.26	-0.66						*C. wuellerstorfi*

Sample Label	Laboratory ID	Age (ka)	Comp. depth (m, MCD)	Adjusted MCD (m, AMCD)	$\delta^{18}O$ (‰, VPDB)	$\delta^{13}C$ (‰, VPDB)	Mg/Ca (mmol/mol)	Fe/Ca (mmol/mol)	Mn/Ca (mmol/mol)	SubT (°C)	$\delta 18O_{sw\text{-}ivc}$ (‰, VPDB)	Species
306-U1313C-5H-5W,96-98	A484	894.2	42.70	42.72	3.45	1.08	0.92	0.00	0.00	2.77		*G. crassaformis*
306-U1313C-5H-5W,96-98	A958	894.2	42.70	42.72	4.24	-0.64						*C. wuellerstorfi*
306-U1313C-5H-5W,101.5-103.5	A485	895.6	42.76	42.78	3.47	1.15	1.17	0.00	0.05	4.74		*G. crassaformis*
306-U1313C-5H-5W,101.5-103.5	A485	895.6	42.76	42.78	3.47	1.15	1.04	0.02	0.02	3.76		*G. crassaformis*
306-U1313C-5H-5W,101.5-103.5	A1073	895.6	42.76	42.78	4.20	0.05						*C. wuellerstorfi*
306-U1313C-5H-5W,106-108	A486	896.7	42.80	42.82	3.30	0.80	1.03	0.00	0.00	3.68		*G. crassaformis*
306-U1313C-5H-5W,110.5-112.5	A487	897.9	42.85	42.86	3.04	1.01	1.03	0.02	0.01	3.71		*G. crassaformis*
306-U1313C-5H-5W,110.5-112.5	A1074	897.9	42.85	42.86	4.11	-0.23						*C. wuellerstorfi*
306-U1313C-5H-5W,115.5-117.5	A488	899.1	42.90	42.91	2.87	0.91	1.08	0.00	0.00	4.09		*G. crassaformis*
306-U1313C-5H-5W,120.5-122.5	A489	900.3	42.95	42.96	2.80	1.12	1.61	0.00	0.08	7.32		*G. crassaformis*
306-U1313C-5H-5W,120.5-122.5	A489	900.3	42.95	42.96	2.80	1.12	1.07	0.01	0.04	4.01		*G. crassaformis*
306-U1313C-5H-5W,120.5-122.5	A1075	900.3	42.95	42.96	3.83	0.65						*C. wuellerstorfi*
306-U1313C-5H-5W,126.5-128.5	A490	901.5	43.01	43.02	2.92	1.06	1.31	0.02	0.10	5.63		*G. crassaformis*
306-U1313C-5H-5W,132-134	A491	902.6	43.06	43.07	2.82	1.06	1.48	0.05	0.03	6.65		*G. crassaformis*
306-U1313C-5H-5W,132-134	A1076	902.6	43.06	43.07	3.61	0.88						*C. wuellerstorfi*
306-U1313C-5H-5W,135.5-137.5	A492	903.3	43.10	43.10	2.62	0.94	1.27	0.00	0.05	5.39		*G. crassaformis*
306-U1313C-5H-5W,140.5-143.5	A493	904.3	43.15	43.15	2.47	1.03	1.32	0.02	0.10	5.72		*G. crassaformis*
306-U1313C-5H-5W,140.5-143.5	A1077	904.3	43.15	43.15	3.90	0.80						*C. wuellerstorfi*
306-U1313C-5H-5W,145.5-147.5	A494	905.2	43.20	43.20	2.17	0.89	1.32	0.09	0.07	5.70		*G. crassaformis*
306-U1313C-5H-6W,2.5-4.5	A495	906.6	43.27	43.27	2.34	0.84	1.30	0.02	0.08	5.59		*G. crassaformis*
306-U1313C-5H-6W,2.5-4.5	A1078	906.6	43.27	43.27	3.64	0.80						*C. wuellerstorfi*
306-U1313C-5H-6W,7.5-9.5	A496	907.6	43.32	43.31	2.48	0.96	1.41	0.05	0.10	6.23		*G. crassaformis*
306-U1313C-5H-6W,11-13	A497	908.3	43.35	43.34	2.34	1.00	1.31	0.03	0.10	5.63		*G. crassaformis*
306-U1313C-5H-6W,11-13	A1079	908.3	43.35	43.34	3.81	-0.07						*C. wuellerstorfi*
306-U1313C-5H-6W,11-13	A1079	908.3	43.35	43.34	3.81	-0.07						*C. wuellerstorfi*
306-U1313C-5H-6W,16-18	A498	909.2	43.40	43.39	2.80	0.74	1.25	0.03	0.09	5.27		*G. crassaformis*
306-U1313C-5H-6W,22-24	A499	910.4	43.46	43.45	2.75	0.97	1.18	0.02	0.08	4.76		*G. crassaformis*

Sample Label	Laboratory ID	Age (ka)	Comp. depth (m, MCD)	Adjusted MCD (m, AMCD)	$\delta^{18}O$ (‰, VPDB)	$\delta^{13}C$ (‰, VPDB)	Mg/Ca (mmol/mol)	Fe/Ca (mmol/mol)	Mn/Ca (mmol/mol)	SubT (°C)	$\delta 18O_{sw\text{-}ivc}$ (‰, VPDB)	Species
306-U1313C-5H-6W,22-24	A1080	910.4	43.46	43.45	3.63	0.59						*C. wuellerstorfi*
306-U1313C-5H-6W,27-29	A500	911.4	43.51	43.50	2.67	0.87	1.23	0.00	0.00	5.15		*G. crassaformis*
306-U1313C-5H-6W,32-34	A501	912.4	43.56	43.55	2.64	0.91	1.47	0.11	0.18	6.56		*G. crassaformis*
306-U1313C-5H-6W,32-34	A1081	912.4	43.56	43.55	3.75	0.45						*C. wuellerstorfi*
306-U1313C-5H-6W,36-38	A502	913.2	43.60	43.58	2.64	0.82	1.30	0.00	0.12	5.60		*G. crassaformis*
306-U1313C-5H-6W,36-38	A959	913.2	43.60	43.58	3.44	0.56						*C. wuellerstorfi*
306-U1313C-5H-6W,41-43	A503	914.1	43.65	43.63	2.46	0.81	1.35	0.00	0.12	5.89		*G. crassaformis*
306-U1313C-5H-6W,41-43	A1082	914.1	43.65	43.63	3.43	0.86						*C. wuellerstorfi*
306-U1313C-5H-6W,51.5-53.5	A1083	916.2	43.76	43.74	3.57	-0.02						*C. wuellerstorfi*
306-U1313C-5H-6W,61-63	A1084	918.1	43.85	43.83	4.08	-0.94						*C. wuellerstorfi*
306-U1313C-5H-6W,71-73	A1085	920.2	43.95	43.93	4.22	-0.69						*C. wuellerstorfi*
306-U1313C-5H-6W,81-83	A1087	922.3	44.05	44.03	3.97	-0.19						*C. wuellerstorfi*
306-U1313C-5H-6W,91-93	A513	924.4	44.15	44.13	2.30	0.18	1.79	0.00	0.00	8.18		*G. crassaformis*
306-U1313C-5H-6W,91-93	A1088	924.4	44.15	44.13	4.23	-0.89						*C. wuellerstorfi*
306-U1313C-5H-6W,101-103	A515	926.6	44.25	44.24	2.32	1.03	1.16	0.00	0.00	4.62		*G. crassaformis*
306-U1313C-5H-6W,101-103	A970	926.6	44.25	44.24	4.08	0.16						*C. wuellerstorfi*
306-U1313C-5H-6W,106-108	A516	927.6	44.30	44.29	2.56	0.72	1.22	0.00	0.00	5.03		*G. crassaformis*
306-U1313C-5H-6W,111-113	A1011	928.7	44.35	44.34	4.07	-0.48						*C. wuellerstorfi*
306-U1313C-5H-6W,116-118	A518	929.7	44.40	44.39	2.24	1.02	1.33	0.00	0.00	5.74		*G. crassaformis*
306-U1313C-5H-6W,116-118	A518	929.7	44.40	44.39	2.24	1.02	1.71	0.14	0.04	7.82		*G. crassaformis*
306-U1313C-5H-6W,116-118	A960	929.7	44.40	44.39	3.78	0.69						*C. wuellerstorfi*
306-U1313C-5H-6W,121-123	A519	930.8	44.45	44.44	2.79	1.22	1.29	0.00	0.00	5.52		*G. crassaformis*
306-U1313C-5H-6W,121-123	A1012	930.8	44.45	44.44	3.54	-0.23						*C. wuellerstorfi*
306-U1313C-5H-6W,126-128	A520	931.8	44.50	44.49	2.29	1.09	1.15	0.00	0.00	4.59		*G. crassaformis*
306-U1313C-5H-6W,131-133	A521	932.9	44.55	44.54	2.30	1.20	1.02	0.00	0.00	3.57		*G. crassaformis*
306-U1313C-5H-6W,131-133	A1013	932.9	44.55	44.54	3.28	0.04						*C. wuellerstorfi*
306-U1313C-5H-6W,136-138	A522	934.0	44.60	44.59	2.31	1.31	1.20	0.04	0.05	4.93		*G. crassaformis*

Sample Label	Laboratory ID	Age (ka)	Comp. depth (m, MCD)	Adjusted MCD (m, AMCD)	$\delta^{18}O$ (‰, VPDB)	$\delta^{13}C$ (‰, VPDB)	Mg/Ca (mmol/mol)	Fe/Ca (mmol/mol)	Mn/Ca (mmol/mol)	SubT (°C)	$\delta 18O_{sw\text{-}ivc}$ (‰, VPDB)	Species
306-U1313C-5H-6W,141-143	A523	935.0	44.65	44.65	2.26	1.32	1.42	0.02	0.06	6.33		*G. crassaformis*
306-U1313C-5H-6W,141-143	A1014	935.0	44.65	44.65	3.48	0.70						*C. wuellerstorfi*
306-U1313C-5H-6W,146-148	A524	936.1	44.70	44.70	2.34	1.20	1.35	0.00	0.07	5.87		*G. crassaformis*
306-U1313C-5H-7W,2.5-4.5	A525	937.4	44.77	44.77	2.30	1.27	1.33	0.06	0.06	5.76		*G. crassaformis*
306-U1313C-5H-7W,2.5-4.5	A1015	937.4	44.77	44.77	3.36	0.07						*C. wuellerstorfi*
306-U1313C-5H-7W,7-9	A526	938.4	44.81	44.81	2.11	1.24	1.33	0.00	0.00	5.75		*G. crassaformis*
306-U1313C-5H-7W,11-13	A527	939.2	44.85	44.85	2.21	1.26	1.20	0.00	0.04	4.96		*G. crassaformis*
306-U1313C-5H-7W,11-13	A1016	939.2	44.85	44.85	3.52	0.51						*C. wuellerstorfi*
306-U1313C-5H-7W,16-18	A528	940.3	44.90	44.90	2.16	1.10	1.26	0.06	0.10	5.30		*G. crassaformis*
306-U1313C-5H-7W,22-24	A529	941.6	44.96	44.96	2.32	1.24	1.23	0.04	0.05	5.12		*G. crassaformis*
306-U1313C-5H-7W,22-24	A971	941.6	44.96	44.96	3.14	0.88						*C. wuellerstorfi*
306-U1313C-5H-7W,27-29	A530	942.6	45.01	45.01	2.35	1.18	1.71	0.04	0.07	7.85		*G. crassaformis*
306-U1313C-5H-7W,31.5-33.5	A531	943.6	45.06	45.06	2.17	1.28	1.28	0.04	0.08	5.44		*G. crassaformis*
306-U1313C-5H-7W,31.5-33.5	A1017	943.6	45.06	45.06	3.14	1.00						*C. wuellerstorfi*
306-U1313C-5H-7W,36-38	A532	944.5	45.10	45.11	2.25	1.16	1.44	0.02	0.08	6.39		*G. crassaformis*
306-U1313C-5H-7W,41-43	A533	945.6	45.15	45.16	2.16	1.32	1.59	0.00	0.00	7.25		*G. crassaformis*
306-U1313C-5H-7W,41-43	A973	945.6	45.15	45.16	3.21	1.01						*C. wuellerstorfi*
306-U1313C-5H-7W,46-48	A534	946.6	45.20	45.21	2.19	1.32	1.57	0.00	0.00	7.10		*G. crassaformis*
306-U1313C-5H-7W,51-53	A535	947.7	45.25	45.26	2.10	1.21	1.30	0.00	0.00	5.55		*G. crassaformis*
306-U1313C-5H-7W,51-53	A1018	947.7	45.25	45.26	2.97	0.92						*C. wuellerstorfi*
306-U1313C-5H-7W,57-59	A536	949.0	45.31	45.32	1.97	1.33	1.46	0.03	0.08	6.54		*G. crassaformis*
306-U1313C-5H-7W,61-63	A537	949.8	45.35	45.36	1.97	1.16	1.61	0.00	0.00	7.31		*G. crassaformis*
306-U1313C-5H-7W,66-68	A538	950.9	45.40	45.41	2.06	1.37	1.24	0.07	0.06	5.16		*G. crassaformis*
306-U1313C-5H-7W,66-68	A1019	950.9	45.40	45.41	2.90	0.68						*C. wuellerstorfi*
306-U1313C-5H-7W,71-73	A539	951.9	45.45	45.46	1.91	1.16	1.41	0.03	0.08	6.22		*G. crassaformis*
306-U1313B-5H-4W,40-42	A87	953.0	45.50	45.52			2.07	0.13	0.00	9.39		*G. crassaformis*
306-U1313C-5H-7W,76-78	A540	953.0	45.50	45.52	2.11	1.20	1.44	0.06	0.09	6.41		*G. crassaformis*

Sample Label	Laboratory ID	Age (ka)	Comp. depth (m, MCD)	Adjusted MCD (m, AMCD)	$\delta^{18}O$ (‰, VPDB)	$\delta^{13}C$ (‰, VPDB)	Mg/Ca (mmol/mol)	Fe/Ca (mmol/mol)	Mn/Ca (mmol/mol)	SubT (°C)	$\delta 18O_{sw\text{-}ivc}$ (‰, VPDB)	Species
306-U1313C-5H-7W,76-78	A961	953.0	45.50	45.52	3.03	0.98						*C. wuellerstorfi*
306-U1313B-5H-4W,40-42	A975	953.0	45.50	45.52	3.02	0.96						*C. wuellerstorfi*
306-U1313B-5H-4W,45-47	A88	954.0	45.55	45.58	2.06	1.19	1.56	0.05	0.10	7.05		*G. crassaformis*
306-U1313B-5H-4W,45-47	A88	954.0	45.55	45.58	2.06	1.19	1.66	0.00	0.06	7.59		*G. crassaformis*
306-U1313B-5H-4W,52-54	A89	955.5	45.62	45.62	2.02	0.88	1.64	0.07	0.00	7.50		*G. crassaformis*
306-U1313B-5H-4W,52-54	A1020	955.5	45.62	45.62	3.06	-0.46						*C. wuellerstorfi*
306-U1313B-5H-4W,57-59	A90	956.6	45.67	45.67	1.70	0.74	1.59	0.00	0.00	7.22		*G. crassaformis*
306-U1313B-5H-4W,57-59	A974	956.6	45.67	45.67	3.30	-0.69						*C. wuellerstorfi*
306-U1313B-5H-4W,60-62	A976	957.2	45.70	45.70	3.36	0.04						*C. wuellerstorfi*
306-U1313B-5H-4W,65-67	A92	958.3	45.75	45.75	1.88	0.76	1.76	0.16	0.00	8.08		*G. crassaformis*
306-U1313B-5H-4W,70-72	A93	959.3	45.80	45.80	2.27	0.69	1.61	0.12	0.16	7.32		*G. crassaformis*
306-U1313B-5H-4W,70-72	A1021	959.3	45.80	45.80	3.43	-0.16						*C. wuellerstorfi*
306-U1313B-5H-4W,85-87	A978	962.5	45.95	45.95	4.13	0.10						*C. wuellerstorfi*
306-U1313B-5H-4W,94.5-96.5	A97	964.5	46.05	46.05	2.64	1.39	1.68	0.00	0.00	7.69		*G. crassaformis*
306-U1313B-5H-4W,94.5-96.5	A1022	964.5	46.05	46.05	4.06	0.50						*C. wuellerstorfi*
306-U1313B-5H-4W,103-105	A98	966.3	46.13	46.13	2.42	1.19	1.17	0.03	0.01	4.69		*G. crassaformis*
306-U1313B-5H-4W,110-112	A99	967.8	46.20	46.20	2.60	1.35	1.10	0.00	0.06	4.22		*G. crassaformis*
306-U1313B-5H-4W,110-112	A1023	967.8	46.20	46.20	3.82	0.50						*C. wuellerstorfi*
306-U1313B-5H-4W,120-122	A101	970.0	46.30	46.30	2.38	1.34	1.56	0.10	0.12	7.09		*G. crassaformis*
306-U1313B-5H-4W,120-122	A101	970.0	46.30	46.30	2.38	1.34	1.27	0.03	0.07	5.38		*G. crassaformis*
306-U1313B-5H-4W,120-122	A1024	970.0	46.30	46.30	3.43	0.83						*C. wuellerstorfi*
306-U1313B-5H-4W,128-130	A102	971.8	46.38	46.38	2.44	1.25	1.17	0.00	0.07	4.71		*G. crassaformis*
306-U1313B-5H-4W,135-137	A103	973.4	46.45	46.45	2.37	1.27	1.10	0.00	0.00	4.18		*G. crassaformis*
306-U1313B-5H-4W,135-137	A1025	973.4	46.45	46.45	3.45	0.89						*C. wuellerstorfi*
306-U1313B-5H-4W,140-142	A104	974.5	46.50	46.50	2.26	1.17	1.45	0.06	0.12	6.50		*G. crassaformis*
306-U1313B-5H-4W,145-147	A105	975.6	46.55	46.55	2.27	1.36	1.17	0.02	0.05	4.74		*G. crassaformis*
306-U1313B-5H-4W,145-147	A1103	975.6	46.55	46.55	3.35	0.57						*C. wuellerstorfi*

Sample Label	Laboratory ID	Age (ka)	Comp. depth (m, MCD)	Adjusted MCD (m, AMCD)	$\delta^{18}O$ (‰, VPDB)	$\delta^{13}C$ (‰, VPDB)	Mg/Ca (mmol/mol)	Fe/Ca (mmol/mol)	Mn/Ca (mmol/mol)	SubT (°C)	$\delta 18O_{sw\text{-}ivc}$ (‰, VPDB)	Species
306-U1313B-5H-5W,6.5-7.5	A106	978.1	46.67	46.67	2.23	1.28	1.64	0.06	0.17	7.48		*G. crassaformis*
306-U1313B-5H-5W,10-12	A107	979.0	46.70	46.70			1.40	0.06	0.06	6.19		*G. crassaformis*
306-U1313B-5H-5W,10-12	A1104	979.0	46.70	46.70	3.41	-0.18						*C. wuellerstorfi*
306-U1313B-5H-5W,15-17	A108	980.1	46.75	46.75	2.39	1.22	1.25	0.00	0.05	5.28		*G. crassaformis*
306-U1313B-5H-5W,22-23	A109	981.6	46.82	46.82	2.63	1.12	1.37	0.03	0.06	6.00		*G. crassaformis*
306-U1313B-5H-5W,22-23	A1105	981.6	46.82	46.82	3.65	0.59						*C. wuellerstorfi*
306-U1313B-5H-5W,31.5-33.5	A110	983.8	46.92	46.92	2.75	1.27	1.15	0.02	0.04	4.55		*G. crassaformis*
306-U1313B-5H-5W,35-37	A111	984.6	46.95	46.95	2.71	1.40	1.19	0.02	0.08	4.85		*G. crassaformis*
306-U1313B-5H-5W,35-37	A1106	984.6	46.95	46.95	3.66	0.70						*C. wuellerstorfi*
306-U1313B-5H-5W,40-42	A112	985.7	47.00	47.00	2.74	1.27	1.16	0.03	0.04	4.67		*G. crassaformis*
306-U1313B-5H-5W,45-47	A113	986.8	47.05	47.05	2.74	1.41	1.16	0.01	0.05	4.67		*G. crassaformis*
306-U1313B-5H-5W,45-47	A1107	986.8	47.05	47.05	3.86	0.11						*C. wuellerstorfi*
306-U1313B-5H-5W,51-53	A114	988.2	47.11	47.11	2.91	1.65	1.07	0.02	0.04	4.02		*G. crassaformis*
306-U1313B-5H-5W,56-58	A115	989.3	47.16	47.16	2.62	1.40	1.27	0.04	0.04	5.41		*G. crassaformis*
306-U1313B-5H-5W,60-62	A116	990.2	47.20	47.20	2.49	1.32	1.63	0.05	0.26	7.44		*G. crassaformis*
306-U1313B-5H-5W,60-62	A116	990.2	47.20	47.20	2.49	1.32	1.15	0.02	0.05	4.58		*G. crassaformis*
306-U1313B-5H-5W,65-67	A117	991.3	47.25	47.25	2.25	1.23	1.11	0.05	0.08	4.29		*G. crassaformis*
306-U1313B-5H-5W,65-67	A1109	991.3	47.25	47.25	3.66	0.98						*C. wuellerstorfi*
306-U1313B-5H-5W,69.5-71.5	A118	992.2	47.30	47.30	2.37	1.47	2.09	0.08	0.06	9.46		*G. crassaformis*
306-U1313B-5H-5W,69.5-71.5	A118	992.2	47.30	47.30	2.37	1.47	1.12	0.02	0.06	4.32		*G. crassaformis*
306-U1313B-5H-5W,76.5-77.5	A119	993.4	47.37	47.37	1.97	1.21	1.28	0.03	0.05	5.44		*G. crassaformis*
306-U1313B-5H-5W,76.5-77.5	A1110	993.4	47.37	47.37	3.25	1.02						*C. wuellerstorfi*
306-U1313B-5H-5W,81-82	A120	994.2	47.41	47.41	2.29	1.29	1.43	0.03	0.10	6.37		*G. crassaformis*
306-U1313B-5H-5W,95-97	A121	996.9	47.55	47.55	2.49	1.43	1.67	0.05	0.22	7.63		*G. crassaformis*
306-U1313B-5H-5W,95-97	A1111	996.9	47.55	47.55	3.46	1.01						*C. wuellerstorfi*
306-U1313B-5H-5W,106.5-107.5	A123	999.0	47.67	47.67	2.77	1.31	1.12	0.03	0.03	4.35		*G. crassaformis*
306-U1313B-5H-5W,106.5-107.5	A1112	999.0	47.67	47.67	3.54	0.41						*C. wuellerstorfi*

Sample Label	Laboratory ID	Age (ka)	Comp. depth (m, MCD)	Adjusted MCD (m, AMCD)	$\delta^{18}O$ (‰, VPDB)	$\delta^{13}C$ (‰, VPDB)	Mg/Ca (mmol/mol)	Fe/Ca (mmol/mol)	Mn/Ca (mmol/mol)	SubT (°C)	$\delta 18O_{sw\text{-}ivc}$ (‰, VPDB)	Species
306-U1313B-5H-5W,112-114	A124	1000.1	47.72	47.72	3.00	1.12	1.38	0.07	0.03	6.06		*G. crassaformis*
306-U1313B-5H-5W,115-117	A125	1000.7	47.75	47.75	3.09	1.01	1.26	0.08	0.04	5.35		*G. crassaformis*
306-U1313B-5H-5W,115-117	A1113	1000.7	47.75	47.75	3.82	-0.10						*C. wuellerstorfi*
306-U1313B-5H-5W,120-122	A126	1001.6	47.80	47.80	3.01	1.20	1.09	0.02	0.04	4.11		*G. crassaformis*
306-U1313B-5H-5W,126.5-127.5	A127	1002.7	47.87	47.87	3.02	1.00	0.98	0.04	0.06	3.23		*G. crassaformis*
306-U1313B-5H-5W,126.5-127.5	A1114	1002.7	47.87	47.87	3.56	0.80						*C. wuellerstorfi*
306-U1313B-5H-5W,132-134	A128	1003.8	47.92	47.92	3.13	1.01	1.13	0.05	0.09	4.41		*G. crassaformis*
306-U1313B-5H-5W,135-137	A129	1004.4	47.95	47.95	2.84	1.12	1.21	0.01	0.07	5.02		*G. crassaformis*
306-U1313B-5H-5W,135-137	A1115	1004.4	47.95	47.95	3.99	-0.03						*C. wuellerstorfi*
306-U1313B-5H-5W,140-142	A130	1005.3	48.00	48.00	2.61	1.15	1.06	0.02	0.09	3.91		*G. crassaformis*
306-U1313B-5H-5W,145-147	A131	1006.2	48.05	48.05	2.85	0.94	1.17	0.05	0.09	4.69		*G. crassaformis*
306-U1313B-5H-5W,145-147	A1116	1006.2	48.05	48.05	3.93	0.94						*C. wuellerstorfi*
306-U1313B-5H-6W,2.5-3.5	A132	1007.5	48.13	48.13	2.65	1.31	1.01	0.02	0.07	3.55		*G. crassaformis*
306-U1313B-5H-6W,2.5-3.5	A980	1007.5	48.13	48.13	3.43	0.65						*C. wuellerstorfi*
306-U1313B-5H-6W,15-17	A134	1010.0	48.25	48.25	2.27	1.29	1.34	0.00	0.00	5.80		*G. crassaformis*
306-U1313B-5H-6W,15-17	A992	1010.0	48.25	48.25	3.73	0.42						*C. wuellerstorfi*
306-U1313B-5H-6W,27-28	A981	1012.1	48.37	48.37	3.91	0.03						*C. wuellerstorfi*
306-U1313B-5H-6W,31.5-33.5	A137	1013.0	48.42	48.42	2.69	1.19	1.17	0.03	0.07	4.68		*G. crassaformis*
306-U1313B-5H-6W,35-37	A138	1013.7	48.45	48.45	2.29	1.13	1.16	0.04	0.10	4.65		*G. crassaformis*
306-U1313B-5H-6W,35-37	A995	1013.7	48.45	48.45	3.76	-0.04						*C. wuellerstorfi*
306-U1313B-5H-6W,39.5-41.5	A139	1014.7	48.50	48.50	2.45	1.25	1.30	0.05	0.03	5.56		*G. crassaformis*
306-U1313B-5H-6W,44.5-46.5	A140	1015.9	48.55	48.55	2.26	1.37	1.37	0.00	0.00	6.00		*G. crassaformis*
306-U1313B-5H-6W,44.5-46.5	A983	1015.9	48.55	48.55	3.19	0.34						*C. wuellerstorfi*
306-U1313B-5H-6W,54-55	A141	1018.1	48.64	48.64	2.64	1.47	1.33	0.04	0.06	5.75		*G. crassaformis*
306-U1313B-5H-6W,54-55	A998	1018.1	48.64	48.64	3.43	1.21						*C. wuellerstorfi*
306-U1313B-5H-6W,60-62	A142	1019.7	48.70	48.98	2.21	1.41	1.34	0.02	0.08	5.81		*G. crassaformis*
306-U1313B-5H-6W,66-68	A143	1021.2	48.76	49.04	2.15	1.41	1.36	0.00	0.06	5.92		*G. crassaformis*

Sample Label	Laboratory ID	Age (ka)	Comp. depth (m, MCD)	Adjusted MCD (m, AMCD)	$\delta^{18}O$ (‰, VPDB)	$\delta^{13}C$ (‰, VPDB)	Mg/Ca (mmol/mol)	Fe/Ca (mmol/mol)	Mn/Ca (mmol/mol)	SubT (°C)	$\delta 18O_{sw\text{-}ivc}$ (‰, VPDB)	Species
306-U1313B-5H-6W,66-68	A985	1021.2	48.76	49.04	3.33	1.12						*C. wuellerstorfi*
306-U1313B-5H-6W,70-72	A144	1022.2	48.80	49.07	2.13	1.36	1.25	0.00	0.04	5.26		*G. crassaformis*
306-U1313B-5H-6W,77-79	A145	1023.9	48.87	49.14	2.12	1.13	1.30	0.02	0.08	5.55		*G. crassaformis*
306-U1313B-5H-6W,77-79	A1001	1023.9	48.87	49.14	3.43	1.21						*C. wuellerstorfi*
306-U1313B-5H-6W,82-84	A146	1025.2	48.92	49.19	1.86	1.36	1.36	0.04	0.07	5.94		*G. crassaformis*
306-U1313C-6H-3W,51-53	A541	1025.9	48.95	49.22	2.80	1.04	1.26	0.04	0.05	5.32		*G. crassaformis*
306-U1313C-6H-3W,56-57	A542	1027.0	49.00	49.26	2.62	0.94	1.43	0.03	0.06	6.34		*G. crassaformis*
306-U1313C-6H-3W,56-57	A986	1027.0	49.00	49.26	3.37	0.92						*C. wuellerstorfi*
306-U1313C-6H-3W,61-62	A543	1028.3	49.05	49.31	2.10	0.95	1.57	0.05	0.16	7.11		*G. crassaformis*
306-U1313C-6H-3W,61-62	A543	1028.3	49.05	49.31	2.10	0.95	1.31	0.02	0.13	5.64		*G. crassaformis*
306-U1313C-6H-3W,65.5-67.5	A544	1029.5	49.10	49.36	2.66	0.79	1.26	0.05	0.08	5.36		*G. crassaformis*
306-U1313C-6H-3W,65.5-67.5	A1003	1029.5	49.10	49.36	3.77	0.22						*C. wuellerstorfi*
306-U1313C-6H-3W,71-73	A545	1030.9	49.15	49.40	2.48	0.92	1.19	0.04	0.12	4.86		*G. crassaformis*
306-U1313C-6H-3W,76.5-77.5	A546	1032.1	49.21	49.44	2.17	0.83	1.57	0.08	0.16	7.14		*G. crassaformis*
306-U1313C-6H-3W,76.5-77.5	A987	1032.1	49.21	49.44	3.60	0.84						*C. wuellerstorfi*
306-U1313C-6H-3W,83.5-85.5	A547	1033.7	49.28	49.50	2.37	0.81	1.42	0.05	0.09	6.32		*G. crassaformis*
306-U1313C-6H-3W,86-88	A548	1034.2	49.30	49.51	2.33	0.92	1.38	0.02	0.15	6.06		*G. crassaformis*
306-U1313C-6H-3W,86-88	A1005	1034.2	49.30	49.51	3.86	1.08						*C. wuellerstorfi*
306-U1313C-6H-3W,91-93	A549	1035.3	49.35	49.55	2.03	0.49	1.51	0.06	0.15	6.82		*G. crassaformis*
306-U1313C-6H-3W,96-98	A550	1036.4	49.40	49.59	2.24	0.94	1.32	0.05	0.15	5.73		*G. crassaformis*
306-U1313C-6H-3W,96-98	A988	1036.4	49.40	49.59	3.86	0.90						*C. wuellerstorfi*
306-U1313C-6H-3W,101-103	A551	1037.4	49.45	49.63	2.36	0.80	1.27	0.02	0.16	5.42		*G. crassaformis*
306-U1313C-6H-3W,106-108	A552	1038.5	49.50	49.67	2.47	1.00	1.26	0.02	0.10	5.32		*G. crassaformis*
306-U1313C-6H-3W,106-108	A1006	1038.5	49.50	49.67	4.02	0.83						*C. wuellerstorfi*
306-U1313C-6H-3W,110-112	A553	1039.3	49.54	49.70	2.49	0.77	1.27	0.09	0.14	5.39		*G. crassaformis*
306-U1313C-6H-3W,115.5-117.5	A554	1040.5	49.60	49.75	2.18	0.95	1.31	0.02	0.13	5.61		*G. crassaformis*
306-U1313C-6H-3W,121-123	A555	1041.7	49.65	49.79	2.40	0.96	1.43	0.02	0.15	6.35		*G. crassaformis*

Sample Label	Laboratory ID	Age (ka)	Comp. depth (m, MCD)	Adjusted MCD (m, AMCD)	$\delta^{18}O$ (‰, VPDB)	$\delta^{13}C$ (‰, VPDB)	Mg/Ca (mmol/mol)	Fe/Ca (mmol/mol)	Mn/Ca (mmol/mol)	SubT (°C)	$\delta 18O_{sw\text{-}ivc}$ (‰, VPDB)	Species
306-U1313C-6H-3W,121-123	A989	1041.7	49.65	49.79	3.89	0.53						*C. wuellerstorfi*
306-U1313C-6H-3W,126.5-127.5	A556	1042.7	49.71	49.83	2.43	0.76	1.28	0.08	0.14	5.46		*G. crassaformis*
306-U1313C-6H-3W,132-134	A557	1044.0	49.76	49.88	2.52	0.86	1.25	0.01	0.08	5.24		*G. crassaformis*
306-U1313C-6H-3W,132-134	A1008	1044.0	49.76	49.88	4.02	0.90						*C. wuellerstorfi*
306-U1313C-6H-3W,136-138	A558	1044.9	49.80	49.91	2.62	0.96	1.19	0.04	0.07	4.89		*G. crassaformis*
306-U1313C-6H-3W,140-142	A559	1045.7	49.84	49.94	2.77	0.97	1.29	0.03	0.08	5.50		*G. crassaformis*
306-U1313C-6H-3W,140-142	A1044	1045.7	49.84	49.94	3.96	0.46						*C. wuellerstorfi*
306-U1313C-6H-3W,146-148	A990	1047.0	49.90	49.99	3.91	0.46						*C. wuellerstorfi*
306-U1313C-6H-4W,1.5-3.5	A561	1048.2	49.96	50.03	3.14	0.99	1.12	0.00	0.00	4.34		*G. crassaformis*
306-U1313C-6H-4W,7-8	A562	1049.2	50.01	50.07	2.65	0.62	1.06	0.02	0.04	3.88		*G. crassaformis*
306-U1313C-6H-4W,7-8	A1033	1049.2	50.01	50.07	4.02	0.60						*C. wuellerstorfi*
306-U1313C-6H-4W,10-12	A563	1050.0	50.04	50.10	3.28	1.11	0.91	0.02	0.00	2.70		*G. crassaformis*
306-U1313C-6H-4W,16-18	A564	1051.2	50.10	50.14	2.92	0.91	0.91	0.01	0.02	2.67		*G. crassaformis*
306-U1313C-6H-4W,16-18	A1034	1051.2	50.10	50.14	3.87	0.13						*C. wuellerstorfi*
306-U1313C-6H-4W,22-23	A565	1052.4	50.16	50.19	2.99	1.23	0.99	0.04	0.00	3.34		*G. crassaformis*
306-U1313C-6H-4W,26-28	A566	1053.4	50.20	50.22	2.88	1.19	0.93	0.01	0.02	2.82		*G. crassaformis*
306-U1313C-6H-4W,26-28	A1036	1053.4	50.20	50.22	3.85	-0.05						*C. wuellerstorfi*
306-U1313C-6H-4W,32-34	A567	1054.6	50.26	50.27	2.99	1.24	0.99	0.02	0.04	3.31		*G. crassaformis*
306-U1313C-6H-4W,36-38	A568	1055.5	50.30	50.30	2.83	1.47	1.11	0.02	0.02	4.29		*G. crassaformis*
306-U1313C-6H-4W,36-38	A1037	1055.5	50.30	50.30	3.66	-0.12						*C. wuellerstorfi*
306-U1313C-6H-4W,41-43	A569	1056.6	50.35	50.34	2.83	1.29	1.09	0.02	0.03	4.14		*G. crassaformis*
306-U1313C-6H-4W,46-48	A570	1057.6	50.40	50.38	2.54	1.10	1.01	0.01	0.02	3.55		*G. crassaformis*
306-U1313C-6H-4W,46-48	A1038	1057.6	50.40	50.38	3.97	-0.45						*C. wuellerstorfi*
306-U1313C-6H-4W,52-54	A571	1058.9	50.46	50.43	2.62	1.28	1.19	0.02	0.04	4.84		*G. crassaformis*
306-U1313C-6H-4W,52-54	A571	1058.9	50.46	50.43	2.62	1.28	1.06	0.02	0.03	3.91		*G. crassaformis*
306-U1313C-6H-4W,56.5-57.5	A572	1059.7	50.51	50.46	2.66	1.23	1.07	0.04	0.04	3.95		*G. crassaformis*
306-U1313C-6H-4W,56.5-57.5	A1039	1059.7	50.51	50.46	3.81	0.73						*C. wuellerstorfi*

Sample Label	Laboratory ID	Age (ka)	Comp. depth (m, MCD)	Adjusted MCD (m, AMCD)	$\delta^{18}O$ (‰, VPDB)	$\delta^{13}C$ (‰, VPDB)	Mg/Ca (mmol/mol)	Fe/Ca (mmol/mol)	Mn/Ca (mmol/mol)	SubT (°C)	$\delta 18O_{sw\text{-}ivc}$ (‰, VPDB)	Species
306-U1313C-6H-4W,60.5-62.5	A573	1060.7	50.55	50.50	2.59	1.16	1.11	0.04	0.06	4.31		*G. crassaformis*
306-U1313C-6H-4W,66-68	A574	1061.9	50.60	50.54	2.45	1.10	1.31	0.03	0.10	5.64		*G. crassaformis*
306-U1313C-6H-4W,66-68	A1040	1061.9	50.60	50.54	3.59	0.13						*C. wuellerstorfi*
306-U1313C-6H-4W,70-73	A575	1062.8	50.64	50.58			1.33	0.02	0.10	5.77		*G. crassaformis*
306-U1313C-6H-4W,76-77	A576	1063.9	50.70	50.63	2.12	1.00	1.42	0.02	0.08	6.29		*G. crassaformis*
306-U1313C-6H-4W,76-77	A1041	1063.9	50.70	50.63	3.34	1.11						*C. wuellerstorfi*
306-U1313C-6H-4W,81-82	A577	1065.0	50.75	50.67	1.88	1.16	1.53	0.00	0.12	6.94		*G. crassaformis*
306-U1313C-6H-4W,86-88	A578	1066.2	50.80	50.71	1.97	1.42	1.29	0.03	0.07	5.54		*G. crassaformis*
306-U1313C-6H-4W,86-88	A1042	1066.2	50.80	50.71	3.01	1.21						*C. wuellerstorfi*
306-U1313C-6H-4W,91-93	A579	1067.3	50.85	50.76	1.78	1.28	1.62	0.04	0.11	7.40		*G. crassaformis*
306-U1313C-6H-4W,91-93	A1308	1067.3	50.85	50.76	2.84	1.00						*C. wuellerstorfi*
306-U1313C-6H-4W,96-98	A580	1068.5	50.90	50.80	1.79	1.25	1.49	0.03	0.08	6.71		*G. crassaformis*
306-U1313C-6H-4W,96-98	A1043	1068.5	50.90	50.80	3.03	1.15						*C. wuellerstorfi*
306-U1313C-6H-4W,101-102	A581	1069.5	50.95	50.85	1.64	1.16	1.78	0.08	0.08	8.16		*G. crassaformis*
306-U1313C-6H-4W,101-102	A1309	1069.5	50.95	50.85	2.83	0.91						*C. wuellerstorfi*
306-U1313C-6H-4W,106-107	A582	1070.6	51.00	50.89	1.62	1.14	1.45	0.02	0.02	6.50		*G. crassaformis*
306-U1313C-6H-4W,106-107	A1127	1070.6	51.00	50.89	2.81	1.13						*C. wuellerstorfi*
306-U1313C-6H-4W,111-113	A583	1071.8	51.05	50.93	1.79	1.23	1.42	0.05	0.00	6.29		*G. crassaformis*
306-U1313C-6H-4W,111-113	A1310	1071.8	51.05	50.93	2.79	1.09						*C. wuellerstorfi*
306-U1313C-6H-4W,116-118	A584	1073.0	51.10	50.97	1.61	1.13	1.53	0.02	0.05	6.93		*G. crassaformis*
306-U1313C-6H-4W,116-118	A1128	1073.0	51.10	50.97	2.90	0.61						*C. wuellerstorfi*
306-U1313C-6H-4W,121-123	A585	1074.1	51.15	51.15	1.70	1.12	1.52	0.12	0.08	6.87		*G. crassaformis*
306-U1313C-6H-4W,127-128	A586	1075.3	51.21	51.21	1.95	1.28	1.29	0.03	0.02	5.49		*G. crassaformis*
306-U1313C-6H-4W,127-128	A1129	1075.3	51.21	51.21	2.89	1.16						*C. wuellerstorfi*
306-U1313C-6H-4W,131.5-133.5	A587	1076.5	51.26	51.26	1.83	1.29	1.43	0.00	0.06	6.38		*G. crassaformis*
306-U1313B-6H-1W,106.5-107.5	A147	1077.7	51.32	51.32			1.51	0.00	0.00	6.79		*G. crassaformis*
306-U1313B-6H-1W,106.5-107.5	A1130	1077.7	51.32	51.32	3.17	0.84						*C. wuellerstorfi*

Sample Label	Laboratory ID	Age (ka)	Comp. depth (m, MCD)	Adjusted MCD (m, AMCD)	$\delta^{18}O$ (‰, VPDB)	$\delta^{13}C$ (‰, VPDB)	Mg/Ca (mmol/mol)	Fe/Ca (mmol/mol)	Mn/Ca (mmol/mol)	SubT (°C)	$\delta 18O_{sw\text{-}ivc}$ (‰, VPDB)	Species
306-U1313B-6H-1W,110-112	A148	1078.6	51.35	51.35	2.44	1.23	1.66	0.05	0.10	7.57		*G. crassaformis*
306-U1313B-6H-1W,116-118	A149	1080.0	51.41	51.41	2.31	1.14	1.46	0.02	0.06	6.52		*G. crassaformis*
306-U1313B-6H-1W,116-118	A1131	1080.0	51.41	51.41	3.17	1.01						*C. wuellerstorfi*
306-U1313B-6H-1W,127-128	A151	1082.3	51.52	51.52	2.06	1.01	1.53	0.07	0.10	6.90		*G. crassaformis*
306-U1313B-6H-1W,131-133	A152	1083.4	51.56	51.56			1.64	0.06	0.10	7.49		*G. crassaformis*
306-U1313B-6H-1W,135-137	A153	1084.3	51.60	51.60	2.39	1.05	1.44	0.03	0.09	6.42		*G. crassaformis*
306-U1313B-6H-1W,135-137	A1133	1084.3	51.60	51.60	3.40	1.02						*C. wuellerstorfi*
306-U1313B-6H-1W,141-143	A154	1085.6	51.66	51.66	2.28	1.17	1.72	0.04	0.13	7.86		*G. crassaformis*
306-U1313B-6H-1W,145-147	A155	1086.6	51.70	51.70	2.24	0.99	1.69	0.09	0.00	7.75		*G. crassaformis*
306-U1313B-6H-1W,145-147	A1134	1086.6	51.70	51.70	3.61	1.25						*C. wuellerstorfi*
306-U1313B-6H-2W,2-3	A156	1088.2	51.77	51.77	2.26	0.94	1.37	0.00	0.00	6.03		*G. crassaformis*
306-U1313B-6H-2W,6.5-8.5	A157	1089.4	51.82	51.82			1.61	0.03	0.11	7.32		*G. crassaformis*
306-U1313B-6H-2W,10-12	A158	1090.3	51.85	51.85	2.68	1.00	1.48	0.11	0.07	6.63		*G. crassaformis*
306-U1313B-6H-2W,15-17	A1136	1091.5	51.90	51.90	3.77	1.18						*C. wuellerstorfi*
306-U1313B-6H-2W,19.5-21.5	A160	1092.6	51.95	51.95	2.95	1.12	1.48	0.05	0.06	6.64		*G. crassaformis*
306-U1313B-6H-2W,31.5-33.5	A161	1095.6	52.07	52.07	3.08	1.07	1.65	0.04	0.08	7.56		*G. crassaformis*
306-U1313B-6H-2W,31.5-33.5	A161	1095.6	52.07	52.07	3.08	1.07	1.32	0.00	0.00	5.73		*G. crassaformis*
306-U1313B-6H-2W,35.5-37.5	A162	1096.6	52.11	52.11			1.41	0.09	0.09	6.27		*G. crassaformis*
306-U1313B-6H-2W,40-42	A163	1097.7	52.15	52.15	2.48	1.11	1.58	0.14	0.10	7.19		*G. crassaformis*
306-U1313B-6H-2W,40-42	A1138	1097.7	52.15	52.15	3.88	0.67						*C. wuellerstorfi*
306-U1313B-6H-2W,45-47	A164	1099.0	52.20	52.20	2.51	0.98	1.49	0.07	0.11	6.67		*G. crassaformis*
306-U1313B-6H-2W,50-52	A165	1100.2	52.25	52.25	3.11	1.06	1.62	0.00	0.00	7.37		*G. crassaformis*
306-U1313B-6H-2W,50-52	A1139	1100.2	52.25	52.25	3.73	1.08						*C. wuellerstorfi*
306-U1313B-6H-2W,56-58	A166	1101.7	52.31	52.31	2.40	0.95	1.51	0.06	0.10	6.82		*G. crassaformis*
306-U1313B-6H-2W,60-62	A1140	1102.7	52.35	52.35	3.54	0.80						*C. wuellerstorfi*
306-U1313B-6H-2W,65-67	A168	1103.9	52.40	52.40	2.27	1.32	1.51	0.04	0.12	6.78		*G. crassaformis*
306-U1313B-6H-2W,70-72	A169	1105.1	52.45	52.45	2.25	0.84	1.22	0.00	0.08	5.05		*G. crassaformis*

Sample Label	Laboratory ID	Age (ka)	Comp. depth (m, MCD)	Adjusted MCD (m, AMCD)	$\delta^{18}O$ (‰, VPDB)	$\delta^{13}C$ (‰, VPDB)	Mg/Ca (mmol/mol)	Fe/Ca (mmol/mol)	Mn/Ca (mmol/mol)	SubT (°C)	$\delta 18O_{sw\text{-}ivc}$ (‰, VPDB)	Species
306-U1313B-6H-2W,70-72	A1141	1105.1	52.45	52.45	3.25	0.35						*C. wuellerstorfi*
306-U1313B-6H-2W,76-78	A170	1106.6	52.51	52.51	2.09	1.19	1.54	0.05	0.13	6.97		*G. crassaformis*
306-U1313B-6H-2W,80.5-82.5	A171	1107.8	52.56	52.56	1.79	1.08	1.58	0.00	0.11	7.20		*G. crassaformis*
306-U1313B-6H-2W,80.5-82.5	A1142	1107.8	52.56	52.56	3.10	1.15						*C. wuellerstorfi*
306-U1313B-6H-2W,90.5-92.5	A1143	1110.2	52.66	52.66	3.29	1.14						*C. wuellerstorfi*
306-U1313B-6H-2W,100-102	A1144	1112.6	52.75	52.75	3.44	0.84						*C. wuellerstorfi*
306-U1313B-6H-2W,110.5-112.5	A1145	1115.2	52.86	52.86	3.69	0.19						*C. wuellerstorfi*
306-U1313B-6H-2W,121-123	A1146	1117.4	52.96	52.96	3.75	0.30						*C. wuellerstorfi*
306-U1313B-6H-2W,131.5-133.5	A1147	1119.4	53.07	53.07	4.02	-0.20						*C. wuellerstorfi*
306-U1313B-6H-2W,140-142	A1148	1121.0	53.15	53.15	3.97	0.03						*C. wuellerstorfi*
306-U1313B-6H-3W,10-12	A1150	1124.8	53.35	53.35	4.09	-0.51						*C. wuellerstorfi*
306-U1313B-6H-3W,21-23	A1151	1127.0	53.46	53.46	3.86	-0.21						*C. wuellerstorfi*
306-U1313B-6H-3W,31.5-32.5	A1152	1128.9	53.57	53.57	3.91	0.85						*C. wuellerstorfi*
306-U1313B-6H-3W,40-42	A1153	1130.6	53.65	53.65	3.79	0.21						*C. wuellerstorfi*
306-U1313B-6H-3W,45-47	A194	1131.5	53.70	53.70	2.37	1.35	1.71	0.00	0.00	7.83		*G. crassaformis*
306-U1313B-6H-3W,51.5-52.5	A195	1132.7	53.77	53.77	2.26	1.30	1.61	0.00	0.00	7.32		*G. crassaformis*
306-U1313B-6H-3W,51.5-52.5	A1154	1132.7	53.77	53.77	3.96	-0.59						*C. wuellerstorfi*
306-U1313B-6H-3W,56.5-57.5	A196	1133.6	53.82	53.82	2.23	1.16	1.59	0.02	0.04	7.21		*G. crassaformis*
306-U1313B-6H-3W,60-62	A197	1134.4	53.85	53.85	2.66	1.05	2.24	0.00	0.00	10.04		*G. crassaformis*
306-U1313B-6H-3W,60-62	A1155	1134.4	53.85	53.85	3.32	0.56						*C. wuellerstorfi*
306-U1313B-6H-3W,65-67	A198	1135.4	53.90	53.90	1.93	1.40	1.62	0.05	0.07	7.39		*G. crassaformis*
306-U1313B-6H-3W,70-72	A199	1136.3	53.95	53.95	1.96	1.25	1.72	0.06	0.07	7.88		*G. crassaformis*
306-U1313B-6H-3W,70-72	A199	1136.3	53.95	53.95	1.96	1.25	1.38	0.00	0.07	6.08		*G. crassaformis*
306-U1313B-6H-3W,70-72	A1156	1136.3	53.95	53.95	3.78	0.80						*C. wuellerstorfi*
306-U1313B-6H-3W,76.5-77.5	A200	1137.5	54.02	54.02	2.13	1.41	1.57	0.05	0.02	7.12		*G. crassaformis*
306-U1313B-6H-3W,81.5-82.5	A201	1138.4	54.07	54.07	2.07	1.47	1.35	0.00	0.00	5.90		*G. crassaformis*
306-U1313B-6H-3W,81.5-82.5	A1157	1138.4	54.07	54.07	3.43	0.87						*C. wuellerstorfi*

Sample Label	Laboratory ID	Age (ka)	Comp. depth (m, MCD)	Adjusted MCD (m, AMCD)	$\delta^{18}O$ (‰, VPDB)	$\delta^{13}C$ (‰, VPDB)	Mg/Ca (mmol/mol)	Fe/Ca (mmol/mol)	Mn/Ca (mmol/mol)	SubT (°C)	$\delta 18O_{sw\text{-}ivc}$ (‰, VPDB)	Species
306-U1313B-6H-3W,84.5-86.5	A202	1139.3	54.10	54.10			1.92	0.08	0.10	8.76		*G. crassaformis*
306-U1313B-6H-3W,89.5-91.5	A203	1140.6	54.15	54.15	1.94	1.35	1.47	0.02	0.07	6.59		*G. crassaformis*
306-U1313B-6H-3W,89.5-91.5	A1158	1140.6	54.15	54.15	3.41	0.44						*C. wuellerstorfi*
306-U1313B-6H-3W,95-97	A204	1142.0	54.20	54.20	2.04	1.47	1.64	0.08	0.11	7.51		*G. crassaformis*
306-U1313B-6H-3W,101-102	A205	1143.4	54.26	54.26	2.07	1.27	1.50	0.04	0.08	6.77		*G. crassaformis*
306-U1313B-6H-3W,101-102	A1159	1143.4	54.26	54.26	3.30	0.68						*C. wuellerstorfi*
306-U1313B-6H-3W,106.5-108	A206	1144.8	54.32	54.32	1.90	1.47	1.47	0.03	0.05	6.58		*G. crassaformis*
306-U1313B-6H-3W,110-112	A207	1145.7	54.35	54.35	1.83	1.26	1.66	0.08	0.10	7.60		*G. crassaformis*
306-U1313B-6H-3W,110-112	A1160	1145.7	54.35	54.35	3.28	0.48						*C. wuellerstorfi*
306-U1313B-6H-3W,115-117	A208	1147.0	54.40	54.40	1.76	1.23	1.61	0.04	0.14	7.34		*G. crassaformis*
306-U1313B-6H-3W,120-122	A209	1148.3	54.45	54.45	1.63	1.37	1.51	0.02	0.09	6.80		*G. crassaformis*
306-U1313B-6H-3W,120-122	A1161	1148.3	54.45	54.45	3.19	1.03						*C. wuellerstorfi*
306-U1313B-6H-3W,126-127	A210	1149.6	54.51	54.51	1.70	1.38	1.80	0.07	0.11	8.25		*G. crassaformis*
306-U1313B-6H-3W,131-133	A211	1151.0	54.56	54.56	1.50	1.12	1.59	0.03	0.10	7.23		*G. crassaformis*
306-U1313B-6H-3W,131-133	A1162	1151.0	54.56	54.56	3.10	1.35						*C. wuellerstorfi*
306-U1313B-6H-3W,135-137	A212	1152.0	54.60	54.60			1.54	0.08	0.09	6.96		*G. crassaformis*
306-U1313B-6H-3W,140-142	A213	1153.3	54.65	54.65	1.50	1.44	1.59	0.00	0.05	7.26		*G. crassaformis*
306-U1313B-6H-3W,140-142	A1163	1153.3	54.65	54.65	3.30	1.20						*C. wuellerstorfi*
306-U1313B-6H-3W,145-147	A214	1154.5	54.70	54.70	1.79	1.50	1.64	0.08	0.09	7.47		*G. crassaformis*
306-U1313B-6H-4W,0-2	A215	1155.8	54.75	54.75	1.82	1.39	1.49	0.03	0.07	6.69		*G. crassaformis*
306-U1313B-6H-4W,0-2	A1164	1155.8	54.75	54.75	3.05	1.36						*C. wuellerstorfi*
306-U1313B-6H-4W,6.5-7.5	A216	1157.3	54.82	54.82	1.73	1.49	1.76	0.08	0.13	8.07		*G. crassaformis*
306-U1313B-6H-4W,10-12	A217	1158.3	54.85	54.85	1.81	1.29	1.61	0.02	0.06	7.32		*G. crassaformis*
306-U1313B-6H-4W,10-12	A1165	1158.3	54.85	54.85	2.93	0.95						*C. wuellerstorfi*
306-U1313B-6H-4W,15-17	A218	1159.6	54.90	54.90	1.80	1.43	1.53	0.04	0.08	6.91		*G. crassaformis*
306-U1313B-6H-4W,22-23	A1166	1161.2	54.97	54.97	3.13	1.14						*C. wuellerstorfi*
306-U1313B-6H-4W,26-27	A220	1162.2	55.01	55.01	1.93	1.31	1.65	0.05	0.10	7.51		*G. crassaformis*

Sample Label	Laboratory ID	Age (ka)	Comp. depth (m, MCD)	Adjusted MCD (m, AMCD)	$\delta^{18}O$ (‰, VPDB)	$\delta^{13}C$ (‰, VPDB)	Mg/Ca (mmol/mol)	Fe/Ca (mmol/mol)	Mn/Ca (mmol/mol)	SubT (°C)	$\delta 18O_{sw\text{-}ivc}$ (‰, VPDB)	Species
306-U1313B-6H-4W,31-32	A221	1163.5	55.06	55.06	2.05	1.06	1.64	0.01	0.08	7.47		*G. crassaformis*
306-U1313B-6H-4W,31-32	A1167	1163.5	55.06	55.06	3.09	1.07						*C. wuellerstorfi*
306-U1313B-6H-4W,35-37	A222	1164.6	55.10	55.10	1.93	1.20	1.78	0.06	0.09	8.16		*G. crassaformis*
306-U1313B-6H-4W,39-41	A1168	1165.6	55.14	55.14	3.20	0.77						*C. wuellerstorfi*
306-U1313B-6H-4W,45-47	A224	1167.1	55.20	55.20	1.90	1.25	1.68	0.04	0.08	7.69		*G. crassaformis*
306-U1313B-6H-4W,52-54	A225	1168.9	55.27	55.27	1.89	1.34	1.62	0.03	0.07	7.39		*G. crassaformis*
306-U1313B-6H-4W,52-54	A1169	1168.9	55.27	55.27	3.15	1.02						*C. wuellerstorfi*
306-U1313B-6H-4W,57-58	A226	1170.0	55.32	55.32	2.09	1.33	1.81	0.07	0.13	8.31		*G. crassaformis*
306-U1313B-6H-4W,60-62	A1170	1170.9	55.35	55.35	3.22	1.15						*C. wuellerstorfi*
306-U1313B-6H-4W,65-67	A228	1172.2	55.40	55.40	2.00	1.32	1.86	0.04	0.15	8.50		*G. crassaformis*
306-U1313B-6H-4W,70-72	A229	1173.4	55.45	55.45	1.94	1.13	1.69	0.06	0.09	7.75		*G. crassaformis*
306-U1313B-6H-4W,70-72	A1171	1173.4	55.45	55.45	2.97	0.90						*C. wuellerstorfi*
306-U1313B-6H-4W,75-76	A230	1174.5	55.50	55.50	1.79	1.15	1.69	0.06	0.11	7.71		*G. crassaformis*
306-U1313B-6H-4W,79-81	A231	1175.7	55.54	55.54	1.99	1.22	1.52	0.03	0.12	6.88		*G. crassaformis*
306-U1313B-6H-4W,79-81	A1172	1175.7	55.54	55.54	3.03	1.15						*C. wuellerstorfi*
306-U1313B-6H-4W,85-87	A232	1177.2	55.60	55.60	1.91	1.09	1.80	0.04	0.12	8.26		*G. crassaformis*
306-U1313B-6H-4W,90-92	A233	1178.4	55.65	55.65	1.82	1.23	1.56	0.02	0.08	7.09		*G. crassaformis*
306-U1313B-6H-4W,90-92	A1173	1178.4	55.65	55.65	3.22	1.15						*C. wuellerstorfi*
306-U1313B-6H-4W,95-97	A234	1179.7	55.70	55.70	1.87	1.28	1.82	0.05	0.17	8.34		*G. crassaformis*
306-U1313B-6H-4W,102-103	A235	1181.3	55.77	55.77	1.93	1.13	1.55	0.05	0.12	7.00		*G. crassaformis*
306-U1313B-6H-4W,102-103	A1174	1181.3	55.77	55.77	3.26	0.79						*C. wuellerstorfi*
306-U1313B-6H-4W,107-109	A236	1182.7	55.82	55.82	1.95	1.10	1.73	0.05	0.10	7.93		*G. crassaformis*
306-U1313B-6H-4W,110-112	A237	1183.5	55.85	55.85	1.88	1.21	1.57	0.00	0.00	7.15		*G. crassaformis*
306-U1313B-6H-4W,110-112	A1175	1183.5	55.85	55.85	3.27	1.17						*C. wuellerstorfi*
306-U1313B-6H-4W,115-117	A238	1184.7	55.90	55.90	1.84	1.18	1.54	0.05	0.16	6.95		*G. crassaformis*
306-U1313B-6H-4W,120-122	A239	1186.0	55.95	55.95	2.03	1.07	1.54	0.05	0.10	6.97		*G. crassaformis*
306-U1313B-6H-4W,120-122	A1176	1186.0	55.95	55.95	3.24	1.30						*C. wuellerstorfi*

Sample Label	Laboratory ID	Age (ka)	Comp. depth (m, MCD)	Adjusted MCD (m, AMCD)	$\delta^{18}O$ (‰, VPDB)	$\delta^{13}C$ (‰, VPDB)	Mg/Ca (mmol/mol)	Fe/Ca (mmol/mol)	Mn/Ca (mmol/mol)	SubT (°C)	$\delta 18O_{sw\text{-}ivc}$ (‰, VPDB)	Species
306-U1313B-6H-4W,126.5-127.5	A240	1187.5	56.02	56.02	2.24	0.72	1.36	0.03	0.08	5.94		*G. crassaformis*
306-U1313B-6H-4W,135-137	A241	1189.8	56.10	56.10	2.04	0.95	1.53	0.05	0.13	6.90		*G. crassaformis*
306-U1313B-6H-4W,135-137	A1177	1189.8	56.10	56.10	3.22	0.88						*C. wuellerstorfi*
306-U1313B-6H-4W,139.5-141.5	A242	1190.7	56.15	56.15	2.60	0.94	1.38	0.02	0.06	6.08		*G. crassaformis*
306-U1313B-6H-4W,145-147	A243	1191.8	56.20	56.20	2.57	1.04	1.22	0.02	0.06	5.06		*G. crassaformis*
306-U1313B-6H-4W,145-147	A1178	1191.8	56.20	56.20	4.02	0.64						*C. wuellerstorfi*
306-U1313B-6H-5W,2-3	A244	1193.1	56.27	56.27	2.65	1.19	1.18	0.00	0.00	4.81		*G. crassaformis*
306-U1313B-6H-5W,7-8	A245	1194.1	56.32	56.32	2.70	0.75	1.17	0.02	0.04	4.75		*G. crassaformis*
306-U1313B-6H-5W,7-8	A245	1194.1	56.32	56.32	2.70	0.75	1.33	0.07	0.05	5.79		*G. crassaformis*
306-U1313B-6H-5W,7-8	A1179	1194.1	56.32	56.32	4.00	0.76						*C. wuellerstorfi*
306-U1313B-6H-5W,10-12	A246	1194.8	56.35	56.35	2.34	0.89	1.26	0.00	0.09	5.34		*G. crassaformis*
306-U1313B-6H-5W,14.5-16.5	A247	1195.8	56.40	56.40	2.51	0.98	1.23	0.00	0.00	5.12		*G. crassaformis*
306-U1313B-6H-5W,14.5-16.5	A1180	1195.8	56.40	56.40	3.98	0.71						*C. wuellerstorfi*
306-U1313B-6H-5W,22-23	A248	1197.2	56.47	56.47	2.65	1.04	1.32	0.08	0.06	5.72		*G. crassaformis*
306-U1313B-6H-5W,25.5-27.5	A249	1198.0	56.51	56.51	3.16	1.18	0.98	0.00	0.00	3.23		*G. crassaformis*
306-U1313B-6H-5W,25.5-27.5	A1181	1198.0	56.51	56.51	4.19	0.34						*C. wuellerstorfi*
306-U1313B-6H-5W,32-34	A250	1199.3	56.57	56.57	2.90	1.08	1.14	0.00	0.00	4.53		*G. crassaformis*
306-U1313B-6H-5W,35-37	A251	1199.9	56.60	56.60	2.51	0.94	1.22	0.05	0.00	5.03		*G. crassaformis*
306-U1313B-6H-5W,35-37	A1182	1199.9	56.60	56.60	4.15	0.53						*C. wuellerstorfi*
306-U1313B-6H-5W,40-42	A252	1200.9	56.65	56.65	2.96	1.17	1.07	0.00	0.05	3.97		*G. crassaformis*
306-U1313B-6H-5W,45-47	A253	1202.0	56.70	56.70	2.68	1.07	1.08	0.00	0.05	4.03		*G. crassaformis*
306-U1313B-6H-5W,45-47	A1183	1202.0	56.70	56.70	4.10	0.88						*C. wuellerstorfi*
306-U1313B-6H-5W,52-54	A254	1203.4	56.77	56.77	2.35	0.63	1.56	0.04	0.11	7.06		*G. crassaformis*
306-U1313B-6H-5W,52-54	A1311	1203.4	56.77	56.77	4.14	0.25						*C. wuellerstorfi*

NATURWISSENSCHAFTLICH-MATHEMATISCHE GESAMTFAKULTÄT

COMBINED FACULTY OF NATURAL SCIENCES AND MATHEMATICS

RUPRECHT-KARLS-
UNIVERSITÄT
HEIDELBERG

Eidesstattliche Versicherung gemäß § 8 der Promotionsordnung für die Naturwissenschaftlich-Mathematische Gesamtfakultät der Universität Heidelberg / Sworn Affidavit according to § 8 of the doctoral degree regulations of the Combined Faculty of Natural Sciences and Mathematics

1. Bei der eingereichten Dissertation zu dem Thema / The thesis I have submitted entitled

   ……

   ……

   handelt es sich um meine eigenständig erbrachte Leistung / is my own work.

2. Ich habe nur die angegebenen Quellen und Hilfsmittel benutzt und mich keiner unzulässigen Hilfe Dritter bedient. Insbesondere habe ich wörtlich oder sinngemäß aus anderen Werken übernommene Inhalte als solche kenntlich gemacht. / I have only used the sources indicated and have not made unauthorised use of services of a third party. Where the work of others has been quoted or reproduced, the source is always given.

3. Die Arbeit oder Teile davon habe ich wie folgt/bislang nicht[1)] an einer Hochschule des In- oder Auslands als Bestandteil einer Prüfungs- oder Qualifikationsleistung vorgelegt. / I have not yet/have already[1)] presented this thesis or parts thereof to a university as part of an examination or degree.

   Titel der Arbeit / Title of the thesis: ……

   Hochschule und Jahr / University and year: ……

   Art der Prüfungs- oder Qualifikationsleistung / Type of examination or degree: ……

4. Die Richtigkeit der vorstehenden Erklärungen bestätige ich. / I confirm that the declarations made above are correct.

5. Die Bedeutung der eidesstattlichen Versicherung und die strafrechtlichen Folgen einer unrichtigen oder unvollständigen eidesstattlichen Versicherung sind mir bekannt. / I am aware of the importance of a sworn affidavit and the criminal prosecution in case of a false or incomplete affidavit.

Ich versichere an Eides statt, dass ich nach bestem Wissen die reine Wahrheit erklärt und nichts verschwiegen habe. / I affirm that the above is the absolute truth to the best of my knowledge and that I have not concealed anything.

…….. ……..

Ort und Datum / Place and date — Unterschrift / Signature

[1)] Nicht Zutreffendes streichen. Bei Bejahung sind anzugeben: der Titel der andernorts vorgelegten Arbeit, die Hochschule, das Jahr der Vorlage und die Art der Prüfungs- oder Qualifikationsleistung. / Please cross out what is not applicable. If applicable, please provide: the title of the thesis that was presented elsewhere, the name of the university, the year of presentation and the type of examination or degree.

The German text is legally binding.